DISSERTATION

NANOSCALE IMAGING OF PHOTONIC AND ENERGY TRANSFER PROCESSES IN PHOTOCATALYTIC NANOMATERIALS

Submitted by

Danielle Lustig

Department of Chemistry

In partial fulfillment of the requirements

For the Degree of Doctor of Philosophy

Colorado State University

Fort Collins, Colorado

Summer 2025

Doctoral Committee:

Advisor: Justin Sambur

Amber Krummel
Alan Van Orden
Martin Gelfand

ABSTRACT

NANOSCALE IMAGING OF PHOTONIC AND ENERGY TRANSFER PROCESSES IN PHOTOCATALYTIC NANOMATERIALS

With the increasing demand for renewable energy, there is an urgent need to develop advanced materials that enhance solar energy conversion and photoelectrochemical reactions. This research addresses these challenges by investigating semiconductor nanomaterials, particularly hybrid molecule-nanocrystal composites, for next-generation photocatalysis and hydrogen production. This work focuses on two key strategies to improve light-harvesting efficiency: defect-mediated energy transfer and photon recycling. Chapters 1 through 5 explore defect-mediated energy transfer using zinc oxide nanocrystals coupled to molecular dye acceptors. Chapter 2 introduces defect-mediated energy transfer at the ensemble-level, while Chapter 3 introduces single-molecule microscopy as a tool to spatially resolve active donor–acceptor pairs and highlights the development of a single-molecule fluorescence microscopy imaging methodology to study defect-mediated energy transfer. Chapter 4 investigates single-molecule measurements of zinc oxide nanocrystal/dye conjugates, revealing how sample heterogeneity impacts energy transfer efficiency, and Chapter 5 discusses future directions to measure the defect donor transition dipole moment. Chapter 6 investigates photon recycling within nanostructured photoanode systems, where emitted photons are reabsorbed locally as a method to improve solar-to-hydrogen efficiency via a correlative widefield microspectroscopy approach. Lastly, Chapter 7 explores using single-molecule fluorescence microscopy to investigate the binding behavior of methyl viologen on the surface of single CdSe/CdS quantum dots via analysis of fluorescence blinking.

Altogether, this dissertation advances the understanding of both photonic and energy transfer mechanisms in photocatalytic nanomaterials. By integrating spectroscopic and single-particle techniques, it lays the foundation for designing hybrid nanomaterials with optimized energy flow and charge dynamics. This research paves the way for designing next-generation materials and technologies to address the pressing need for sustainable energy solutions.

ACKNOWLEDGMENTS

I would like to first thank my amazing advisor, Professor Justin Sambur for being the most encouraging mentor I could ask for. I feel incredibly lucky to have had him in my corner throughout this journey. Every interaction with Justin begins or ends with “you are doing great,” and that unwavering support has meant the world to me. Having a kind, supportive, and encouraging mentor is invaluable, and Justin has been that for me from the very beginning. I know that throughout the rest of my career, he will continue to be a mentor and role model to me. Justin has been my biggest advocate throughout graduate school; he has nominated me for awards, written many letters of recommendations, and sent me to a conference in Switzerland after only my second year in grad school! It was a pivotal experience that shaped the trajectory of my graduate research and motivated me in the years that followed. It also gave my family the opportunity to experience our first international trip together, a memory we will always cherish. Most importantly, Justin taught me what true collaboration means: creating space for each other’s feelings, questions, and ideas– not with the desire to be right, but with genuine curiosity and respect. Not only is Justin a wonderful mentor and scientist, but he is also kind, compassionate, and truly a great person. Thank you for everything.

I would like to thank all past and present members of the Sambur group. I have so many fond memories of group breakfasts at Butters, celebrating in the group office, “ault-o-ween”, and of course inner-tube water polo (my one and only appearance). I was welcomed into the group with open arms and have valued each of my relationships with every group member. I was fortunate to be a part of a kind and light-hearted group and found people who I can lean on when I was stressed (which was most of the time). Graduate school is a long and difficult journey, but

you all made every day a little easier. I want to thank Dr. Zach Nilsson, who was a fantastic mentor to me when I first joined the group. His patience, kindness, and guidance set an example that I have carried with me throughout my time here. Zach has continued to check in and support me throughout my graduate career and for that I really appreciate him.

I want to thank my committee members, Professor Amber Krummel, Professor Alan Van Orden, and Professor Martin Gelfand who have endlessly supported me throughout my PhD, wrote letters of recommendations for me, connected me with other scientists, and attended my conference talks. They were always willing to meet with me and offer advice for continuing after graduate school. They have truly been a positive support over the years, and I have been able to lean on them for help and guidance.

I want to thank Professor Shane Ardo, our fearless leader of the Department of Energy's Ensembles of Photosynthetic Nanoreactors, Energy Frontier Research Center. Shane has been a huge support person for me throughout graduate school, including writing letters of recommendation, offering scientific career advice, and always being available to help or discuss science. I have never met anyone who is as passionate and excited about science as him, and *truly* believes we can change the world. I want to thank him for being such a positive influence for me, for all his crazy ideas, and for his kindness. I know his aspirations for change will continue to inspire others, just like it did for me, for many years to come.

I want to thank all my outstanding collaborators who not only contributed to this work, but have also supported my growth as a scientist. I want to specifically thank the Dukovic group at CU Boulder (Professor Gordana Dukovic, Dr. Sophia Click, and Olivia Bird), the Patterson Group at UCI (Professor Joe Patterson, Dr. Justin Mulvey, and Raj Prasad), and Professor Kevin

Kittilstved and Dr. Enes Buz. I have been lucky to work with these scientists on multiple projects and they have provided me support and guidance both scientifically and professionally.

This research was supported as part of Ensembles of Photosynthetic Nanoreactors (EPN), an Energy Frontier Research Center funded by the U.S. Department of Energy, Office of Science (DE-SC0023431). This work received assistance from the Analytical Research Core facility at Colorado State University (SCR-021758). TEM was performed at the UC Irvine Materials Research Institute (IMRI), supported in part by the National Science Foundation Materials Research Science and Engineering Center program through the UC Irvine Center for Complex and Active Materials (DMR-2011967). Additionally, there are many people who supported this work. I want to thank Dr. Zach Nilsson, Dr. Duncan Ryan, Prof. Alan Van Orden for assistance with experimental setup, training, and providing thoughtful insight about the overall project. I want to thank Dr. Jean Chung for use of her fluorimeter for steady-state fluorescence spectroscopy experiments. I want to thank Dr. Justin Toole for assistance in writing the code for the Monte Carlo simulation. I want to thank Dr. Michael Van Erdewyk for his assistance in writing the code to fit the TRPL data. Lastly, thank you to Dr. Rebecca Miller of the Analytical Resource Core for help with XPS measurements and analysis.

I want to thank my REU advisor, Dr. Leah Casabianca, for giving me my first laboratory research opportunity and for convincing me to apply to graduate school– an encouragement that set me on this path. I am also deeply grateful to my wonderful undergraduate professors at the University of Puget Sound. Whether checking in on me while I studied in Harned Hall or Oppenheimer Café, celebrating my first publication with genuine excitement, or even inviting my REU advisor to give a lecture at UPS, their support has meant so much. Their encouragement

didn't stop at graduation– they have continued to support me throughout my graduate journey, and for that, I am incredibly thankful.

I want to thank my family for their unwavering long-distance love and support. I was lucky to group up in a creative and academically driven family, where our dinner conversations would be centered around the key question, "what did you learn to do today that you didn't know how to do yesterday?" I owe much of my scientific curiosity to my dad, who always encouraged me to explore, build, and question the world around me. Watching MythBusters together as a kid sparked my fascination with experimentation, and that curiosity only grew from there. In fourth grade, we built a Rube Goldberg machine, affectionately nicknamed the "Waternator 3000", and I never looked back. Your approach to projects, no matter how big or small, shaped the way I tackle challenges. When we set out to build a cabin from 2,000 popsicle sticks in third grade, you didn't hesitate to buy a giant circular saw to make the cuts easier and to turn our garage completely into our cabin workshop. The final product was so impressive that my classmates didn't even believe we had made it ourselves! Moments like these instilled in me the drive to not just complete a task, but to go above and beyond– just as you always say, *if you're going to do it, overdo it.*

I want to thank my mom for her endless love and support in all my academic endeavors. From my fourth and fifth-grade application to the Magnet Program to where I am today, you have been by my side every step of the way. Your dedication and passion have always been an inspiration to me. Going back to graduate school while raising three girls to pursue your dream of teaching English as a second language is a testament to your perseverance, love for learning, and changing lives. I can only hope to love what I do just as much as you. Thanks to you, I strive to lead by the idea that *people may not remember what you said or what you did, but they will always remember how you made them feel*.

Both my older sisters have excelled in traditionally male-dominated fields and their achievements have been a constant source of inspiration for me. I cherish all our sister FoCo visits and look forward to the day where I can finally treat both of you! Growing up, I was always following in both of your footsteps. Because of Allie's academic excellence, my teachers held me to high expectations. With Robbie, however, they approached me with some skepticism, expecting trouble– though they never failed to brag about how funny and colorful her personality was. Of course, we all found our way as a computer engineer, a lawyer, and a scientist. Thank you for being the best older sisters and supporting your pequeña with any and every "Endeavor".

I want to thank my friends for providing endless long-distance support and for checking in the only way you knew how, asking "how are the lasers and crystals?" I want to thank them for all the coffee Venmos and giving me grace when I would be heads down for months on end and not always have the time or bandwidth for regular catchups. I also want to thank all my lifelong friends I have made here since moving to Fort Collins. They have offered endless support and community while navigating grad school.

Finally, to my wonderful partner Drew– words cannot begin to describe how thankful I am to have you by my side. Our senior year together at UPS, when I said I wanted to attend graduate school, there was no hesitation from you that you were going to come with me. We trekked from Seattle to Fort Collins in 2020 at the height of COVID and moved into our 570 square foot apartment, where you had to listen to all my online chemistry lectures during the pandemic. Since then, you have listened to countless practice talks, celebrated any and every achievement (big or small), and always believed in me even when I struggled to believe in myself. Of course, it is not always easy being away from our hometown and moving across the country (and soon, the world), so I want to thank you for embarking on and continuing this journey with me. You are my rock

through the windiest of storms, and I truly could not have done this without you. I am so excited for our next adventures ahead (now me, you, and Banjo). Thank you for everything.

DEDICATION

This work is dedicated to those in the acknowledgements, as well as my friends and family for their love and support. Thank you for everything.

TABLE OF CONTENTS

ABSTRACT ii
ACKNOWLEDGMENTS iv
DEDICATION x
CHAPTER 1: INTRODUCTION TO FÖRSTER RESONANCE ENERGY TRANSFER (FRET) AND DEFECT-MEDIATED ENERGY TRANSFER 1
1.1 Introduction to Förster Resonance Energy Transfer (FRET) 1
1.2 Introduction to Defect-Mediated Energy Transfer 2
1.3 Overview of the Following Dissertation Chapters 3
1.4 Professional and Research Development 5
REFERENCES 8
CHAPTER 2: CHARACTERIZING THE LIGAND SHELL MORPHOLOGY OF PEG-COATED ZnO NANOCRYSTALS USING FRET SPECTROSCOPY 9
2.1 Overview 9
2.2 Introduction 10
2.3 Methods 13
2.3.1 Uncoated ZnO NC Synthesis (ZnO-0) 13
2.3.2 PEG-silane coated ZnO Nanocrystal Synthesis 14
2.3.3 Nanocrystal Characterization 15
2.3.4 EnT Measurements 16
2.4 Results 17
2.4.1 Sample Design and Characterization 17
2.4.2 Defect-Mediated EnT between ZnO NC Donors and Dye Acceptors 20
2.4.3 EnT Efficiency as a Function of Ligand Chain Length 23
2.5 Discussion 27
2.6 Conclusion 33
2.7 Author Contributions 34
REFERENCES 35
CHAPTER 3: TOWARDS IMAGING DEFECT-MEDIATED ENERGY TRANSFER BETWEEN SINGLE NANOCRYSTAL DONORS AND SINGLE MOLECULE ACCEPTORS 41

3.1 Overview 41
3.2 Introduction 42
3.3 Experimental Methods 45
3.3.1 Nanocrystal Synthesis 45
3.3.2 Nanocrystal Characterization 45
3.3.3 Single Molecule Fluorescence Microscopy 46
3.4 Results 47
3.4.1 Ensemble-level Defect-mediated EnT Between ZnO NCs and A555 47
3.4.2 Single Molecule, Single NC-level Imaging Methodology 48
3.4.3 Super-resolution Imaging Analysis of ZnO/NC Pairs 51
3.4.4 Single molecule, Single NC-level Trajectory Analysis 52
3.4.5 Single molecule, single NC-level Channel Ratio Analysis 56
3.5 Discussion 58
3.6 Conclusion 60
3.7 Author Contributions 61
REFERENCES 62
CHAPTER 4: SINGLE-MOLECULE FLUORESCENCE MICROSCOPY REVEALS ENERGY TRANSFER ACTIVE VERSUS INACTIVE NANOCRYSTAL/DYE CONJUGATE PAIRS .. 68
4.1 Overview 68
4.2 Introduction 69
4.3 Methods 71
4.3.1 Materials 71
4.3.2 Synthesis of APTMS Capped ZnO Nanocrystals 72
4.3.3 Dye Chemical Conjugation 72
4.3.4 Nanocrystal Characterization 73
4.3.5 Single Molecule Fluorescence Microscopy 74
4.3.6 Kinetic Monte Carlo (kMC) simulations 74
4.4 Results 76
4.4.1 A555/APTMS/ZnO Conjugate and Ensemble-level EnT Characterization 76
4.4.2 Single NC, single molecule-level imaging of defect-mediated EnT 81
4.4.3 Single-Molecule Statistical Analyses 89
4.5 Discussion 93
4.6 Conclusion 97
4.7 Author Contributions 97

CHAPTER 5: OUTLOOK AND FUTURE DIRECTIONS: IDENTIFYING THE DEFECT DONOR TRANSITION DIPOLE MOMENT FOR CONTROLLING ENERGY FLOW IN NANOCRSYTAL/MOLECULE ENERGY TRANSFER SYSTEMS 104
5.1 Overview 104
5.2 Introduction 105
5.3 Future Directions to Measure the Three-dimensional Defect Donor Transition Dipole Orientation in ZnO NCs 108
5.3.1 Experimental Methods 110
5.3.2 Expected Results 113
5.4 Future Directions to Demonstrate controlled directionality of an Emitted Photon based on the Orientation of the Transition Donor Dipole within an NC Crystal Lattice 114
5.4.1 Experimental Methods 115
5.4.2 Expected Results 116
REFERENCES 119
CHAPTER 6: MODELS AND MEASUREMENTS QUANTIFY PHOTON RECYCLING, CHARGE CARRIER DIFFUSION, AND PHOTON SCATTERING CONTRIBUTIONS TO PHOTOLUMINESCENCE IN InP NANOWIRE ARRAYS 124
6.1 Overview 124
6.2 Introduction 125
6.3 Experimental & Theoretical Methods 130
6.3.1 Sample preparation 130
6.3.3 Reflectance and Absorptance Characterization 131
6.3.4 Spatially and Temporally Correlated PL Microspectroscopy and Widefield PL Imaging 132
6.3.5 Geometric Predictions of Re-absorption Probability 133
6.3.6 MC simulations 133
6.3.7 Continuum-Level Modeling Domain and Assumptions 134
6.4 Results and Discussion 136
6.5 Conclusion 153
6.6 Author Contributions 155
REFERENCES 156
CHAPTER 7: SINGLE-MOLECULE ANALYSIS OF METHYL VIOLOGEN BINDING TO CdSe/CdS CORE-SHELL QUNTUM DOTS VIA PHOTOLUMINESCENCE BLINKING ... 161

7.1 Overview 161
7.2 Introduction 160
7.3 Methods 164
7.3.1 Materials 164
7.3.2 Preparation of Cd-Oleate Precursor 164
7.3.3 Synthesis of CdSe Quantum Dots 164
7.3.4 Synthesis of CdSe/CdS Core-Shell Quantum Dots 165
7.3.5 Quantum Dot Characterization 166
7.3.6 Ensemble-level Charge Transfer Measurements 167
7.3.7 Sample Preparation for Imaging 167
7.3.8 Single-Molecule Fluorescence Microscopy 168
7.4 Results 168
7.5 Discussion 175
7.6 Conclusion 178
7.7 Author Contributions 179
REFERENCES 181
CHAPTER 8: SUMMARY AND OUTLOOK 184
APPENDIX A: SUPPORTING INFORMATION FOR CHAPTER 2 186
APPENDIX B: SUPPORTING INFORMATION FOR CHAPTER 3 193
APPENDIX C: SUPPORTING INFORMATION FOR CHAPTER 4 207
APPENDIX D: SUPPORTING INFORMATION FOR CHAPTER 6 215
APPENDIX E: SUPPORTING INFORMATION FOR CHAPTER 7 248

CHAPTER 1: INTRODUCTION TO FÖRSTER RESONANCE ENERGY TRANSFER (FRET) AND DEFECT-MEDIATED ENERGY TRANSFER

1.1 Introduction to Förster Resonance Energy Transfer (FRET)

Förster Resonance Energy Transfer (FRET) is a non-radiative process by which energy is transferred from an excited donor molecule to an acceptor molecule through long range dipole-dipole interactions.[1] FRET has been widely studied in molecular systems and is referred to as a "spectroscopic ruler" in molecular and biomolecular systems due to small changes in donor-acceptor distance (R) causing large changes in fluorescence intensities and the overall energy transfer efficiency.[2,3] In a FRET process, the energy of an excited donor is transferred to a ground-state acceptor positioned in its vicinity through Coulombic dipole−dipole interactions.[4,5] The efficiency and rate of energy transfer (EnT) are governed by the distance between the donor and the acceptor (typically 10 nm or less), the extent of spectral overlap between the emission of the donor and the absorption of the acceptor, and the relative orientation of the donor and acceptor transition dipole moments with respect to each other.[4,5] The term 'resonance' signifies that in order for the FRET interaction to occur, the electronic excited states of the donor and acceptor need to have some correspondence between their energy levels.[6] This factor is incorporated in FRET theory by the overlap integral which describes the probability that transitions in the donor and acceptor will have the same frequency (i.e. be in resonance) as shown in Equation 1.[5,6] In Equation 1, $F_D(\lambda)$ is the normalized emission spectrum of the donor and $\varepsilon_A(\lambda)$ is the extinction coefficient spectrum for the acceptor with units of $M^{-1}cm^{-1}$.[5]

$$J(\lambda) = \int_0^\infty F_D(\lambda)\varepsilon_A(\lambda)\lambda^4 d\lambda \qquad \text{(Eq. 1.1)}$$

The rate of EnT, $k_T(r)$ is given by Equation 2 where the lifetime of the donor is τ_D in the absence of the acceptor, the Förster distance is R_0, and the average donor-acceptor distance R.[5]

$$k_T(r) = \frac{1}{\tau_D}\left(\frac{R_0}{R}\right)^6 \quad \text{(Eq. 1.2)}$$

The Förster distance (R_0) is defined by Equation 3 in terms of the overlap integral J, the quantum yield of the donor Q_D, the dipole orientation factor κ^2, N_A is Avogadro's number, and n is the refractive index of the medium.[5]

$$R_0 = \sqrt[6]{\frac{9000\ln(10)\kappa^2 Q_D J}{128\pi^5 N_A n^4}} \quad \text{(Eq. 1.3)}$$

Lastly, FRET efficiency can be calculated using the Förster distance and the average donor-acceptor distance as shown in Equation 4.[5] This equation depicts that FRET efficiency scales with R^{-6} distance dependence for dipole-dipole EnT systems.

$$E = \frac{1}{1+\left(\frac{R}{R_0}\right)^6} \quad \text{(Eq. 1.4)}$$

1.2 Introduction to Defect-Mediated Energy Transfer

Defects in semiconductor nanocrystals (NCs), such as ZnO or perovskites, can introduce localized states within the bandgap that participate in EnT processes.[7] These defect states can serve as intermediate energy levels, facilitating non-radiative EnT to acceptor molecules in a manner similar to traditional FRET, but influenced by defect-related recombination processes. This mechanism enables tunable EnT properties that depend on the density and nature of the defects.

1.3 Overview of the Following Dissertation Chapters

This research aims to improve solar energy conversion in semiconductors through controlling energy flow from donor NCs to acceptor dye molecules through utilizing intrinsic defects in the crystal lattice, a concept most of the community believes to be a hindrance rather than an opportunity to enhance device performance and provide a sustainable pathway for solid-state lighting. Chapter 1 introduces the concept of defect-mediated EnT at the ensemble level, using a model system of ZnO NCs and dye acceptors.[8] This chapter explores the potential of utilizing defects to enhance EnT and improve solar energy conversion efficiency and evaluated the validity of the point dipole approximation via a spectroscopic distance-dependence FRET study. However, ensemble-level studies are limited by the inability to spatially resolve individual defect sites, necessitating the use of single-molecule fluorescence microscopy to pinpoint emissive defect locations and distinguish active acceptor dye molecules.

Chapter 2 outlines progress in the development of a super-optical resolution imaging method to pinpoint defects on single ZnO nanocrystals.[9] A key scientific achievement of this work is the development of an alternating ultraviolet-visible laser excitation pulse sequence combined with multicolor photon detection, which successfully distinguishes between isolated nanocrystals and nanocrystals coated with molecules. This research provides a molecular-level description of the role defects and surface facets play in EnT, paving the way for controlling energy flow between nanocrystals and molecules, an exciting prospect for photocatalysis and solid-state lighting applications.

Chapter 3 presents work in single-molecule measurements of conjugate systems. The efficiency of EnT is influenced by the number of dye molecules attached to each NC and the donor-acceptor distance, both of which vary across individual NCs in a sample. While ensemble-level

steady-state and time-resolved fluorescence spectroscopy have provided average values for donor-acceptor distances, dye-to-NC ratios, and EnT rate constants in colloidal samples, questions remain about the impact of donor/acceptor heterogeneity on observed EnT efficiencies. Notably, ensemble measurements cannot distinguish between bare NCs, EnT-active NC/dye pairs, and inactive conjugates, limiting the ability to design systems with 100% EnT efficiency. To address this, defect-mediated EnT between ZnO NC donors and AlexaFluor dye acceptors was studied at the single-molecule and single-nanocrystal levels. Super-optical resolution imaging analysis revealed that 16% of the colloidal ZnO/dye conjugate sample consists of bare ZnO NCs and 20% of dye/NC pairs are EnT-inactive, likely contributing to residual defect photoluminescence (PL) observed in ensemble-level measurements and reducing overall EnT efficiency. Additionally, PL trajectories of NC/dye conjugates exhibited distinct micro-fluctuations, which are absent in isolated ZnO NCs. The micro-fluctuations indicate a dynamic EnT process where the ZnO/dye conjugate fluctuates between EnT "on" and "off" states faster than the millisecond time resolution of the experiment, supported by a photophysical model analyzed via kinetic Monte Carlo (kMC) simulations. These findings highlight the impact of sample heterogeneity on EnT processes and provide insights for designing light-harvesting systems with optimized EnT efficiency. Future aims of this research include imaging single defects on larger nanostructures and exploiting their photocatalytic properties. The transformative outcome of this work will result in a molecular-level description of the role of defects in the EnT process and ultimately enable the nanoscience community to control energy flow between NCs and molecules, creating exciting opportunities for photocatalysis and solid-state lighting applications. Chapter 5 discusses the identification of the defect donor transition dipole moment for controlling energy flow in nanocrystal/molecule EnT systems.

Understanding the dipole orientation of defect states is crucial for optimizing EnT efficiency and designing energy conversion systems that leverage defect-mediated pathways.

Chapter 6 addresses photon recycling, a process that enhances efficiency by re-absorbing emitted light between neighboring nanoreactors in an ensemble to improve solar-to-hydrogen conversion efficiency. The mutual influence of several proximal nanoreactors was characterized using a simultaneous widefield/confocal PL microspectroscopy technique developed to compare widefield maps from optical excitation on single and neighboring nanoreactors with correlative scanning electron microscopy images. Lastly, Chapter 7 focuses on current research analyzing charge transfer through single-molecule blinking trajectory measurements of core-shell CdS/CdSe quantum dots coupled with methyl viologen.

Together, this dissertation research addresses critical challenges in sustainable energy by advancing the understanding of defect-mediated EnT, photocatalysis, and photon recycling. By investigating the role of defects in semiconductor nanomaterials, this work contributes to improving solar energy conversion and hydrogen production, providing insights into the development of next-generation materials for sustainable energy technologies.

1.4 Professional and Research Development

This dissertation investigates defect-mediated EnT across multiple scales and systems. This first chapter of this dissertation investigates defect-mediated EnT at the ensemble-level using steady-state and time-resolved PL spectroscopy, which resulted in a publication in the Journal of Physical Chemistry B (Lustig, D., Buz, E., Mulvey, J., Patterson, J., Kittilstved, K., and Sambur, J., Characterizing the Ligand Shell Morphology of PEG-Coated ZnO Nanocrystals Using FRET Spectroscopy, *J Phys Chem B* **2023** *127* (41), 8961-897)[8]. Chapter 2 explores the development of a fluorescence microscopy imaging technique to evaluate defect-mediated EnT at

the single-molecule level, which was published in the Journal of Chemical and Biomedical Imaging (Lustig, D., Nilsson, N., Mulvey, J., Zang, W., Pan, X., Patterson, J., and Sambur, J., Toward Imaging Defect-Mediated Energy Transfer between Single Nanocrystal Donors and Single Molecule Acceptors, *Chem. Biomed. Imaging* **2023** *1* (2), 168-178).[9] Chapter 3 shows the use of the developed imaging methodology on evaluating the defect-mediated EnT activity in ZnO NC/dye conjugate pairs, published in the Journal of Chemical and Biomedical Imaging (Lustig, D., Buz, E., Mulvey, J., Prasad, P., Bird, O., Dukovic, G., Kittilstved, K., Patterson, J., and Sambur, J., Single-Molecule Fluorescence Microscopy Reveals Energy Transfer Active versus Inactive Nanocrystal/Dye Conjugate Pairs, *Chem. Biomed. Imaging* **2025,** https://doi.org/10.1021/cbmi.5c00009).[10] Chapter 4 outlines future directions, including polarization-resolved measurements to analyze the transition dipole moment of defect donors; this work contributed to a successful user proposal at the Los Alamos National Laboratory Center for Integrated Nanotechnologies (Lustig, D., Sambur, J., Van Orden, A., Imaging Defect-Mediated Energy Transfer between Single Nanocrystal Donors and Single Molecule Acceptors. Los Alamos National Laboratory Center for Integrated Nanotechnologies User Proposal, #2024AU0169).

As part of the Department of Energy's Energy Frontier Research Center (EFRC), *Ensembles of Photochemical Nanoreactors*, Chapter 5 investigates photon recycling in pseudo-random arrays of III–V nanowires. This Chapter shows the development of a custom-built simultaneous widefield/confocal photoluminescence microspectroscopy technique that resolves optical coupling phenomena between individual nanoreactors, which was published in the Journal of Physical Chemistry C (Lustig, D., Chen, F., Zhang, W., Bird, O., J., Fajardo Jr. Ardo, S., Hu, S., Talin, A., Bala Chandran, R., and Sambur, J., Models and Measurements Quantify Photon

Recycling, Charge-Carrier Diffusion, and Photon Scattering Contributions to Photoluminescence in InP Nanowire Arrays, *J Phys Chem C* **2025**, 129, 17, 8270–8283).[11]

My dissertation research has culminated in four first-author peer-reviewed publications, over ten conference posters and presentations, including the opportunities to attend and present at an international Gordon Research Conference, speaking at the American Chemical Society's Fall 2024 Meeting's *Rising Stars in Analytical Chemistry* symposium, and presenting at the 2023 EFRC PI Meeting. Additionally, this research has been supported by competitive fellowships from CSU's College of Natural Sciences, the Department of Chemistry, and the Energy Institute, including the Office of the Vice President for Research Fellowship, the Teresa Fonseca Memorial award, the Kathleen, Thor, and Kara Juneau Fellowship in Chemistry, the Gary E. Maciel Fellowship, and a Cogen Summer Intern Fellowship at CSU's Energy Institute.

Mentorship has been a cornerstone of my graduate research. I have supervised four STEM undergraduate researchers via the CSU MURALS program, one M.A. student in teaching English as a foreign language via the CSU graduate peer mentoring program, one physics M.S. student, and one physical chemistry Ph.D. student. My mentees contributed to experimental design, data collection, and presentations. Many have since gone on to pursue graduate or professional careers in science and engineering.

REFERENCES

(1) Förster, T. Zwischenmolekulare Energiewanderung und Fluoreszenz. *Ann. Phys.* **1948**, *437* (1–2), 55–75. https://doi.org/10.1002/andp.19484370105.
(2) Nilsson, Z. N.; Beck, L. M.; Sambur, J. B. Ensemble-Level Energy Transfer Measurements Can Reveal the Spatial Distribution of Defect Sites in Semiconductor Nanocrystals. *J. Chem. Phys.* **2021**, *154* (5), 054704. https://doi.org/10.1063/5.0034775.
(3) Sobakinskaya, E.; Schmidt am Busch, M.; Renger, T. Theory of FRET "Spectroscopic Ruler" for Short Distances: Application to Polyproline. *J. Phys. Chem. B* **2018**, *122* (1), 54–67. https://doi.org/10.1021/acs.jpcb.7b09535.
(4) Sadhu, S.; Tachiya, M.; Patra, A. A Stochastic Model for Energy Transfer from CdS Quantum Dots/Rods (Donors) to Nile Red Dye (Acceptors). *J. Phys. Chem. C* **2009**, *113* (45), 19488–19492. https://doi.org/10.1021/jp906160z.
(5) Govorov, A.; Hernández Martínez, P. L.; Demir, H. V. *Understanding and Modeling Förster-Type Resonance Energy Transfer (FRET)*; SpringerBriefs in Applied Sciences and Technology; Springer Singapore: Singapore, 2016. https://doi.org/10.1007/978-981-287-378-1.
(6) Andrews, D. L.; Curutchet, C.; Scholes, G. D. Resonance Energy Transfer: Beyond the Limits. *Laser Photonics Rev.* **2011**, *5* (1), 114–123. https://doi.org/10.1002/lpor.201000004.
(7) Zheng, X.; Hou, Y.; Sun, H.-T.; Mohammed, O. F.; Sargent, E. H.; Bakr, O. M. Reducing Defects in Halide Perovskite Nanocrystals for Light-Emitting Applications. *J. Phys. Chem. Lett.* **2019**, *10* (10), 2629–2640. https://doi.org/10.1021/acs.jpclett.9b00689.
(8) Lustig, D. R.; Buz, E.; Mulvey, J. T.; Patterson, J. P.; Kittilstved, K. R.; Sambur, J. B. Characterizing the Ligand Shell Morphology of PEG-Coated ZnO Nanocrystals Using FRET Spectroscopy. *J. Phys. Chem. B* **2023**, *127* (41), 8961–8973. https://doi.org/10.1021/acs.jpcb.3c04900.
(9) Lustig, D. R.; Nilsson, Z. N.; Mulvey, J. T.; Zang, W.; Pan, X.; Patterson, J. P.; Sambur, J. B. Toward Imaging Defect-Mediated Energy Transfer between Single Nanocrystal Donors and Single Molecule Acceptors. *Chem. Biomed. Imaging* **2023**, *1* (2), 168–178. https://doi.org/10.1021/cbmi.3c00015.
(10) Lustig, D. R.; Buz, E.; Bird, O. F.; Mulvey, J. T.; Prasad, P. R.; Patterson, J. P.; Dukovic, G.; Kittilstved, K. R.; Sambur, J. B. Single-Molecule Fluorescence Microscopy Reveals Energy Transfer Active versus Inactive Nanocrystal/Dye Conjugate Pairs. *Chem. Biomed. Imaging* **2025**, cbmi.5c00009. https://doi.org/10.1021/cbmi.5c00009.
(11) Lustig, D. R.; Chen, F.; Zhang, W.; Bird, O. F.; Fajardo, J.; Ardo, S.; Hu, S.; Dukovic, G.; Talin, A. A.; Bala Chandran, R.; Sambur, J. B. Models and Measurements Quantify Photon Recycling, Charge-Carrier Diffusion and Photon Scattering Contributions to Photoluminescence in InP Nanowire Arrays. *J. Phys. Chem. C* **2025**, *129* (17), 8270–8283. https://doi.org/10.1021/acs.jpcc.5c01618.

CHAPTER 2: CHARACTERIZING THE LIGAND SHELL MORPHOLOGY OF PEG-COATED ZnO NANOCRYSTALS USING FRET SPECTROSCOPY[1]

2.1 Overview

Polyethylene glycol (PEG) ligands can inhibit proteins and other biomolecules from adhering to underlying surfaces, making them excellent surface ligands for nanocrystal-based drug carriers. Quantifying the PEG ligand shell morphology is important because its structure determines the permeability of biomolecules through the shell to the nanocrystal (NC) surface. However, few in situ analytical tools can reveal whether the PEG ligands form either an impenetrable barrier or a porous coating surrounding the NC. Here, we present a Förster resonance energy transfer (FRET) spectroscopy-based approach that can assess the permeability of molecules through PEG-coated ZnO NCs. In this approach, ZnO NCs serve as FRET donors and freely diffusing molecules in the bulk solution are FRET acceptors. We synthesized a series of variable chain length PEG-silane-coated ZnO NCs such that the longest chain length ligands far exceed the Förster radius (R_0), where the energy transfer (EnT) efficiency is 50%. We quantified the EnT efficiency as a function of ligand chain length using time-resolved photoluminescence lifetime (TRPL) spectroscopy within the framework of FRET theory. Unexpectedly, the longest PEG-silane ligand showed equivalent EnT efficiency as bare, hydroxyl-passivated ZnO NCs. These results indicate that the "rigid shell" model fails, and the PEG ligand shell morphology is more likely porous or in a patchy "mushroom state", consistent with transmission electron microscopy

[1]Reproduced with permissions from Lustig, D., Buz, E., Mulvey, J., Patterson, J., Kittilstved, K., and Sambur, J. Characterizing the Ligand Shell Morphology of PEG-Coated ZnO Nanocrystals Using FRET Spectroscopy. Journal of Physical Chemistry B 2023, 127(41): 8961-8973. Copyright 2023, American Chemical Society.

data. While the spectroscopic measurements and data analysis procedures discussed herein cannot directly visualize the ligand shell morphology in real space, the in-situ spectroscopy approach can provide researchers with valuable information regarding the permeability of species through the ligand shell under practical biological conditions.

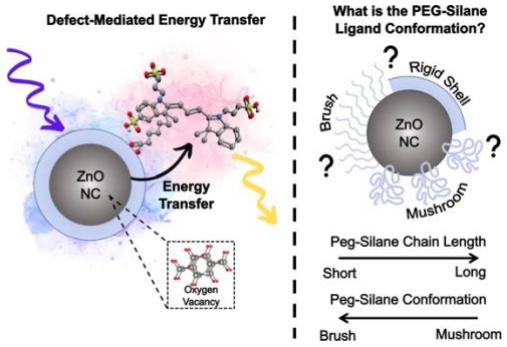

Figure 2.1. Chapter 1 overview: cartoon illustration of defect-mediated EnT between ZnO NC donors and A555 acceptors. Identifying the PEG-silane ligand conformation through FRET spectroscopy.

2.2 Introduction

Nanocrystals (NCs) are attractive image contrast agents[1–3] and drug delivery vehicles[2–10] due to their high photostability and diverse surface functionality.[1,4–6,11] NC surfaces can be tailored with surface capping ligands that serve multiple purposes. First, the ligand chemistry and structure determines how the NC interacts with the environment, such as the ability to target and bind specific biomolecules via receptors.[11–15] Second, ligand properties determine the colloidal stability of NCs.[11,14–17] Understanding the ligand shell morphology is important because it partially determines the long-term colloidal stability and chemical and/or structural integrity of the NC core.

Of all the candidate ligands, PEG-containing ligands with anchoring groups to the NC core are widely employed and studied for pharmaceutical and other biomedical applications.[14,18] PEG is widely used as a "gold standard" polymer in nanomedicine because it can extend the half-life of drug carriers by prolonging circulation in the bloodstream, thereby improving drug efficacy.[5,6,19–22] PEG chains achieve this long-term stability by inhibiting plasma proteins and other biomolecules

from adhering to NC surfaces.[12,23–30] This beneficial stability requires the PEG ligand shell to form an impenetrable barrier between the NC core and external environment.

Monitoring protein adsorption through PEG ligands has been used as a proxy to study the surface coating morphology because adsorption of plasma proteins to the underlying NC is the most influential factor deciding NC stability for drug delivery applications.[6] Considerable research efforts on plasma protein adsorption to NC surfaces has revealed some degree of permeability through PEG barriers.[12,23,24,26] Du et al. showed that coating a lipid monolayer with PEG5000 (molecular weight (MW) = 5000 Da)[31] inhibits protein absorption when the lipid surface is completely covered by PEG.[25] Under these high coverage conditions, grafting density calculations predicted that the PEG coating adopts a brush-like conformation, resulting in the inhibition of protein adhesion.[25] Conversely, Gref et al. observed that increasing the PEG MW above 5000 units does not further decrease or completely inhibit plasma protein adsorption.[26] Hence, experimental observations of permeability through PEG membranes, as evidenced by plasma protein adsorption to the underlying NC surface are not completely consistent,[6,12] and likely vary due to the MW and surface density of the PEG ligand.[28] Conflicting reports on PEG's ability to inhibit protein adsorption or corona formation[32] has questioned its efficacy for drug delivery applications.[5,19,33,34]

One possible reason for the conflicting reports on PEG coating durability is that few straightforward analytical techniques exist that have the potential to characterize the ligand shell permeability under practical conditions for drug delivery (e.g., at room temperature and in a complex solvent matrix). ^{1}H NMR spectroscopy can be used to determine the interactions between PEG ligands and estimate the ligand density coverage (ligands/nm^2).[35,36] The ^{1}H NMR relaxation time has been used to determine the PEG chain conformation near a solid surface.[28] However, assigning the peaks can be challenging and long data acquisition times are necessary, which limits

the ability to quantify or even detect dynamic changes in the surface coating.[36] Furthermore, sample preparation such as freeze-drying causes particle aggregation, which complicates data interpretation due to an unknown amount of PEG-coated surface area.[6] Dynamic light scattering (DLS) spectroscopy can measure protein and biomolecule MW distributions in solution.[37] This technique measures changes in the Brownian motion of particles,[37] which could be related to whether the NCs are coated by a thin dense shell or a thick porous coating.[38] Difficulties in sample preparation and methods to characterize the surface ligand structure under practical conditions[6,35] has motivated computer simulations to predict PEG morphology under various conditions.[6,12,39] Experimental techniques are needed to assess the PEG ligand shell morphology and/or permeability under the same solution-phase conditions as the simulations.

Here, we develop a FRET spectroscopy-based approach to characterize PEG ligand shell permeability in liquid solvent at room temperature. FRET has been applied as a "spectroscopic ruler" for measuring intermolecular distances between peptides[40] and quantifying real-time dynamic changes of proteins[41] and DNA[42] under biologically relevant conditions. In this study, PEG-silane coated colloidal ZnO semiconductor NCs serve as FRET donors and Alexa Fluor 555 (A555) dye molecules are FRET acceptors. ZnO NCs were chosen as a model metal oxide NC core material because (1) ZnO NCs are non-toxic, inexpensive, and have excellent biocompatibility;[7,8,43–45] (2) ZnO is listed as a safe substance by the United States Food and Drug Administration and exhibits long-term stability in air and sunlight;[1,46] and (3) ZnO NCs exhibit a broad visible "defect" emission upon being excited with supra-bandgap illumination and a wide range of commercially available acceptor dye molecules can engage in defect-mediated EnT with the NC core.[47–50] We synthesized a series of variable chain length PEG-coated NCs and characterized EnT efficiency as a function of PEG chain length. We hypothesized that if the PEG-

silane ligand acts as a rigid shell with radius R surrounding the NC core, then EnT efficiency would decrease with increasing chain length with an R^{-6} dependence, in agreement with FRET theory.[51,52] TRPL measurements showed that EnT efficiency initially decreased with increasing chain length, but not with the expected R^{-6} dependence. Surprisingly, EnT efficiency increased even as the ligand length increased far beyond the critical Förster radius R_0, where EnT efficiency is 50%. We discuss the most likely ligand shell morphology based on literature and transmission electron microscopy (TEM) data. We envision that this FRET spectroscopy-based approach can be applied to a wide range of organic or inorganic ligand-coated NC materials.

2.3 Methods

2.3.1 Uncoated ZnO NC Synthesis (ZnO-0)

The following reagents were purchased and used as received: zinc acetate dihydrate ($Zn(OAc)_2 \cdot 2H_2O$, Sigma Aldrich or Fisher), 200-proof ethanol (100%, Pharmco-Aeper), ethanol (spectroscopic grade, Sigma Aldrich), tetramethylammonium hydroxide (TMAOH, 25% in methanol, Sigma Aldrich), tetramethylammonium hydroxide pentahydrate ($TMAOH \cdot 5H_2O$, 97%, Acros Organics), heptane (99.6% Fisher), and hexanes (99.9%, Fisher). The following PEG-silanes were purchased from Gelest, Inc. and used as received: methoxytriethyleneoxypropyltrimethoxysilane (PEG-3, 92%), 3-[methoxy(polyethyleneoxy)$_{6\text{-}9}$propyl]trimethoxysilane (PEG-(6-9), 90%, technical grade), 3-[methoxy(polyethyleneoxy)$_{9\text{-}12}$propyl]trimethoxysilane (PEG-(9-12), technical grade), and 3-[methoxy(polyethyleneoxy)$_{21\text{-}24}$propyl]trimethoxysilane (PEG-(21-24), technical grade). The fluorescent dye, A555 carboxylic acid, tris(triethylammonium) salt was received as a powder and dissolved in spectrophotometric grade ethanol to a final concentration of 600 nM (Thermo Fisher, catalog number A33080).

ZnO NCs were synthesized via a base hydrolysis reaction using zinc acetate dihydrate in ethanol, following the approach of Wood et al.[53] This reaction produces ZnO NCs coated with acetate and hydroxyl groups. We refer to this sample as ZnO-0 because no PEG ligands are present on the ZnO NC surface. In a typical reaction, $Zn(OAc)_2 \cdot 2H_2O$ (1.0 g, 4.56 mmol) was dissolved in ethanol (100 mL) in a 250-mL round bottom flask. The solution was heated to 68 °C and stirred to ensure the complete dissolution of the zinc acetate. Once the zinc acetate precursor dissolved, 2 mL of a 25% methanolic solution of TMAOH was added to the flask as quickly as possible and initiated ZnO nucleation and growth via base-catalyzed hydrolysis and condensation. We define the TMAOH injection step as $t = 0$. At $t = 378$ min, 10 mL of the reaction mixture was extracted from the flask and injected into 30 mL of hexanes, causing the NCs to precipitate. This reaction time produces 4.3 ± 0.5 nm diameter ZnO NCs.[54] The mixture was centrifuged to separate the NCs from the unreacted Zn^{2+} and TMAOH. The supernatant was discarded and the NCs were resuspended in spectrophotometric grade ethanol. This washing procedure was repeated five times. The washed NCs were stored at 4°C. All reagents were used as received and without further purification.

2.3.2 PEG-silane coated ZnO Nanocrystal Synthesis

Silane-capped colloidal ZnO NCs were synthesized by the modification of the ZnO-0 NC synthesis. In a typical reaction, $Zn(OAc)_2 \cdot 2H_2O$ (0.88 g, 4.0 mmol) was dissolved in ethanol (20 mL) at 75 °C under argon flow. Prior to addition of the hydroxide reactant, PEG-silane (40 mol% relative to the zinc precursor, 0.4 equivalent of PEG-silane to Zn^{2+}) was added while stirring. The reaction was initiated by dropwise addition of an ethanolic solution of 1 M TMAOH (8 mL), prepared from $TMAOH \cdot 5H_2O$ over the course of ~3 minutes. The reaction was allowed to continue at 75 °C for 30 minutes after TMAOH addition. The flask was then cooled down to room

temperature and the PEG-silane ZnO NCs were precipitated from ethanol by adding heptane and collected via centrifugation. The NCs were washed with heptane three times, resuspended in ethanol, and stored in the fridge at 4 °C. For all PEG-silane coated ZnO NC syntheses the mole ratio of OH^-:Zn^{2+} was 2 and the [OH^-]:[Zn^{2+}] concentration ratio was 5.

2.3.3 Nanocrystal Characterization

The absorbance and emission properties of the ZnO NCs were characterized by UV-Vis absorption spectroscopy and steady-state photoluminescence (PL) spectroscopy (Horiba Duetta Fluorescence and Absorbance Spectrometer). All spectra were measured at room temperature using colloidal NC suspensions in spectrophotometric grade ethanol and 1 cm pathlength quartz cuvettes. Figure A1 shows the absorbance spectra of all PEG-silane ligands. The absolute quantum yield (QY) measurement method was used to determine the PL QY of the NC defect emission (Edinburgh Instruments FS5 spectrophotometer equipped with an integrating sphere).[55] The NC diameters were determined using powder X-ray diffraction (XRD, Rigaku Smartlab SE) using the Halder-Wagner (H-W) method[56] using reference database: 01-080-0075: PDF-2.[57] Further details of the size determination routine and data are given in the Supporting Information (see Figure A2). ZnO NCs were prepared for high-resolution TEM analysis by drop casting the NCs from a solution of ethanol onto a lacey carbon TEM grid (Electron Microscopy Sciences) and allowing for complete solvent evaporation at room temperature. TEM images were obtained on a JEOL-2100F TEM using a Schottky-type field emission gun operating at 200 keV and collected using a Gatan OneView camera.

We estimated the molarity of the ZnO NC samples using the average particle size determined by powder XRD and the total Zn^{2+} concentration determined by inductively coupled plasma - optical emission spectroscopy (ICP-OES; Perkin Elmer Optima 4300 DV). To determine

the total Zn^{2+} NC concentration, 0.2 µL of the NC stock solution was dissolved in 2 mL of concentrated nitric acid and was stirred overnight. The solution was further diluted to achieve 5% nitric acid solution for analysis. To calculate the concentration of NCs in each aliquot, we determined the total number of NCs that could be formed from the total number of Zn atoms in the solution assuming that the ZnO NCs were spherical and calculated the particle from the XRD data in Figure 2.2c. We utilized the unit cell volume for wurtzite ZnO (47.66 $Å^3$) and 2 formula units per wurtzite unit cell to calculate the total number of Zn atoms per NC. We also assumed that the ZnO lattice parameters do not change with NC size. Table A1 contains the concentration for all NC samples.

2.3.4 EnT Measurements

Steady-state and TRPL spectroscopy were used to study EnT from ZnO NC donors to dye acceptors. TRPL measurements were performed on an Edinburgh Instruments FS5 equipped with a 300 nm pulsed LED (EPLED, 100 kHz). The optical density of the exciton peak was adjusted to 0.1 for all colloidal NC samples to prevent NC aggregation, as evidenced by a prominent scattering tail in the visible region of absorbance spectra. For the steady-state PL experiments, microliter volumes of the 600 nM ethanolic A555 dye were incrementally injected into 3 mL of colloidal ZnO NC solution. PL spectra of ZnO/dye mixtures were excited at 340 nm. All TRPL data was acquired at 576 nm. The defect PL peak maxima for all samples is 580 ± 10 nm. Multi-channel scaling (MSC) photon counting mode was used because this method is suitable for the ZnO NC donors with long lifetimes (ns). TRPL data was deconvoluted from the instrument response function (IRF) using a general exponential equation with a background offset (Edinburgh, Fluoracle). Figure A3 shows representative examples of the IRF deconvolution procedure.

2.4 Results

2.4.1 Sample Design and Characterization

We first designed a series of ZnO NC samples coated with variable chain length ligands and then studied how EnT efficiency varies as a function of chain length. If the ligand chains conformally coat the NC surface and extend into solution, forming a rigid ligand shell as shown in Figure 2.2a, then we expect EnT efficiency to decrease with chain length and equal 50% when the chain length is R_0. To test the rigid ligand shell hypothesis, we synthesized hydroxyl-coated (ZnO-0) and PEG-coated ZnO NC samples (ZnO-3, ZnO-(6-9), ZnO-(9-12), and ZnO-(21-24), where the numbers indicate the number or range in numbers of ethylene glycol repeat units in the non-hydrolyzable silane chain in Figure 2.2a) using established literature protocols.

Figure 2.2b shows absorbance spectra of the hydroxyl and PEG-coated ZnO NCs in ethanol. All absorbance spectra exhibit a sharp onset at 360 nm and an excitonic absorption peak between 330 and 340 nm. The XRD peak profiles of ZnO NCs were analyzed by the Halder-Wagner (H-W) method to estimate the average particle size, yielding 4.3 ± 0.5, 5.8 ± 0.5, 5.7 ± 0.4, 5.0 ± 0.6, and 3.7 ± 0.7 nm core diameters for the ZnO-0, ZnO-3, ZnO-(6-9), ZnO-(9-12), and ZnO-(21-24) samples, respectively (see Figure A2 for details).[56] Figure 2.2a depicts the final sample morphologies, considering the slightly different NC core sizes for each sample. The NC core size changes slightly for each sample for two reasons. First, the PEG-silane ligands are present in the reaction mixture during NC growth. The presence of the ligand can change the viscosity of the solution and, therefore, the rate of the reaction can vary for each ligand. Second, the NC core diameter is expected to decrease with increasing chain length, as demonstrated by Nolf et al. for CdSe NCs.[58] Those authors observed smaller NCs formed in the presence of longer and longer chain length ligands due to the change in the diffusion coefficient and solubility of the CdSe

solute.[58] Nonetheless, our data analysis model accounts for the minor differences in photophysical properties for the slightly different core sizes. XRD results (Figure 2.2c) confirm all the NC samples share the same hexagonal wurtzite crystal structure,[59] and no significant impurity phase appear in the reaction products.[60] Furthermore, we do not find any significant change in XRD patterns of ZnO NCs for PEG-silane chain lengths of 3, 6-9, or 9-12, confirming that increasing PEG-silane coating does not influence the crystallinity of the NCs. However, one additional peak appears in the XRD pattern of ZnO-(21-24) (Figure 2.2c, asterisk). This peak may be attributed to excess PEG monomer in solution. The substantial size of this long PEG ligand may adversely affect the ZnO NC growth kinetics, causing slow consumption of PEG monomers.

The ATR-FTIR (attenuated total reflectance – Fourier transform infrared) spectra of PEG-coated ZnO NCs confirm that each sample is successfully coated with a PEG ligand (Figure 2.2d). The following absorption features increase with increasing chain length. The broad absorption peak at 3440 cm^{-1} observed in all samples can be assigned to the –OH stretching of hydroxyl groups present on the NC surface.[60] The strong absorption peak at 2860 cm^{-1} and the shoulder at 2930 cm^{-1} can be assigned to symmetric and asymmetric stretching of -CH_2, respectively.[60] Symmetric and asymmetric –CH_2 stretching originates from the propyl and ethylene glycol repeat unit in all PEG ligands. We observe an increase in the intensity of the –CH_2 stretching peak at 2860 cm^{-1} as the repeating unit increases from PEG-3 to PEG-(21-24).[60] Ligand specific peaks at 1350 cm^{-1} and 1245 cm^{-1} can be assigned to ethylene glycol –CH_2 wagging and twisting modes, respectively.[61] The peak at approximately 1100 cm^{-1} can be assigned to Si–O–Si asymmetrical stretching, indicating the presence of siloxane layer.[62–64] The peak at approximately 855 cm^{-1} can be assigned to Zn–O–Si stretching, which is a strong indication of silane capping along with the presence of different –CH_2 stretching modes.[48,60] Since trialkoxysilanes are well-known self-

assembled monolayer (SAM) molecules, we expect to form a siloxane monolayer on the surface of ZnO NCs.[65,66] We also note that C–O–C stretching in the ethylene glycol unit will also appear approximately at the same region of the IR spectrum. The pronounced shoulder at 1135 cm^{-1} for all PEG-coated ZnO NCs may be attributed to the C–O–C stretching.[63] Like the $–CH_2$ stretching mode at 2840 cm^{-1}, we observe an increase in the intensity of wagging and twisting modes with increasing number of repeating units. The peak intensities increase with increasing chain length because, under conditions of nominally equivalent NC concentration, more and more bond vibrations in the longer and longer PEG chains contribute to the absorption signal. In summary, we successfully prepared a series of ligand-coated ZnO NCs that should allow us to test the hypothesis that EnT efficiency decreases as the rigid ligand shell extends beyond R_0.

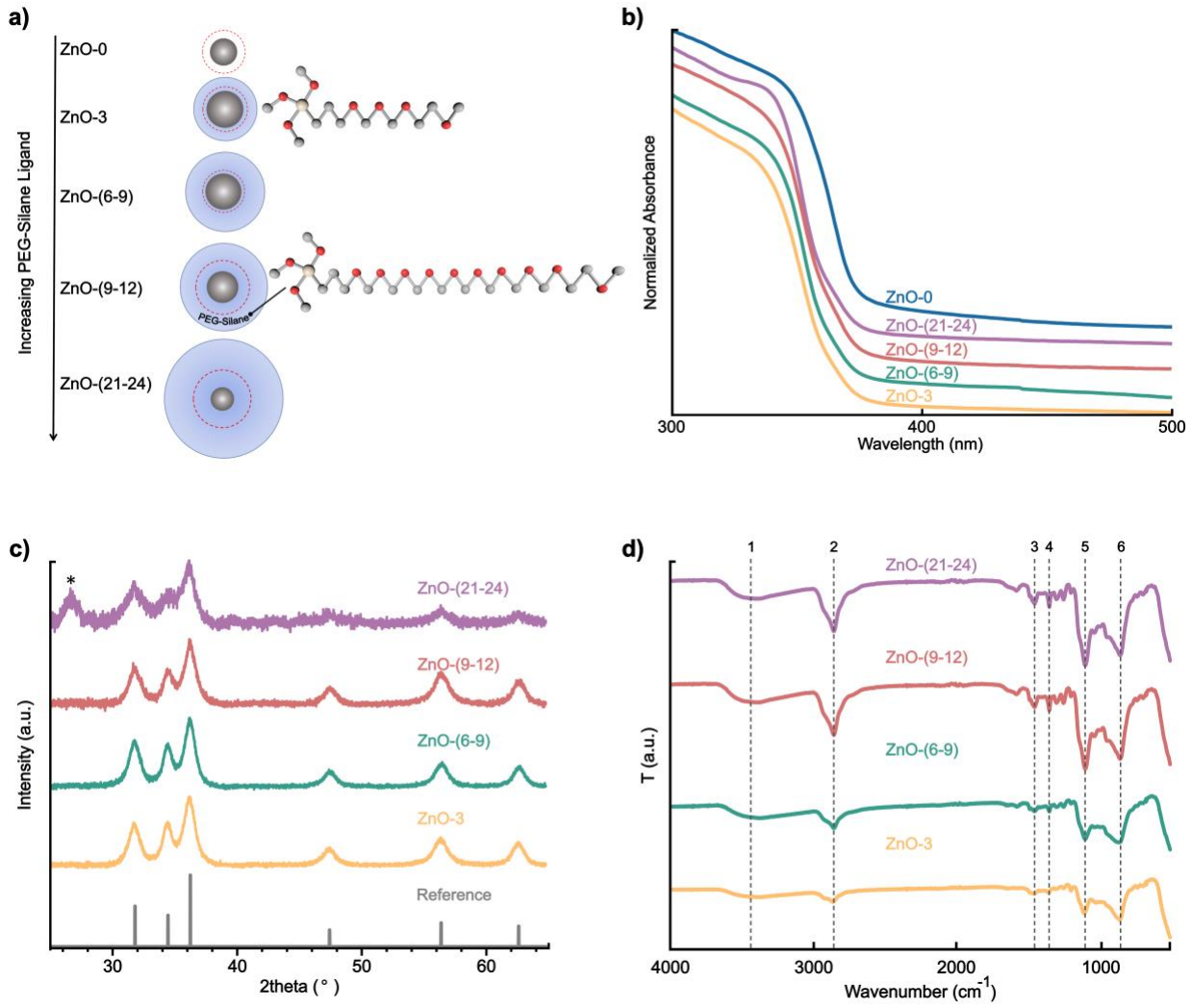

Figure 2.2 (a) Cartoon illustration of hydroxyl and PEG-coated ZnO NCs drawn to scale. The blue shaded region surrounding the NC core represents the PEG-silane ligand shell thickness if the coating forms a rigid, impermeable shell. The red dashed circle represents R_0, assuming the donor dipole is located at the NC core. The atomic structure of the PEG-silane ligand is provided for clarity and not drawn to scale. The red, white, and grey atoms are oxygen, silicon, and carbon atoms respectively. (b) Normalized absorbance spectra in ethanol, (c) powder XRD patterns of PEG-coated ZnO NCs. The reference pattern for the bulk hexagonal wurtzite structure of ZnO is shown as the grey lines (01-080-0075: PDF-2). (d) ATR-FTIR spectra of PEG-coated ZnO NCs. The dashed lines indicate the important peaks in the FTIR spectra (see main text for details) and are numbered from 1 to 6 where 1 = –OH stretching, 2 = –CH_2 stretching, 3 = –CH_2 wagging (ether), 4 = –CH_2 twisting (ether), 5 = Si–O–Si stretching, 6 = Zn–O–Si.

2.4.2 Defect-Mediated EnT between ZnO NC Donors and Dye Acceptors

Figure 2.3a shows a cartoon illustration of the EnT process between ZnO NCs and A555 acceptors. Upon exciting the bandgap of ZnO NCs with 340 nm light, defect energy levels in the NC bandgap can trap charge carriers. These trapped carriers can decay radiatively, resulting in a broad visible PL peak at 585 nm (Figure 2.3b). Although the origin of the visible emission is highly

debated, it is most likely attributed to oxygen vacancies for these samples[48–50,67–72] and/or hole trapping at surface hydroxyl groups.[73] Because the absorption of A555 overlaps with the defect PL (see pink shaded region in Figure 2.3b), the trapped carriers can also participate in a defect-mediated EnT process with A555 at or near the NC-solution interface, as schematically shown in Figure 2.3a.[54,67,74] Note, A555 absorbs very little UV light, specifically at photon energies that also excite the ZnO NCs. Hence, the absorption properties of the donor and acceptor allow us to selectively excite the ZnO NC donor in the presence of the acceptor.

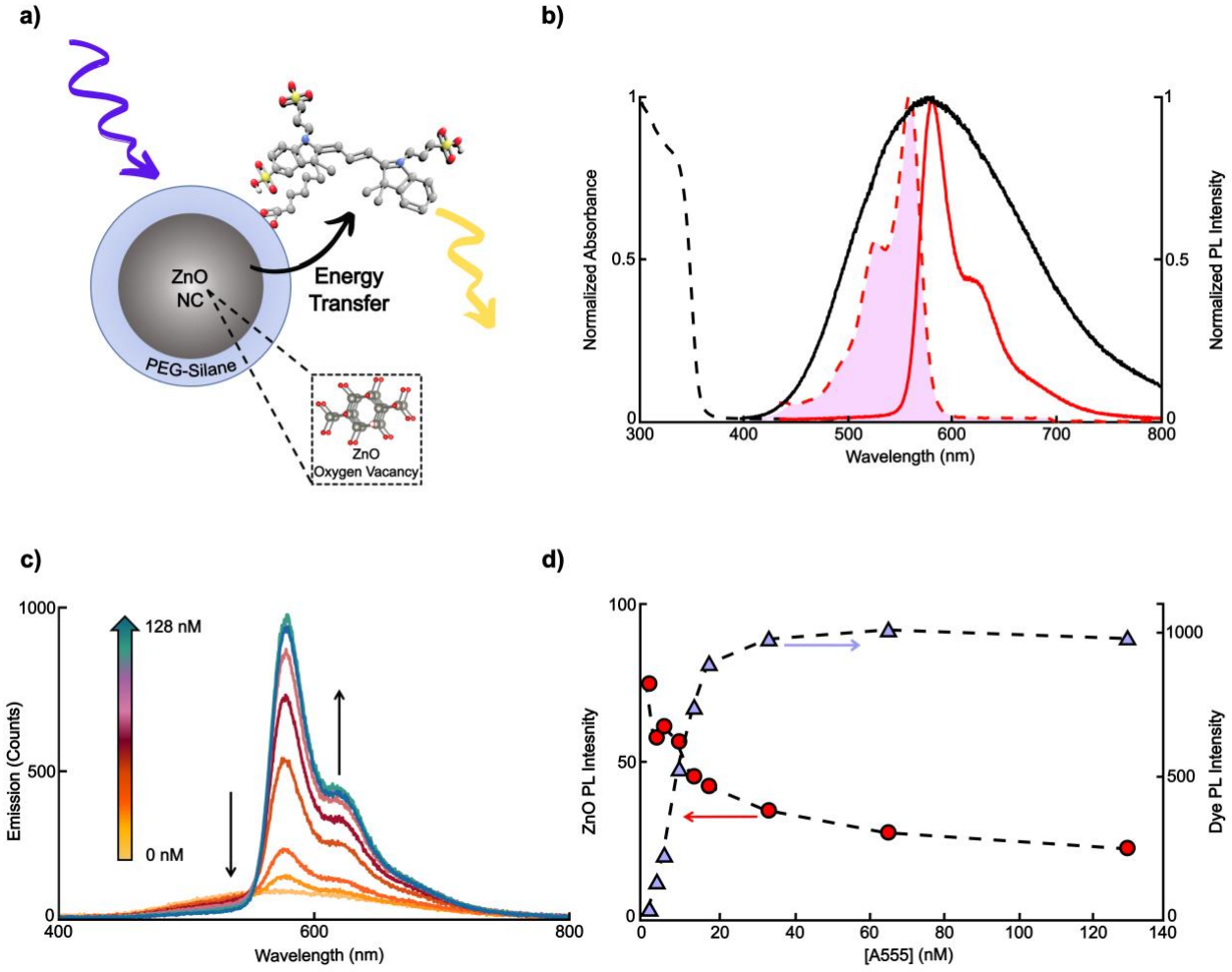

Figure 2.3. (a) Cartoon illustration of defect-mediated EnT between ZnO NC donors and A555 acceptors. (b) Normalized absorbance (dashed lines) and emission spectra (solid lines) of ZnO-(21-24) NCs (black lines) and A555 dye (red lines) in ethanol. The overlap integral between the ZnO PL emission and the A555 dye acceptor absorption is depicted as the pink shaded region. (c) Representative steady-state PL spectrum for ZnO-(9-12) NCs with increasing concentrations of A555 dye. The yellow trace represents the emission spectrum of bare ZnO NCs. All other traces represent ZnO/dye mixtures. The excitation wavelength was 340 nm. (d) PL intensities versus bulk dye concentration

from the data in panel c. The red circles represent the ZnO defect emission at 515 nm. The blue triangles represent the dye emission intensity at 587 nm.

We employed steady-state and TRPL spectroscopy to demonstrate the EnT process between PEG-coated ZnO NCs and A555 dye acceptors. FRET requires a spectral overlap between the donor's emission spectrum and the acceptor's absorbance spectrum. There is significant spectral overlap between the ZnO NC defect emission and the A555 dye absorbance (pink shaded region in Figure 2.3b), which allows FRET to proceed through a defect-mediated process. Figure 2.3c shows representative steady-state PL spectra of ZnO-(9-12) NCs as a function of increasing A555 concentration. The yellow spectral trace is the defect emission for ZnO NCs alone in ethanol. Upon exciting the ZnO NCs with 340 nm light, the defect emission (400 nm - 540 nm) gradually decreases with increasing bulk A555 concentration. At the same time, the A555 fluorescence intensity at 587 nm dramatically increases (Figure 2.3c). Figure A4 shows that acceptor emission enhancement in the presence of the donor cannot be explained by direct excitation of the dye because we only observe weak fluorescence intensity from the isolated dye under 340 nm excitation light. Figure 2.3d shows how the donor emission decreases and acceptor emission increases versus A555 concentration. The simultaneous donor PL quenching and acceptor PL enhancement in Figure 2.3d indicates that the photoexcited ZnO NCs induce the A555 fluorescence via a defect-mediated EnT process (Figure 2.3d).[54,67,74] We observed the same trends in Figure 2.3 for all ZnO NC samples. However, we quantified the EnT efficiency of the NC-dye mixtures using TRPL experiments because the PL lifetime measurements are more accurate than steady-state PL quenching efficiencies; lamp fluctuations can impact the interpretation of steady-state data.[71]

2.4.3 EnT Efficiency as a Function of Ligand Chain Length

EnT efficiency can be calculated from TRPL data by monitoring how the NC defect donor PL lifetime changes with increasing acceptor concentration.[71] Calculating EnT efficiency is important because it allows us to assess PEG shell permeability and to estimate the average donor-acceptor distance *R*, which sheds light on the likely PEG shell morphology. Figure 2.4a shows a representative TRPL decay data for ZnO-(6-9) NCs as a function of bulk acceptor concentration. The TRPL curves have been deconvoluted from the IRF through a fitting procedure (see Figure A3). The ZnO NC defect PL decays faster in the presence of A555 acceptors, and this trend occurs for all NC samples (see Figure A5). PL decay quenching indicates the EnT processes between the NC donor and dye acceptor outpaces radiative recombination within the NC.

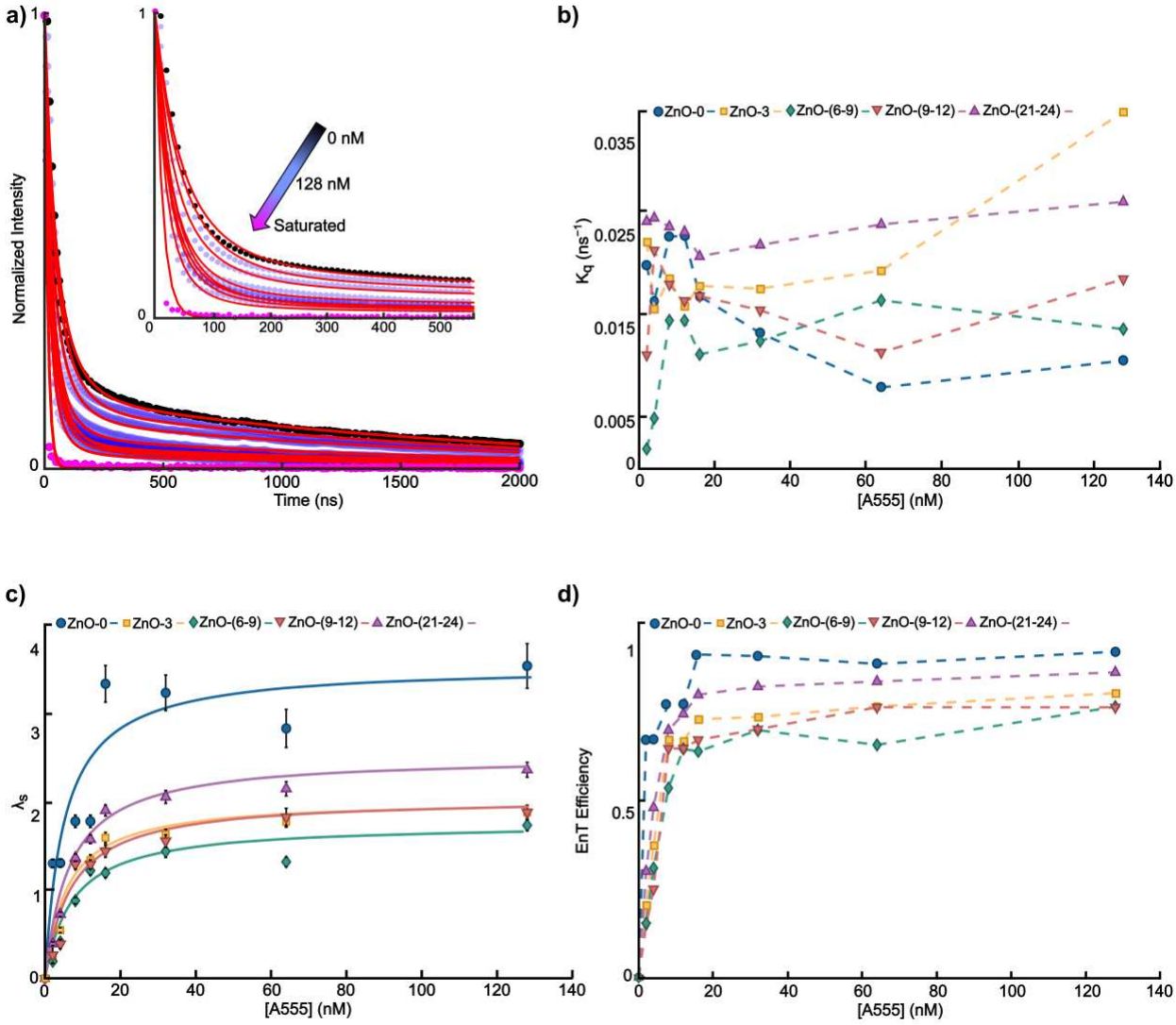

Figure 2.4. (a) Normalized TRPL decay traces for ZnO-(6-9) NCs alone (black dots) and in the presence of increasing concentrations of A555 (blue dots). The pink dots represent a saturated concentration (300 nM) of A555. Red lines represent fits of the data using Eqs. 2.1 and 2.2 for the NCs alone and mixtures, respectively. (b) The EnT rate constant (k_q) for all PEG-silane ZnO samples as a function of increasing acceptor concentration. The dashed lines are guides for the eye. (c) λ_s as a function of increasing A555 concentration for all PEG-silane ZnO samples. Error bars represent 95% confidence intervals. The solid lines are fits to a Langmuir adsorption isotherm (Eq. A2). (d) EnT efficiency calculated using Eq. 2.3 as a function of increasing A555 concentration for ZnO samples with varying PEG-silane length. The dashed lines are guides for the eye.

Next, we analyzed the TRPL decay data for ZnO NC samples as a function of acceptor concentration using the stochastic binding model developed by Sadhu et. al.[71] This model was originally developed to quantify EnT kinetics between CdS quantum dot donors and Nile Red dye acceptors,[71] and was recently adapted to study defect-mediated EnT between bare ZnO NCs and

dye acceptors.[54,67] Beane et al. adapted the model for defect-mediated EnT between ZnO NCs and dye acceptors.[67] Our group also adapted the model in a size-dependent defect-mediated EnT study, which allowed us to reveal the average separation distance between emissive defects in ZnO NCs and surface-adsorbed A555 acceptors.[54] The stochastic binding model assumes (1) EnT between the NC donor and dye acceptor occurs in competition with unimolecular decay processes, specifically the radiative decay of the NC donor; (2) the distribution of the number of dye molecules attached to one NC follows a Poisson distribution; (3) all attached dye molecules quench the donor emission equally; (4) the intrinsic decay processes of the NCs are unaffected by the attachment of the dye molecules; and (5) any acceptor molecule can participate in EnT; adsorbed and near-surface molecules that penetrate the ligand shell can participate in EnT.[71] Additionally, the model also accounts for the PL decay of the ZnO NC donors does not follow single exponential kinetics.[71] First, we fit the TRPL decay curve of the ZnO NC donors alone (see red line fit to black data points in Figure 2.4a) using Eq. 2.1,

$$\frac{I(t)}{I_0} = exp\{-k_0 t - \lambda_t[1 - exp(-k_{qt}t)]\} \quad \text{(Eq. 2.1)}$$

where I is the intensity at any time t, I_0 is the intensity of the decay curve at time $t = 0$ s, k_0 is the radiative decay rate of photoexcited NCs in the absence of the acceptor molecule, λ_t is the average number of non-radiative trap states per NC, which are distributed according to Poisson statistics, and k_{qt} is the quenching rate due to the presence of the non-radiative traps. Next, we fit the TRPL decay data as a function of increasing acceptor concentration using Eq. 2.2

$$\frac{I(t)}{I_0} = exp\{-k_0 t - \lambda_t[1 - exp(-k_{qt}t)] - \lambda_s[1 - exp(-k_q t)]\} \quad \text{(Eq. 2.2)}$$

where λ_s is the mean number of dye molecules per NC according to Poisson statistics and k_q is the rate of EnT.[71] We initially fit the TRPL decay data to determine k_q and λ_s using fixed values of λ_t, k_{qt}, and k_0 obtained from control, donor-alone experiments. Figure 2.4b shows that k_q is essentially

independent of acceptor concentration for all NC samples, consistent with the fact that k_q is a rate constant. To minimize the error in λ_s, we re-fit all the TRPL data using Eq. 2.2 using a single, averaged k_q value obtained from all acceptor concentrations. Figure 2.4c shows that λ_s expectedly increases with bulk A555 concentration and saturates at approximately 2 molecules per NC for the ligand-coated NC samples. The bare ZnO NC samples bind more A555 dye molecules (4 per NC), likely because their surfaces are not covered by bulky ligands. We fit the λ_S curves in Figure 2.4d to a simple Langmuir adsorption isotherm (Eq. A2, dashed lines), which yields the equilibrium binding constant, *K*. Figure A6 shows that the equilibrium binding constant of the bare ZnO NCs is about 50% larger than the ligand-coated samples. However, *K* is independent of ligand length, likely because the linker chemistry between the ZnO NC surface and PEG-silane groups does not depend on chain length. Thus, any change in EnT efficiency is likely not due to different binding affinities between the variable chain length PEG-silane ligands and the NC surface.

Finally, we calculate the EnT efficiency for each NC/dye system according to Eq. 2.3,

$$\Phi_{EnT} = 1 - \frac{\sum_{n=0}^{\infty}\sum_{n=0}^{\infty}\frac{\left(\frac{\lambda_S^n e^{-\lambda_S}}{n!}\right)\left(\frac{\lambda_t^{n'} e^{-\lambda_t}}{n'!}\right)}{\left[1+\frac{nk_q}{k_0}+\frac{n'k_{qt}}{k_0}\right]}}{\sum_{n'=0}^{\infty}\frac{\left(\frac{\lambda_t^{n'} e^{-\lambda_t}}{n'!}\right)}{\left[1+\frac{n'k_{qt}}{k_0}\right]}} \qquad \text{(Eq. 2.3)}$$

where n is the integer number of attached dye molecules per NC and n' is the integer number of non-radiative traps.[71] Figure 2.4d shows that EnT efficiency is greatest for the ZnO-0 sample and surprisingly independent of chain length. Unexpectedly, the sample with the longest PEG-silane chain length, ZnO-(21-24), exhibits an EnT value close to that of ZnO-0. In the Discussion Section that follows, we explore how the EnT data in Figure 2.4d can be used to deduce a qualitative description of the ligand shell morphology for these PEG-silane capped ZnO NCs.

2.5 Discussion

Surprisingly, we observed that defect-mediated EnT efficiency between PEG-silane-coated ZnO NCs and A555 acceptors was independent of ligand chain length (Figure 2.4d). The blue circles in Figure 2.5 plot the maximum EnT values from Figure 2.4d versus ligand chain length. In this view, the EnT efficiency decreases slightly from ZnO-0 to ZnO-(6-9), and then the EnT efficiency surprisingly increases with increasing PEG chain length. This observation starkly contrasts what would be expected if the PEG ligands formed a rigid shell surrounding the NC core, as will be discussed below.

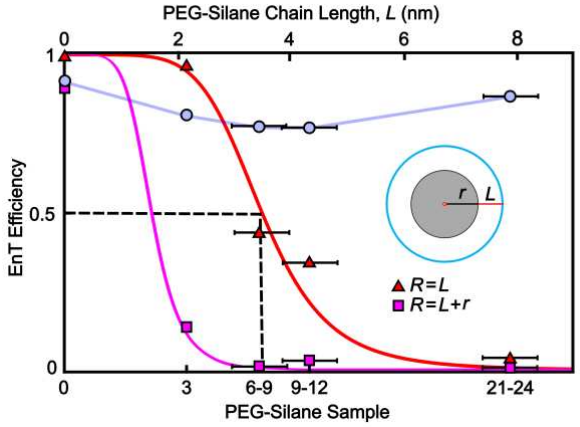

Figure 2.5. EnT efficiency as a function of varying PEG-silane length in units of nm. Blue data points are experimentally determined EnT values at 128 nM A555 dye concentrations from Figure 2.4d. The blue line is a guide for the eye. Red data points are calculated using Eq. 4, where the R_0 values were calculated for each NC sample using Eq. A3 and R = L (see inset and main text for discussion). The solid red line is a guide for the eye, calculated via Eq. 4 using R_0 = 3.5 nm (see vertical black dashed line). Horizontal error bars are ± 1.5 nm for the distribution of PEG-silane ligand lengths in the sample. Pink data points were calculated using the same procedure as the red data points, but for R = L + r. The pink solid line is a guide for the eye, calculated via Eq. 4 using R_0 = 2.2 nm.

We first consider whether the PEG-silane ligands extend from the NC surface and form a dense surface coating that is impenetrable to dye molecules from the bulk solution. Scheme 2.1 shows a cartoon illustration of this rigid ligand shell model geometry for each NC sample. The cartoon illustrations consider a single defect site per NC and 2 surface-bound molecules, corresponding to the number of surface-bound molecules determined experimentally for the PEG-

silane capped samples (Figure 2.4c). The large gray circles and small red dots represent the ZnO NCs and defect donor sites, respectively. The solid blue circles represent the rigid ligand shell diameter if the ligands extended radially from the NC surface in a dense, packed morphology. Scheme 2.1 also considers two extreme cases for the defect site locations. In one case (top row), the defect sites reside at the NC core. In another case (bottom row), the defects exist at the NC surface (right side of Scheme 2.1). The dashed red circles in Scheme 2.1 represent the critical Förster distance R_0 (Eq. A3), defined as a circle with a centroid position at the defect site and a radius R_0. According to Förster theory, any acceptor molecule located within a distance R_0, and with the proper orientation factor relative to the donor dipole, will participate in the EnT process with >50% efficiency.[52] Molecules located within R_0 can participate in EnT and are indicated by pink ovals; the white ovals represent EnT-inactive dye molecules.

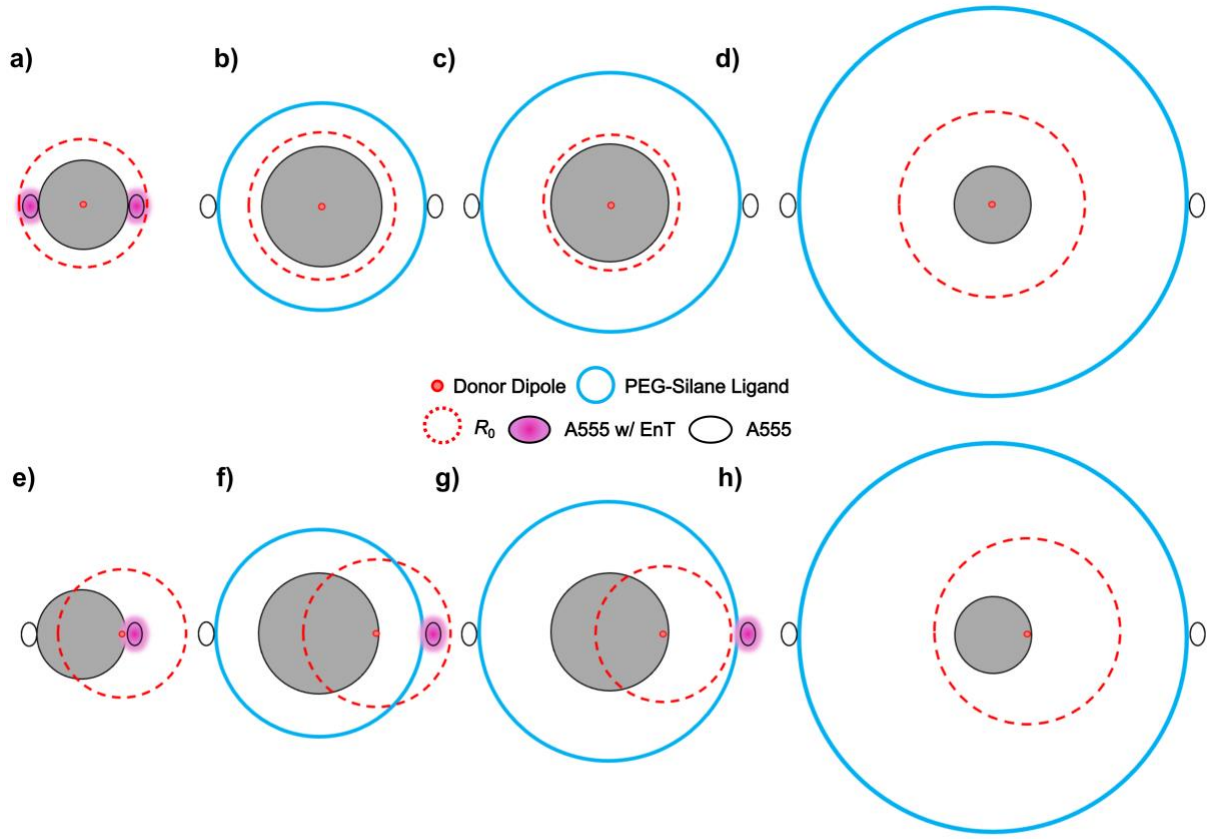

Scheme 2.1. Cartoon models that illustrate the rigid shell geometry of the PEG-silane coated ZnO NCs. (a-d) Geometric model for ZnO NCs with defect sites located at the core. (a) ZnO-0, (b) ZnO-(3); (c) ZnO-(6-9); and (d) ZnO-(21-24). All features drawn to scale. (e-h) same as (a-d), but for defect sites located at the NC surface. See main text for details.

Having developed a simple geometric model of these ligand-coated NCs, we then calculated the expected EnT efficiency for each sample in Scheme 2.1 using Eq. 2.4. In one scenario, where the defect dipole is located at the NC core, R in Eq. 2.4 is defined as the sum of the radius of the NC (r) and the ligand chain length (L, see inset of Figure 2.5). The pink squares in Figure 2.5 represent calculated E values assuming this geometry. In another scenario, where the defect sites are located at the NC surface (red triangles in Figure 2.5), R is just the ligand chain length. We also account for the sample dependent R_0 values (Table A1). The predicted EnT efficiency values decrease faster with increasing chain length for the core defect case because

acceptor molecules are farther way from the donor dipole located at the NC core. Figure 2.5 shows that the experimentally determined EnT values do not follow the trend predicted by the rigid shell model, regardless of the defect site locations within the NC.

$$E = \frac{1}{1+\left(\frac{R}{R_0}\right)^6} \quad \text{(Eq. 2.4)}$$

Next, we compare and attempt to rationalize differences between the experimental and predicted values in Figure 2.5. For the ZnO-0 samples, all surface bound molecules lie within a distance R_0 if all defects are located at the NC core (Scheme 2.1a). If the defect site resides at the surface (Scheme 2.1f), then it is possible that molecules located on the opposite side of the NC will not participate in EnT. This geometry effect could explain why the observed EnT efficiency of the ZnO-0 samples is slightly less than the predicted values (Figure 2.5).

The difference between experimental and predicted EnT efficiency values widens for the ZnO-3 sample (Figure 2.5), which can be rationalized by the cartoon geometry in Scheme 2.1b,f. Scheme 2.1b shows the geometry of the ZnO-3 sample with the defect sites located at the NC core. For this sample, R_0 is smaller than the rigid ligand shell boundary and, therefore, we would not expect to observe EnT because molecules cannot penetrate through the ligand shell to a distance R_0 from the core defect. If instead the defect is located at the NC surface (Scheme 2.1f), then it is possible that dye molecules can approach a distance R_0 from the surface defect. The observed EnT efficiency for ZnO-3 is >50% indicates that the defect sites responsible for EnT are likely located at the NC surface. The EnT efficiency for ZnO-3 is lower than ZnO-0 likely because the ligand shell prevents some molecules from reaching a distance R_0 from the surface and/or core defects.

The situation changes for longer chain length samples because R_0 becomes much shorter than the ligand shell diameter. For the ZnO-(6-9) sample, dye molecules can no longer engage in EnT with the core defects (Scheme 2.1c) and can barely approach R_0 for the surface defect case

(Scheme 2.1g). Interestingly, the experimental EnT efficiency remains high (>75%) even though the rigid shell model predicts EnT efficiency <50%. Surprisingly, the EnT efficiency further increases for the ZnO-(9-12) sample and reaches a maximum for the ZnO-(21-24) sample. The high EnT efficiency of the ZnO-(21-24) sample cannot be explained by surface defect location because the ligand length is much longer than R_0 (Scheme 2.1f). In summary, the "rigid shell" model could explain the results for the ZnO-0, ZnO-3, and ZnO-(6-9) samples, but is likely invalid for the long chain PEG-silane ligands (i.e., ZnO-(9-12) and ZnO-(21-24)).

An alternative explanation for the high EnT efficiency values for the ZnO-(9-12) and ZnO-(21-24) samples is that molecules can penetrate the ligand shell through either gaps between PEG chains or pinholes. For example, Scheme 2.2a shows a cartoon illustration of molecules intercalating into void space between PEG chains. Literature evidence for this possibility exists. Lin et al. observed the greatest steric repulsion between colloidal gold nanoparticles with high molecular weight PEG ligands,[75] suggesting that long PEG chain ligands (both within the same nanoparticle and between neighboring particles) generally repel each other. An alternative scenario is that the PEG ligand morphology can be described as the so-called "mushroom state", where ligand chains coil together and form sparse patches on the NC surface (Scheme 2.2b). This ligand coiling effect can produce gaps on the NC surface that allows for acceptor molecules to approach the NC surface. Indeed, Lee et al. performed molecular dynamics simulations of protein binding to PEGylated lipid bilayers and observed that proteins penetrate through bare lipid patches in the bilayer because the PEG chains exist in a flexible mushroom state.[12] Relatedly, Rahme et al. also observed for colloidal gold nanoparticles that PEG ligand density decreased with increasing PEG chain length, which could also be explained by the mushroom state effect.[37] Xu et al. observed a similar mushroom conformation for PEG-coated poly(lactic-*co*-glycolic acid) particles.[76]

Unfortunately, ensemble-level FRET spectroscopy cannot directly image and, therefore, distinguish between the two cases in Scheme 2.2.

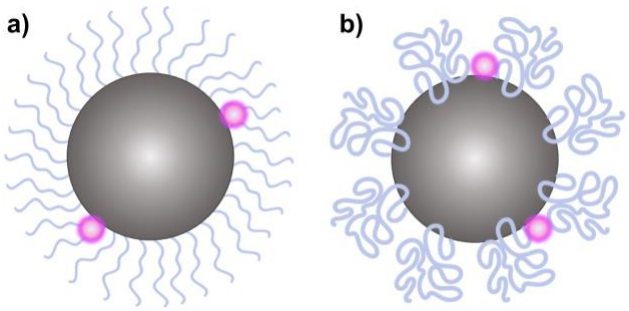

Scheme 2.2. Models for the NC/PEG-silane donor-acceptor systems, where the PEG-silane ligand conformation is depicted in blue. The number of acceptor molecules bound to the NC surface was determined from λs values (pink circles). (a) Model for a shorter length PEG-silane ligand in the brush conformation. (b) Model for a longer PEG-silane ligand in the mushroom conformation.

We attempted to directly image the ligand shell morphology using TEM. This task is difficult because the PEG coating has very low contrast compared to the ZnO core. To do so, we prepared dried films of particles that formed layers over holes in the TEM grid. This enabled us to image particle surfaces and interfaces between particles without interface from the TEM grid material. Figure 2.6a shows a representative TEM image of the ZnO-0 sample that does not contain PEG chains on the NC surface. Distinct surface facets appear for each NC, and the NC surface boundaries exhibit well-defined edges in the TEM images. However, for the ZnO-(21-24) sample coated with long PEG chains, a light-contrast amorphous coating can be seen on the NC surfaces (Figure 2.6b yellow arrows). Figure A7 shows lower magnification TEM images of PEG-silane coated ZnO particles. Interestingly, some NC surfaces exhibit the coating (Figure 2.6b,c yellow arrows) while other NC surfaces appear bare, or have significantly reduced coating density (Figure 2.6b,c red arrows). This suggests that the PEG coating is heterogeneously distributed across the surfaces of the nanoparticles, consistent with our TRPL results. This ligand shell heterogeneity could explain how dye molecules penetrate through gaps in the ligand shell and engage in EnT with the NC core/surface defect sites. The TEM images support the FRET spectroscopy

measurements, but only provide a snapshot of the sample under dry conditions. The advantage of the FRET spectroscopy approach is that it provides an estimate of ligand shell permeability under solution-phase conditions.

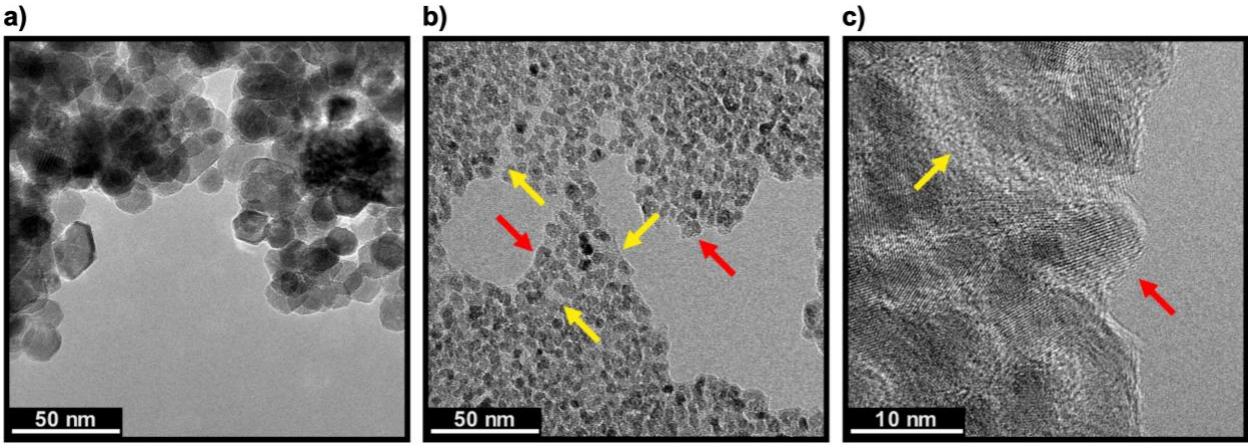

Figure 2.6. TEM images of (a) ZnO-0 and (b-c) ZnO-(21-24) on a lacey carbon TEM grid. Yellow arrows indicate amorphous material on the NC surface. Red arrows indicate bare or sparsely coated NC surface regions.

The significance of the results presented herein is that ensemble-level FRET-based measurements, coupled with a geometric model-based analysis (i.e., Scheme 2.1), can provide information regarding the ability of small molecules from the external environment to access NC surfaces through a ligand shell. Researchers can disperse ligand-coated NCs in pure solvent and/or a complex matrix containing a dye FRET pair and use the procedures presented herein to assess whether the NC core remains isolated from species in the bulk solution, or whether those species can penetrate through the ligand shell. We envision this approach will be beneficial for researchers in the colloidal nanoparticle community.

2.6 Conclusion

We synthesized a series of variable chain length PEG-silane coated ZnO NCs and quantified the efficiency of a defect-mediated EnT process between the NCs and dye molecules using TRPL spectroscopy. The EnT efficiency did not sharply decrease with increasing ligand length (i.e., the expected R^{-6} dependence within the FRET framework). A555 dye molecules can

apparently penetrate to the NC core and participate in the EnT process even though 8 nm long PEG ligands coat the NC surface. These results could not be explained by a "rigid shell" model where the PEG ligands extend radially from the NC core and form an impenetrable barrier to solution phase dye molecules. Instead, molecules likely either intercalate into a porous PEG shell or directly access voids between coiled PEG chains. While the spectroscopic measurements and data analysis procedures discussed herein cannot directly characterize the ligand shell morphology, the approach can provide researchers in the colloidal NC community with valuable information regarding the permeability of species from the external environment through the ligand shell. One exciting possibility is to leverage a large library of commercially available ligands and dye molecules to study the relationship between ligand structure/chemistry and ligand shell permeability for a wide range of NC materials.

2.7 Author Contributions

According to CRediT criteria, my contributions to this work included conceptualization, data curation, formal analysis, investigation, methodology, visualization, writing – original draft, and writing – reviewing and editing. E.B. synthesized PEG-silane-coated ZnO NCs and performed UV/Vis, XRD, and FTIR characterization measurements. K.R.K. provided characterization interpretation. J.T.M. and J.P.P. performed TEM measurements and provided TEM data interpretation. D.R.L. and J.B.S. designed all experiments and wrote the manuscript.

REFERENCES

(1) Xiong, H.-M. ZnO Nanoparticles Applied to Bioimaging and Drug Delivery. *Adv. Mater.* **2013**, *25* (37), 5329–5335. https://doi.org/10.1002/adma.201301732.
(2) Eixenberger, J. E.; Anders, C. B.; Wada, K.; Reddy, K. M.; Brown, R. J.; Moreno-Ramirez, J.; Weltner, A. E.; Karthik, C.; Tenne, D. A.; Fologea, D.; Wingett, D. G. Defect Engineering of ZnO Nanoparticles for Bioimaging Applications. *ACS Appl. Mater. Interfaces* **2019**, *11* (28), 24933–24944. https://doi.org/10.1021/acsami.9b01582.
(3) Sahoo, R. K.; Rani, S.; Kumar, V.; Gupta, U. Zinc Oxide Nanoparticles for Bioimaging and Drug Delivery. In *Nanostructured Zinc Oxide*; Elsevier, 2021; pp 483–509. https://doi.org/10.1016/B978-0-12-818900-9.00021-8.
(4) Mitchell, M. J.; Billingsley, M. M.; Haley, R. M.; Wechsler, M. E.; Peppas, N. A.; Langer, R. Engineering Precision Nanoparticles for Drug Delivery. *Nat. Rev. Drug Discov.* **2021**, *20* (2), 101–124. https://doi.org/10.1038/s41573-020-0090-8.
(5) Hoang Thi, T. T.; Pilkington, E. H.; Nguyen, D. H.; Lee, J. S.; Park, K. D.; Truong, N. P. The Importance of Poly(Ethylene Glycol) Alternatives for Overcoming PEG Immunogenicity in Drug Delivery and Bioconjugation. *Polymers* **2020**, *12* (2), 298. https://doi.org/10.3390/polym12020298.
(6) Shi, L.; Zhang, J.; Zhao, M.; Tang, S.; Cheng, X.; Zhang, W.; Li, W.; Liu, X.; Peng, H.; Wang, Q. Effects of Polyethylene Glycol on the Surface of Nanoparticles for Targeted Drug Delivery. *Nanoscale* **2021**, *13* (24), 10748–10764. https://doi.org/10.1039/D1NR02065J.
(7) Martínez-Carmona, M.; Gun'ko, Y.; Vallet-Regí, M. ZnO Nanostructures for Drug Delivery and Theranostic Applications. *Nanomaterials* **2018**, *8* (4), 268. https://doi.org/10.3390/nano8040268.
(8) Yuan, Q.; Hein, S.; Misra, R. D. K. New Generation of Chitosan-Encapsulated ZnO Quantum Dots Loaded with Drug: Synthesis, Characterization and in Vitro Drug Delivery Response. *Acta Biomater.* **2010**, *6* (7), 2732–2739. https://doi.org/10.1016/j.actbio.2010.01.025.
(9) Zheng, F.-F.; Zhang, P.-H.; Xi, Y.; Chen, J.-J.; Li, L.-L.; Zhu, J.-J. Aptamer/Graphene Quantum Dots Nanocomposite Capped Fluorescent Mesoporous Silica Nanoparticles for Intracellular Drug Delivery and Real-Time Monitoring of Drug Release. *Anal. Chem.* **2015**, *87* (23), 11739–11745. https://doi.org/10.1021/acs.analchem.5b03131.
(10) Li, Y.-C.; Rissanen, S.; Stepniewski, M.; Cramariuc, O.; Róg, T.; Mirza, S.; Xhaard, H.; Wytrwal, M.; Kepczynski, M.; Bunker, A. Study of Interaction Between PEG Carrier and Three Relevant Drug Molecules: Piroxicam, Paclitaxel, and Hematoporphyrin. *J. Phys. Chem. B* **2012**, *116* (24), 7334–7341. https://doi.org/10.1021/jp300301z.
(11) Rizvi, S. A. A.; Saleh, A. M. Applications of Nanoparticle Systems in Drug Delivery Technology. *Saudi Pharm. J.* **2018**, *26* (1), 64–70. https://doi.org/10.1016/j.jsps.2017.10.012.
(12) Lee, H.; Larson, R. G. Adsorption of Plasma Proteins onto PEGylated Lipid Bilayers: The Effect of PEG Size and Grafting Density. *Biomacromolecules* **2016**, *17* (5), 1757–1765. https://doi.org/10.1021/acs.biomac.6b00146.
(13) Friedl, J. D.; Nele, V.; De Rosa, G.; Bernkop-Schnürch, A. Bioinert, Stealth or Interactive: How Surface Chemistry of Nanocarriers Determines Their Fate In Vivo. *Adv. Funct. Mater.* **2021**, *31* (34), 2103347. https://doi.org/10.1002/adfm.202103347.

(14) Otsuka, H.; Nagasaki, Y.; Kataoka, K. PEGylated Nanoparticles for Biological and Pharmaceutical Applications. *Adv. Drug Deliv. Rev.* **2003**, *55* (3), 403–419. https://doi.org/10.1016/S0169-409X(02)00226-0.
(15) Heuer-Jungemann, A.; Feliu, N.; Bakaimi, I.; Hamaly, M.; Alkilany, A.; Chakraborty, I.; Masood, A.; Casula, M. F.; Kostopoulou, A.; Oh, E.; Susumu, K.; Stewart, M. H.; Medintz, I. L.; Stratakis, E.; Parak, W. J.; Kanaras, A. G. The Role of Ligands in the Chemical Synthesis and Applications of Inorganic Nanoparticles. *Chem. Rev.* **2019**, *119* (8), 4819–4880. https://doi.org/10.1021/acs.chemrev.8b00733.
(16) Yang, C.; Gao, S.; Dagnæs-Hansen, F.; Jakobsen, M.; Kjems, J. Impact of PEG Chain Length on the Physical Properties and Bioactivity of PEGylated Chitosan/SiRNA Nanoparticles in Vitro and in Vivo. *ACS Appl. Mater. Interfaces* **2017**, *9* (14), 12203–12216. https://doi.org/10.1021/acsami.6b16556.
(17) Endres, T.; Zheng, M.; Kılıç, A.; Turowska, A.; Beck-Broichsitter, M.; Renz, H.; Merkel, O. M.; Kissel, T. Amphiphilic Biodegradable PEG-PCL-PEI Triblock Copolymers for FRET-Capable *in Vitro* and *in Vivo* Delivery of SiRNA and Quantum Dots. *Mol. Pharm.* **2014**, *11* (4), 1273–1281. https://doi.org/10.1021/mp400744a.
(18) Steinmetz, N. F.; Manchester, M. PEGylated Viral Nanoparticles for Biomedicine: The Impact of PEG Chain Length on VNP Cell Interactions In Vitro and Ex Vivo. *Biomacromolecules* **2009**, *10* (4), 784–792. https://doi.org/10.1021/bm8012742.
(19) Knop, K.; Hoogenboom, R.; Fischer, D.; Schubert, U. S. Poly(Ethylene Glycol) in Drug Delivery: Pros and Cons as Well as Potential Alternatives. *Angew. Chem. Int. Ed.* **2010**, *49* (36), 6288–6308. https://doi.org/10.1002/anie.200902672.
(20) Daou, T. J.; Li, L.; Reiss, P.; Josserand, V.; Texier, I. Effect of Poly(Ethylene Glycol) Length on the in Vivo Behavior of Coated Quantum Dots. *Langmuir* **2009**, *25* (5), 3040–3044. https://doi.org/10.1021/la8035083.
(21) Suk, J. S.; Xu, Q.; Kim, N.; Hanes, J.; Ensign, L. M. PEGylation as a Strategy for Improving Nanoparticle-Based Drug and Gene Delivery. *Adv. Drug Deliv. Rev.* **2016**, *99*, 28–51. https://doi.org/10.1016/j.addr.2015.09.012.
(22) Li, S.-D.; Huang, L. Stealth Nanoparticles: High Density but Sheddable PEG Is a Key for Tumor Targeting. *J. Controlled Release* **2010**, *145* (3), 178–181. https://doi.org/10.1016/j.jconrel.2010.03.016.
(23) Pelaz, B.; del Pino, P.; Maffre, P.; Hartmann, R.; Gallego, M.; Rivera-Fernández, S.; de la Fuente, J. M.; Nienhaus, G. U.; Parak, W. J. Surface Functionalization of Nanoparticles with Polyethylene Glycol: Effects on Protein Adsorption and Cellular Uptake. *ACS Nano* **2015**, *9* (7), 6996–7008. https://doi.org/10.1021/acsnano.5b01326.
(24) Sacchetti, C.; Motamedchaboki, K.; Magrini, A.; Palmieri, G.; Mattei, M.; Bernardini, S.; Rosato, N.; Bottini, N.; Bottini, M. Surface Polyethylene Glycol Conformation Influences the Protein Corona of Polyethylene Glycol-Modified Single-Walled Carbon Nanotubes: Potential Implications on Biological Performance. *ACS Nano* **2013**, *7* (3), 1974–1989. https://doi.org/10.1021/nn400409h.
(25) Du, H.; Chandaroy, P.; Hui, S. W. Grafted Poly-(Ethylene Glycol) on Lipid Surfaces Inhibits Protein Adsorption and Cell Adhesion. *Biochim. Biophys. Acta BBA - Biomembr.* **1997**, *1326* (2), 236–248. https://doi.org/10.1016/S0005-2736(97)00027-8.
(26) Gref, R.; Lück, M.; Quellec, P.; Marchand, M.; Dellacherie, E.; Harnisch, S.; Blunk, T.; Müller, R. H. 'Stealth' Corona-Core Nanoparticles Surface Modified by Polyethylene Glycol (PEG): Influences of the Corona (PEG Chain Length and Surface Density) and of the Core

Composition on Phagocytic Uptake and Plasma Protein Adsorption. *Colloids Surf. B Biointerfaces* **2000**, *18* (3–4), 301–313. https://doi.org/10.1016/S0927-7765(99)00156-3.
(27) Efremova, N. V.; Bondurant, B.; O'Brie, D. F.; Leckband, D. E. Measurements of Interbilayer Forces and Protein Adsorption on Uncharged Lipid Bilayers Displaying Poly(Ethylene Glycol) Chains †. *Biochemistry* **2000**, *39* (12), 3441–3451. https://doi.org/10.1021/bi992095r.
(28) Li, M.; Jiang, S.; Simon, J.; Paßlick, D.; Frey, M.-L.; Wagner, M.; Mailänder, V.; Crespy, D.; Landfester, K. Brush Conformation of Polyethylene Glycol Determines the Stealth Effect of Nanocarriers in the Low Protein Adsorption Regime. *Nano Lett.* **2021**, *21* (4), 1591–1598. https://doi.org/10.1021/acs.nanolett.0c03756.
(29) Zhao, F.; Cheng, X.; Liu, G.; Zhang, G. Interaction of Hydrophobically End-Capped Poly(Ethylene Glycol) with Phospholipid Vesicles: The Hydrocarbon End-Chain Length Dependence. *J. Phys. Chem. B* **2010**, *114* (3), 1271–1276. https://doi.org/10.1021/jp910024n.
(30) Timor, R.; Weitman, H.; Waiskopf, N.; Banin, U.; Ehrenberg, B. PEG-Phospholipids Coated Quantum Rods as Amplifiers of the Photosensitization Process by FRET. *ACS Appl. Mater. Interfaces* **2015**, *7* (38), 21107–21114. https://doi.org/10.1021/acsami.5b04318.
(31) Abuchowski, A.; McCoy, J. R.; Palczuk, N. C.; Van Es, T.; Davis, F. F. Effect of Covalent Attachment of Polyethylene Glycol on Immunogenicity and Circulating Life of Bovine Liver Catalase. *J. Biol. Chem.* **1977**, *252* (11), 3582–3586. https://doi.org/10.1016/S0021-9258(17)40292-4.
(32) Moyano, D. F.; Saha, K.; Prakash, G.; Yan, B.; Kong, H.; Yazdani, M.; Rotello, V. M. Fabrication of Corona-Free Nanoparticles with Tunable Hydrophobicity. *ACS Nano* **2014**, *8* (7), 6748–6755. https://doi.org/10.1021/nn5006478.
(33) Verhoef, J. J. F.; Anchordoquy, T. J. Questioning the Use of PEGylation for Drug Delivery. *Drug Deliv. Transl. Res.* **2013**, *3* (6), 499–503. https://doi.org/10.1007/s13346-013-0176-5.
(34) Bunker, A. Poly(Ethylene Glycol) in Drug Delivery, Why Does It Work, and Can We Do Better? All Atom Molecular Dynamics Simulation Provides Some Answers. *Phys. Procedia* **2012**, *34*, 24–33. https://doi.org/10.1016/j.phpro.2012.05.004.
(35) Garcia-Fuentes, M.; Torres, D.; Martín-Pastor, M.; Alonso, M. J. Application of NMR Spectroscopy to the Characterization of PEG-Stabilized Lipid Nanoparticles. *Langmuir* **2004**, *20* (20), 8839–8845. https://doi.org/10.1021/la049505j.
(36) Smith, A. M.; Johnston, K. A.; Crawford, S. E.; Marbella, L. E.; Millstone, J. E. Ligand Density Quantification on Colloidal Inorganic Nanoparticles. *The Analyst* **2017**, *142* (1), 11–29. https://doi.org/10.1039/C6AN02206E.
(37) Rahme, K.; Chen, L.; Hobbs, R. G.; Morris, M. A.; O'Driscoll, C.; Holmes, J. D. PEGylated Gold Nanoparticles: Polymer Quantification as a Function of PEG Lengths and Nanoparticle Dimensions. *RSC Adv* **2013**, *3* (17), 6085–6094. https://doi.org/10.1039/C3RA22739A.
(38) Jokerst, J. V.; Lobovkina, T.; Zare, R. N.; Gambhir, S. S. Nanoparticle PEGylation for Imaging and Therapy. *Nanomed.* **2011**, *6* (4), 715–728. https://doi.org/10.2217/nnm.11.19.
(39) Pannuzzo, M.; Horta, B. A. C.; La Rosa, C.; Decuzzi, P. Predicting the Miscibility and Rigidity of Poly(Lactic- *Co* -Glycolic Acid)/Polyethylene Glycol Blends via Molecular Dynamics Simulations. *Macromolecules* **2020**, *53* (10), 3643–3654. https://doi.org/10.1021/acs.macromol.0c00110.

(40) Stryer, L.; Haugland, R. P. Energy Transfer: A Spectroscopic Ruler. *Proc. Natl. Acad. Sci. U. S. A.* **1967**, *58* (2), 719–726.
(41) Sobakinskaya, E.; Schmidt am Busch, M.; Renger, T. Theory of FRET "Spectroscopic Ruler" for Short Distances: Application to Polyproline. *J. Phys. Chem. B* **2018**, *122* (1), 54–67. https://doi.org/10.1021/acs.jpcb.7b09535.
(42) Didenko, V. V. DNA Probes Using Fluorescence Resonance Energy Transfer (FRET): Designs and Applications. *BioTechniques* **2001**, *31* (5), 1106–1121. https://doi.org/10.2144/01315rv02.
(43) Van Embden, J.; Gross, S.; Kittilstved, K. R.; Della Gaspera, E. Colloidal Approaches to Zinc Oxide Nanocrystals. *Chem. Rev.* **2023**, *123* (1), 271–326. https://doi.org/10.1021/acs.chemrev.2c00456.
(44) Zhang, Z.-Y.; Xiong, H.-M. Photoluminescent ZnO Nanoparticles and Their Biological Applications. *Materials* **2015**, *8* (6), 3101–3127. https://doi.org/10.3390/ma8063101.
(45) Jiang, J.; Pi, J.; Cai, J. The Advancing of Zinc Oxide Nanoparticles for Biomedical Applications. *Bioinorg. Chem. Appl.* **2018**, *2018*, 1–18. https://doi.org/10.1155/2018/1062562.
(46) Rasmussen, J. W.; Martinez, E.; Louka, P.; Wingett, D. G. Zinc Oxide Nanoparticles for Selective Destruction of Tumor Cells and Potential for Drug Delivery Applications. *Expert Opin. Drug Deliv.* **2010**, *7* (9), 1063–1077. https://doi.org/10.1517/17425247.2010.502560.
(47) Lyons, J. L.; Varley, J. B.; Steiauf, D.; Janotti, A.; Van de Walle, C. G. First-Principles Characterization of Native-Defect-Related Optical Transitions in ZnO. *J. Appl. Phys.* **2017**, *122* (3), 035704. https://doi.org/10.1063/1.4992128.
(48) Layek, A.; Stanish, P. C.; Chirmanov, V.; Radovanovic, P. V. Hybrid ZnO-Based Nanoconjugate for Efficient and Sustainable White Light Generation. *Chem. Mater.* **2015**, *27* (3), 1021–1030. https://doi.org/10.1021/cm504330k.
(49) Zhang, L.; Yin, L.; Wang, C.; lun, N.; Qi, Y.; Xiang, D. Origin of Visible Photoluminescence of ZnO Quantum Dots: Defect-Dependent and Size-Dependent. *J. Phys. Chem. C* **2010**, *114* (21), 9651–9658. https://doi.org/10.1021/jp101324a.
(50) van Dijken, A.; Meulenkamp, E. A.; Vanmaekelbergh, D.; Meijerink, A. Identification of the Transition Responsible for the Visible Emission in ZnO Using Quantum Size Effects. *J. Lumin.* **2000**, *90* (3–4), 123–128. https://doi.org/10.1016/S0022-2313(99)00599-2.
(51) Beljonne, D.; Curutchet, C.; Scholes, G. D.; Silbey, R. J. Beyond Förster Resonance Energy Transfer in Biological and Nanoscale Systems. *J. Phys. Chem. B* **2009**, *113* (19), 6583–6599. https://doi.org/10.1021/jp900708f.
(52) Govorov, A.; Hernández Martínez, P. L.; Demir, H. V. *Understanding and Modeling Förster-Type Resonance Energy Transfer (FRET)*; SpringerBriefs in Applied Sciences and Technology; Springer Singapore: Singapore, 2016. https://doi.org/10.1007/978-981-287-378-1.
(53) Wood, A.; Giersig, M.; Hilgendorff, M.; Vilas-Campos, A.; Liz-Marzán, L. M.; Mulvaney, P. Size Effects in ZnO: The Cluster to Quantum Dot Transition. *Aust. J. Chem.* **2003**, *56* (10), 1051. https://doi.org/10.1071/CH03120.
(54) Nilsson, Z. N.; Beck, L. M.; Sambur, J. B. Ensemble-Level Energy Transfer Measurements Can Reveal the Spatial Distribution of Defect Sites in Semiconductor Nanocrystals. *J. Chem. Phys.* **2021**, *154* (5), 054704. https://doi.org/10.1063/5.0034775.
(55) Lakowicz, J. R. *Principles of Fluorescence Spectroscopy*, 3rd ed.; Springer: New York, 2006.

(56) Nath, D.; Singh, F.; Das, R. X-Ray Diffraction Analysis by Williamson-Hall, Halder-Wagner and Size-Strain Plot Methods of CdSe Nanoparticles- a Comparative Study. *Mater. Chem. Phys.* **2020**, *239*, 122021. https://doi.org/10.1016/j.matchemphys.2019.122021.
(57) Garciamartinez, O.; Rojas, R.; Vila, E.; Devidales, J. Microstructural Characterization of Nanocrystals of ZnO and CuO Obtained from Basic Salts. *Solid State Ion.* **1993**, *63–65*, 442–449. https://doi.org/10.1016/0167-2738(93)90142-P.
(58) De Nolf, K.; Capek, R. K.; Abe, S.; Sluydts, M.; Jang, Y.; Martins, J. C.; Cottenier, S.; Lifshitz, E.; Hens, Z. Controlling the Size of Hot Injection Made Nanocrystals by Manipulating the Diffusion Coefficient of the Solute. *J. Am. Chem. Soc.* **2015**, *137* (7), 2495–2505. https://doi.org/10.1021/ja509941g.
(59) Khorsand Zak, A.; Razali; Abd Majid, W. H. B.; Darroudi, M. Synthesis and Characterization of a Narrow Size Distribution of Zinc Oxide Nanoparticles. *Int. J. Nanomedicine* **2011**, 1399. https://doi.org/10.2147/IJN.S19693.
(60) Pranjali, P.; Meher, M. K.; Raj, R.; Prasad, N.; Poluri, K. M.; Kumar, D.; Guleria, A. Physicochemical and Antibacterial Properties of PEGylated Zinc Oxide Nanoparticles Dispersed in Peritoneal Dialysis Fluid. *ACS Omega* **2019**, *4* (21), 19255–19264. https://doi.org/10.1021/acsomega.9b02615.
(61) Harder, P.; Grunze, M.; Dahint, R.; Whitesides, G. M.; Laibinis, P. E. Molecular Conformation in Oligo(Ethylene Glycol)-Terminated Self-Assembled Monolayers on Gold and Silver Surfaces Determines Their Ability To Resist Protein Adsorption. *J. Phys. Chem. B* **1998**, *102* (2), 426–436. https://doi.org/10.1021/jp972635z.
(62) Huang, H.-C.; Hsieh, T.-E. Highly Stable Precursor Solution Containing ZnO Nanoparticles for the Preparation of ZnO Thin Film Transistors. *Nanotechnology* **2010**, *21* (29), 295707. https://doi.org/10.1088/0957-4484/21/29/295707.
(63) Adumeau, L.; Genevois, C.; Roudier, L.; Schatz, C.; Couillaud, F.; Mornet, S. Impact of Surface Grafting Density of PEG Macromolecules on Dually Fluorescent Silica Nanoparticles Used for the in Vivo Imaging of Subcutaneous Tumors. *Biochim. Biophys. Acta BBA - Gen. Subj.* **2017**, *1861* (6), 1587–1596. https://doi.org/10.1016/j.bbagen.2017.01.036.
(64) Shang, X.; Zhu, Z.; Yin, J.; Ma, X. Compatibility of Soluble Polyimide/Silica Hybrids Induced by a Coupling Agent. *Chem. Mater.* **2002**, *14* (1), 71–77. https://doi.org/10.1021/cm010088v.
(65) Tucker-Schwartz, A. K.; Farrell, R. A.; Garrell, R. L. Thiol–Ene Click Reaction as a General Route to Functional Trialkoxysilanes for Surface Coating Applications. *J. Am. Chem. Soc.* **2011**, *133* (29), 11026–11029. https://doi.org/10.1021/ja202292q.
(66) Chen, G.-S.; Chang, W.-H.; Chang, C.-C.; Chien, Y.-H.; Fang, J.-S.; Cheng, Y.-L. Structural Models and Barrier Properties of Amine-Terminated Trialkoxysilane Monolayers Incubated in Nonpolar vs. Polar Protic Solvents. *Mater. Chem. Phys.* **2021**, *274*, 125113. https://doi.org/10.1016/j.matchemphys.2021.125113.
(67) Beane, G. A.; Morfa, A. J.; Funston, A. M.; Mulvaney, P. Defect-Mediated Energy Transfer between ZnO Nanocrystals and a Conjugated Dye. *J. Phys. Chem. C* **2012**, 120125142738004. https://doi.org/10.1021/jp209638g.
(68) Vanheusden, K.; Warren, W. L.; Seager, C. H.; Tallant, D. R.; Voigt, J. A.; Gnade, B. E. Mechanisms behind Green Photoluminescence in ZnO Phosphor Powders. *J. Appl. Phys.* **1996**, *79* (10), 7983–7990. https://doi.org/10.1063/1.362349.
(69) Janotti, A.; Van de Walle, C. G. Oxygen Vacancies in ZnO. *Appl. Phys. Lett.* **2005**, *87* (12), 122102. https://doi.org/10.1063/1.2053360.

(70) Wang, D.; Xing, G.; Gao, M.; Yang, L.; Yang, J.; Wu, T. Defects-Mediated Energy Transfer in Red-Light-Emitting Eu-Doped ZnO Nanowire Arrays. *J. Phys. Chem. C* **2011**, *115* (46), 22729–22735. https://doi.org/10.1021/jp204572v.
(71) Sadhu, S.; Tachiya, M.; Patra, A. A Stochastic Model for Energy Transfer from CdS Quantum Dots/Rods (Donors) to Nile Red Dye (Acceptors). *J. Phys. Chem. C* **2009**, *113* (45), 19488–19492. https://doi.org/10.1021/jp906160z.
(72) van Dijken, A.; Meulenkamp, E. A.; Vanmaekelbergh, D.; Meijerink, A. The Kinetics of the Radiative and Nonradiative Processes in Nanocrystalline ZnO Particles upon Photoexcitation. *J. Phys. Chem. B* **2000**, *104* (8), 1715–1723. https://doi.org/10.1021/jp993327z.
(73) Norberg, N. S.; Gamelin, D. R. Influence of Surface Modification on the Luminescence of Colloidal ZnO Nanocrystals. *J. Phys. Chem. B* **2005**, *109* (44), 20810–20816. https://doi.org/10.1021/jp0535285.
(74) Lustig, D. R.; Nilsson, Z. N.; Mulvey, J. T.; Zang, W.; Pan, X.; Patterson, J. P.; Sambur, J. B. Toward Imaging Defect-Mediated Energy Transfer between Single Nanocrystal Donors and Single Molecule Acceptors. *Chem. Biomed. Imaging* **2023**, *1* (2), 168–178. https://doi.org/10.1021/cbmi.3c00015.
(75) Lin, J.; Zhang, H.; Morovati, V.; Dargazany, R. PEGylation on Mixed Monolayer Gold Nanoparticles: Effect of Grafting Density, Chain Length, and Surface Curvature. *J. Colloid Interface Sci.* **2017**, *504*, 325–333. https://doi.org/10.1016/j.jcis.2017.05.046.
(76) Xu, Q.; Ensign, L. M.; Boylan, N. J.; Schön, A.; Gong, X.; Yang, J.-C.; Lamb, N. W.; Cai, S.; Yu, T.; Freire, E.; Hanes, J. Impact of Surface Polyethylene Glycol (PEG) Density on Biodegradable Nanoparticle Transport in Mucus *Ex Vivo* and Distribution *in Vivo*. *ACS Nano* **2015**, *9* (9), 9217–9227. https://doi.org/10.1021/acsnano.5b03876.

CHAPTER 3: TOWARDS IMAGING DEFECT-MEDIATED ENERGY TRANSFER BETWEEN SINGLE NANOCRYSTAL DONORS AND SINGLE MOLECULE ACCEPTORS[2]

3.1 Overview

Defect-mediated energy transfer is an energy transfer process between midgap electronic states in a semiconductor nanocrystal (NC) and molecular acceptors, such as fluorescent dye molecules. Super-resolution fluorescence microscopy represents an exciting technique to pinpoint the nanoscale positions of lattice defect sites in, for example, a micrometer-sized particle or thin film sample by spatially resolving the location of the acceptor dye molecules with nanometer resolution. Toward this goal, our group performed ensemble-level, time-resolved fluorescence spectroscopy measurements of ZnO NC/Alexafluor 555 (A555) mixtures and calculated that the emissive defect sites are located, on average, 0.5 nm from the NC surface (Nilsson et al., *J. Chem. Phys.* **2021**, *154* (5), 054704). However, ensemble-level measurements cannot spatially resolve the defect sites on single particles, nor can they distinguish between surface adsorbed dye molecules that participate in the energy transfer process from those that do not. In this work, we compared the photoluminescence (PL) intensity trajectories of 789 isolated, single ZnO NC donors to that of 73 non-specifically bound and 5 specifically bound ZnO NC/A555 pairs, where the donor and acceptor centroid positions were separated by a distance less than our localization precision (40 nm). We observed minor fluorescence intensity fluctuations in the donor and defect channels instead of clear anti-correlated intensity fluctuations, which could be explained by (1) the presence of multiple emissive defect sites per NC; (2) donor-acceptor separation distances slightly larger than the Förster radius (R_0 = 3.1 nm; defined as the distance at which energy transfer is 50% efficient); and/or (3) poor dipole-dipole coupling. The single molecule imaging methodology we developed, alternating ultraviolet-visible excitation

[2] Reproduced with permissions from Lustig, D., Nilsson, N., Mulvey, J., Zang, W., Pan, X., Patterson, J., and Sambur, J., Toward Imaging Defect-Mediated Energy Transfer between Single Nanocrystal Donors and Single Molecule Acceptors. Chemical & Biomedical Imaging 2023, 1(2): 168-178 Copyright 2023, American Chemical Society.

sequence combined with multi-color photon detection, successfully distinguishes specifically bound and non-specifically bound NC/dye pairs and can be applied to study a wide range of hybrid NC/dye energy transfer systems.

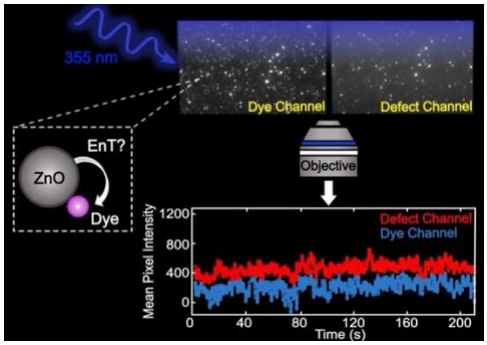

Figure 3.1. Chapter 3 overview: cartoon illustration of defect-mediated EnT between ZnO NC donors and A555 acceptors using single-molecule fluorescence microscopy.

3.2 Introduction

Semiconductor nanocrystal (NC) donors engage in energy transfer (EnT) with molecular acceptors such as organic dyes[1–9] and metal coordination complexes.[10–16] In this scenario, an electronically excited semiconductor nanocrystal "donor" transfers its energy to a molecular "acceptor". When the absorption of the dye acceptor overlaps with the NC bandgap emission, the EnT process has been physically modeled using Förster theory where singlet exciton transfer occurs via through-space dipole-dipole coupling from the donor dipole located at the NC center to a surface adsorbed dye acceptor.[17,18]

Aside from band edge electronic states, defect electronic states can participate in the EnT process. Time-resolved spectroscopy experiments have revealed that surface defect sites on PbS NCs can serve as intermediates in triplet-triplet EnT.[14,19] There is also some indication that defect states in CdSe NCs also participate in triplet-triplet EnT.[20–22] Alternatively, Mulvaney and co-workers demonstrated a particularly interesting defect-mediated singlet exciton EnT process between ZnO NCs and AlexaFluor dyes.[23] The same phenomenon was also observed with Ga_2O_3

NCs and ATTO 590 dyes.[24] Furthermore, defect-mediated EnT of ZnO nanowire arrays[25] and more recently, thin films[26] with rare earth ions has been observed. In the singlet exciton defect-mediated process, the energy exchange process occurs between a trapped exciton, located in an energy level inside the forbidden band gap of the semiconductor, and an acceptor molecule positioned at or near the NC surface.[14,20] The defect-related energy level is commonly referred to as a midgap state, a surface defect state, or a surface state in the literature.[14,27–29]

Both the band edge and defect-mediated EnT process has been physically modeled using Förster resonance energy transfer (FRET) theory[23,24,30–37], which is well established for molecular donor/acceptor pairs. Our group showed that ensemble-level time-resolved photoluminescence (TRPL) spectroscopy can reveal the average separation distance between emissive defects in ZnO NCs and surface adsorbed A555 acceptors when the NC radius is larger than the Förster radius (R_0).[38] In that study, we discussed how FRET-based analyses cannot reveal the locations of emissive defect sites in semiconductor NCs when R_0 is larger than the NC radius even when the geometry of the NC is taken into account using a restricted geometry model[30] of NC-molecule EnT.[38]

Unfortunately, ensemble-level measurements are unable to measure the spatial distribution of emissive defects for the following reasons. In general, the error in estimating the number of adsorbed dye molecules per NC is large because the semiconductor NC concentration in bulk solution is not trivial to measure. Moreover, ensemble-level EnT measurements cannot distinguish which surface adsorbed acceptor molecules participate in the EnT process. Distinguishing active versus inactive acceptor molecules could help to understand the donor dipole orientation factor and whether all molecules contribute equally to defect PL quenching, which is an assumption in the stochastic binding model of EnT.[31] FRET-based models also assume that donor dipoles are

located at the NC center (i.e., the point dipole approximation fails),[40–44] which has important consequences for a related underlying assumption that the dipole orientation factor $\kappa^2 = \frac{2}{3}$. Because many underlying assumptions in FRET-based models likely do not hold for NC-molecule donor-acceptor pairs, the community is unable to correctly analyze and interpret ensemble-level steady-state and TRPL data.

Single molecule, super-resolution fluorescence microscopy experiments performed at the single NC-level could overcome the complications and limitations described above. Single molecule EnT experiments have the potential to pinpoint the locations of emissive defect sites in thin films, large nanostructures, or microwires, assuming the defect sites are spatially separated by a distance larger than the spatial resolution in single-molecule fluorescence microscopy experiments (typically 20-40 nm).[45] At the same time, distinguish EnT-active from spectator molecules by selectively exciting the donor and acceptor species in the NC-dye conjugate, as Banin and co-workers showed for single CdSe/CdS nanorod donors in the presence of multiple Atto 590 acceptors.[46] The authors observed step-like changes in both acceptor and donor emission, enabling them to calculate the EnT efficiency and donor-acceptor distances. However, the single molecule, single NC approach has not been applied to study defect-mediated EnT. Additionally, the super-optical resolution imaging method has not been applied to dye/NC systems to pinpoint EnT events with nanometer spatial resolution. We note that scanning tunneling microscopy and super-optical resolution imaging of nanocrystal emission have been used to image energy flow in nanocrystal solids,[47,48] but they have not been applied to nanocrystal/molecule systems under solution phase or photocatalytic conditions. In this work, we develop a single molecule, single NC-level imaging methodology to study defect-mediated EnT between semiconductor NCs and molecular dyes.

3.3 Experimental Methods

3.3.1 Nanocrystal Synthesis

4.5 nm-diameter ZnO NCs were synthesized using a base hydrolysis of zinc acetate dihydrate in ethanol following the approach of Wood et al.[49] 1.0 g $Zn(OAc)_2 \cdot 2H_2O$ (Sigma Aldrich) was added to 100 mL of 200 proof ethanol (Pharmco-Aaper) in a 250-mL round bottom flask. The solution was stirred and heated to 68 °C to dissolve the zinc acetate. Then, 2 mL of a 20% methanolic solution of tetramethylammonium hydroxide (TMAOH, Sigma Aldrich) was added to the flask as quickly as possible. The solution was stirred and the reaction temperature was maintained at 68 °C for 500 min. Then, the reaction was quenched by injecting a 10 mL aliquot of the reaction mixture into 30 mL of hexanes, causing the NCs to precipitate. The mixture was centrifuged to separate the NCs from the unreacted Zn^{2+} and TMAOH. This washing procedure was repeated 5 times with hexanes. The washed NCs were suspended in spectrophotometric grade ethanol and stored at –4 °C when not in use. All reagents were used as received and without further purification.

3.3.2 Nanocrystal Characterization

The absorbance and PL spectra of the ZnO NCs were measured using a HP 8452A Diode Array Spectrophotometer and Edinburgh Instruments FS5, respectively. All spectra were measured at room temperature in spectrophotometric grade ethanol in 1 cm quartz cuvettes. TEM samples were prepared by drop casting the NCs from a hexane solution onto a lacey carbon grid. The average and standard deviation values for the NC diameter were determined from transmission electron microscopy (TEM, JEOL JEM-2100F, 200 keV) of at least 50 NCs. The molarity of the ZnO NC samples were calculated from TEM and elemental analysis following the approach of Yu et al.,[50] and described in detail in our previous work.[38] The scanning transmission electron

microscopy (STEM) characterization was performed on a JEOL Grand ARM 300CF microscope equipped with a cold field emission gun (FEG) and double spherical aberration correctors operated at 300 kV. All the high-angle annular dark-field-scanning transmission electron microscopy (HAADF-STEM) images were recorded with a probe current of 23 pA, using a convergence semi-angle of 21 mrad and inner- and outer- collection angles of 79 and 180 mrad, respectively.

3.3.3 Single Molecule Fluorescence Microscopy

Details regarding sample preparation, the experimental setup, and image analysis procedures can be found in the Appendix B. Briefly, quartz slides (Delta Technologies, QS-0310) were immersed in Piranha solution for at least 12 hours. The quartz slides were rinsed with 10 MΩ water and stored in spectrophotometric grade ethanol. Approximately 20 μL of the ethanolic ZnO NC solution was spin coated on a clean quartz slide rotating at 1000 RPM. ZnO NC-dye samples were prepared by drop-casting 40 μL of 0.1 nM dye solution on the quartz slide. The dye droplet remained on the slide for 1 min before removing the liquid with a nitrogen gas stream. A drop of Immersol W 2010 immersion oil (Zeiss) was placed between the NC-dye-coated quartz slide and a #1 glass coverslip (19904). The Immersol oil was chosen because (1) the NCs and A555 molecules are not soluble in this media and, therefore, the fluid prevents the NCs and molecules from detaching from the quartz slide; (2) the ZnO NC emission decays in air; (3) the ZnO NCs and molecules detach from the slide if the experiments were performed in the same ethanol solvent used for ensemble-level testing; (4) the Immersol fluid is index-matched to our 60× water immersion objective (NA = 1.2, Olympus, UPLANSAPO60×/W).

The NC-dye-coated quartz slide sample was placed on the stage of an Olympus IX73 inverted microscope equipped with a prism-type total internal reflection fluorescence (TIRF) microscopy setup. Two excitation lasers illuminated the sample: a 355 nm laser (Coherent Genesis

CX) selectively excited the ZnO NCs while a 532 nm laser (Coherent Obis) selectively excited the A555 molecules. A programmable Thorlabs shutter allowed us to excite with either one or with both lasers at the same time. Photons emitted from the sample were collected through the objective, passed through a long pass filter (cutoff wavelength: 440 nm) in the filter cube of the Olympus microscope, and then directed to an image splitter (Hamamatsu Gemini W-view), which uses a dichroic mirror (cutoff wavelength: 550 nm) to split the photon stream into two channels defined by the band pass filters used for each channel. One bandpass filter was chosen to match the emission signal from the A555 molecules (585/40 bandpass). This channel represents the "dye channel". The second bandpass filter was chosen to match the defect emission from ZnO only (490/60 bandpass), forming the "defect channel". The two channels were projected onto an EMCCD camera (Andor iXon 897) operated to produce a single image, split vertically. Figure B1 shows a representative example of the split image before subsequent image processing. Fluorescence images were continuously acquired at a 25 ms frame rate while the excitation lasers were alternated in an on/off fashion, as described in more detail below. The intensity trajectories of single ZnO NCs and dye molecules from the image stacks, or movies, were extracted using the detailed image analysis algorithm described in the Appendix B (see Figure B2-B5).

3.4 Results

3.4.1 Ensemble-level Defect-mediated EnT Between ZnO NCs and A555

We synthesized 4.5 ± 0.67 nm-diameter (N = 50 NCs) ZnO NCs (Figure 3.2a) and demonstrated these NCs participate in defect-mediated EnT with A555 molecules using ensemble-level fluorescence spectroscopy. Figure 3.2b shows the absorption and emission properties of the ZnO NC donors and A555 acceptors. Upon exciting the ZnO NC bandgap with UV light, a broad defect emission peak appears at 600 nm that has been attributed to oxygen vacancies.[51-51] This

ZnO defect emission peak overlaps completely with the absorption spectrum of A555 acceptors. Upon mixing 70 nM ZnO NCs with 32 nM A555 and exciting the band gap of the ZnO NCs with 355 nm light, the defect PL peak is quenched and the donor fluorescence increases by a factor of 6 beyond the intensity observed in the absence of the donor (Figure 3.2c, top blue trace versus grey trace). Hence, ensemble-level measurements show clear defect-mediated EnT behavior when the ZnO NCs donors and A555 acceptors freely diffuse in ethanol. We recognize that the dye emission overlaps strongly with the broad defect PL, which presents experimental complications such as unambiguously distinguishing photons emitted from A555 acceptors from NC donors. However, the rationale for choosing the A555 acceptor is that this molecule does not absorb the 355 nm excitation laser light source used to excite the ZnO NC donors. AlexaFluor dyes with red-shifted emission profiles such as A595 strongly absorb the UV excitation light.

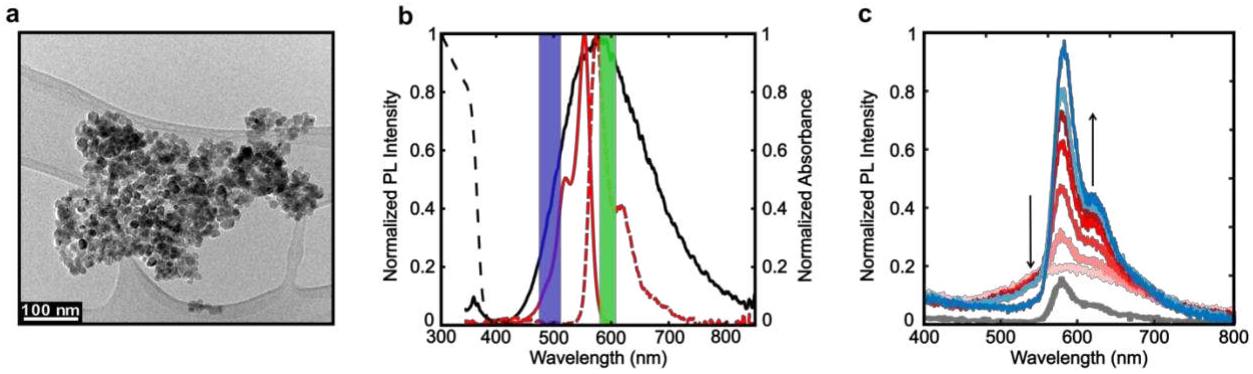

Figure 3.2. a) TEM image of ZnO NCs. The average diameters = 4.5 ± 0.67 nm from N = 50 NCs. b) Normalized absorption and emission spectra for ZnO NCs (black dashed line and black solid line, respectively) and normalized absorption and emission of A555 dye (red solid and red dashed lines, respectively). The blue shaded region represents the bandpass filter (490/60 nm) for the "defect channel" in single molecule imaging experiments. The green shaded region refers to the 585/40 nm bandpass filter for the "dye channel". c) Steady-state emission spectra of ZnO alone (light pink spectra) and mixtures of ZnO donors with increasing A555 acceptor concentration (0-32 nM) where the teal is the highest concentration of acceptor. The gray spectrum shows 32 nM A555 dye alone.

3.4.2 Single Molecule, Single NC-level Imaging Methodology

Having demonstrated that these ZnO NC donors participate in EnT with freely diffusing A555 acceptors in solution, we deposited the NC donors and A555 acceptors on a quartz substrate and studied their emission behaviors using single molecule fluorescence microscopy. In a typical

experiment, ZnO NCs and A555 solutions were sequentially spin coated onto a clean quartz slide and mounted on the stage of an inverted optical microscope equipped with a prism-type TIRF setup as shown in Figure 3.3a. Two laser sources excite the sample: a 355 nm laser selectively excited the ZnO bandgap while a 532 nm laser selectively excited A555 molecules. A high numerical aperture 60×/NA 1.2 objective collects the photons emitted from the sample. Image splitting optics provide dual wavelength images for simultaneous monitoring of the "defect" and "dye" channels, as defined by the band pass filters shown in Figure 3.2b.

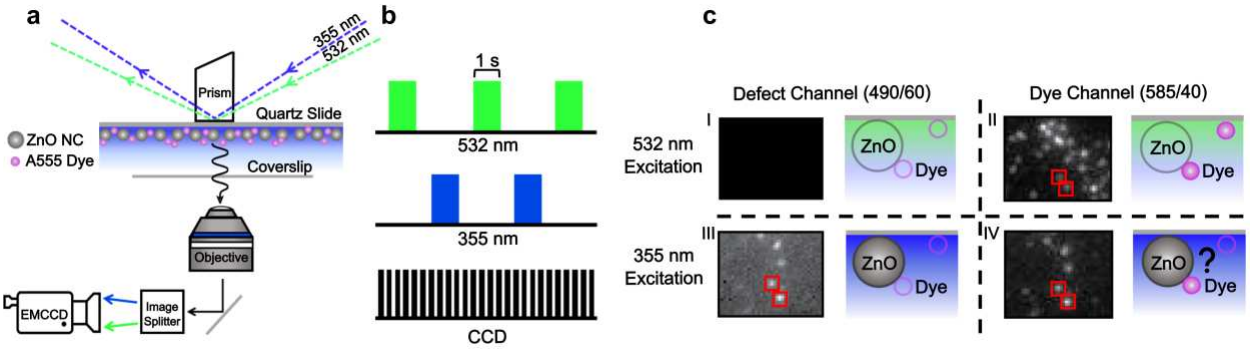

Figure 3.3. a) Single molecule fluorescence microscopy of defect-mediated EnT. A 6 mW 355 nm laser excites ZnO NC donors and a 6 mW 532 nm laser excites A555 acceptors immobilized on a quartz slide. The photons emitted from the sample were sent through an image splitter to produce "dye" and "defect" channels on the EM-CCD camera, defined by the filter sets in Figure 3.2b. b) Excitation sequence for the 355 and 532 nm lasers. See main text for rationale. The EM-CCD camera continuously operated at 40 Hz frame rate. c) Representative images and schematic illustrations of the possible entities being imaged (I-IV) using the alternating excitation laser sequence and two channel detection scheme.

Figure 3.3b shows the pulse sequence for both laser sources. Each laser illuminates the sample for 1 s with a 0.5 s dark time between each pulse. This alternating excitation sequence starts with the 532 nm laser pulse to first image all A555 molecules in the field of view. Then, the first 355 nm laser pulse excites all ZnO NCs and should presumably induce defect mediated EnT for some NC-dye pairs if an A555 molecule is located near the defect site, specifically a distance less than R_0 = 3.1 nm according to our previous work.[38] The rationale for alternating the excitation sequence is to track the dye emission as a function of increasing UV exposure time, which could cause unwanted photo-bleaching or photocatalytic oxidation of the dye via hole transfer from the

NC to the dye. Hence, this excitation/detection scheme allows us to independently excite and detect photons emitted from ZnO NCs and A555 molecules. The widefield imaging approach enables us to simultaneously monitor hundreds of individual NCs and molecules, providing many isolated NCs and dye molecules that serve as valuable internal control data to potentially distinguish from the much smaller number of NC-dye pairs (defined in greater detail below). The EM-CCD camera was continuously operated at 25 ms exposure time (i.e., 40 Hz frame rate). Figure 3.3c shows representative widefield fluorescence images for each excitation laser sequence and each detection channel. Dark shaded rectangles denote the wavelengths covered by the bandpass filters in the image splitter as shown in Figure 3.2b. Upon exciting the sample with the 532 nm laser, no signal appears in the ZnO defect channel (Figure 3.3c-I) because the 2.33 eV excitation photons do not have sufficient energy to excite the ZnO bandgap (3.4 eV). However, many individual fluorescent spots appear in the dye channel (Figure 3.3c-II). The fluorescent spots in the dye channel could represent non-specifically bound molecules adsorbed on the quartz slide as well as specifically bound dye molecules adsorbed on NCs, as schematically shown in Figure 3.3c -II.

Upon exciting the same sample region with the 355 nm laser (bottom row in Figure 3.3c), bright spots appear in both the dye and defect channels. The emission intensity in the defect channel (Figure 3.3c-III) can only represent ZnO NCs. To distinguish single NCs from NC clusters (Figure B6), we analyzed the intensities of all bright spots in the defect channel under 355 nm excitation and defined the large population or low intensity objects as single NCs (Scheme B1, Figure B7). On the other hand, the intensity of bright spots in the dye channel could stem from photo-excited ZnO NCs alone or NC-dye pairs (Figure 3.3c-IV) because the dye emission and ZnO defect PL signals overlap, as shown in Figure 3.2b-c. One strategy to distinguish ZnO NCs

alone from the ZnO/dye pair is to co-localize dye molecules observed in the dye channel under 532 nm excitation (red boxes in Figure 3.3c-II) with single ZnO NCs observed in the defect channel under 355 nm excitation (red boxes in Figure 3.3c-III).

3.4.3 Super-resolution Imaging Analysis of ZnO/NC Pairs

We developed the following algorithm to identify single dye molecules "specifically bound" to single ZnO NCs. We define "specifically bound" NC/dye pairs as those entities whose individual donor and acceptor centroid positions are separated by a distance less than our localization precision (40 nm).[55] To do so, we first classified the bright spots in Figure 3.3c-III as single ZnO NCs using an intensity thresholding procedure shown in Figure B7. Next, we segmented all single ZnO NCs into two populations: (1) 789 isolated ZnO NCs; and (2) 78 ZnO NCs with A555 molecules located within the same diffraction-limited region of interest (ROI) in the image (i.e., a dye molecule and a single NC appears in the red boxes of Figure 3.3c). Figure B8 describes the procedure for identifying an A555 dye in the same ROI as an NC. Super-resolution imaging analysis[56] of the A555 dye acceptor under the first 532 nm excitation pulse and the ZnO NC donor under the first 355 nm excitation pulse revealed two different populations: non-specifically bound and specifically bound NC/dye pairs. Figure B9 depicts the localization procedure used in this study.

Figure 3.4a shows a representative example of the non-specifically bound population (73/78 pairs), where the individual centroid positions in every frame for 355 nm and 532 nm laser illumination are shown as blue and green crosses, respectively. The black data points represent the average coordinates of the individual centroid locations, and the large circles represent the error in the individual fits (2 standard deviations). The majority of candidate NC-dye pairs are located in the same diffraction-limited ROI, but are separated by a distance larger than our spatial resolution

(Figure 3.4a). The second, smaller population (5/78) can be defined as a NC/dye pair separated by a distance smaller than our spatial resolution (Figure 3.4b). Next, we analyzed the fluorescence intensity trajectories of the specifically bound 5 NC/dye pairs and compared the results to the large population of isolated ZnO NCs and non-specifically bound ZnO/dye pairs; both serve as internal control data because the donor-acceptor distances are much larger than R_0 = 3.1 nm.

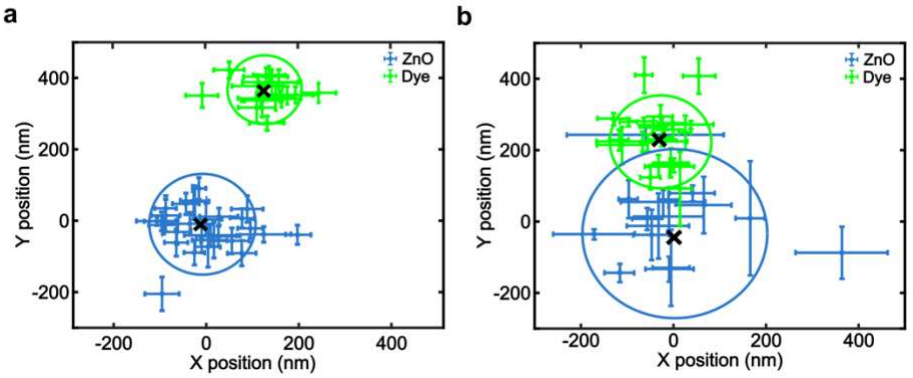

Figure 3.4. Super-resolution analysis of ZnO NC/A555 dye pairs separated by a distance (a) larger and (b) smaller than our spatial resolution. The green and blue lines represent the coordinates and localization precision of A555 dyes and ZnO NCs for the first 1 s of 532 nm and 355 nm laser illumination, respectively. The black "x" points represent the average coordinates of all individual fits. The circles represent the error of the individual fits (2 standard deviations). The ZnO centroid positions were determined from defect channel images under 355 nm excitation. The dye molecule positions were determined from dye channel images under 532 nm excitation.

3.4.4 Single molecule, Single NC-level Trajectory Analysis

Figure 3.5 shows representative fluorescence intensity trajectories for isolated ZnO NCs, non-specifically bound NC/dye pair, and a specifically bound NC/dye pair. Figure 3.5a,e,i show representative fluorescence images from the dye channel during 532 nm excitation. The bright spots represent A555 molecules. Figure 3.5b,f,j show the fluorescence intensity trajectory of the ROIs in Figure 3.5a,e,i (see green squares), where the black trajectory represents the intensity in the dye channel and the blue data points represent the intensity in the defect channel. Figure 3.5c,g,k show fluorescence images from the defect channel under 355 nm laser excitation. The bright spots represent ZnO NCs. Figure 3.5d,h,l show the trajectories in the dye and defect

channels from the ZnO NC ROIs in Figure 3.5c,g,k. The red trajectories in represent dye/defect channel intensity ratio, which will be discussed further in the next section.

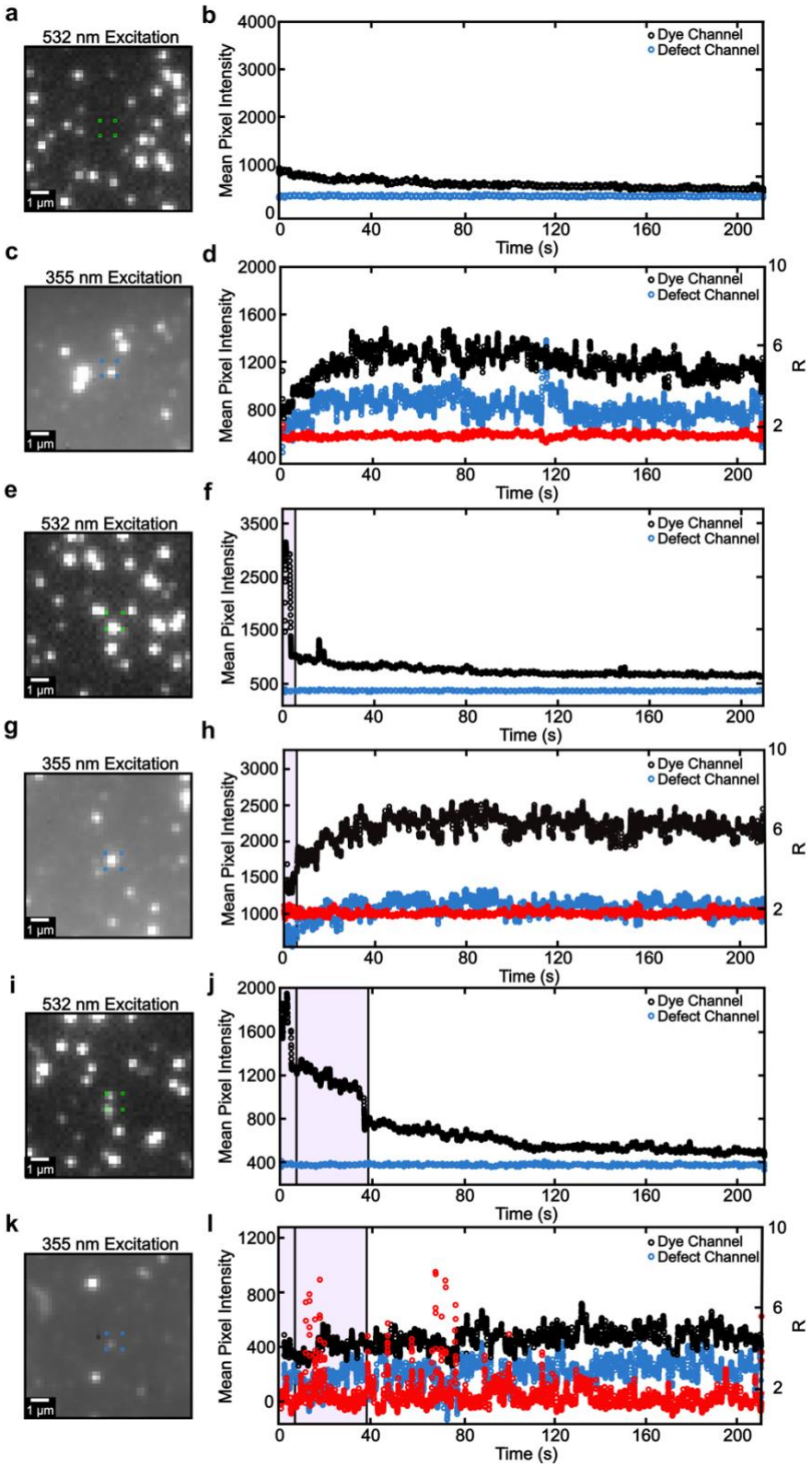

Figure 3.5. Trajectory analysis of (a-d) isolated ZnO NC, (e-h) non-specifically bound NC/dye pair, and (i-l) specifically bound NC/dye pair. (a) Fluorescence image from the dye channel under 532 nm excitation. (b) Intensity trajectory from the ROI in panel a (green squares) in the dye (black trajectory) and defect (blue trajectory) channels. The pink shaded region highlights the time where the dye molecule is "bright" under 532 nm excitation. (c)

Fluorescence image from the defect channel under 355 nm excitation. (d) same as b, but for 355 nm excitation. The red points show the dye/defect channel intensity ratio R (right axis). (e-h) and (i-l) same as (a-d), but for non-specifically bound NC/dye and specifically bound NC/dye pair, respectively.

Figure 3.5a-d shows an example of an isolated NC. The fluorescence image in Figure 3.5a shows no emissive objects inside the ROI of the dye channel during 532 nm excitation, but a clear bright spot appears in the same diffraction-limited volume in the defect channel under 355 nm excitation (Figure 3.5c). The fluorescence intensity trajectory in Figure 3.5b gradually decreases over time likely because the high intensity laser excites emissive impurities in the solvent or substrate. The weak signal decays in about 60 s, likely due to photobleaching of those impurities. The trajectories under 355 nm excitation show a slow intensity increase for the first 35 s (Figure 3.5d). One explanation for the slow rise can be attributed to chemisorbed oxygen, which can initially quench the defect emission, which was experimentally observed through ensemble-level results by van Dijken et al.[57]

Figure 3.5e-h shows a representative example of a non-specifically bound NC/dye pair. A molecule appears in the same diffraction-limited volume as the NC (Figure 3.5e) and the fluorescence intensity in the dye channel during 532 nm excitation (Figure 3.5f, black trajectory) shows clear single step photobleaching behavior that is characteristic of a single molecule (pink shaded region); note the low intensity in the defect channel (Figure 3.5f, blue trajectory) because the A555 emission does not contribute intensity to the defect channel. Figure 3.5g shows a representative image of the single ZnO NC present in the same diffraction-limited location as the dye molecule in Figure 3.5e. Both the defect and dye channel trajectories under 355 nm illumination show a slow intensity increase over the first 35 seconds of the movie (Figure 3.5h), similar to the isolated NC in Figure 3.5d.

Figure 3.5i-l shows a representative example of a specifically bound NC/dye pair. In this case, two dye molecules appear in Figure 3.5i, evidence by two distinct photobleaching events in

Figure 3.5j (shaded pink regions). We would have expected to observe simultaneous intensity bursts in the dye channel and intensity decreases in the defect channel under 355 nm excitation if EnT occurred. However, Figure 3.5l depicts only minor periods of anti-correlated intensity fluctuation behavior during the first 80 seconds of the movie. The intensity fluctuations, quantified in more detail below, do not appear in control data (Figure 3.5a-h). Unexpectedly, the fluctuations in Figure 3.5l extend beyond the photobleaching period of the second dye (second pink shaded region in Figure 3.5j). One possible cause of the intensity fluctuations is an adsorbed "dark" dye molecule remains on the NC surface and provides a non-emissive pathway for photogenerated carriers in the NC, resulting in a lower defect emission from the NC. Figure B10 depicts photobleaching times for A555 dye acceptors, showing that "bright" dye molecules can exist for at least 60 seconds under these illumination conditions. Additionally, adsorbed molecular species such as O_2 and ligands are known to quench NC emission.[57]

Regardless of the exact origin of the fluctuations, we performed further quantitative analysis to identify an EnT signature in these specifically bound NC/dye pairs that do not show clear anti-correlated FRET behavior. To do so, we calculated the dye/defect channel intensity ratio ($R = I_{dye}/I_{defect}$) for trajectories under 355 nm excitation. We would expect large R values to indicate EnT occurs because the process should experimentally manifest as an increase in the dye channel intensity and a simultaneous decrease in the defect channel intensity (see ensemble-level results in Figure 3.2c). The R values remain constant in control experiments (Figure 3.5d,h). However, distinct R intensity fluctuations appear in the specifically bound case (Figure 3.5l).

3.4.5 Single molecule, single NC-level Channel Ratio Analysis

Next, we quantitatively compared the intensity trajectories of isolated NCs to specifically bound NC-dye pairs. Our hypothesis is that EnT is most likely to manifest as intensity fluctuations

in the beginning of the trajectory. To test this hypothesis, we calculated a single R value for each NC, $\overline{R}$, by dividing the average R of the first 30 frames by the average R of the last 30 frames. If EnT occurs in the specifically bound NC/dye pairs, we would expect to observe larger $\overline{R}$ values in the specifically bound cases because the dye channel intensity should increase more and the defect channel intensity should decrease more during the beginning of the experiment than at the end of the experiment.

Figure 3.6 shows the distribution of $\overline{R}$ values for 789 isolated NCs versus the average of 5 specifically bound NC/dye pairs. The average $\overline{R}$ value of the isolated NCs is 0.92. We would have expected this value to equal 1.0 if the defect emission of the ZnO NCs was stable with illumination time. However, we observe that the low energy portion of the broad defect PL peak (dye channel) increases in some NCs (large $\overline{R}$ values in the distribution) and decreases in others (low $\overline{R}$ values). This phenomenon could be due to an evolution of optically active emissive defects in ZnO (e.g., zinc interstitials versus oxygen vacancies) under these illumination conditions, as observed previously.[58–72] Despite the complex defect emission photophysics of these ZnO NCs[66,73–75], we consistently observe larger $\overline{R}$ values for the specifically bound pairs than for the isolated ensemble average (Figure 3.6 inset). In some cases, we observe negative $\bar{R}$ values because the background ROI intensity can exceed the NC ROI intensity during the first frame. The calculated p-value for the data in Figure 3.6 is 0.65. One explanation for the large p-value is the significantly different sample size (789 vs 5). Amassing experimental data from a larger population of specifically-bound NC-dye pairs could provide further evidence that the photophysics of ZnO NCs alone differ from specifically-bound NC-dye pairs. In summary, Figure 3.6 shows a quantitative difference between isolated NCs and specifically bound NC/dye pairs that is consistent with the ensemble-level results in Figure 3.2c (i.e., dye channel enhancement and defect channel quenching). The Discussion

Section focuses on possible reasons why we did not observe clear anti-correlated FRET behavior under these experimental conditions.

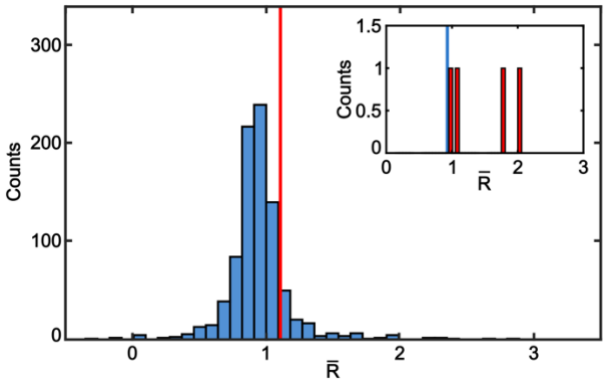

Figure 3.6. Distribution of $\bar{R}$ values for 789 isolated NCs (blue) versus the average value of 5 specifically bound ZnO/dye pairs (vertical red line). $\bar{R}$ values represent *the* average $R = I_{dye}/I_{defect}$ under 355 nm excitation of the first 30 frames divided by the average R of the last 30 frames. The inset shows the individual values of the 4 pairs whose $\bar{R}>1$. The blue vertical line is the average value of the isolated NCs.

3.5 Discussion

Here we ask the critical question: "Why do the trajectories of specifically bound NC/dye pairs *not* show clear anti-correlated FRET intensity fluctuations even though ensemble-level studies show clear FRET behavior?" One possibility is that the separation distance of the NC/dye pairs in these "specifically bound" pairs is larger than R_0 (3.1 nm). Our lab is pursuing the synthesis of ZnO/dye conjugates, where a silane layer encapsulated dye molecules around the NC core, based on a previously published synthesis.[33] Chemically linking the NC and dye is likely necessary to study a statistically meaningful population of specifically-bound pairs because our Monte Carlo simulations (Figure B11) suggest that random co-localization of the NCs and dyes only produces at least 1 non-specifically bound NC-dye pair in 50% of deposition experiments. These physically attached NC/dye constructs will allow us to rule out the possibility that the minor intensity fluctuations in Figure 3.5l are not a consequence of the spin coating method producing "specifically bound" pairs with a slightly larger separation distance than R_0.

Another possibility is the defect transition dipole moment of the NC donor does not overlap with the dye acceptor.[76–80] The ensemble-level measurements permit freely diffusing dye molecules to approach and/or temporarily adsorb to all surfaces of the ZnO NCs. This random attachment likely allows for effective dipole-dipole coupling between NC donors and dye acceptors.[2] On the other hand, both the orientation factor and separation distance of the donor and acceptor are "locked" in the single molecule imaging experiments. It is possible that the dipole moment of the defect donor site does not overlap with the single surface-adsorbed molecule. It is also possible that the dye molecule binds to the opposite side of the 4.5 nm-diameter NC where the defect site is located, causing the donor-acceptor distance to exceed $R_0 = 3.1$ nm. Synthesizing and imaging the silane encapsulated dye/NC conjugates mentioned above with polarization-dependent illumination conditions should allow us to quantify a larger number of NC/dye orientations with minimal separation distance.

Another explanation for the lack of defect emission quenching is multiple defect sites contribute to the emission signal. In this scenario, multiple emitters dominate the emission signal and the single defect site participating in EnT cannot be observed. High resolution TEM imaging of our NC sample (Figure 3.7) revealed defective voids that could be associated with multiple lattice defect sites.[68,69,81–86]

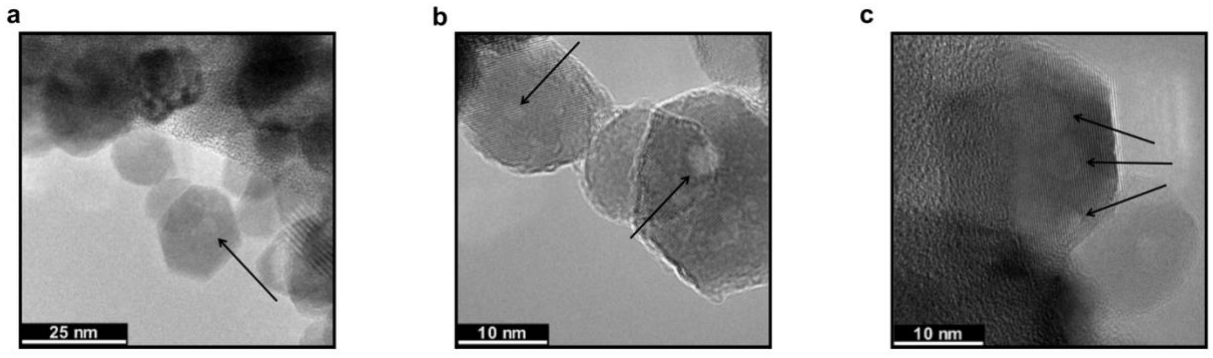

Figure 3.7. TEM images of ZnO NCs with various defective regions highlighted by the black arrows. Note: a) and b) shows the same NCs at different magnifications. c) A single ZnO NC showing multiple defective regions.

Additionally, we performed a focal series of cross-sectional STEM images to understand the distribution of porous defects in three dimensions. Figure 3.8 shows the images selected from the STEM focal series, which revealed that porous defects exist within the NC core and at the surface. Multiple nanometer-scale voids of various shapes appear in a single particle as the focus position changes. The theoretical description of the donor dipole moment and its orientation relative to the acceptor dipole remains unclear for these large crystallographic defects. We also calculated the number of defects per NC based on literature values of O and Zn vacancy concentrations (Table B1). We concluded that there are, on average, 0.5 defects per NC, in addition to the large defective voids in Figure 3.7. In summary, these NCs likely have more than 1 defect site per NC and, therefore, a single dye molecule may not fully quench the defect emission from the sample.

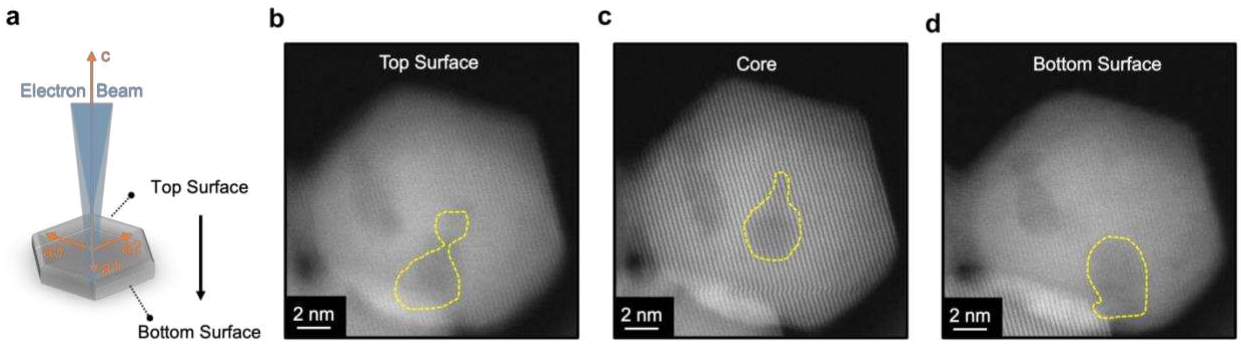

Figure 3.8. STEM images of a single nanocrystal acquired with different defocus values. (a) Cartoon illustration of the imaging scheme, where STEM images are acquired as a function of z focus position. (b-d) STEM images of the (b) top surface, (c) core, and (d) bottom surface of the NC. Yellow dashed lines show different shapes of multiple defective regions.

3.6 Conclusion

We studied defect-mediated EnT between ZnO NC donors and A555 dye acceptors using ensemble-level fluorescence spectroscopy and single molecule-level fluorescence microscopy. The ensemble-level experiments show clear FRET behavior, where the dye acceptor emission enhances and the NC donor emission quenches. Spin coating the dye on NC-coated quartz slide samples produced 73 NC/dye pairs in the same diffraction-limited space and 5 specifically bound

NC/dye pairs. We observed minor fluorescence intensity fluctuations in the trajectories of specifically bound pairs that did not appear in the trajectories of isolated NCs. Large separation distances and poor dipole-dipole coupling could explain why clear anti-correlated donor/acceptor intensity fluctuations do not appear in the intensity trajectories under these experimental conditions.

3.7 Author Contributions

According to CRediT criteria, my contributions to this work included conceptualization, data curation, formal analysis, investigation, methodology, visualization, writing – original draft, and writing – reviewing and editing. J.T.M. and J.P.P. performed TEM measurements and interpreted TEM data. W.Z. and X.P. performed STEM measurements and provided STEM data interpretation. Z.N.N., J.B.S., and D.R.L. analyzed the data and wrote the Matlab scripts. Z.N.N., J.B.S., and D.R.L. wrote the manuscript.

REFERENCES

(1) Stryer, L.; Haugland, R. P. Energy Transfer: A Spectroscopic Ruler. *Proc. Natl. Acad. Sci. U. S. A.* **1967**, *58* (2), 719–726.
(2) Clegg, R. M. Chapter 1 Förster Resonance Energy Transfer—FRET What Is It, Why Do It, and How It's Done. In *Laboratory Techniques in Biochemistry and Molecular Biology*; Elsevier, 2009; Vol. 33, pp 1–57. https://doi.org/10.1016/S0075-7535(08)00001-6.
(3) Struck, D. K.; Hoekstra, D.; Pagano, R. E. Use of Resonance Energy Transfer to Monitor Membrane Fusion. *Biochemistry* **1981**, *20* (14), 4093–4099. https://doi.org/10.1021/bi00517a023.
(4) Beardsley, K.; Tao, T.; Cantor, C. R. Conformation of the Anticodon Loop of Phenylalanine Transfer Ribonucleic Acid. Effect of Environment on the Fluorescence of the Y Base. *Biochemistry* **1970**, *9* (18), 3524–3532. https://doi.org/10.1021/bi00820a005.
(5) Gohlke, C.; Murchie, A. I.; Lilley, D. M.; Clegg, R. M. Kinking of DNA and RNA Helices by Bulged Nucleotides Observed by Fluorescence Resonance Energy Transfer. *Proc. Natl. Acad. Sci.* **1994**, *91* (24), 11660–11664. https://doi.org/10.1073/pnas.91.24.11660.
(6) Lakowicz, J. R.; Gryczynski, I.; Wiczk, W.; Laczko, G.; Prendergast, F. C.; Johnson, M. L. Conformational Distributions of Melittin in Water / Methanol Mixtures from Frequency-Domain Measurements of Nonradiative Energy Transfer. *Biophys. Chem.* **1990**, *36* (2), 99–115. https://doi.org/10.1016/0301-4622(90)85014-W.
(7) Sapsford, K. E.; Berti, L.; Medintz, I. L. Materials for Fluorescence Resonance Energy Transfer Analysis: Beyond Traditional Donor–Acceptor Combinations. *Angew. Chem. Int. Ed.* **2006**, *45* (28), 4562–4589. https://doi.org/10.1002/anie.200503873.
(8) Bruchez, M.; Moronne, M.; Gin, P.; Weiss, S.; Alivisatos, A. P. Semiconductor Nanocrystals as Fluorescent Biological Labels. *Science* **1998**, *281* (5385), 2013–2016. https://doi.org/10.1126/science.281.5385.2013.
(9) Resch-Genger, U.; Grabolle, M.; Cavaliere-Jaricot, S.; Nitschke, R.; Nann, T. Quantum Dots versus Organic Dyes as Fluorescent Labels. *Nat. Methods* **2008**, *5* (9), 763–775. https://doi.org/10.1038/nmeth.1248.
(10) Chan, W. C. W.; Nie, S. Quantum Dot Bioconjugates for Ultrasensitive Nonisotopic Detection. *Science* **1998**, *281* (5385), 2016–2018. https://doi.org/10.1126/science.281.5385.2016.
(11) Kodaimati, M. S.; Lian, S.; Schatz, G. C.; Weiss, E. A. Energy Transfer-Enhanced Photocatalytic Reduction of Protons within Quantum Dot Light-Harvesting–Catalyst Assemblies. *Proc. Natl. Acad. Sci.* **2018**, *115* (33), 8290–8295. https://doi.org/10.1073/pnas.1805625115.
(12) Zhang, Z.; Rogers, C. R.; Weiss, E. A. Energy Transfer from CdS QDs to a Photogenerated Pd Complex Enhances the Rate and Selectivity of a Pd-Photocatalyzed Heck Reaction. *J. Am. Chem. Soc.* **2020**, *142* (1), 495–501. https://doi.org/10.1021/jacs.9b11278.
(13) Mongin, C.; Garakyaraghi, S.; Razgoniaeva, N.; Zamkov, M.; Castellano, F. N. Direct Observation of Triplet Energy Transfer from Semiconductor Nanocrystals. *Science* **2016**, *351* (6271), 369–372. https://doi.org/10.1126/science.aad6378.
(14) Bender, J. A.; Raulerson, E. K.; Li, X.; Goldzak, T.; Xia, P.; Van Voorhis, T.; Tang, M. L.; Roberts, S. T. Surface States Mediate Triplet Energy Transfer in Nanocrystal–Acene Composite Systems. *J. Am. Chem. Soc.* **2018**, *140* (24), 7543–7553. https://doi.org/10.1021/jacs.8b01966.
(15) Huang, Z.; Lee Tang, M. Semiconductor Nanocrystal Light Absorbers for Photon Upconversion. *J. Phys. Chem. Lett.* **2018**, *9* (21), 6198–6206. https://doi.org/10.1021/acs.jpclett.8b02154.

(16) Wu, M.; Congreve, D. N.; Wilson, M. W. B.; Jean, J.; Geva, N.; Welborn, M.; Van Voorhis, T.; Bulović, V.; Bawendi, M. G.; Baldo, M. A. Solid-State Infrared-to-Visible Upconversion Sensitized by Colloidal Nanocrystals. *Nat. Photonics* **2016**, *10* (1), 31–34. https://doi.org/10.1038/nphoton.2015.226.
(17) Sadhu, S.; Patra, A. Donor-Acceptor Systems: Energy Transfer from CdS Quantum Dots/Rods to Nile Red Dye. *ChemPhysChem* **2008**, *9* (14), 2052–2058. https://doi.org/10.1002/cphc.200800298.
(18) Guzelturk, B.; Hernandez Martinez, P. L.; Zhao, D.; Sun, X. W.; Demir, H. V. Singlet and Triplet Exciton Harvesting in the Thin Films of Colloidal Quantum Dots Interfacing Phosphorescent Small Organic Molecules. *J. Phys. Chem. C* **2014**, *118* (45), 25964–25969. https://doi.org/10.1021/jp509799r.
(19) Zhao, G.; Chen, Z.; Xiong, K.; Liang, G.; Zhang, J.; Wu, K. Triplet Energy Migration Pathways from PbS Quantum Dots to Surface-Anchored Polyacenes Controlled by Charge Transfer. *Nanoscale* **2021**, *13* (2), 1303–1310. https://doi.org/10.1039/D0NR07837A.
(20) Jin, T.; Lian, T. Trap State Mediated Triplet Energy Transfer from CdSe Quantum Dots to Molecular Acceptors. *J. Chem. Phys.* **2020**, *153* (7), 074703. https://doi.org/10.1063/5.0022061.
(21) Halivni, S.; Sitt, A.; Hadar, I.; Banin, U. Effect of Nanoparticle Dimensionality on Fluorescence Resonance Energy Transfer in Nanoparticle–Dye Conjugated Systems. *ACS Nano* **2012**, 120217093438002. https://doi.org/10.1021/nn300216v.
(22) Li, X.; Huang, Z.; Zavala, R.; Tang, M. L. Distance-Dependent Triplet Energy Transfer between CdSe Nanocrystals and Surface Bound Anthracene. *J. Phys. Chem. Lett.* **2016**, *7* (11), 1955–1959. https://doi.org/10.1021/acs.jpclett.6b00761.
(23) Beane, G. A.; Morfa, A. J.; Funston, A. M.; Mulvaney, P. Defect-Mediated Energy Transfer between ZnO Nanocrystals and a Conjugated Dye. *J. Phys. Chem. C* **2012**, 120125142738004. https://doi.org/10.1021/jp209638g.
(24) Chirmanov, V.; Stanish, P. C.; Layek, A.; Radovanovic, P. V. Distance-Dependent Energy Transfer between Ga2O3 Nanocrystal Defect States and Conjugated Organic Fluorophores in Hybrid White-Light-Emitting Nanophosphors. *J. Phys. Chem. C* **2015**, *119* (10), 5687–5696. https://doi.org/10.1021/jp512417h.
(25) Wang, D.; Xing, G.; Gao, M.; Yang, L.; Yang, J.; Wu, T. Defects-Mediated Energy Transfer in Red-Light-Emitting Eu-Doped ZnO Nanowire Arrays. *J. Phys. Chem. C* **2011**, *115* (46), 22729–22735. https://doi.org/10.1021/jp204572v.
(26) Yatskiv, R.; Grym, J.; Bašinová, N.; Kučerová, Š.; Vaniš, J.; Piliai, L.; Vorokhta, M.; Veselý, J.; Maixner, J. Defect-Mediated Energy Transfer in ZnO Thin Films Doped with Rare-Earth Ions. *J. Lumin.* **2023**, *253*, 119462. https://doi.org/10.1016/j.jlumin.2022.119462.
(27) Nagpal, P.; Klimov, V. I. Role of Mid-Gap States in Charge Transport and Photoconductivity in Semiconductor Nanocrystal Films. *Nat. Commun.* **2011**, *2* (1), 486. https://doi.org/10.1038/ncomms1492.
(28) Voznyy, O. Mobile Surface Traps in CdSe Nanocrystals with Carboxylic Acid Ligands. *J. Phys. Chem. C* **2011**, *115* (32), 15927–15932. https://doi.org/10.1021/jp205784g.
(29) Park, B.; Whitham, K.; Bian, K.; Lim, Y.-F.; Hanrath, T. Probing Surface States in PbS Nanocrystal Films Using Pentacene Field Effect Transistors: Controlling Carrier Concentration and Charge Transport in Pentacene. *Phys Chem Chem Phys* **2014**, *16* (47), 25729–25733. https://doi.org/10.1039/C4CP01507J.
(30) Sitt, A.; Even-Dar, N.; Halivni, S.; Faust, A.; Yedidya, L.; Banin, U. Analysis of Shape and Dimensionality Effects on Fluorescence Resonance Energy Transfer from Nanocrystals to

Multiple Acceptors. *J. Phys. Chem. C* **2013**, *117* (43), 22186–22197. https://doi.org/10.1021/jp308243p.
(31) Sadhu, S.; Tachiya, M.; Patra, A. A Stochastic Model for Energy Transfer from CdS Quantum Dots/Rods (Donors) to Nile Red Dye (Acceptors). *J. Phys. Chem. C* **2009**, *113* (45), 19488–19492. https://doi.org/10.1021/jp906160z.
(32) Bora, T.; Lakshman, K. K.; Sarkar, S.; Makhal, A.; Sardar, S.; Pal, S. K.; Dutta, J. Modulation of Defect-Mediated Energy Transfer from ZnO Nanoparticles for the Photocatalytic Degradation of Bilirubin. *Beilstein J. Nanotechnol.* **2013**, *4*, 714–725. https://doi.org/10.3762/bjnano.4.81.
(33) Layek, A.; Stanish, P. C.; Chirmanov, V.; Radovanovic, P. V. Hybrid ZnO-Based Nanoconjugate for Efficient and Sustainable White Light Generation. *Chem. Mater.* **2015**, *27* (3), 1021–1030. https://doi.org/10.1021/cm504330k.
(34) Curutchet, C.; Franceschetti, A.; Zunger, A.; Scholes, G. D. Examining Förster Energy Transfer for Semiconductor Nanocrystalline Quantum Dot Donors and Acceptors. *J. Phys. Chem. C* **2008**, *112* (35), 13336–13341. https://doi.org/10.1021/jp805682m.
(35) Adarsh, K. S.; Singh, M. K.; Shivkumar, M. A.; Rabinal, M. K.; Jagatap, B. N.; Mulimani, B. G.; Savadatti, M. I.; Inamdar, S. R. FRET from Core and Core–Shell Quantum Dots to Laser Dye: A Comparative Investigation. *J. Lumin.* **2015**, *160*, 216–222. https://doi.org/10.1016/j.jlumin.2014.12.014.
(36) Conroy, E. M.; Li, J. J.; Kim, H.; Algar, W. R. Self-Quenching, Dimerization, and Homo-FRET in Hetero-FRET Assemblies with Quantum Dot Donors and Multiple Dye Acceptors. *J. Phys. Chem. C* **2016**, *120* (31), 17817–17828. https://doi.org/10.1021/acs.jpcc.6b05886.
(37) Chowdhury, P. S.; Sen, P.; Patra, A. Optical Properties of CdS Nanoparticles and the Energy Transfer from CdS Nanoparticles to Rhodamine 6G. *Chem. Phys. Lett.* **2005**, *413* (4–6), 311–314. https://doi.org/10.1016/j.cplett.2005.07.088.
(38) Nilsson, Z. N.; Beck, L. M.; Sambur, J. B. Ensemble-Level Energy Transfer Measurements Can Reveal the Spatial Distribution of Defect Sites in Semiconductor Nanocrystals. *J. Chem. Phys.* **2021**, *154* (5), 054704. https://doi.org/10.1063/5.0034775.
(39) Nilsson, Z. N.; Beck, L. M.; Sambur, J. B. Ensemble-Level Energy Transfer Measurements Can Reveal the Spatial Distribution of Defect Sites in Semiconductor Nanocrystals. *J. Chem. Phys.* **2021**, *154* (5), 054704. https://doi.org/10.1063/5.0034775.
(40) Giménez, S.; Rogach, A. L.; Lutich, A. A.; Gross, D.; Poeschl, A.; Susha, A. S.; Mora-Seró, I.; Lana-Villarreal, T.; Bisquert, J. Energy Transfer versus Charge Separation in Hybrid Systems of Semiconductor Quantum Dots and Ru-Dyes as Potential Co-Sensitizers of TiO_2 -Based Solar Cells. *J. Appl. Phys.* **2011**, *110* (1), 014314. https://doi.org/10.1063/1.3605486.
(41) Härmä, H.; Soukka, T.; Shavel, A.; Gaponik, N.; Weller, H. Luminescent Energy Transfer between Cadmium Telluride Nanoparticle and Lanthanide(III) Chelate in Competitive Bioaffinity Assays of Biotin and Estradiol. *Anal. Chim. Acta* **2007**, *604* (2), 177–183. https://doi.org/10.1016/j.aca.2007.10.003.
(42) Geißler, D.; Linden, S.; Liermann, K.; Wegner, K. D.; Charbonnière, L. J.; Hildebrandt, N. Lanthanides and Quantum Dots as Förster Resonance Energy Transfer Agents for Diagnostics and Cellular Imaging. *Inorg. Chem.* **2014**, *53* (4), 1824–1838. https://doi.org/10.1021/ic4017883.
(43) McLaurin, E. J.; Greytak, A. B.; Bawendi, M. G.; Nocera, D. G. Two-Photon Absorbing Nanocrystal Sensors for Ratiometric Detection of Oxygen. *J. Am. Chem. Soc.* **2009**, *131* (36), 12994–13001. https://doi.org/10.1021/ja902712b.

(44) Britton, J.; Antunes, E.; Nyokong, T. Fluorescence Quenching and Energy Transfer in Conjugates of Quantum Dots with Zinc and Indium Tetraamino Phthalocyanines. *J. Photochem. Photobiol. Chem.* **2010**, *210* (1), 1–7. https://doi.org/10.1016/j.jphotochem.2009.12.013.
(45) Sambur, J. B.; Chen, P. Approaches to Single-Nanoparticle Catalysis. *Annu. Rev. Phys. Chem.* **2014**, *65* (1), 395–422. https://doi.org/10.1146/annurev-physchem-040513-103729.
(46) Hadar, I.; Halivni, S.; Even-Dar, N.; Faust, A.; Banin, U. Dimensionality Effects on Fluorescence Resonance Energy Transfer between Single Semiconductor Nanocrystals and Multiple Dye Acceptors. *J. Phys. Chem. C* **2015**, *119* (7), 3849–3856. https://doi.org/10.1021/jp512678j.
(47) Wang, Y. S.; Thomas, P. J.; O'Brien, P. Optical Properties of ZnO Nanocrystals Doped with Cd, Mg, Mn, and Fe Ions. *J. Phys. Chem. B* **2006**, *110* (43), 21412–21415. https://doi.org/10.1021/jp0654415.
(48) Xu, C. X.; Sun, X. W.; Zhang, X. H.; Ke, L.; Chua, S. J. Photoluminescent Properties of Copper-Doped Zinc Oxide Nanowires. *Nanotechnology* **2004**, *15* (7), 856–861. https://doi.org/10.1088/0957-4484/15/7/026.
(49) Wood, A.; Giersig, M.; Hilgendorff, M.; Vilas-Campos, A.; Liz-Marzán, L. M.; Mulvaney, P. Size Effects in ZnO: The Cluster to Quantum Dot Transition. *Aust. J. Chem.* **2003**, *56* (10), 1051. https://doi.org/10.1071/CH03120.
(50) Yu, W. W.; Qu, L.; Guo, W.; Peng, X. Experimental Determination of the Extinction Coefficient of CdTe, CdSe, and CdS Nanocrystals. *Chem. Mater.* **2003**, *15* (14), 2854–2860. https://doi.org/10.1021/cm034081k.
(51) Zhang, L.; Yin, L.; Wang, C.; lun, N.; Qi, Y.; Xiang, D. Origin of Visible Photoluminescence of ZnO Quantum Dots: Defect-Dependent and Size-Dependent. *J. Phys. Chem. C* **2010**, *114* (21), 9651–9658. https://doi.org/10.1021/jp101324a.
(52) Vanheusden, K.; Warren, W. L.; Seager, C. H.; Tallant, D. R.; Voigt, J. A.; Gnade, B. E. Mechanisms behind Green Photoluminescence in ZnO Phosphor Powders. *J. Appl. Phys.* **1996**, *79* (10), 7983–7990. https://doi.org/10.1063/1.362349.
(53) van Dijken, A.; Meulenkamp, E. A.; Vanmaekelbergh, D.; Meijerink, A. Identification of the Transition Responsible for the Visible Emission in ZnO Using Quantum Size Effects. *J. Lumin.* **2000**, *90* (3–4), 123–128. https://doi.org/10.1016/S0022-2313(99)00599-2.
(54) Janotti, A.; Van de Walle, C. G. Oxygen Vacancies in ZnO. *Appl. Phys. Lett.* **2005**, *87* (12), 122102. https://doi.org/10.1063/1.2053360.
(55) Thompson, R. E.; Larson, D. R.; Webb, W. W. Precise Nanometer Localization Analysis for Individual Fluorescent Probes. *Biophys. J.* **2002**, *82* (5), 2775–2783. https://doi.org/10.1016/S0006-3495(02)75618-X.
(56) Sambur, J. B.; Chen, T.-Y.; Choudhary, E.; Chen, G.; Nissen, E. J.; Thomas, E. M.; Zou, N.; Chen, P. Sub-Particle Reaction and Photocurrent Mapping to Optimize Catalyst-Modified Photoanodes. *Nature* **2016**, *530* (7588), 77–80. https://doi.org/10.1038/nature16534.
(57) van Dijken, A.; Meulenkamp, E. A.; Vanmaekelbergh, D.; Meijerink, A. Influence of Adsorbed Oxygen on the Emission Properties of Nanocrystalline ZnO Particles. *J. Phys. Chem. B* **2000**, *104* (18), 4355–4360. https://doi.org/10.1021/jp993998x.
(58) Özgür, Ü.; Alivov, Ya. I.; Liu, C.; Teke, A.; Reshchikov, M. A.; Doğan, S.; Avrutin, V.; Cho, S.-J.; Morkoç, H. A Comprehensive Review of ZnO Materials and Devices. *J. Appl. Phys.* **2005**, *98* (4), 041301. https://doi.org/10.1063/1.1992666.

(59) Sett, D.; Basak, D. Toward Understanding the Role of V ZnDefect on the Photoconductivity of Surface-Passivated ZnO NRs. *J. Phys. Chem. C* **2017**, *121* (44), 24495–24504. https://doi.org/10.1021/acs.jpcc.7b06393.
(60) Lyons, J. L.; Varley, J. B.; Steiauf, D.; Janotti, A.; Van de Walle, C. G. First-Principles Characterization of Native-Defect-Related Optical Transitions in ZnO. *J. Appl. Phys.* **2017**, *122* (3), 035704. https://doi.org/10.1063/1.4992128.
(61) Jeem, M.; Zhang, L.; Ishioka, J.; Shibayama, T.; Iwasaki, T.; Kato, T.; Watanabe, S. Tuning Optoelectrical Properties of ZnO Nanorods with Excitonic Defects via Submerged Illumination. *Nano Lett.* **2017**, *17* (3), 2088–2093. https://doi.org/10.1021/acs.nanolett.7b00324.
(62) Repp, S.; Weber, S.; Erdem, E. Defect Evolution of Nonstoichiometric ZnO Quantum Dots. *J. Phys. Chem. C* **2016**, *120* (43), 25124–25130. https://doi.org/10.1021/acs.jpcc.6b09108.
(63) Villafuerte, M.; Ferreyra, J. M.; Zapata, C.; Barzola-Quiquia, J.; Iikawa, F.; Esquinazi, P.; Heluani, S. P.; de Lima Jr., M. M.; Cantarero, A. Defect Spectroscopy of Single ZnO Microwires. *J. Appl. Phys.* **2014**, *115* (13), 133101–133106. https://doi.org/10.1063/1.4869555.
(64) Kumar, P.; Pal, S. K. Role of Decoupled Defect Transitions of ZnO Nanocrystals in Energy Transfer. *J. Photochem. Photobiol. Chem.* **2014**, *278*, 46–52. https://doi.org/10.1016/j.jphotochem.2013.12.021.
(65) Jungwirth, N. R.; Pai, Y. Y.; Chang, H. S.; MacQuarrie, E. R.; Nguyen, K. X.; Fuchs, G. D. A Single-Molecule Approach to ZnO Defect Studies: Single Photons and Single Defects. *J. Appl. Phys.* **2014**, *116* (4), 043509. https://doi.org/10.1063/1.4890979.
(66) Layek, A.; Manna, B.; Chowdhury, A. Carrier Recombination Dynamics through Defect States of ZnO Nanocrystals: From Nanoparticles to Nanorods. *Chem. Phys. Lett.* **2012**, *539–540* (C), 133–138. https://doi.org/10.1016/j.cplett.2012.05.028.
(67) Cai, J.; Xu, J.; Zhang, X.; Niu, X.; Xing, T.; Ji, T.; Li, L. Defect-Related Visible Luminescence of ZnO Nanorods Annealed in Oxygen Ambient. *Optoelectron. Lett.* **2012**, *8* (1), 4–8. https://doi.org/10.1007/s11801-012-1042-2.
(68) McCluskey, M. D.; Jokela, S. J. Defects in ZnO. *J. Appl. Phys.* **2009**, *106* (7), 071101–071114. https://doi.org/10.1063/1.3216464.
(69) Janotti, A.; Van De Walle, C. G. Native Point Defects in ZnO. *Phys. Rev. B* **2007**, *76* (16), 869–22. https://doi.org/10.1103/PhysRevB.76.165202.
(70) Djurisic, A. B.; Leung, Y. H.; Tam, K. H. Defect Emissions in ZnO Nanostructures. *Opt. Ldots* **2005**. https://doi.org/10.1088/0957-4484/20/15/155603.
(71) Ong, H. The Evolution of Defect Emissions in Oxygen-Deficient and -Surplus ZnO Thin Films: The Implication of Different Growth Modes. *J. Cryst. Growth* **2004**, *265* (3–4), 471–475. https://doi.org/10.1016/j.jcrysgro.2004.02.010.
(72) Layek, A.; De, S.; Thorat, R.; Chowdhury, A. Spectrally Resolved Photoluminescence Imaging of ZnO Nanocrystals at Single-Particle Levels. *J. Phys. Chem. Lett.* **2011**, *2* (11), 1241–1247. https://doi.org/10.1021/jz200370s.
(73) Choi, S.; Phillips, M. R.; Aharonovich, I.; Pornsuwan, S.; Cowie, B. C. C.; Ton-That, C. Photophysics of Point Defects in ZnO Nanoparticles. *Adv. Opt. Mater.* **2015**, *3* (6), 821–827. https://doi.org/10.1002/adom.201400592.
(74) Wang, J.; Liu, P.; Fu, X.; Li, Z.; Han, W.; Wang, X. Relationship between Oxygen Defects and the Photocatalytic Property of ZnO Nanocrystals in Nafion Membranes. *Langmuir ACS J. Surf. Colloids* **2009**, *25* (2), 1218–1223. https://doi.org/10.1021/la803370z.

(75) Zhang, X.; Qin, J.; Xue, Y.; Yu, P.; Zhang, B.; Wang, L.; Liu, R. Effect of Aspect Ratio and Surface Defects on the Photocatalytic Activity of ZnO Nanorods. *Sci. Rep.* **2014**, *4*, 1–8. https://doi.org/10.1038/srep04596.
(76) Backlund, M. P.; Lew, M. D.; Backer, A. S.; Sahl, S. J.; Moerner, W. E. The Role of Molecular Dipole Orientation in Single-Molecule Fluorescence Microscopy and Implications for Super-Resolution Imaging. *ChemPhysChem* **2014**, *15* (4), 587–599. https://doi.org/10.1002/cphc.201300880.
(77) Wong, C. Y.; Curutchet, C.; Tretiak, S.; Scholes, G. D. Ideal Dipole Approximation Fails to Predict Electronic Coupling and Energy Transfer between Semiconducting Single-Wall Carbon Nanotubes. *J. Chem. Phys.* **2009**, *130* (8), 081104. https://doi.org/10.1063/1.3088846.
(78) Zheng, K.; Žídek, K.; Abdellah, M.; Zhu, N.; Chábera, P.; Lenngren, N.; Chi, Q.; Pullerits, T. Directed Energy Transfer in Films of CdSe Quantum Dots: Beyond the Point Dipole Approximation. *J. Am. Chem. Soc.* **2014**, *136* (17), 6259–6268. https://doi.org/10.1021/ja411127w.
(79) Baer, R.; Rabani, E. Theory of Resonance Energy Transfer Involving Nanocrystals: The Role of High Multipoles. *J. Chem. Phys.* **2008**, *128* (18), 184710. https://doi.org/10.1063/1.2913247.
(80) Hellenkamp, B.; Schmid, S.; Doroshenko, O.; Opanasyuk, O.; Kühnemuth, R.; Rezaei Adariani, S.; Ambrose, B.; Aznauryan, M.; Barth, A.; Birkedal, V.; Bowen, M. E.; Chen, H.; Cordes, T.; Eilert, T.; Fijen, C.; Gebhardt, C.; Götz, M.; Gouridis, G.; Gratton, E.; Ha, T.; Hao, P.; Hanke, C. A.; Hartmann, A.; Hendrix, J.; Hildebrandt, L. L.; Hirschfeld, V.; Hohlbein, J.; Hua, B.; Hübner, C. G.; Kallis, E.; Kapanidis, A. N.; Kim, J.-Y.; Krainer, G.; Lamb, D. C.; Lee, N. K.; Lemke, E. A.; Levesque, B.; Levitus, M.; McCann, J. J.; Naredi-Rainer, N.; Nettels, D.; Ngo, T.; Qiu, R.; Robb, N. C.; Röcker, C.; Sanabria, H.; Schlierf, M.; Schröder, T.; Schuler, B.; Seidel, H.; Streit, L.; Thurn, J.; Tinnefeld, P.; Tyagi, S.; Vandenberk, N.; Vera, A. M.; Weninger, K. R.; Wünsch, B.; Yanez-Orozco, I. S.; Michaelis, J.; Seidel, C. A. M.; Craggs, T. D.; Hugel, T. Precision and Accuracy of Single-Molecule FRET Measurements—a Multi-Laboratory Benchmark Study. *Nat. Methods* **2018**, *15* (9), 669–676. https://doi.org/10.1038/s41592-018-0085-0.
(81) Clark, S. J.; Robertson, J.; Lany, S.; Zunger, A. Intrinsic Defects in ZnO Calculated by Screened Exchange and Hybrid Density Functionals. *Phys. Rev. B* **2010**, *81* (11), 115311. https://doi.org/10.1103/PhysRevB.81.115311.
(82) Lany, S.; Zunger, A. Dopability, Intrinsic Conductivity, and Nonstoichiometry of Transparent Conducting Oxides. *Phys. Rev. Lett.* **2007**, *98* (4), 045501. https://doi.org/10.1103/PhysRevLett.98.045501.
(83) Saarinen, K.; Hautakangas, S.; Tuomisto, F. Dominant Intrinsic Acceptors in GaN and ZnO. *Phys. Scr.* **2006**, *T126*, 105–109. https://doi.org/10.1088/0031-8949/2006/T126/024.
(84) Halliburton, L. E.; Giles, N. C.; Garces, N. Y.; Luo, M.; Xu, C.; Bai, L.; Boatner, L. A. Production of Native Donors in ZnO by Annealing at High Temperature in Zn Vapor. *Appl. Phys. Lett.* **2005**, *87* (17), 172108. https://doi.org/10.1063/1.2117630.
(85) Look, D. C.; Farlow, G. C.; Reunchan, P.; Limpijumnong, S.; Zhang, S. B.; Nordlund, K. Evidence for Native-Defect Donors in n -Type ZnO. *Phys. Rev. Lett.* **2005**, *95* (22), 225502. https://doi.org/10.1103/PhysRevLett.95.225502.
(86) Oba, F.; Choi, M.; Togo, A.; Tanaka, I. Point Defects in ZnO: An Approach from First Principles. *Sci. Technol. Adv. Mater.* **2011**, *12* (3), 034302. https://doi.org/10.1088/1468-6996/12/3/034302.

CHAPTER 4: SINGLE-MOLECULE FLUORESCENCE MICROSCOPY REVEALS ENERGY TRANSFER ACTIVE VERSUS INACTIVE NANOCRYSTAL/DYE CONJUGATE PAIRS[3]

4.1 Overview

Defect-mediated energy transfer is a radiative process that occurs between donor defect states in the forbidden bandgap of semiconductor nanocrystals (NCs) and dye molecules bound to their surfaces. The energy transfer efficiency depends on the number of dye molecules attached to each NC, the donor-acceptor distance, and the dipole orientation factor between the donor and acceptor, all of which vary across *all* individual NCs in a sample. While ensemble-level fluorescence spectroscopy measurements have provided *average* values for donor-acceptor distances, dye-to-NC ratios, and energy transfer rate constants, questions remain about the impact of donor/acceptor heterogeneity on observed energy transfer efficiencies. Notably, ensemble-level measurements cannot distinguish between bare NCs and energy transfer-active versus inactive NC/dye pairs in the same sample batch, limiting the ability to design systems with 100% energy transfer efficiency. To address this, we studied defect-mediated energy transfer between AlexaFluor 555 dye acceptors chemically bound to ZnO NC donors at the level of single molecules and single NCs. Interestingly, 20% of bound dye/NC pairs are energy transfer-inactive, likely contributing to residual defect photoluminescence (PL) observed in ensemble-level measurements and reducing overall energy transfer efficiency. Single particle-level ZnO defect PL and acceptor

[3]Reproduced with permissions from Lustig, D., Buz, E., Mulvey, J., Prasad, P., Bird, O., Dukovic, G., Kittilstved, K., Patterson, J., and Sambur, J., Single-Molecule Fluorescence Microscopy Reveals Energy Transfer Active versus Inactive Nanocrystal/Dye Conjugate Pairs. Chemical & Biomedical Imaging 2025, Copyright 2025, American Chemical Society.

fluorescence trajectories exhibited distinct micro-fluctuations, which are absent in bare ZnO NCs. We hypothesized that our observations can be explained with a competitive dye fluorescence quenching pathway, possibly due to charge transfer between the excited state dye and the ZnO NC. Numerical simulations of single-molecule PL traces for this scenario produced micro-fluctuations consistent with the experimental results. These findings highlight the impact of sample heterogeneity on energy transfer processes and provide insights for designing light-harvesting systems with optimized energy transfer efficiency.

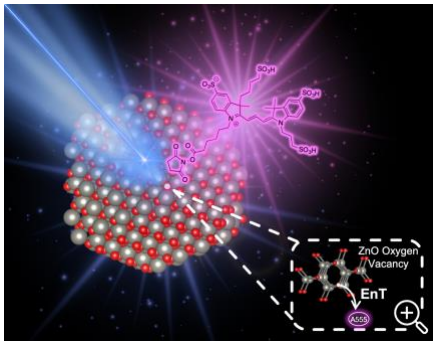

Figure 4.1. Chapter 4 overview: cartoon illustration of defect-mediated EnT between ZnO NC donors and A555 acceptors in a nanocrystal/dye conjugate pair.

4.2 Introduction

Semiconductor NCs can act as energy donors in energy transfer (EnT) processes with molecular acceptors, including organic dyes[1–12] and metal coordination complexes.[13–16] In these systems, the electronically excited NC "donor" transfers energy to a molecular "acceptor." In the defect-mediated EnT process, the donor states are electronic energy levels in the forbidden semiconductor band gap. This process occurs when the absorption spectrum of the dye acceptor overlaps with the NC's defect emission.[17] Defect-mediated EnT processes are actively being explored in a broad range of photonics and photocatalytic applications.[18–23] One exciting photonics application is to leverage the defect-mediated EnT process to control the resulting light emission energy, propagation direction, and polarization. Controlling size-dependent optical properties in

NC/dye hybrids enables tunable color emission, ultimately resulting in white light with targeted chromaticity and high color rendition.[24,25]

The fundamental photophysical defect-mediated EnT process has been widely studied in hybrid systems where molecular fluorophores are either randomly mixed with NCs in solution or chemically conjugated to their surfaces.[17,21,24–30] However, the defect-mediated process is inherently heterogeneous at the nanoscale, as defects vary from one NC to another, and the binding geometry between these defects and acceptor molecules differs across NCs. This variability within the sample influences the EnT rate for each NC/dye pair, as the rate depends on both the donor-acceptor distance and the orientation factor between the donor and acceptor.[31] This variability leads to diverse EnT pathways that conventional Förster resonance energy transfer (FRET) models cannot fully capture.[26] Ensemble-level measurements can accurately determine the *average* number of dye molecules adsorbed per NC in a bulk solution.[26,29] However, for systems with EnT efficiency <100%, which is typical of most systems as no FRET process is 100% efficient[32], ensemble-level measurements cannot distinguish active versus inactive NC/dye pairs in the sample. EnT from a single semiconductor NC to dye molecules has the potential to achieve efficiencies of >90%, with Hua et al. reporting an EnT efficiency of 94.5%.[9] Thus, identifying active versus inactive NC/dye conjugates within a sample batch could provide valuable insights for designing highly efficient EnT systems.

This study aims to measure the extent of heterogeneity in EnT behavior among different ZnO NC donors and AlexaFluor A555 (A555) dye acceptors within a heterogeneous sample batch and investigate the role of defect states in NCs and their impact on dye emission and quenching processes. We selected ZnO NCs for this study due to their broad defect PL spectrum and prior evidence from ensemble-level steady-state and time-resolved PL spectroscopy demonstrating their

participation in defect-mediated EnT with A555 dyes[17,26,27,29] and Eu^{3+} ions.[22] These findings emphasize the critical role of oxygen vacancy defects in the EnT process.[22] The open questions that we aim to address in this study are *How many bare NCs exist in a sample batch of chemically conjugated NC/dye pairs?* and *How many bound NC/dye pairs are EnT-inactive?* Here, we quantify defect-mediated EnT active versus inactive NC/dye pairs in a heterogeneous conjugate sample using single molecule, single NC-level fluorescence microscopy. We synthesized (3-Aminopropyl)trimethoxysilane (APTMS)-capped ZnO NCs and chemically linked A555 dyes to the NC surfaces (referred as A555/APTMS/ZnO conjugates). By systematically comparing single-molecule widefield PL trajectories of the conjugates to isolated APTMS-capped ZnO NCs, we observe distinct micro-fluctuations in the conjugate samples that do not appear in the isolated APTMS-capped ZnO NCs. We find that 5 out of 25 nanoconjugates with a bound dye are EnT-inactive (20%), perhaps due to the orientation mismatch between the donor and acceptor dipole moments. These results emphasize the importance of characterizing sub-populations to address sample heterogeneity, offering valuable insights for enhancing EnT processes and designing nanomaterial-based photonic systems with optimized light-harvesting efficiency.

4.3 Methods

4.3.1 Materials

The following chemicals were purchased and used as received: zinc acetate dihydrate (Ricca Chemical), dimethylsulfoxide (DMSO, 99.9%, Thermo Fisher), tetramethylammonium hydroxide pentahydrate (98%, Acros Organics), 3-aminopropyltriethoxysilane (APTMS, Gelest), and hydrogen peroxide (30% in water, Thermo Fisher). The fluorescent dye, AlexaFluor 555 NHS ester (Succinimidyl Ester, Thermo Fisher, catalog number A20009), was received as a powder, dissolved in high-quality anhydrous dimethylformamide (DMF, Sigma-Aldrich), and diluted to a

final concentration of 0.01 mg/mL before the chemical conjugation (Thermo Fisher, catalog number A20009).

4.3.2 Synthesis of APTMS Capped ZnO Nanocrystals

ZnO NCs were synthesized at room temperature following a modified procedure previously reported.[32,33] Briefly, zinc acetate dihydrate (1 mmol) was dissolved in 10 mL of DMSO. Separately, 3 mL of a 0.5 M ethanolic solution of tetramethylammonium hydroxide pentahydrate (1.5 mmol) was added dropwise to the Zn^{2+} solution under constant stirring at room temperature to initiate ZnO nucleation and growth. Particle growth was monitored by collecting aliquots and analyzing the electronic absorption spectra of the first excitonic transition according to Meulenkamp.[34] To accelerate particle growth, the reaction flask was transferred to a pre-heated sand bath at 60 °C. The reaction was terminated once the desired position of the first excitonic peak of ZnO NCs was achieved (355 nm). To remove excess precursors, 1% hydrogen peroxide (30% in water) was added, and the reaction mixture was sonicated for 10 minutes. The resulting nanoparticles were mixed with oleylamine in a ligand-exchange reaction step. The oleylamine-capped ZnO NCs (10 mg/mL) were suspended in 10 mL of ethanol and transferred to a clean flask. The flask was placed in a sand bath at 60 °C, and 30 µL of APTMS was added immediately to the suspension. The mixture was stirred vigorously for 2 hours before being cooled to room temperature. The silane-functionalized NCs were collected by centrifugation, washed twice with toluene, and resuspended in water. The aqueous suspension of APTMS-capped ZnO NCs was stored at 4 °C.

4.3.3 Dye Chemical Conjugation

APTMS-capped ZnO NCs were suspended in water at a concentration of 12.5 mg/mL, and the pH was adjusted to 6.00-6.50 using acetic acid to optimize dye conjugation efficiency. To

enhance colloidal stability, a small amount of DMSO (<10%) was added to the suspension. A555 dye was dissolved in high-quality DMF and diluted to a final concentration of 0.01 mg/mL. For the conjugation reaction, 10 μL and 50 μL of the A555 dye solution were mixed with 200 μL of the 12 mg/mL APTMS-coated ZnO NC suspension. The reaction was stirred vigorously at room temperature for 3 hours in the dark. The resulting conjugates were in a water/DMF mixture.

4.3.4 Nanocrystal Characterization

ATR-FTIR (attenuated total reflectance-Fourier transform infrared) spectroscopic studies were carried out using a Nicolet-iS50 FTIR spectrometer equipped with a diamond ATR attachment (ThermoFisher). X-ray photoelectron spectroscopy (XPS) data was collected on a Physical Electronics, Inc. 5800 Multi-Technique X-ray Photoelectron Spectrometer. The pass energies used were 187.8 eV and 23.50 eV for the survey and high-resolution spectra, respectively. The survey spectra are unshifted. The high-resolution spectra were shifted, moving the C-C binding environment of the C 1s peak to 284.8 eV. APTMS-capped ZnO NCs and A555/APTMS/ZnO conjugates were prepared for high-resolution transmission electron microscopy (TEM) analysis by drop casting the NCs from a solution of water/DMF onto a lacey carbon TEM grid (Electron Microscopy Sciences) and allowing for complete solvent evaporation at room temperature. TEM images were obtained on a JEOL-JEM-2100F TEM instrument using a Schottky-type field emission gun operating at 200 keV and collected using a Gatan OneView camera. The average and standard deviation values for the NC diameter were determined via TEM (Figure C1). Additional higher magnification TEM images of APTMS-capped ZnO NCs are shown in Figure C2. Elemental mapping was performed using scanning tunneling electron microscopy energy dispersive X-ray spectroscopy (STEM-EDS) on a JEOL JEM-2800 electron microscope operating at 200kV as shown in Figure C3. The absorbance and emission properties

of the APTMS-capped ZnO NCs and the A555/APTMS/ZnO conjugates were characterized by UV-Vis absorption spectroscopy and steady-state PL spectroscopy (Varian Cary 50 Bio and Varian Cary Eclipse, respectively).

4.3.5 Single Molecule Fluorescence Microscopy

Comprehensive details on sample preparation, the single molecule total internal reflection fluorescence (TIRF) experimental setup, and image analysis procedures are available in our previous work.[27] Briefly, APTMS-capped ZnO NC controls or A555/APTMS/ZnO conjugates were diluted with water, sonicated for one hour, and subsequently drop cast onto a quartz slide. For imaging, a drop of Immersol oil (W 2010 Zeiss) was placed between the quartz slide and a #1 glass coverslip (19904). The Immersol oil features an identical refractive index to water (1.33) and does not evaporate during the timescale of the experiment. A 60× water immersion objective (NA = 1.2, Olympus, UPLANSAPO60×/W) was used for imaging. The two-color excitation and two-channel imaging methodology is described in our previous work.[27] Briefly, we employ two lasers to excite the NC donors and dye molecule acceptors: a 12 mW 355 nm laser (Coherent Genesis CX) focused to an 68 μm × 49 μm area (yielding 3.6 kW/cm^2) excites the ZnO NCs in the conjugate, while a 0.6 mW 532 nm laser (Coherent Obis) focused to an 69 μm × 49 μm area (yielding 0.18 kW/cm^2) selectively excites the A555 molecules in the conjugate. Fluorescence images were continuously acquired at a 50 ms exposure time (20 frames per second) while the excitation lasers were alternated in an on/off fashion, with 1 s pulses. The PL intensity trajectories of conjugates from the movies, were extracted using the detailed image analysis algorithm described previously.[27] No unexpected or unusually high safety hazards were encountered.

4.3.6 Kinetic Monte Carlo (kMC) simulations

A numerical simulation was developed to qualitatively predict the A555/APTMS/ZnO

conjugate PL intensity trajectories. The kMC simulation examines the evolution of a NC-dye conjugate through various decay pathways, based on a previously hypothesized mechanism.[29,31] The time evolution of the system is modeled by taking the time before each step occurs, calculated according to Eq. 4.1:

$$t = -\left(\frac{1}{k}\right) \times \ln\,(1 - r) \qquad \text{Eq. 4.1}$$

where t is the time before the relevant process occurs, k is the rate constant of the relevant process, and r is a random number drawn from a uniform distribution between 0 and 1. The first step of each excitation is to calculate t prior to excitation. The excitation frequency (k_{Exc}) of a single NC was estimated as $k_{Exc} = 1.36\times10^{8}$ s^{-1}, based on the 355 nm laser power of 3.6 kW/cm^2 used for single-molecule experiments and a NC cross section of 2.12×10^{-13} cm^2. In the simulation, after excitation, the excited electron instantaneously cools to either a dark trap state or light trap state, with the fraction directed to each state determined by the PL quantum yield ($\approx$ 4.4%) as previously measured for similar samples.[29] If the electron is trapped in a dark state, its decay time is calculated according to Eq. 4.1, where $k_{Trap} = 1.1\times10^{7}$ s^{-1}.[29] If the electron decays to a light trap, it can subsequently decay via two possible pathways: (1) radiative electron-hole recombination with a rate constant $k_0 = 6.2\times10^{5}$ s^{-1},[29] or (2) EnT with $k_{FRET} = 2.0\times10^{7}$ s^{-1}.[29] The times for each pathway are calculated using Eq. 4.1 with separate random numbers drawn for each, and the faster process is selected via the "first reaction method", commonly used for pathway selection in kMC simulations.[35,36] Similarly, if EnT occurs and excites the dye, the dye can decay either radiatively as described by $k_{Fl} = 3.3\times10^{8}$ s^{-1},[37] or non-radiatively due to quenching by the NC, described by k_{Quench}, which is varied as the independent variable in the simulation.

Each time a NC emits a photon, a count is added to the defect channel, along with the time at which the event occurred. Similarly, when photon emission from the dye occurs, a count is

added to the dye channel. The time was calculated by summing the times for each process leading up to emission. For each time point, an emission event in a given channel was tracked by assigning it a value of "1", while the absence of emission is assigned a value of "0". A total of 5×10^7 excitations are simulated for each condition. Given that many (> 10,000) excitations occur within each frame of the experimental framerate of 0.005 s the simulation results were averaged over each interval of 0.005 s. This averaging mimics the experimental integration of all events observed within each frame during the experiment. The channel ratio, CR, was then calculated as the quotient of the dye channel counts over the defect channel counts, after averaging.

4.4 Results

4.4.1 A555/APTMS/ZnO Conjugate and Ensemble-level EnT Characterization

We designed and synthesized A555/APTMS/ZnO conjugates to investigate defect-mediated EnT using single-molecule fluorescence microscopy. Scheme 4.1 illustrates the key synthetic steps: first, oleylamine-capped ZnO NCs underwent a surface ligand exchange reaction to produce APTMS-capped ZnO NCs. This modification introduced primary amine groups on the nanoparticle surface, providing functionality for subsequent conjugation. The APTMS-capped ZnO NCs served as essential controls in our system. Next, the NCs were reacted with the NHS-ester derivative of the A555 dye in acetic acid at a pH of 6-6.5, forming stable amide bonds that effectively conjugated the dye to the nanoparticle surface. Previous work by Hadar et al. also achieved successful chemical conjugation via chemical amide bond formation between the amine group of glutathione and the carboxylic group of the dye molecule, accompanied by the release of the dye NHS ester group.[38] This two-step process allowed us to create amine-functionalized ZnO NCs and subsequently integrate them with A555 dye molecules, enabling the study of EnT processes at the single-molecule level.

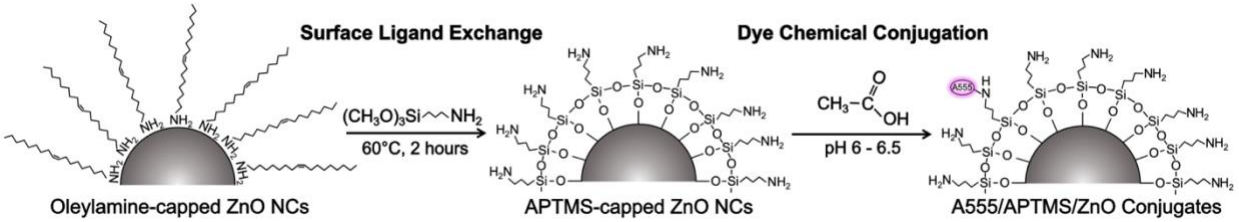

Scheme 4.1. Cartoon schematic of A555/APTMS/ZnO conjugate synthesis. The first step is a surface ligand exchange process of oleylamine-coated ZnO NCs with APTMS. In the dye conjugation step, the covalent conjugation occurs between the NHS ester group on the dye and the primary amines on the APTMS ligand. The dye chemical conjugation occurs at a pH of 6-6.5 in acetic acid. The final product is APTMS-capped ZnO NCs with A555 dye molecules covalently conjugated to the NC surface.

We verified the presence of APTMS ligands on the NC surface and the chemical conjugation of dye molecules to the APTMS ligand using multiple analytical techniques, including ATR-FTIR spectroscopy, XPS, electron microscopy, UV-Vis spectroscopy, and steady-state PL spectroscopy. Figure 4.2a-b shows the ATR-FTIR spectra of APTMS-capped ZnO NCs (blue traces), A555/APTMS/ZnO conjugates (pink traces), and A555 dye alone in DMF solvent (green traces). Both the APTMS-capped ZnO NCs and the A555/APTMS/ZnO conjugates contain a wide absorption peak in the range of 3000-3500 cm^{-1}, attributed to the stretching modes of surface –OH groups.[39,40] The peak at 1006 cm^{-1} corresponds to Si–O–Zn bonds, indicating the formation of covalent bonds between the ZnO surface and APTMS due to the successful capping of ZnO NCs by silane.[40,25] The free A555 dye spectra (green trace) depicts CH peaks at 2900 cm^{-1}, 2987 cm^{-1}, 1384 cm^{-1}, 657 cm^{-1}, and 870 cm^{-1}, indicative of pure DMF from the dye solution (green trace).[41,42] The CH peak at 1384 cm^{-1} also appears in the A555/APTMS/ZnO conjugates (pink trace), and is absent in the APTMS-capped ZnO NCs (blue trace), indicative of DMS present in the conjugate samples from the dye chemical conjugation procedure. Additionally, the free A555 dye and the A555/APTMS/ZnO conjugates show two bands at 1414 cm^{-1} and 1489 cm^{-1} that are attributed to the carbonyl groups of the NHS ester.[43] The stretching at 1650 cm^{-1} belongs to the carbonyl and is slightly shifted to higher energies upon chemical conjugation.[44] The appearance of

a weak band ~3300 cm^{-1} is attributed to the stretching of N−H primary amine.[44] The covalent bond formation of the chemical conjugation of the NHS ester and the APTMS ligand is indicated by the CN and CO peaks present in both the conjugate and the free dye. Figure 4.2c-d shows XPS measurements of APTMS-capped ZnO NCs (blue trace) and A555/APTMS/ZnO conjugates (pink trace) to reveal Si and N due to the presence of the APTMS ligand. Additionally, high resolution XPS of the A555/APTMS/ZnO conjugates revealed a small S presence due to the A555 NHS ester dye that did not appear in the APTMS-capped ZnO NCs as shown in Figure 4.2d.

Figure 4.2e shows a representative TEM image of the APTMS-capped ZnO NCs. The synthesis procedure produces hexagonal plate-like particles, consistent with the hexagonal wurtzite structure of ZnO NCs.[45,46] The average NC diameter is 5.2 nm ± 1.2 nm (N = 50, Figure C1). We also observe an amorphous film surrounding the NCs (highlighted by the blue arrows in Figure 4.2e) that we attribute to the APTMS ligand because this film does not appear in unconjugated samples[26,27] and STEM-EDS imaging detected Zn, O, and Si in the samples (Figure C3). The presence of the thick, amorphous film in Figure 4.2e indicates that the APTMS coating likely exceeds a monolayer, suggesting multilayer formation or polymerization during deposition.

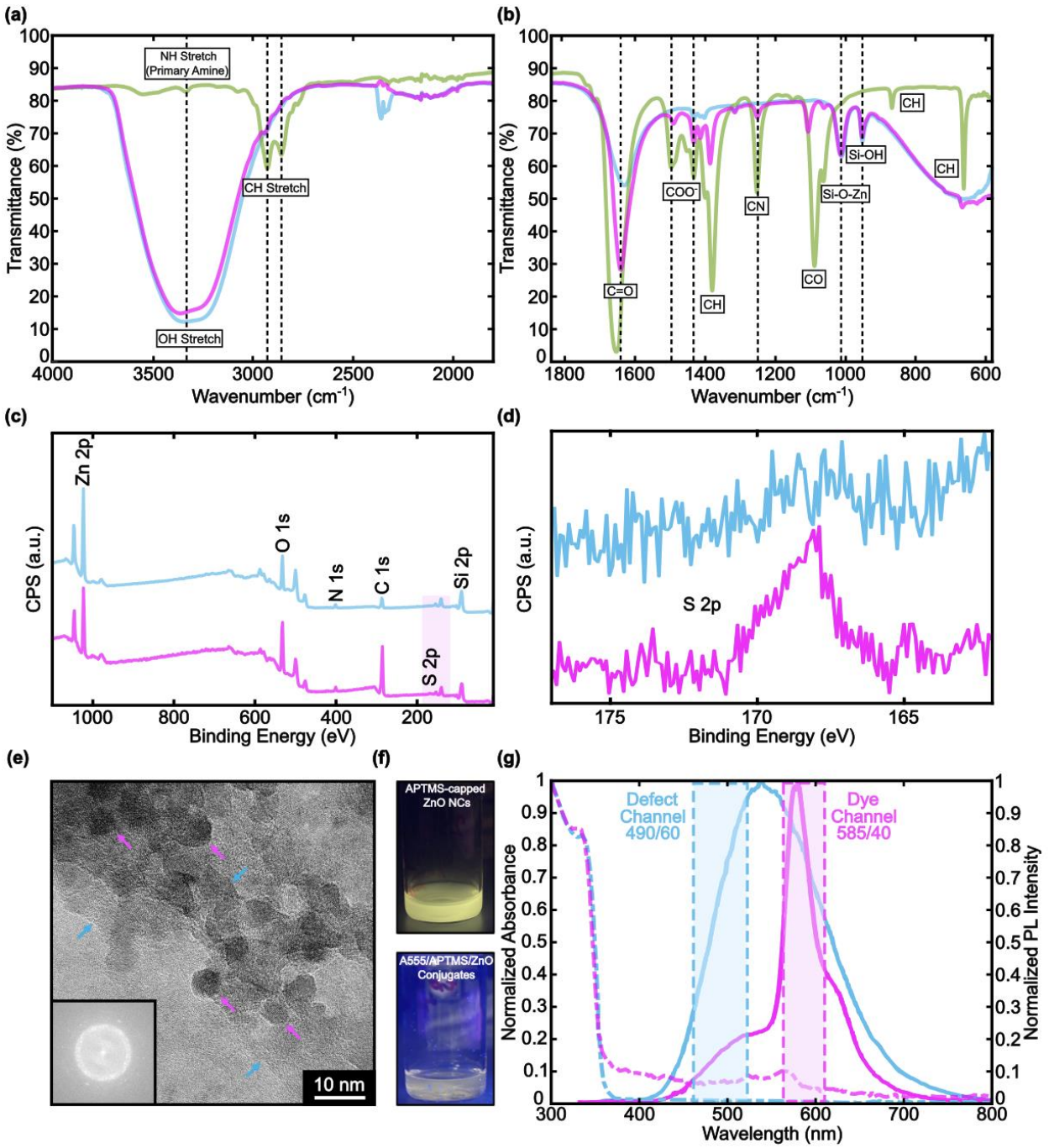

Figure 4.2. (a)-(b) ATR-FTIR spectra of APTMS-capped ZnO NCs (blue traces), A555/APTMS/ZnO conjugates (pink traces), and A555 dye in DMF (green traces). The dashed lines indicate notable peak assignments in the FTIR spectra. (c) Survey XPS spectra of APTMS-capped ZnO NCs (blue trace) and A555/APTMS/ZnO conjugates (pink trace). The pink rectangle highlights the S 2p region as shown in (d). (d) High-resolution XPS spectra of the S 2p peak for the APTMS-capped ZnO NCs (blue trace) and the A555/APTMS/ZnO conjugates (pink trace) respectively. (e) Bright-field TEM image of APTMS-capped ZnO NCs on a lacey carbon grid. Pink arrows indicate distinct hexagonal NCs and blue arrows correspond to the film. Image inset shows a cropped view of FFT confirming polycrystalline ZnO NCs (Figure C2). (f) Photographs of colloidal APTMS-capped ZnO NCs (top) and A555/APTMS/ZnO conjugates (bottom) under UV illumination. (g) Normalized absorbance (dashed lines) and emission spectra (solid lines) of APTMS-capped ZnO NCs (blue lines) and A555/APTMS/ZnO conjugates (pink lines). The blue shaded

region represents the bandpass filter (490/60 nm) for the "defect channel" in single molecule imaging experiments. The pink shaded region refers to the 585/40 nm bandpass filter for the "dye channel". Emission spectra were acquired using 355 nm excitation.

Next, we validated defect-mediated EnT occurring upon exciting the ZnO NC donors with UV light. Figure 4.2f shows photographs of colloidal APTMS-capped ZnO NCs (top) and A555/APTMS/ZnO conjugates (bottom) under UV illumination. The photographs qualitatively indicate significant optical property changes upon covalently linking the A555 dye to the NC surface. Spectroscopic measurements show that the ZnO defect emission is quenched in the presence of the A555 acceptor. Figure 4.2g compares the absorption and emission properties of APTMS-capped ZnO NCs (blue dashed and blue solid traces respectively) and of A555/APTMS/ZnO conjugates (pink dashed and pink solid traces respectively). The A555/APTMS/ZnO conjugate absorbance (Figure 4.2g, dashed pink trace) exhibits an optical change compared to the APTMS-capped ZnO NCs absorption (Figure 4.2g, blue dashed trace). Both samples exhibit an absorption onset at 355 nm. The conjugate absorption displays the spectral signature of the A555 dye absorbance at 555 nm that can be attributed to surface attached A555 molecules, indicating its presence in the conjugate samples. The A555 dye peak does not appear in the APTMS-capped ZnO NCs alone. The APTMS-capped ZnO NCs exhibit strong defect PL at 548 nm upon exciting the bandgap transition with 355 nm light. In contrast, the defect PL peak of the A555/APTMS/ZnO conjugate sample is quenched, with a strong dye PL peak emerging at 585 nm. This ZnO NC donor PL quenching and A555 dye acceptor PL enhancement is the spectroscopic signature of defect-mediated EnT.[17,26,27,29] In previous work with bare 4.7 nm ZnO NC donors and freely diffusing A555 dye molecule acceptors in solution, we observed complete ZnO defect emission quenching at an average dye:NC ratio of 1.5.[26] In this chemically conjugated sample, with an average dye:NC ratio of 1 determined through single particle-level measurements, we did not observe complete ZnO defect emission quenching in ensemble-level measurements.

The residual defect emission in Figure 4.2g can be attributed to the presence of bare ZnO NCs in the sample or inactive dye/ZnO NC pairs.

The ensemble-level results in Figure 4.2g help guide our selection of excitation lasers and detection channels for imaging the EnT process at the level of single NCs and single molecules. The blue shaded region in Figure 4.2g represents the bandpass filter (490/60 nm) for the "defect channel" in single molecule imaging experiments. The pink shaded region refers to the bandpass filter (585/40 nm) for the "dye channel". We quantify the extent to which defect-mediated EnT occurs via the channel ratio, CR, which refers to the integrated intensity of the "dye channel" divided by the integrated intensity of the "defect channel". The ensemble-level CR value for APTMS-capped ZnO NCs alone is 1.25. The ensemble-level CR value for A555/APTMS/ZnO conjugates is 5.23. The larger CR value for the NC/dye conjugate sample shows that the acceptor channel increases, and the defect channel decreases when defect-mediated EnT occurs. Hence, the ensemble-level CR value provides a baseline quantitative value to compare when evaluating the defect-mediated EnT process at the single NC-level.

4.4.2 Single NC, single molecule-level imaging of defect-mediated EnT

Ensemble-level EnT measurements do not reveal how many ZnO-dye pairs participate in the EnT process. Answering this question is important because it is unclear whether the residual defect PL emission in Figure 4.2g is due to bare APTMS-capped ZnO NCs in the conjugate sample or A555/APTMS/ZnO conjugates with low EnT efficiency. To answer this critical question, we performed single NC-level EnT measurements using widefield fluorescence microscopy. To do so, we employed a two-color excitation and two-channel imaging sequence as shown in Scheme 4.2. In a typical experiment, we drop cast A555/APTMS/ZnO conjugates on to a clean quartz slide and mounted the sample on the stage of an inverted optical microscope equipped with a prism-

type TIRF setup. Two laser sources excite the sample in an alternating fashion: a 1-second 532 nm laser pulse selectively excites the A555 dye molecules and then a 1-second 355 nm laser excites the ZnO bandgap. We repeat this sequence for 100 total cycles. The first 532 nm pulse allows us to localize the centroid position of dye molecules anywhere on the sample using the super-optical resolution imaging method.[47,48] The second 355 nm pulse allows us to localize the centroid position of ZnO NCs via their defect PL signals and induce defect-mediated EnT between ZnO NC donors and surface-attached dye acceptors. A high-numerical aperture 60×/NA 1.2 objective collects photons emitted from the sample. Image splitting optics project the collected photons onto two halves, or "channels" of an EM-CCD camera. The two channels represent dual wavelength images for simultaneous monitoring of the "defect" and "dye" channels, as defined by the bandpass filters shown in Figure 4.2g.

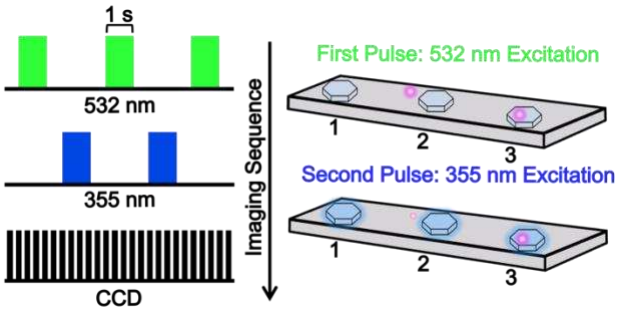

Scheme 4.2. Cartoon illustration of the two-color excitation imaging sequence. The first 532 nm pulse selectively excites dye molecules only whereas the second 355 nm pulse excites ZnO NCs. The numbers 1, 2, and 3, represent three possible ZnO NC-dye binding configurations: case 1 is an isolated ZnO NC; case 2 is a non-specifically bound ZnO NC/dye pair; and case 3 is a specifically bound NC/dye pair.

Figure 4.3 shows representative widefield two-channel images under 532 nm and 355 nm illumination for three different samples: APTMS-capped ZnO NCs alone, A555 dye alone, and A555/APTMS/ZnO conjugates. The left and right halves of each image in Figure 4.3 represent the dye and defect channels, respectively. Figure 4.3a shows that ZnO NCs excited with 355 nm light produce diffraction-limited spots in both channels, in agreement with the spectrum in Figure 4.2e. We use a robust intensity-based threshold analysis to isolate and study individual ZnO NCs,

effectively filtering out large clusters or ZnO NC aggregates.[27] Table C1 presents the total count of ZnO NC objects detected in widefield images, along with the breakdown of single NCs and clusters identified from those objects. Illuminating ZnO NCs alone with 532 nm light produces only background signals in the defect or dye channels (Figure 4.3b). In contrast, excitation of dye molecules alone with 355 nm light does not produce localized fluorescence intensity spots in either channel (Figure 4.3c). However, excitation with 532 nm light generates bright spots exclusively in the dye channel (Figure 4.3d-left). The NC and dye control experiments in Figure 4.3a-d enable us to set intensity-based thresholds to identify and study single NCs and dye molecules. Figure 4.3e shows A555/APTMS/ZnO conjugate samples excited with 355 nm excitation produce bright spots in both channels. Unlike the ZnO NCs alone, exciting the A555/APTMS/ZnO conjugate samples with 532 nm light produces many bright spots in the dye channel (compare Figure 4.3b-left versus Figure 4.3f-left). If every NC had a surface-attached dye molecule, we would expect a clear correlation between the bright spots in Figure 4.3e and Figure 4.3f. However, a qualitative comparison of these images reveals that not all bright spots overlap. This lack of correlation suggests that the conjugate sample includes a mixture of isolated or unlabeled ZnO NCs, free dye molecules, and NC/dye conjugates. The next section describes how we distinguish these cases using intensity- and super-optical resolution distance-based analyses.

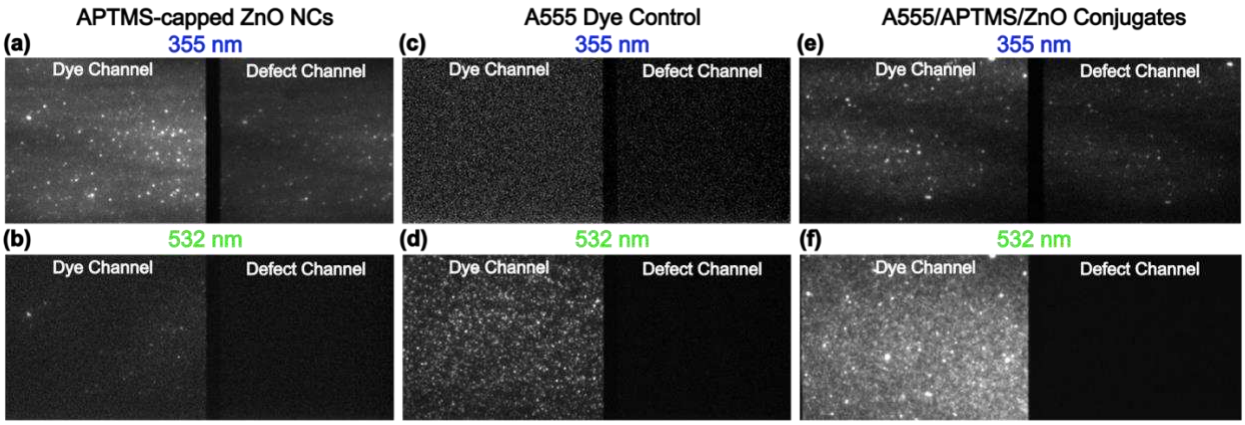

Figure 4.3. Widefield dual channel images of (a-b) the APTMS-capped ZnO NCs sample excited with (a) 355 nm excitation and (b) 532 nm excitation. The left and right halves of each image represent the dye and defect channels, respectively. (c-d) and (e-f) are the same as (a-b) but for A555 dye alone and A555/APTMS/ZnO conjugates, respectively. Each image represents the average image calculated from the entire movie. The total image area is 130 μm × 49 μm.

Figure 4.4 shows representative fluorescence intensity trajectories and super-resolution imaging results obtained using the two-color excitation, two-channel imaging sequence. We previously developed an intensity-based and donor-acceptor distance (*R*)-based image processing algorithm[27] to differentiate between three possible ZnO NC-dye binding configurations, or cases, as shown in Figure 4.4a,g,m. Case 1 is a bare ZnO NC (Figure 4.4a-f). When the 532 nm laser excites a bare ZnO NC (Figure 4.4a), we do not observe significant defect PL emission in the defect channel (Figure 4.4b-blue circles) because 532 nm illumination does not excite the ZnO bandgap. We also observe weak dye fluorescence intensity in the dye channel (Figure 4.4b-pink circles) because no dye molecules are bound to the NC surface. Note, the data in Figure 4.4b is slightly higher in intensity due to the trajectory belonging to an internal control (extracted from the A555/APTMS/ZnO conjugate movies). Thus, the dye channel has higher overall intensity (see Figure 4.3f), but there is no dye object identified in the region of interest (ROI); see Figure C3a for the corresponding widefield image for the trajectory in Figure 4.4b. Figure C3 shows all the representative widefield images for the trajectories shown in Figure 4.4. On the other hand, we observe strong defect PL under 355 nm excitation (schematically shown in Figure 4.4d). Figure

4.4e shows fluorescence intensity trajectories for the case shown in Figure 4.4d. The trajectory under 355 nm excitation shows a slow intensity increase for the first 35 s, which has been attributed to chemisorbed oxygen that initially quenches the defect PL emission,[49] presumably due to charge transfer from photo-excited conduction band electrons to adsorbed O_2 molecules.[50] The CR trajectory, where $CR(t) = I_{dye}(t)/I_{defect}(t)$ (Figure 4.4e, white trajectory), exhibits an average value of 0.98 (Figure 4.4f), which is in agreement with the ensemble CR value of 1.25 measured in Figure 4.4e. Figure 4.4c shows the super-resolution localization results for case 1. Each blue cross represents the centroid position obtained from a 2D Gaussian fit to a diffraction-limited bright spot in the defect channel under 355 nm excitation. The width and height of the cross represents the localization precision of each fit; the average error for each fit is 30 nm. The white × in Figure 4.4c represents the average (x,y) coordinates from all the individual centroid fits (i.e., the ZnO NC position). The white dashed circle represents two standard deviations from all the individual centroid fits (i.e., the dashed circle diameter in Figure 4.4c).

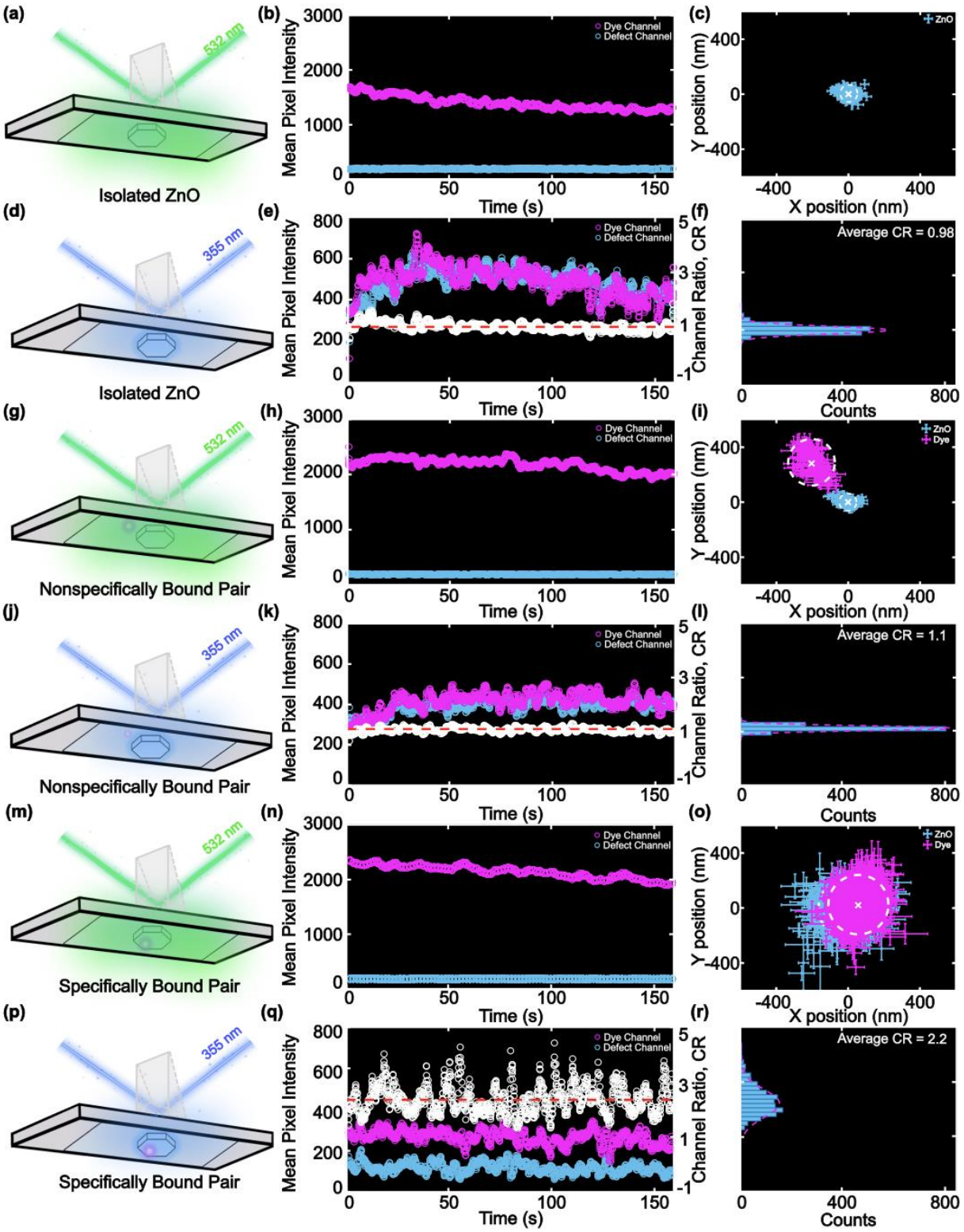

Figure 4.4. Representative fluorescence intensity trajectory analysis and super-resolution imaging results for three possible ZnO NC/dye binding configurations: case 1 is isolated single ZnO NC; case 2 is non-specifically bound ZnO NC/dye pair; and case 3 is a specifically bound NC/dye pair. See main text for details. (a,d) Cartoon illustration of an isolated ZnO NC excited with (a) 532 nm and (d) 355 nm laser excitation in the prism type TIRF configuration. (b)

Intensity trajectories of a 4 × 4 pixel ROI in the dye channel (pink circles) and defect channel (blue circles) under 532 nm excitation. (e) Same as panel b, but for 355 nm excitation. The white circles represent CR values. The red dashed line is the average CR value. Panel f shows the CR value distribution. The Gaussian fit yields an average CR value of 0.98. (c) The blue crosses represent NC centroid positions obtained from 2D Gaussian fitting of all diffraction-limited bright spots obtained in the defect channel under 355 nm illumination. The white × represents the average (x,y) coordinates from all individual fits. The dashed white circles represent the error of the individual fits (two standard deviations). (g-l) and (m-r) Same as panels (a-f), but for non-specifically bound NC/dye pairs and specifically bound NC/dye pairs, respectively. Note, the pink crosses in panels i and o represent dye molecule centroid positions obtained from 2D Gaussian fitting of all diffraction-limited bright spots obtained in the dye channel under 532 nm illumination.

Case 2 (Figure 4.4g-l) represents a non-specifically bound conjugate pair, defined as a situation where a dye molecule and a single ZnO NC appear in the same diffraction-limited area of the sample, but the two are separated by a distance exceeding our super-optical spatial resolution limit (≈30 nm, as shown in Figure C4). Case 2 can occur when free dye molecules present in the conjugate solution adsorb near ZnO NCs during the drop cast step (see in Figure 4.3e-f). Specifically, we define non-specifically bound ZnO NC/dye pairs if the white dashed circles in Figure 4.4i do not overlap, meaning the average NC and dye centroid positions plus two-standard deviations do not overlap. Figure 4.4h shows slightly higher intensity in the dye channel under 532 nm illumination (pink trajectory) compared to the isolated NC case (Figure 4.4b), indicative of dye fluorescence under 532 nm excitation (Figure C4c). Interestingly, we observed no significant variations in the defect PL intensity trajectory under 355 nm illumination (Figure 4.4k), nor any differences in CR values as compared to case 1. The average CR value is 1.1 (Figure 4.4l), which is nearly identical to the bare ZnO NC in Figure 4.4f, suggesting that the emission from this NC is not affected by the presence of the dye molecule in the same diffraction-limited spot of the sample. We note that the defect and dye channel trajectories under 355 nm illumination show a slow intensity increase over the first 35 s of the movie (Figure 4.4k), similar to that of the isolated NC in Figure 4.4e. The super-resolution imaging results in Figure 4.4i reveal why this ZnO NC/dye pair exhibits similar fluorescence intensity characteristics as the bare ZnO NC case. Each pink cross in Figure 4.4i represents a 2D Gaussian fit to a bright spot in the dye channel under 532 nm

illumination (i.e., the dye position). The average ZnO NC and dye positions do not overlap within error (i.e., they are a non-specifically bound pair), which explains why these entities produce fluorescence intensity trajectories reminiscent of isolated dye molecules and NCs.

Finally, case 3 represents a specifically bound pair (Figure 4.4m-r), where a dye molecule is detected under 532 nm excitation (Figure 4.4n) and a ZnO NC is detected under 355 nm excitation (Figure 4.4q). In this case, the dye molecule and NC are separated by a distance smaller than our spatial resolution, as indicated by the overlapping white dashed circles in Figure 4.4o. The distinguishing feature of specifically bound ZnO NC/dye pairs is intensity fluctuations in both the dye and defect channels under 355 nm laser excitation (Figure 4.4q). The intensity fluctuations do not appear in control data (Figure 4.4a-f) or the non-specifically bound pair (Figure 4.4g-l). In molecular donor-acceptor FRET systems like Cy3/Cy5,[51] donor intensity quenching and acceptor intensity enhancement are typically more pronounced, stepwise, and persist for several seconds. In contrast, the fluctuation periods in this NC/dye donor-acceptor system are brief, occurring within a single frame. The Discussion Section explores potential reasons why clear anticorrelated FRET behavior, characterized by extended "on" and "off" periods, was not observed under these experimental conditions.

Interestingly, the CR value fluctuations approach 5, in agreement with the ensemble-level result in Figure 4.2g. The average CR value increases to 2.2 (Figure 4.4r), which is also in agreement with the expectation that, on average, the dye channel intensity increases, and the defect channel intensity decreases when defect-mediated EnT occurs. In summary, the two-color excitation and two-channel imaging approach allows us to isolate and study bare ZnO NCs from ZnO NC/dye pairs that are both present in the conjugate sample batch and whose fluorescence

intensity contributions cannot be deconvoluted in conventional ensemble-level spectroscopy measurements.

4.4.3 Single-Molecule Statistical Analyses

To address the first critical question—*what fraction of the conjugate sample consists of bare ZnO NCs?*—we quantified fractional population of cases 1-3 in Scheme 4.2 and Figure 4.4 by analyzing fluorescence intensity values and CR histograms for 30 individual ZnO NCs. The cumulative results, shown in Table 4.1, were then compared to our previous study on unconjugated ZnO NCs, where ZnO NCs and A555 molecules were mixed in solution and drop-cast onto a quartz slide.[27] In the conjugate sample, we observed only 1 single, bare ZnO NC out of 30 possible single ZnO NCs. In our previous study, we observed that 91% of all possible single ZnO NCs on the quartz slide were unbound to dye molecules and not located in the same diffraction-limited area as a dye molecule. Hence, chemical conjugation drastically reduces the total number of free ZnO NCs in the sample as compared to relying on physisorption alone. While the chemical conjugation step did not result in labeling all ZnO NCs, we excitingly observed a major difference in case 2 versus case 3 populations from our previous study.

Table 4.1. Statistical comparison of the fractional populations of case 1: isolated ZnO NCs, case 2: non-specifically bound NCs, and case 3: specifically bound NCs present in chemically conjugated samples versus randomly mixed samples. Specifically bound pairs were analyzed for EnT activity as discussed in the main text. Adapted in part with permission from reference 27. Copyright 2023, American Chemical Society.

Case	Fractional Population in Conjugated Sample	Fractional Population in Randomly Mixed Sample
1: Isolated ZnO NC	1/30 (3%)	789/867 (91%)
2: Non-Specifically Bound	4/30 (13%)	73/867 (8%)
3: Specifically Bound	25/30 (83%)	5/867 (1%)
EnT-Active Pairs	20/25 (80%)	
EnT-Inactive Pairs	5/25 (20%)	

To answer the second critical question—*what fraction of specifically bound ZnO-dye pairs participate in the EnT process?*— we focused on analyzing the intensity fluctuations in Figure

4.4q because those fluctuations appear to be the experimental signature of defect-mediated EnT. Our hypothesis is that EnT-active NC/dye pairs exhibit more CR value fluctuations than EnT-inactive pairs. To test this hypothesis, we calculated a fluctuation magnitude, FM, defined as the difference between the CR value of every frame and the average CR value obtained from Gaussian fitting (red dashed line in Figure 4.4e,k,q). Figure 4.5a shows the quantitative comparison of FM values for 20 isolated APTMS-capped ZnO NCs (blue distribution) versus 25 A555/APTMS/ZnO specifically-bound conjugate pairs (pink distribution). Both populations exhibit a peak at 0 FM, indicating that positive and negative intensity fluctuations occur from a common baseline. Importantly, the A555/APTMS/ZnO conjugate pairs exhibit a much broader distribution than the control isolated APTMS-capped ZnO NC population, which is most notably observed when plotting the distributions on a log scale (Figure 4.5a, inset). In summary, Figure 4.5a shows a quantitative difference between isolated NCs and specifically bound NC/dye pairs that is consistent with the ensemble-level results in Figure 4.2g (i.e., dye channel intensity enhancement and defect channel quenching).

Next, to quantify the number of fluctuation events at the single NC level, we calculated a global threshold from the distributions shown in Figure 4.5a and subsequently determined the number of positive or negative events for each NC. The global threshold for positive events was defined as three standard deviations above the mean ($\mu + 3\sigma$, $FM^{+}_{thresh} = 0.40$), while the negative threshold was set as three standard deviations below the mean ($\mu - 3\sigma$, $FM^{-}_{thresh} = -0.42$), based on a Gaussian fit to the isolated ZnO control population. Figure C5 shows a representative example of this classification process for a single NC/dye pair. The shaded red and blue regions in Figure 4.5a indicate all possible positive and negative fluctuations that pass this threshold value. Figure 4.5b shows the distribution of positive events per NC after the thresholding step for bare APTMS-

capped ZnO NCs (blue bars) and A555/APTMS/ZnO conjugate pairs (pink bars). On average, the NC/dye pairs exhibit about 94 positive events over the 7 min experiment (see Gaussian fit-red dashed line in Figure 4.5b). The broad distribution of events per NC could be due to a heterogeneous distribution of (i) donor defect states per NC (and their associated distribution of photophysical rate constants to/from NC defect states to dye acceptors), (ii) donor-acceptor distances, and/or (iii) orientation factors between the donor and acceptor dipole moments, as examined in the Discussion Section. Since a major fraction of control ZnO NCs exhibit <25 events, we define the fraction of specifically bound ZnO-dye pairs that participate in the EnT process as all those NC/dye pairs that exhibit >25 events/7 min, which corresponds to 20 EnT-active NC/dye pairs out of 25 possible specifically-bound candidates (80%). Regarding the correlation between fluctuations and average EnT activity, Figure 4.5b-inset shows a strong positive correlation between the total number of positive and negative events per NC for both the control and pair data. The calculated Pearson correlation coefficient, r, for the control data is $r = 0.871 \pm 0.0365$ and for the pairs $r = 0.846 \pm 0.0385$ with the error calculated according to Han et al.[52] Figure 4.5c shows a positive correlation between the total number of combined events and the average CR value. In other words, dye/NC pairs that exhibit greater fluctuation activity also exhibit greater dye fluorescence intensity enhancement and defect PL quenching over the entire experiment (parameterized by the CR value), in agreement with the ensemble-level result in Figure 4.2g. The physical origin of the positive and negative events will also be discussed below.

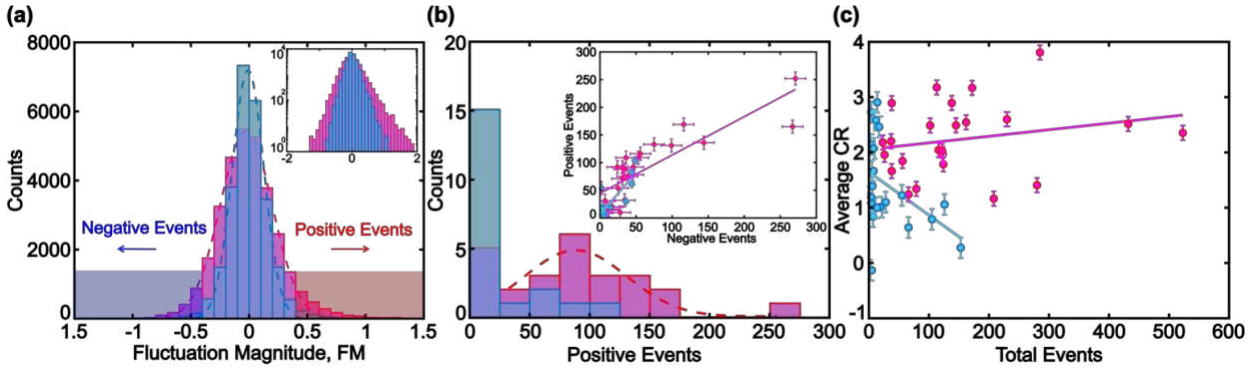

Figure 4.5. (a) Fluctuation magnitude distributions for 20 isolated ZnO NCs (blue histogram) and 25 A555/APTMS/ZnO conjugate pairs (pink histogram). Blue and red dashed lines are Gaussian fits to the distributions. The inset shows a log scale to emphasize the difference between the two distributions. The red shaded region shows the positive events determined from the positive threshold (0.40) and the blue shaded region shows the negative events determined from the negative threshold (−0.42). (b) Distribution of total number of positive events per NC for 20 isolated ZnO NCs (blue histogram) and 25 NC/dye conjugate pairs (pink histogram). The inset shows the total number of positive versus total number of negative events per NC. The error bars represent the standard error of the mean. (c) Scatter plot of the single particle-level average CR value versus the total combined number of positive and negative events per NC. The blue and pink circles represent data from single bare ZnO NCs and dye/NC pairs, respectively. The CR error bar represents the standard error of the mean.

Table 4.1 summarizes the sub-populations identified in the chemically conjugated A555/APTMS/ZnO sample batch, based on single-molecule imaging experiments. Among the single ZnO NCs analyzed, 83% (25 out of 30) formed specifically bound NC/dye pairs. In contrast, unconjugated samples contained only 0.6% specifically bound pairs.[27] Approximately 20% of the chemically conjugated NC/dye pairs were EnT-inactive, likely due to factors such as large donor-acceptor distances or unfavorable orientation factors between their dipole moments. Additionally, 16% of the sample consisted of bare, unconjugated ZnO NCs, determined as the combined population of isolated NCs and non-specifically bound NC/dye pairs listed in Table 4.1. These single-particle-level measurements required analyzing only a small volume of the colloidal sample batch. However, this approach revealed sub-populations of bare ZnO NCs and EnT-inactive NC/dye pairs, which likely contribute to the residual defect PL signal observed in Figure 4.2g. It is unclear how nanoparticle aggregates contribute to the residual defect PL signal in Figure 4.2g because our single particle-level study did not analyze ZnO NC aggregates.

4.5 Discussion

Our single molecule, single NC-level imaging data supports that (i) a small fraction (≈16%) of the conjugate sample consists of bare ZnO NCs; (ii) the EnT activity, parameterized by the number of fluctuations and the CR value, varies widely from NC to NC in the conjugate sample; and (iii) defect PL and dye fluorescence intensity fluctuations are the experimental signature of defect-mediated EnT under these imaging conditions. Here we discuss several possible explanations for major results (ii) and (iii).

One possible explanation for the broad distribution of single particle-level EnT activities in Figure 4.5b is that dye/NC pairs with long donor-acceptor distances (R) exhibit lower EnT efficiency than dye/NC pairs with short distances. Here, we ask the question: *Do dye/NC pairs with shorter donor-acceptor distances exhibit greater EnT activity?* One hypothesis is that large, positive FM value events exhibit shorter R values and large, negative FM value events exhibit longer R values because EnT efficiency scales inversely with R^6.[53] To test this hypothesis, we calculated R values for all positive and negative events using the centroid position of the ZnO NC donor under 355 nm excitation and the dye molecule position under 532 nm illumination. Note, we measure the ZnO NC position at the exact time of the positive or negative event and measure the dye molecule position about 100-1000 ms after the event, when the 532 nm light pulse excites all dye molecules on the sample. Supporting Information Section C5 details the algorithm for the R calculation procedure. Figure 4.6a shows the FM values of positive (pink squares) and negative events (blue triangles) versus R for all 25 candidate A555/APTMS/ZnO conjugate pairs. Figure 4.6b-c shows a zoom-in view of the data for the positive and negative events because R values are less than 100 nm. Note, the R values in Figure 4.6 exceed the physical size of the ZnO NC due to the error associated with overlaying the centroid positions from one image channel onto the other

(40 nm) and the localization error from 2D Gaussian fitting of the donor and acceptor (40 nm).[54] Hence, we focus on the general trends in Figure 4.6b-c rather than trends in absolute values. Surprisingly, Figure 4.6b shows the positive FM magnitude is independent of R, where $r = 0.185 \pm 0.040$. Figure 4.6c shows a very weak correlation between the negative FM values and increasing R, where $r = -0.160 \pm 0.033$. The weak correlation could perhaps be that EnT "shuts off" as the dye molecule temporarily moves away from the NC centroid position. However, the correlations in Figure 4.6b-c are weak. Hence, we conclude that intensity fluctuations in single molecule imaging experiments are likely not due to variations in surface-attached dye motion during the course of the experiment. It is possible that the orientation factor between the donor and acceptor varies during the timescale of the experiment. Future polarization-dependent measurements can test the hypothesis that intensity fluctuations occur due to time-dependent changes in orientation factor.

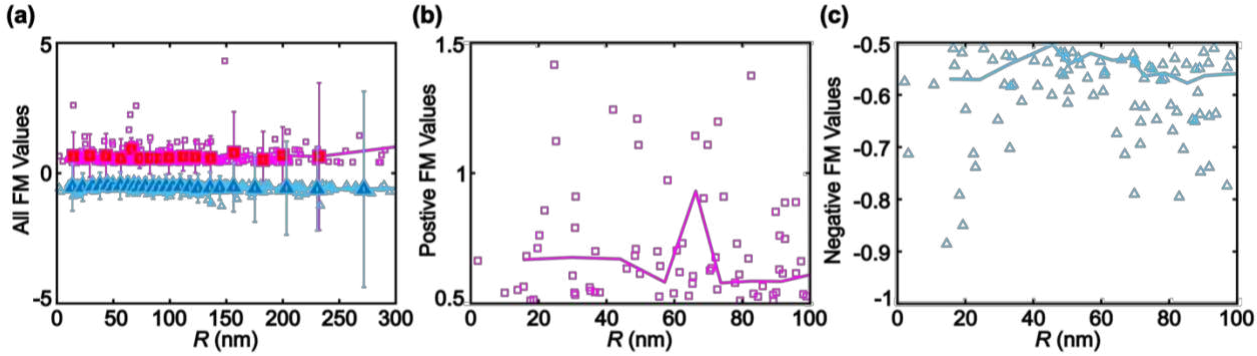

Figure 4.6. Events analysis as a function of average donor-acceptor distance. (a) positive (pink squares) and negative (blue triangles) events as a function of average donor-acceptor distance. The smaller shapes represent the experimentally determined FM values, while the larger shapes indicate the binned and averaged experimentally determined data (30 data points). The error bars indicate the standard error of the mean of the binned data points in both x and y. (b)-(c) same as (a) with smaller scales and error bars removed to clearly identify trends. The red and blue solid lines are the binned and averaged trend lines for positive and negative event analysis respectively.

There are likely multiple physical mechanisms which could lead to fluctuations associated with defect-mediated EnT in the A555/APTMS/ZnO conjugates, which can be modulated by fluctuations in emission from both the NC and the dye. We consider one mechanism, illustrated in Figure 4.7a, that builds on the literature precedent. This scheme shows the excited-state decay

processes in A555/APTMS/ZnO conjugates, based on a model originally proposed by Sadhu et al.,[31] with one significant modification: our model incorporates the possibility that the NC quenches the dye excited state, potentially through electron transfer from the dye to the ZnO NC. This addition is motivated by ensemble-level excitation spectra of ZnO/dye samples, which show fluorescence quenching when dye molecules are directly excited in the presence of ZnO NCs.[17] Wang et al. proposed a similar model to describe defect-mediated EnT from ZnO nanowires to Eu^{3+} ions.[22] Upon excitation of the ZnO bandgap with UV light, the model considers the following decay rates and processes: k_{Trap} is the quenching rate due to the presence of the non-radiative traps, k_0 is the radiative defect PL rate of photo-excited NCs in the absence of the acceptor molecule, k_{FRET} is the defect-mediated EnT rate to a single dye molecule, k_{Fl} is the fluorescence rate of A555 and k_{Quench} is the non-radiative quenching rate of the excited state dye in the presence of the NC.[17,26,29,31] All rate constants are based on experimental results, except k_{Quench} which is manually changed as an independent variable. The defect PL mechanism in ZnO NCs has been widely studied[55-66] and there are strong indications that the defect PL involves surface states and possibly multiple emissive centers. For computational simplicity, we use recombination of trapped electrons with valence band holes as the origin of the defect emission. We assume that nonradiative traps do not participate in the defect-mediated EnT process.[26]

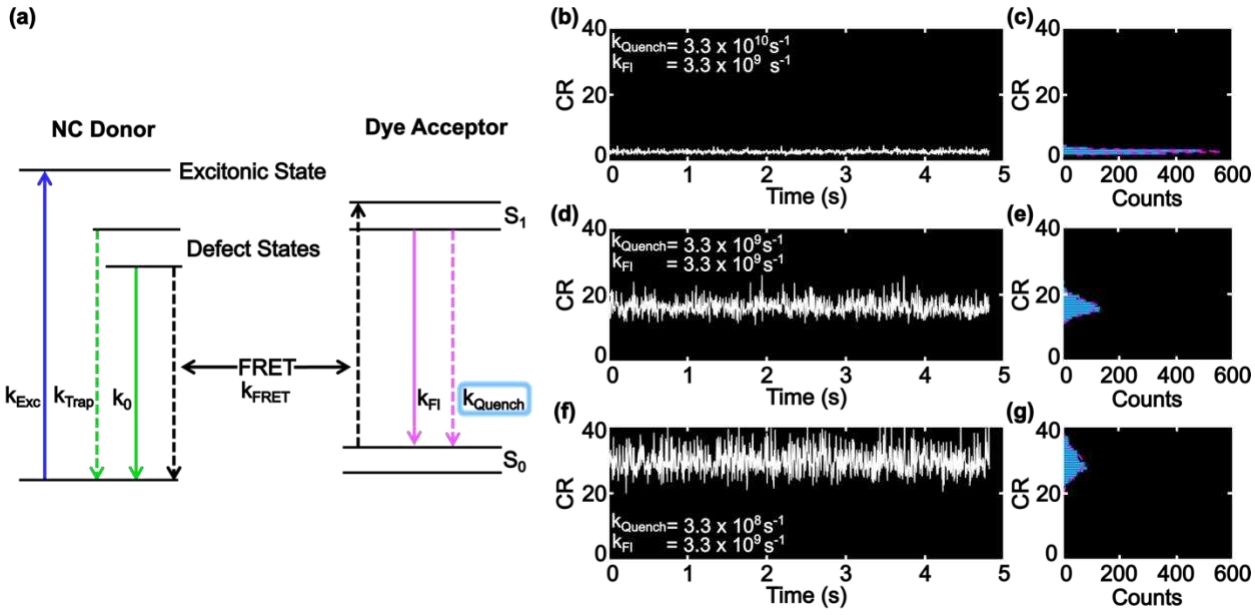

Figure 4.7. kMC CR trajectory simulations. (a) Schematic representation of the photophysical processes in ZnO NCs, dye molecules, and the possible EnT process of A555/APTMS/ZnO conjugates. k_{Exc} is the excitation frequency, k_{Trap} is the quenching rate due to the presence of the non-radiative traps, k_0 is the radiative defect PL rate of photo-excited NCs in the absence of the acceptor molecule, k_{FRET} is the defect-mediated EnT rate to a single dye molecule, k_{Fl} is the fluorescence rate of A555, and k_{Quench} is the non-radiative quenching rate of the excited state dye in the presence of the NC. k_{Quench} was varied as highlighted by the blue box, while the other rates were kept constant. See the Methods Section for the specific values used in the simulations. Solid and dashed arrows represent radiative and non-radiative processes respectively. (b-c) Simulated intensity CR trajectory for $k_{Quench} > k_{Fl}$ with the corresponding distribution. (d-e) and (f-g) is the same as (b-c) for $k_{Quench} = k_{Fl}$ and $k_{Quench} < k_{Fl}$.

Figure 4.7b-g shows the results of numerical kMC simulations of the CR trajectories associated with this model. When the dye quenching exceeds the fluorescence rate ($k_{Quench} > k_{Fl}$, Figure 4.7b-c), the intensity of the dye channel is significantly reduced. This reduction leads to a lower average CR and diminishes the magnitude of fluctuations. In contrast, decreasing the quenching rate ($k_{Quench} < k_{Fl}$) enhances dye emission by favoring the fluorescence pathway over the quenching pathway, as shown in Figure 4.7f-g. This enhancement results in a higher average CR and more pronounced fluctuations. Importantly, the simulation results offer a plausible explanation for the increased micro-fluctuations observed in the experimental data. When quenching reduces the intensity of the dye channel, the overall CR signal decreases, along with the noise, as noise constitutes a relatively constant fraction of the signal. Therefore, the primary

cause of the increased micro-fluctuations at lower k_{Quench} appears to be noise amplification as the signal intensity increases. These insights deepen our understanding of photophysical dynamics in ZnO NC/dye systems and highlight potential strategies to tune micro-fluctuations by controlling quenching and fluorescence processes in future experiments.

4.6 Conclusion

Our investigation of defect-mediated EnT in ZnO NC/dye conjugate systems at the single-particle level provides critical insights into the role of sample heterogeneity in determining EnT efficiency. We identified that 16% of the sample batch consists of bare ZnO NCs, while 20% of NC/dye pairs are EnT-inactive, contributing to residual defect PL and limiting overall EnT performance. Furthermore, distinct micro-fluctuations observed in single-particle fluorescence trajectories were linked to a competitive dye fluorescence quenching pathway. These results underscore the importance of minimizing heterogeneity and optimizing donor-acceptor interactions to enhance the efficiency of light-harvesting systems. By addressing these challenges, future designs can achieve higher EnT efficiency and improved performance in energy conversion applications.

4.7 Author Contributions

According to CRediT criteria, my contributions to this work included conceptualization, data curation, formal analysis, investigation, methodology, visualization, writing – original draft, and writing – reviewing and editing. E.B. synthesized ZnO NCs and conjugate samples and performed ensemble UV/Vis and PL characterization measurements. K.R.K. provided synthesis guidance and characterization interpretation. J.T.M., and P.R.P. performed TEM and STEM-EDS measurements and J.T.M., P.R.P., and J.P.P. provided TEM and STEM-EDS data interpretation.

O.F.B. performed kinetic Monte Carlo simulations and O.F.B. and G.D. provided simulation interpretation. D.R.L. and J.B.S. designed experiments and wrote the manuscript.

REFERENCES

(1) Bruchez, M.; Moronne, M.; Gin, P.; Weiss, S.; Alivisatos, A. P. Semiconductor Nanocrystals as Fluorescent Biological Labels. *Science* **1998**, *281* (5385), 2013–2016. https://doi.org/10.1126/science.281.5385.2013.
(2) Resch-Genger, U.; Grabolle, M.; Cavaliere-Jaricot, S.; Nitschke, R.; Nann, T. Quantum Dots versus Organic Dyes as Fluorescent Labels. *Nat. Methods* **2008**, *5* (9), 763–775. https://doi.org/10.1038/nmeth.1248.
(3) Becker, K.; Lupton, J. M.; Müller, J.; Rogach, A. L.; Talapin, D. V.; Weller, H.; Feldmann, J. Electrical Control of Förster Energy Transfer. *Nat. Mater.* **2006**, *5* (10), 777–781. https://doi.org/10.1038/nmat1738.
(4) Ren, T.; Mandal, P. K.; Erker, W.; Liu, Z.; Avlasevich, Y.; Puhl, L.; Müllen, K.; Basché, T. A Simple and Versatile Route to Stable Quantum Dot−Dye Hybrids in Nonaqueous and Aqueous Solutions. *J. Am. Chem. Soc.* **2008**, *130* (51), 17242–17243. https://doi.org/10.1021/ja8073962.
(5) Soujon, D.; Becker, K.; Rogach, A. L.; Feldmann, J.; Weller, H.; Talapin, D. V.; Lupton, J. M. Time-Resolved Förster Energy Transfer from Individual Semiconductor Nanoantennae to Single Dye Molecules. *J. Phys. Chem. C* **2007**, *111* (31), 11511–11515. https://doi.org/10.1021/jp073556i.
(6) Chandrasiri, H. B.; Jing, H.; Perera, T.; Hu, Y. S.; Snee, P. T. Fluorescence Intermittency of Quantum Dot–Organic Dye Conjugates: Implications for Alternative Energy and Biological Imaging. *J. Phys. Chem. Lett.* **2023**, *14* (15), 3621–3626. https://doi.org/10.1021/acs.jpclett.3c00076.
(7) Clapp, A. R.; Medintz, I. L.; Fisher, B. R.; Anderson, G. P.; Mattoussi, H. Can Luminescent Quantum Dots Be Efficient Energy Acceptors with Organic Dye Donors? *J. Am. Chem. Soc.* **2005**, *127* (4), 1242–1250. https://doi.org/10.1021/ja045676z.
(8) Muhr, V.; Würth, C.; Kraft, M.; Buchner, M.; Baeumner, A. J.; Resch-Genger, U.; Hirsch, T. Particle-Size-Dependent Förster Resonance Energy Transfer from Upconversion Nanoparticles to Organic Dyes. *Anal. Chem.* **2017**, *89* (9), 4868–4874. https://doi.org/10.1021/acs.analchem.6b04662.
(9) Hua, Z.; Xu, Q.; Huang, X.; Zhang, C.; Wang, X.; Xiao, M. Energy Transfer from a Single Semiconductor Nanocrystal to Dye Molecules. *ACS Nano* **2014**, *8* (7), 7060–7066. https://doi.org/10.1021/nn5019736.
(10) Gerlach, F.; Täuber, D.; Von Borczyskowski, C. Correlated Blinking via Time Dependent Energy Transfer in Single CdSe Quantum Dot-Dye Nanoassemblies. *Chem. Phys. Lett.* **2013**, *572*, 90–95. https://doi.org/10.1016/j.cplett.2013.04.034.
(11) Kowerko, D.; Schuster, J.; Amecke, N.; Abdel-Mottaleb, M.; Dobrawa, R.; Würthner, F.; Von Borczyskowski, C. FRET and Ligand Related NON-FRET Processes in Single Quantum Dot-Perylene Bisimide Assemblies. *Phys. Chem. Chem. Phys.* **2010**, *12* (16), 4112. https://doi.org/10.1039/b910308b.
(12) Zhang, C.-Y.; Yeh, H.-C.; Kuroki, M. T.; Wang, T.-H. Single-Quantum-Dot-Based DNA Nanosensor. *Nat. Mater.* **2005**, *4* (11), 826–831. https://doi.org/10.1038/nmat1508.
(13) Zhang, Z.; Rogers, C. R.; Weiss, E. A. Energy Transfer from CdS QDs to a Photogenerated Pd Complex Enhances the Rate and Selectivity of a Pd-Photocatalyzed Heck Reaction. *J. Am. Chem. Soc.* **2020**, *142* (1), 495–501. https://doi.org/10.1021/jacs.9b11278.

(14) Bender, J. A.; Raulerson, E. K.; Li, X.; Goldzak, T.; Xia, P.; Van Voorhis, T.; Tang, M. L.; Roberts, S. T. Surface States Mediate Triplet Energy Transfer in Nanocrystal–Acene Composite Systems. *J. Am. Chem. Soc.* **2018**, *140* (24), 7543–7553. https://doi.org/10.1021/jacs.8b01966.
(15) Huang, Z.; Lee Tang, M. Semiconductor Nanocrystal Light Absorbers for Photon Upconversion. *J. Phys. Chem. Lett.* **2018**, *9* (21), 6198–6206. https://doi.org/10.1021/acs.jpclett.8b02154.
(16) Wu, M.; Congreve, D. N.; Wilson, M. W. B.; Jean, J.; Geva, N.; Welborn, M.; Van Voorhis, T.; Bulović, V.; Bawendi, M. G.; Baldo, M. A. Solid-State Infrared-to-Visible Upconversion Sensitized by Colloidal Nanocrystals. *Nat. Photonics* **2016**, *10* (1), 31–34. https://doi.org/10.1038/nphoton.2015.226.
(17) Beane, G. A.; Morfa, A. J.; Funston, A. M.; Mulvaney, P. Defect-Mediated Energy Transfer between ZnO Nanocrystals and a Conjugated Dye. *J. Phys. Chem. C* **2012**, 120125142738004. https://doi.org/10.1021/jp209638g.
(18) Zhong, Y.; Zi, J.; Wu, F.; Li, Z.; Luan, X.; Gao, F.; Lian, Z. Defect-Mediated Electron Transfer in Pt-$CuInS_2$ /CdS Heterostructured Nanocrystals for Enhanced Photocatalytic H_2 Evolution. *ACS Appl. Nano Mater.* **2022**, *5* (6), 7704–7713. https://doi.org/10.1021/acsanm.2c00154.
(19) Lian, Z.; Wu, F.; Zi, J.; Li, G.; Wang, W.; Li, H. Infrared Light-Induced Anomalous Defect-Mediated Plasmonic Hot Electron Transfer for Enhanced Photocatalytic Hydrogen Evolution. *J. Am. Chem. Soc.* **2023**, *145* (28), 15482–15487. https://doi.org/10.1021/jacs.3c03990.
(20) Maharana, G.; Jayavelu, Y.; Muniramaiah, R.; Paul Joseph, D.; Baskar, L.; Manavalan, K. Visible Light Driven Defect Mediated Photocatalytic Activity of Spray Pyrolyzed Ga and Al Doped ZnO Thin Film Electrodes. *ChemistrySelect* **2024**, *9* (41), e202402590. https://doi.org/10.1002/slct.202402590.
(21) Bora, T.; Lakshman, K. K.; Sarkar, S.; Makhal, A.; Sardar, S.; Pal, S. K.; Dutta, J. Modulation of Defect-Mediated Energy Transfer from ZnO Nanoparticles for the Photocatalytic Degradation of Bilirubin. *Beilstein J. Nanotechnol.* **2013**, *4*, 714–725. https://doi.org/10.3762/bjnano.4.81.
(22) Wang, D.; Xing, G.; Gao, M.; Yang, L.; Yang, J.; Wu, T. Defects-Mediated Energy Transfer in Red-Light-Emitting Eu-Doped ZnO Nanowire Arrays. *J. Phys. Chem. C* **2011**, *115* (46), 22729–22735. https://doi.org/10.1021/jp204572v.
(23) Shukla, A.; Kaur, G.; Babu, K. J.; Kaur, A.; Yadav, D. K.; Ghosh, H. N. Defect-Interceded Cascading Energy Transfer and Underlying Charge Transfer in Europium-Doped $CsPbCl_3$ Nanocrystals. *J. Phys. Chem. Lett.* **2022**, *13* (1), 83–90. https://doi.org/10.1021/acs.jpclett.1c03661.
(24) Chirmanov, V.; Stanish, P. C.; Layek, A.; Radovanovic, P. V. Distance-Dependent Energy Transfer between Ga2O3 Nanocrystal Defect States and Conjugated Organic Fluorophores in Hybrid White-Light-Emitting Nanophosphors. *J. Phys. Chem. C* **2015**, *119* (10), 5687–5696. https://doi.org/10.1021/jp512417h.
(25) Layek, A.; Stanish, P. C.; Chirmanov, V.; Radovanovic, P. V. Hybrid ZnO-Based Nanoconjugate for Efficient and Sustainable White Light Generation. *Chem. Mater.* **2015**, *27* (3), 1021–1030. https://doi.org/10.1021/cm504330k.
(26) Nilsson, Z. N.; Beck, L. M.; Sambur, J. B. Ensemble-Level Energy Transfer Measurements Can Reveal the Spatial Distribution of Defect Sites in Semiconductor Nanocrystals. *J. Chem. Phys.* **2021**, *154* (5), 054704. https://doi.org/10.1063/5.0034775.

(27) Lustig, D. R.; Nilsson, Z. N.; Mulvey, J. T.; Zang, W.; Pan, X.; Patterson, J. P.; Sambur, J. B. Toward Imaging Defect-Mediated Energy Transfer between Single Nanocrystal Donors and Single Molecule Acceptors. *Chem. Biomed. Imaging* **2023**, *1* (2), 168–178. https://doi.org/10.1021/cbmi.3c00015.
(28) Kumar, P.; Pal, S. K. Role of Decoupled Defect Transitions of ZnO Nanocrystals in Energy Transfer. *J. Photochem. Photobiol. Chem.* **2014**, *278*, 46–52. https://doi.org/10.1016/j.jphotochem.2013.12.021.
(29) Lustig, D. R.; Buz, E.; Mulvey, J. T.; Patterson, J. P.; Kittilstved, K. R.; Sambur, J. B. Characterizing the Ligand Shell Morphology of PEG-Coated ZnO Nanocrystals Using FRET Spectroscopy. *J. Phys. Chem. B* **2023**, *127* (41), 8961–8973. https://doi.org/10.1021/acs.jpcb.3c04900.
(30) Rakshit, S.; Vasudevan, S. Resonance Energy Transfer from β-Cyclodextrin-Capped ZnO:MgO Nanocrystals to Included Nile Red Guest Molecules in Aqueous Media. *ACS Nano* **2008**, *2* (7), 1473–1479. https://doi.org/10.1021/nn800152a.
(31) Sadhu, S.; Tachiya, M.; Patra, A. A Stochastic Model for Energy Transfer from CdS Quantum Dots/Rods (Donors) to Nile Red Dye (Acceptors). *J. Phys. Chem. C* **2009**, *113* (45), 19488–19492. https://doi.org/10.1021/jp906160z.
(32) Medintz, I. L.; Clapp, A. R.; Mattoussi, H.; Goldman, E. R.; Fisher, B.; Mauro, J. M. Self-Assembled Nanoscale Biosensors Based on Quantum Dot FRET Donors. *Nat. Mater.* **2003**, *2* (9), 630–638. https://doi.org/10.1038/nmat961.
(33) Wolska-Pietkiewicz, M.; Jędrzejewska, M.; Tokarska, K.; Wielgórska, J.; Chudy, M.; Grzonka, J.; Lewiński, J. Towards Bio-Safe and Easily Redispersible Bare ZnO Quantum Dots Engineered via Organometallic Wet-Chemical Processing. *Chem. Eng. J.* **2023**, *455*, 140497. https://doi.org/10.1016/j.cej.2022.140497.
(34) Panasiuk, Y. V.; Raevskaya, O. E.; Stroyuk, O. L.; Kuchmiy, S. Y.; Dzhagan, V. M.; Hietschold, M.; Zahn, D. R. T. Colloidal ZnO Nanocrystals in Dimethylsulfoxide: A New Synthesis, Optical, Photo- and Electroluminescent Properties. *Nanotechnology* **2014**, *25* (7), 075601. https://doi.org/10.1088/0957-4484/25/7/075601.
(35) Meulenkamp, E. A. Synthesis and Growth of ZnO Nanoparticles. *J. Phys. Chem. B* **1998**, *102* (29), 5566–5572. https://doi.org/10.1021/jp980730h.
(36) Gillespie, D. T. A General Method for Numerically Simulating the Stochastic Time Evolution of Coupled Chemical Reactions. *J. Comput. Phys.* **1976**, *22* (4), 403–434. https://doi.org/10.1016/0021-9991(76)90041-3.
(37) Voter, A. F. INTRODUCTION TO THE KINETIC MONTE CARLO METHOD. In *Radiation Effects in Solids*; Sickafus, K. E., Kotomin, E. A., Uberuaga, B. P., Eds.; NATO Science Series; Springer Netherlands: Dordrecht, 2007; Vol. 235, pp 1–23. https://doi.org/10.1007/978-1-4020-5295-8_1.
(38) *Fluorescence quantum yields (QY) and lifetimes (τ) for Alexa Fluor dyes—Table 1.5 - US*. https://www.thermofisher.com/us/en/home/references/molecular-probes-the-handbook/tables/fluorescence-quantum-yields-and-lifetimes-for-alexa-fluor-dyes.html (accessed 2025-01-21).
(39) Hadar, I.; Halivni, S.; Even-Dar, N.; Faust, A.; Banin, U. Dimensionality Effects on Fluorescence Resonance Energy Transfer between Single Semiconductor Nanocrystals and Multiple Dye Acceptors. *J. Phys. Chem. C* **2015**, *119* (7), 3849–3856. https://doi.org/10.1021/jp512678j.

(40) Elhamdi, I.; Souissi, H.; Taktak, O.; Elghoul, J.; Kammoun, S.; Dhahri, E.; Costa, B. F. O. Experimental and Modeling Study of ZnO:Ni Nanoparticles for near-Infrared Light Emitting Diodes. *RSC Adv.* **2022**, *12* (21), 13074–13086. https://doi.org/10.1039/D2RA00452F.
(41) Wei, J.; Ji, G.; Zhang, C.; Yan, L.; Luo, Q.; Wang, C.; Chen, Q.; Yang, J.; Chen, L.; Ma, C.-Q. Silane-Capped ZnO Nanoparticles for Use as the Electron Transport Layer in Inverted Organic Solar Cells. *ACS Nano* **2018**, *12* (6), 5518–5529. https://doi.org/10.1021/acsnano.8b01178.
(42) Sun, W.; Zhou, W. Growth Mechanism and Microstructures of Cu2O/PVP Spherulites. *RSC Adv.* **2022**, *12* (31), 20022–20028. https://doi.org/10.1039/D2RA03302J.
(43) Zhu, P.; Ma, Y.; Wang, Y.; Yang, Y.; Qian, G. Separation and Recovery of Materials from the Waste Light Emitting Diode (LED) Modules by Solvent Method. *J. Mater. Cycles Waste Manag.* **2020**, *22* (4), 1184–1195. https://doi.org/10.1007/s10163-020-01012-7.
(44) Aydın, E. B.; Aydın, M.; Sezgintürk, M. K. The Development of an Ultra-Sensitive Electrochemical Immunosensor Using a PPyr-NHS Functionalized Disposable ITO Sheet for the Detection of Interleukin 6 in Real Human Serums. *New J. Chem.* **2020**, *44* (33), 14228–14238. https://doi.org/10.1039/D0NJ03183F.
(45) Chuacharoen, T.; Sabliov, C. M. Zein Nanoparticles as Delivery Systems for Covalently Linked and Physically Entrapped Folic Acid. *J. Nanoparticle Res.* **2017**, *19* (2), 81. https://doi.org/10.1007/s11051-017-3763-4.
(46) Ramya, M.; Nideep, T. K.; Nampoori, V. P. N.; Kailasnath, M. Solvent Assisted Evolution and Growth Mechanism of Zero to Three Dimensional ZnO Nanostructures for Dye Sensitized Solar Cell Applications. *Sci. Rep.* **2021**, *11* (1), 6159. https://doi.org/10.1038/s41598-021-85701-9.
(47) Van Embden, J.; Gross, S.; Kittilstved, K. R.; Della Gaspera, E. Colloidal Approaches to Zinc Oxide Nanocrystals. *Chem. Rev.* **2023**, *123* (1), 271–326. https://doi.org/10.1021/acs.chemrev.2c00456.
(48) Patterson, G.; Davidson, M.; Manley, S.; Lippincott-Schwartz, J. Superresolution Imaging Using Single-Molecule Localization. *Annu. Rev. Phys. Chem.* **2010**, *61* (1), 345–367. https://doi.org/10.1146/annurev.physchem.012809.103444.
(49) Rust, M. J.; Bates, M.; Zhuang, X. Sub-Diffraction-Limit Imaging by Stochastic Optical Reconstruction Microscopy (STORM). *Nat. Methods* **2006**, *3* (10), 793–796. https://doi.org/10.1038/nmeth929.
(50) Van Dijken, A.; Meulenkamp, E. A.; Vanmaekelbergh, D.; Meijerink, A. Influence of Adsorbed Oxygen on the Emission Properties of Nanocrystalline ZnO Particles. *J. Phys. Chem. B* **2000**, *104* (18), 4355–4360. https://doi.org/10.1021/jp993998x.
(51) Ma, Y.; Choi, T.-W.; Cheung, S. H.; Cheng, Y.; Xu, X.; Xie, Y.-M.; Li, H.-W.; Li, M.; Luo, H.; Zhang, W.; So, S. K.; Chen, S.; Tsang, S.-W. Charge Transfer-Induced Photoluminescence in ZnO Nanoparticles. *Nanoscale* **2019**, *11* (18), 8736–8743. https://doi.org/10.1039/C9NR02020A.
(52) Roy, R.; Hohng, S.; Ha, T. A Practical Guide to Single-Molecule FRET. *Nat. Methods* **2008**, *5* (6), 507–516. https://doi.org/10.1038/nmeth.1208.
(53) Han, K. S.; Liu, G.; Zhou, X.; Medina, R. E.; Chen, P. How Does a Single Pt Nanocatalyst Behave in Two Different Reactions? A Single-Molecule Study. *Nano Lett.* **2012**, *12* (3), 1253–1259. https://doi.org/10.1021/nl203677b.

(54) Govorov, A.; Hernández Martínez, P. L.; Demir, H. V. *Understanding and Modeling Förster-Type Resonance Energy Transfer (FRET)*; SpringerBriefs in Applied Sciences and Technology; Springer Singapore: Singapore, 2016. https://doi.org/10.1007/978-981-287-378-1.
(55) Sambur, J. B.; Chen, T.-Y.; Choudhary, E.; Chen, G.; Nissen, E. J.; Thomas, E. M.; Zou, N.; Chen, P. Sub-Particle Reaction and Photocurrent Mapping to Optimize Catalyst-Modified Photoanodes. *Nature* **2016**, *530* (7588), 77–80. https://doi.org/10.1038/nature16534.
(56) Lin, J.-H.; Patil, R. A.; Devan, R. S.; Liu, Z.-A.; Wang, Y.-P.; Ho, C.-H.; Liou, Y.; Ma, Y.-R. Photoluminescence Mechanisms of Metallic Zn Nanospheres, Semiconducting ZnO Nanoballoons and Metal-Semiconductor Zn/ZnO Nanospheres. *Sci. Rep.* **2014**, *4* (1), 6967. https://doi.org/10.1038/srep06967.
(57) Vanheusden, K.; Warren, W. L.; Seager, C. H.; Tallant, D. R.; Voigt, J. A.; Gnade, B. E. Mechanisms behind Green Photoluminescence in ZnO Phosphor Powders. *J. Appl. Phys.* **1996**, *79* (10), 7983–7990. https://doi.org/10.1063/1.362349.
(58) Damberga, D.; Viter, R.; Fedorenko, V.; Iatsunskyi, I.; Coy, E.; Graniel, O.; Balme, S.; Miele, P.; Bechelany, M. Photoluminescence Study of Defects in ZnO-Coated Polyacrylonitrile Nanofibers. *J. Phys. Chem. C* **2020**, *124* (17), 9434–9441. https://doi.org/10.1021/acs.jpcc.0c00326.
(59) Chen, R.; Pang, S.; An, H.; Dittrich, T.; Fan, F.; Li, C. Giant Defect-Induced Effects on Nanoscale Charge Separation in Semiconductor Photocatalysts. *Nano Lett.* **2019**, *19* (1), 426–432. https://doi.org/10.1021/acs.nanolett.8b04245.
(60) Appavoo, K.; Liu, M.; Sfeir, M. Y. Role of Size and Defects in Ultrafast Broadband Emission Dynamics of ZnO Nanostructures. *Appl. Phys. Lett.* **2014**, *104* (13), 133101–133105. https://doi.org/10.1063/1.4868534.
(61) Zhang, L.; Yin, L.; Wang, C.; lun, N.; Qi, Y.; Xiang, D. Origin of Visible Photoluminescence of ZnO Quantum Dots: Defect-Dependent and Size-Dependent. *J. Phys. Chem. C* **2010**, *114* (21), 9651–9658. https://doi.org/10.1021/jp101324a.
(62) Zeng, H.; Duan, G.; Li, Y.; Yang, S.; Xu, X.; Cai, W. Blue Luminescence of ZnO Nanoparticles Based on Non-Equilibrium Processes: Defect Origins and Emission Controls. *Adv. Funct. Mater.* **2010**, *20* (4), 561–572. https://doi.org/10.1002/adfm.200901884.
(63) Lin, B.; Fu, Z.; Jia, Y.; Liao, G. Defect Photoluminescence of Undoping ZnO Films and Its Dependence on Annealing Conditions. *J. Electrochem. Soc.* **2001**, *148* (3), G110. https://doi.org/10.1149/1.1346616.
(64) Cai, J.; Xu, J.; Zhang, X.; Niu, X.; Xing, T.; Ji, T.; Li, L. Defect-Related Visible Luminescence of ZnO Nanorods Annealed in Oxygen Ambient. *Optoelectron. Lett.* **2012**, *8* (1), 4–8. https://doi.org/10.1007/s11801-012-1042-2.
(65) Lyons, J. L.; Varley, J. B.; Steiauf, D.; Janotti, A.; Van de Walle, C. G. First-Principles Characterization of Native-Defect-Related Optical Transitions in ZnO. *J. Appl. Phys.* **2017**, *122* (3), 035704. https://doi.org/10.1063/1.4992128.
(66) Morfa, A. J.; Gibson, B. C.; Karg, M.; Karle, T. J.; Greentree, A. D.; Mulvaney, P.; Tomljenovic-Hanic, S. Single-Photon Emission and Quantum Characterization of Zinc Oxide Defects. *Nano Lett.* **2012**, *12* (2), 949–954. https://doi.org/10.1021/nl204010e.
(67) Djurisic, A. B.; Leung, Y. H.; Tam, K. H. Defect Emissions in ZnO Nanostructures. *Opt. Ldots* **2005**. https://doi.org/10.1088/0957-4484/20/15/155603.

CHAPTER 5: OUTLOOK AND FUTURE DIRECTIONS: IDENTIFYING THE DEFECT DONOR TRANSITION DIPOLE MOMENT FOR CONTROLLING ENERGY FLOW IN NANOCRSYTAL/MOLECULE ENERGY TRANSFER SYSTEMS[4]

5.1 Overview

Developing nanomaterial systems that emit photons with controlled polarization and propagation direction upon excitation by a non-directional stimulus (e.g., sunlight or a voltage pulse) has significant implications for photonics, solid-state lighting, optical sensors, and quantum information processing units. This chapter investigates a strategy for achieving energy flow control through defect-mediated energy transfer between semiconductor nanocrystals (NCs) and molecules. In this approach, a photo- or electrically-excited semiconductor NC undergoes an energy transfer process with surface-bound molecular dye acceptors. Energy flow is facilitated by first trapping the excitation at a defect site in the NC lattice and ensuring that energy transfer preferentially occurs between molecules bound to specific NC surface facets, a phenomenon known as defect-mediated energy transfer. Defect-mediated energy transfer has been physically modeled using Förster resonance energy transfer (FRET) theory, which is a well-established model for molecular donor/acceptor pairs. However, the assumptions the field typically use to predict EnT efficiency between molecules stemming from FRET theory fail for many systems, specifically the transition dipole orientation of the donor. This chapter explores the extension of the research described in Chapters 2, 3, and 4 by providing future directions for the ability to control the

[4]Portions of this chapter were reproduced with permissions from Lustig, D., Sambur, J., Van Orden, A., Imaging Defect-Mediated Energy Transfer between Single Nanocrystal Donors and Single Molecule Acceptors. Los Alamos National Laboratory Center for Integrated Nanotechnologies User Proposal, #2024AU0169.

orientation of the defect dipole moment. Specifically, the orientation of the donor dipole relative to the NC facets must be controlled. The key objectives will be to: (1) to measure the transition defect donor dipole orientation within semiconductor NCs and (2) to demonstrate controlled directionality of emitted photons based on the orientation of the transition donor dipole relative to a nearby acceptor. By refining the fundamental understanding of energy transfer in defect donor-acceptor systems, this future work will advance the rational design of NC/dye conjugate systems for highly efficient and directional energy transfer. Furthermore, accurately measuring dipole orientation provides a pathway for controlling light emission directionality in NC/dye conjugate systems, with potential applications in quantum sensing and optoelectronic devices.

5.2 Introduction

FRET is a widely used technique based on energy transfer (EnT) between donor and acceptor molecules, where the photoexcited donor transfers energy non-radiatively to a nearby acceptor molecule via a dipole-dipole coupling mechanism.[1–4] FRET theory is a well-established model for molecular donor/acceptor pairs.[5,6] Additionally, defect-mediated EnT has been physically modeled using FRET theory as depicted in Figure 5.1, where the donor is localized defects within the NC.[7–15]

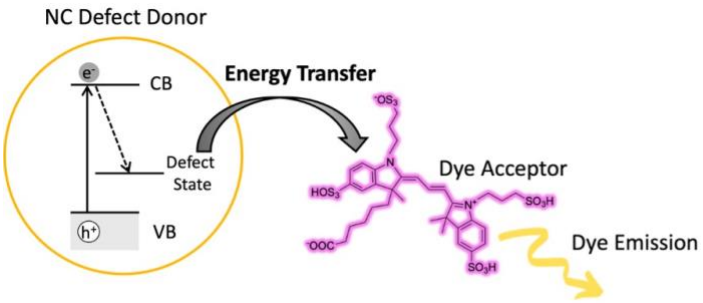

Figure 5.1. Defect-mediated EnT from a localized defect site in a NC donor to a fluorescent dye acceptor.

However, two critical challenges arise for EnT occurring between NC donor/molecular acceptor systems: (1) the predicted EnT efficiencies are *significantly less* for NC-dye pairs than for molecule-molecule interactions[11] and (2) key assumptions from FRET theory, particularly regarding transition dipole orientation, do not hold for many NC-based systems.[16–19] Specifically, the field typically assumes freely diffusing donor and acceptor molecules are randomly oriented in solution, and therefore, $\kappa^2 = 2/3$[4,20–22] as described in Figure 5.2a. More specifically, in defect-mediated EnT NC/dye donor-acceptor systems, when a defect site acts as the donor, the problem is that the orientation of the transition donor dipole is unknown[16,18,23–26], allowing for potential overestimations of FRET efficiency in the field as shown in Figure 5.2b. Addressing this issue requires the ability to both measure and control the orientation of the transition defect donor dipole moment relative to NC facets. Additionally, optimizing EnT efficiency necessitates precise control over acceptor molecule binding relative to the defect donor dipole moment.

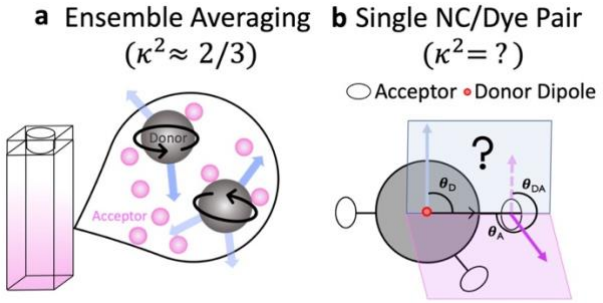

Figure 5.2. (a) Ensemble-level averaging of the donor dipole orientation factor (b) unknown donor/acceptor dipole orientation for a single NC/dye pair.

This chapter explores the fundamental role of defects in FRET-based EnT processes, providing a comprehensive understanding of how defect-mediated EnT can be controlled and optimized. Specifically, two key questions are investigated: (1) Can the orientation factor of the transition defect donor dipole be measured? (2) Can the directionality and polarization of emitted photons be controlled based on the orientation of the transition donor dipole? By addressing these

questions, this study aims to refine how fundamental insights are extracted from FRET theory in NC-dye conjugate systems. This discovered knowledge will pave the way for controlling the directionality of light emission[27–30] in NC/dye conjugate systems for quantum sensing applications.[31–33]

A widely adopted assumption in FRET theory for molecular donor-acceptor pairs is the dipole orientation factor, κ^2. The field typically assumes freely diffusing donor and acceptor molecules are randomly oriented in solution, and therefore, $\kappa^2 = 2/3$.[4,20–22] The accuracy of this assumption is critical, as κ^2 directly impacts the calculation of the Förster distance, R_0, which is the distance between a single donor-acceptor pair at which the EnT efficiency is equal to 50%.[4] However, this assumption fails in systems where dipole motion is restricted, such as FRET experiments involving fluorescent proteins, where the chromophore's rigidity within a protein structure prevents random dipole orientation.[18] This restricted motion is an example of a very specific orientation where the averaging of κ^2 is no longer applicable.[18] A similar challenge arises in semiconductor NC-molecule systems, where the dipole orientation of defect-based donors is often unknown. Thus, κ^2 is often considered a barrier because it represents significant uncertainty in the donor-acceptor distance obtained through the FRET technique.[19]

In semiconductor NCs containing a high number of defects, it is essential to determine the orientation of the defect dipoles for accurate FRET measurements. When the defect acts as the donor, this increases variables that impact κ^2 as depicted in Figure 5.3: (1) how many defect dipoles exist per donor NC? (2) where are the defect dipoles located? (3) which direction are the defect dipoles oriented in relation to the crystal lattice when FRET occurs?

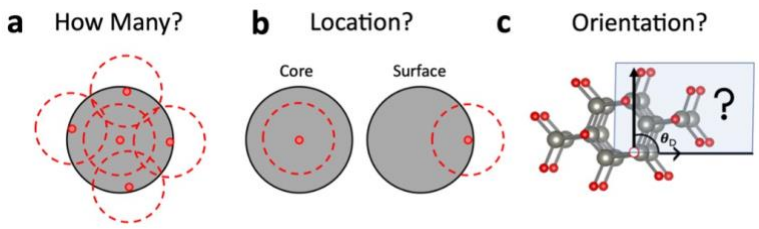

Figure 5.3. Variables that impact κ^2. (a) Multiple localized defects can exist for a single NC. (b) various locations of defect sites for a single NC. (c) unknown orientation of the donor defect dipole.

Addressing these unknowns is crucial for accurately determining κ^2 and refining FRET-based distance measurements in defect-mediated EnT systems. Although there have been experimental and theoretical studies measuring the dipole orientation of defects[31–36], to the best of our knowledge there has not been any experimental studies measuring the *transition dipole moment of single defects in a material*. Through rational understanding of the donor defect dipole, this will pave the way to synthesize and utilize defect engineering in an NC crystal lattice to directionally control photon emission and energy flow. The results of our proposed research will enable rational design of a donor-acceptor system where EnT is optimized. This is a key step in enhancing the performance of light harvesting devices[37], improving solar cell systems[37–39], and quantum sensing applications.[31–33]

5.3 Future Directions to Measure the Three-dimensional Defect Donor Transition Dipole Orientation in ZnO NCs

A key challenge in understanding defect-mediated EnT is to identify (1) how many molecules engage in EnT with a single NC and (2) how many defect sites engage in EnT on a single NC. In addition, it is also possible that both active and inactive NC sub-populations exist in heterogeneous sample. All the above open questions are hidden in ensemble-level measurements.[9,14] These complexities highlight the need for single-molecule imaging techniques that can resolve the fundamental mechanisms underlying defect-mediated EnT. To address these challenges, a future study will employ single-molecule fluorescence polarization microscopy

(smFPM) to directly identify the transition dipole moment of defects in individual NCs. By establishing a detailed understanding of defect dipole orientation, we aim to optimize defect-mediated EnT from single NCs to single acceptor dye molecules. ZnO NCs are chosen as an ideal NC material because they exhibit a broad visible "defect" emission as shown in the inset in Figure 5.4a upon being excited with UV illumination and a wide range of commercially available acceptor dye molecules can engage in defect-mediated EnT with the NC core and/or surface defects.[40] Through this approach, we seek to overcome the limitations of ensemble-based studies and provide new insights into the role of defects in EnT processes.

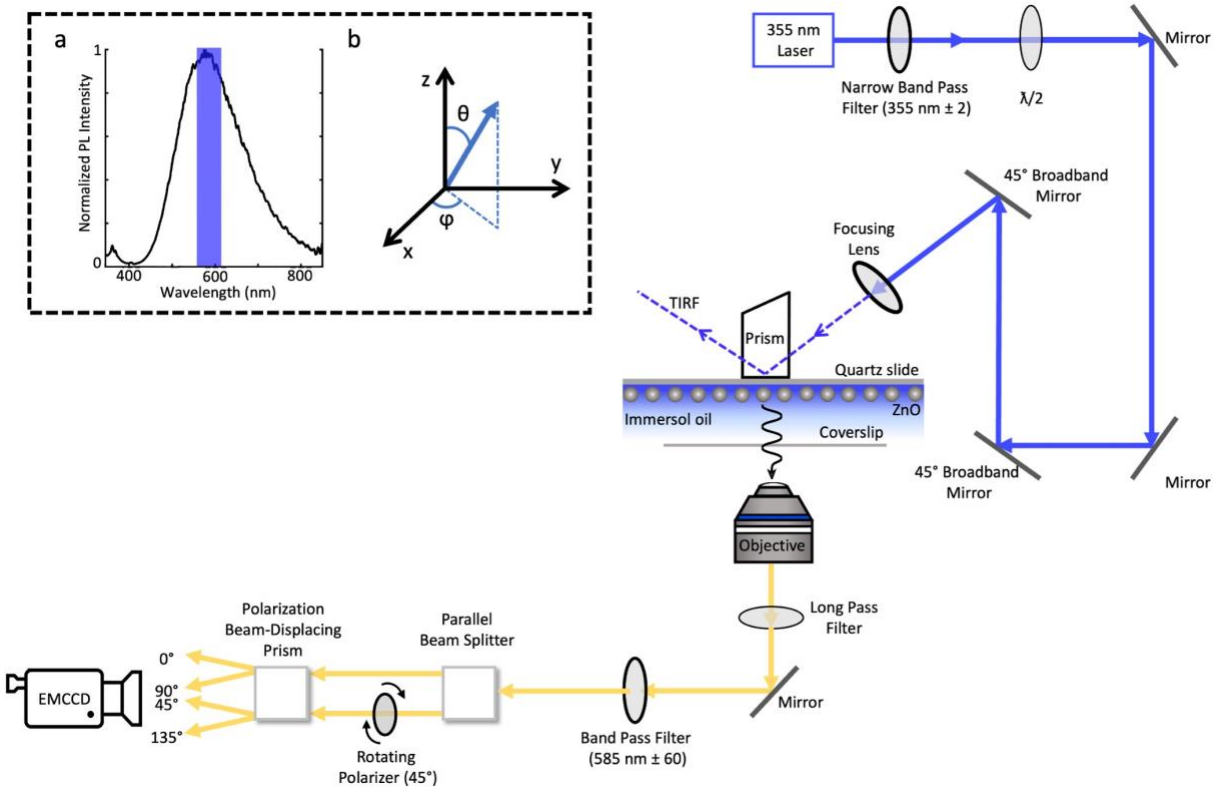

Figure 5.4. Proposed set-up for smFPM coupled with TIRF microscopy to measure the transition dipole orientation of the defect donor in single NCs. Inset: (a) ensemble-level ZnO defect PL showing the 585/60 bandpass filter. (b) 3D orientation of a dipole transition in a spherical coordinate system, where XY is the sample plane of the fluorescence microscope. A molecular dipole is represented by a blue arrow. θ is the polar angle made with the optical Z axis. φ is the azimuthal angle about the Z axis.

In order to determine the transition dipole orientation of the defect donor in single NCs, it is crucial to observe the absorption and emission dipole moment. Combinations of polarization excitation and polarization emission are required to simultaneously analyze both dipole orientations. In the optical path, linear polarized light is used to excite in-plane NCs and the resultant fluorescence is projected into two orthogonal components whose directions are parallel and perpendicular to the incident light, respectively.[41] Now, if excited with rotated linearly polarized excitation, then the intensity of molecules will be modulated with different phases determined by their orientation.[42] This is because the probability of excitation depends on the polarization angle.[43] Here, we utilize smFPM coupled with total internal reflection fluorescence (TIRF) microscopy.[44] The technique uses the unique polarizations of evanescent waves generated by total internal reflection to excite the dipole moment of individual NCs. The TIRF excitation offers an advantage over epifluorescence and confocal microscopy of a strong polarization component along the z axis (optical axis of the microscope) as well as along the x and y axes, making it possible to determine the three-dimensional orientation of single NCs as shown in the inset of Figure 5.4b.[45,46] A molecular dipole is represented by a blue arrow. θ is the polar angle made with the optical Z axis and φ is the azimuthal angle about the Z axis.[36,41,47] To identify the nature of the transition dipole for defects in ZnO NCs, polarization anisotropy values (ρ), defined as $\rho = \frac{I_{\parallel} - I_{\perp}}{I_{\parallel} + I_{\perp}}$ (5.1) where $I_{\parallel}$ and $I_{\perp}$ are the fluorescence emission intensities for polarizations detected parallel and perpendicular to the excitation light polarization direction respectively.[48–52]

5.3.1 Experimental Methods

smFPM measurements will be performed using a wide field inverted epifluorescence microscope coupled with a TIRF excitation. A dilute solution of ZnO NCs are spin-cast onto a quartz slide and a drop of immersol oil is placed over the NCs and a glass coverslip is placed on

top. The quartz slide is placed on the stage of an inverted microscope equipped with a prism-type TIRF microscopy setup with a 355 nm laser to excite the ZnO NCs. Laser light is directed into the prism at such an angle that it undergoes total internal reflection within the quartz slide at the interface with the immersol oil. The total internal reflection process produces an evanescent field on the immersol side of the slide. The intensity of the field decays exponentially with distance from the reflection surface, enabling excitation of NCs on the slide surface while limiting the penetration of the field into the solution, reducing background signal. The laser emits linearly polarized light and a half-wave plate was used to control the orientation of the polarization at the objective back aperture to adjust the absorption dipole moment.[48] Photons emitted from the sample are collected through a 60x oil-immersion microscope objective, passed through a long-pass filter to further clean up fluorescent signal and remove stray background light, and then through a selective bandpass filter, which is chosen to select the defect emission from ZnO defects (585/60 bandpass) as shown in Figure 5.4a. To monitor orientation dynamics in real time, an optical layout measures two polarization anisotropy values from four polarization components of the emission from individual NCs. Following established work to measure the transition dipole moment of single CdSe quantum dots, the experimental procedure is adopted and adjusted for measuring the transition dipole moment for defects in ZnO NCs.[52] The defect emission is further split into two parallel beams by a set of three prisms. One of the beams is rotated by 45° with a polarization rotator.[52] The parallel beams are then split further according to their polarization by using a polarization-displacement prism to yield the 0, 90, 45, and 135° polarization components of the emission for each NC.[52] This splits the fluorescence light on four polarization components with 45° shift in the orientation of the electric field vector.[48] In this case no emission analyzer rotation is needed, because having four orientations is enough to reconstruct the whole emission

polarization properties for given excitation polarization.[48] Two polarization anisotropy values are defined by the 0 and 90° components and the 45 and 135° components, respectively.[52] The time trace of anisotropy values then translates into a corresponding angular rotational time trace.[52] The four polarization components (0, 90, 45, and 135°) of a single NC are projected onto an electron multiplying charge collection device (EMCCD) camera and fluorescence images are continuously acquired for further data analysis. A series of these images creates a time series of anisotropy values. The fluorescence intensity at different polarization angles will be extracted from the movies using a custom MATLAB script.

To ensure stable imaging conditions, the ZnO NCs are embedded in a drop of Immersol oil, "sandwiched" between a quartz slide and a coverslip. This preparation method is necessary due to the instability of ZnO defect emission in air.[14] While the assumption is made that the NCs adhere to the quartz slide and do not freely diffuse in the oil, some degree of rotational or translational motion may still occur. To minimize such motion, the ZnO NCs are spin-cast onto the quartz slide and subsequently annealed to enhance surface contact and reduce mobility. smFPM imaging is performed using a multi-channel detection scheme, where the original signal is split into four or more channels. This division inherently reduces the signal-to-noise ratio in each channel.[48] To compensate, acquisition times are optimized to maximize signal collection while maintaining an acceptable noise level. To accurately quantify fluorescence anisotropy, careful background subtraction is performed to prevent artificially low values for the degree of polarization.[52] TIRF excitation is employed to enhance the signal-to-noise ratio and minimize background interference. Additional measures, including extended acquisition times and rigorous background subtraction, are implemented to ensure accurate polarization measurements. Control

experiments using only the quartz slide are conducted to verify that background contributions do not artificially suppress polarization values.

5.3.2 Expected Results

The continuously acquired fluorescence images should capture the polarized fluorescence signal of each component (parallel and perpendicular) for a single NC and will be used to obtain polarization anisotropy values and show modulating intensities of the defect emission as defined by Eq. 5.1 above. The transition dipole from single NCs is shown by rotating the polarization displacement prism from 0 to 180° and the anisotropy values of the single ZnO NC are plotted to display a sinusoidal pattern over the rotated angles (Figure 5.5).[52] The key result will depict fluorescence intensity from the imaging on the y axis as a function of polarization angle (θ) on the x axis.[44,50,52–55] To relate the fluorescence intensity vs polarization angle result with the dipole moment, it is possible to fit the sinusoidal polarization trace result where the orientation of each dipole, *d* is determined by its polar and azimuthal components as shown in Figure 5.4b: $I(\varphi_{ex})=I[1+M_{ex}\cos(2[\varphi_{ex}-\theta_{ex}])]$ where I is the average fluorescence intensity over φ_{ex}, M_{ex} is the modulation depth of fluorescence excitation, and θ_{ex} is the fluorescence excitation modulation phase.[48,54–56] Similarly, the polarization properties of fluorescence emission of an individual object can be determined by measuring the dependence between the fluorescence intensity of the object and the orientation angle of the emision analyzer, φ_{em}, while exciting with polarized light: $I(\varphi_{em})=I[1+M_{em}\cos(2[\varphi_{em}-\theta_{em}])]$.[48] Here, the modulation depths describe the degree of alignment of the transition dipole moments responsible for fluorescence excitation (M_{ex}) or emission (M_{em}), and its values range from 0 to 1 for isotropic to uniaxial, respectively and θ represent the main orientation axis of the absorbing (θ_{ex}) and emissive (θ_{em}) dipoles. Through fitting the fluorescence intensity

function of polarization angle (θ), φ is extracted and the absorbance and emission transition dipoles can be determined.

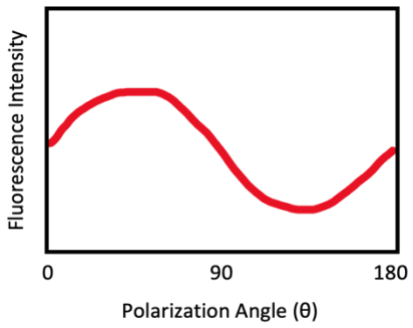

Figure 5.5. Example of a key result which will depict fluorescence intensity from the imaging procedure on the y axis as a function of polarization angle (θ) on the x axis.

5.4 Future Directions to Demonstrate controlled directionality of an Emitted Photon based on the Orientation of the Transition Donor Dipole within an NC Crystal Lattice

The efficiency of EnT is dependent on the relative orientations of the transition moments of the donor and acceptor.[16,57,58] When the transition moments are aligned, EnT is optimized. If the defect donor transition dipole moment is known, it may be possible to control the energy flow from discrete locations on the donor to optimize EnT efficiency. Previous work showed that defects most likely lie on the surface of ZnO NCs.[9] The exact location of where the defects *actually* exist on the surface has not been determined. Our hypothesis is that the transition donor defect dipole orientation factor exists at fixed sites on the surface of the NC donor, specifically on the facets of the NC. If true, EnT would be surface-facet dependent. Then, if NC/dye conjugates are synthesized such that an acceptor molecule is located on a specific facet location of the crystal lattice, defect mediated EnT can be maximized. We will test this hypothesis using ZnO samples with well-defined facets[59,60] as shown in Figure 5.6 and utilize single molecule measurements coupled with transmission electron microscopy (TEM), which highlights how a single NC is sitting. ZnO NC/dye conjugates will be synthesized such that dye molecules can be molecularly

linked to highly faceted ZnO NCs. By monitoring dye molecules bound to ZnO NCs during induced defect-mediated EnT, we can uncover the position of defects on well-defined NC facets. This information is once again crucial for optimizing these EnT systems to improve the overall EnT efficiency.[16,57,58]

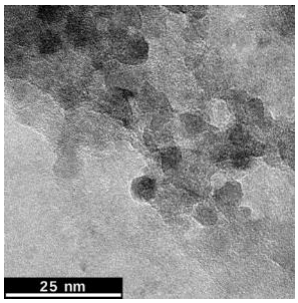

Figure 5.6. TEM of ZnO NCs, depicting hexagonal wurtzite structure with defined facets.

5.4.1 Experimental Methods

Single molecule measurements will be performed following the above TIRF microscopy experimental design, while inducing defect-mediated EnT. The 355 nm excitation excites defects within the ZnO NC lattice, and if there is a dye acceptor nearby (<10 nm), the dye will emit. AlexaFluor 555 (A555) dye molecules are chosen due to the dye absorption (max = 556 nm) having a strong overlap with the defect PL of ZnO. Photons emitted from the sample are collected through the objective, passed through a long-pass filter (cutoff wavelength of 440 nm) in the filter cube of the microscope, and then directed to an image splitter, which uses a dichroic mirror (cutoff wavelength of 550 nm) to split the photon stream into two channels defined by the bandpass filters used for each channel. One bandpass filter is chosen to match the emission signal from the A555 dye molecules (585/40 bandpass). This channel represents the "dye channel". The second bandpass filter was chosen to match the defect emission from ZnO only (490/60 bandpass), forming the "defect channel". The two channels are projected onto an EMCCD camera operated to produce a

single image, split vertically. The intensity trajectories of single ZnO NCs and dye molecules from the image stacks, or movies, are extracted using a detailed image analysis algorithm in Matlab.

To achieve an adequate experimental signal-to-noise ratio, photons need to be detected before the photobleaching of the dye molecule. To overcome this, a dye with a sufficiently long lifetime and high PL quantum yield must be chosen.[20] Additionally, the verification of where the dye is bound to the ZnO will be a challenge. If we see high PL coming from the dye channel, it must be verified that this is due to EnT from a localized defect in ZnO. To ensure this, control experiments can be performed with little defect PL from the ZnO and/or control experiments where dye molecules are not bound to a specific facet. This will ensure that the EnT that is observed is due to controlled energy flow from defects on ZnO facets to single dye molecules.

5.4.2 Expected Results

A fluorescent molecule has the greatest probability of absorption when its absorption transition dipole moment orientation is parallel to the direction of polarized light.[41,46] Fluorophores absorb light with a probability proportional to the square of the dot product of the local optical electric field and the molecular transition dipole moment.[22,44,48] Thus, when a dye binds in a defined orientation it emits highly polarized anisotropic fluorescence.[44] Through defect-mediated EnT, if the emitted light from the defect center of the donor can be aligned with the absorbance of the acceptor, the absorption transition moment of the fluorophore is aligned with the direction of polarization of the incoming light and the chance of the fluorophore being excited is a maximum, and thus the emitted intensity from the fluorophore will be large.[22] On the other hand, when the orientation of the fluorophore is perpendicular to the polarization of the excitation light, the fluorophore will not be excited, and the re-emitted intensity will be zero.[22] If the defect donor

dipole is oriented along a specific facet where a dye molecule is located, then defect-mediated EnT efficiency will be maximized as highlighted by the dye fluorescing in the dye channel.

5.5 Conclusion and Outlook

This chapter outlines the methods used to measure defect donor dipole orientation and explores strategies for controlling light polarization in NC/dye conjugate systems. Understanding and controlling the orientation of defect donor transition dipoles is critical for optimizing EnT in nanocrystal (NC)-based systems. This chapter explores two key questions: (1) *Can the defect donor transition dipole orientation factor be measured?* and (2) *Can the directionality of emitted photons be controlled based on the orientation of the transition donor dipole to enhance defect-mediated EnT efficiency?* Addressing these questions provides fundamental insights into FRET mechanisms in semiconductor NCs and enables rational design of donor-acceptor systems where EnT is optimized.

Optimizing EnT is essential for the performance of light harvesting devices[37] and quantum sensing applications.[29,31–33] In addition to improving the FRET efficiency, controlling the transition dipole orientation would be a significant advantage in improving optoelectronic devices.[35,61] For example, the external quantum efficiency of LEDs can be improved if emissive molecules are oriented such that their transition dipole moment is parallel to the surface plane.[62–64] Additionally, accurate measurements of defect dipole orientation in ZnO NCs will advance scientific understanding of how donor dipole orientation influences FRET efficiency and directional emission.[57]

Beyond measuring dipole orientations, this research will investigate the ability to control the orientation of the defect donor transition dipole moment relative to the NC crystal facets. By combining single molecule measurements with TEM, it is possible to determine the orientation of

defect dipoles and apply this knowledge to the rational design of donor-acceptor systems for improved EnT efficiency. This approach enables the development of intrinsically directional light emitters, which are crucial for photonic applications[38,62], including lasing and energy-efficient display technologies.[30] These findings provide a foundation for designing EnT systems with higher efficiency and directionally controlled EnT [57,58], with implications for quantum sensing[29,31–33] and other advanced photonic applications.

REFERENCES

(1) Sitt, A.; Even-Dar, N.; Halivni, S.; Faust, A.; Yedidya, L.; Banin, U. Analysis of Shape and Dimensionality Effects on Fluorescence Resonance Energy Transfer from Nanocrystals to Multiple Acceptors. *J. Phys. Chem. C* **2013**, *117* (43), 22186–22197. https://doi.org/10.1021/jp308243p.
(2) Sadhu, S.; Patra, A. Donor-Acceptor Systems: Energy Transfer from CdS Quantum Dots/Rods to Nile Red Dye. *ChemPhysChem* **2008**, *9* (14), 2052–2058. https://doi.org/10.1002/cphc.200800298.
(3) Lakowicz, J. R. *Principles of Fluorescence Spectroscopy*, 3rd ed.; Springer: New York, 2006.
(4) Clegg, R. M. Chapter 1 Förster Resonance Energy Transfer—FRET What Is It, Why Do It, and How It's Done. In *Laboratory Techniques in Biochemistry and Molecular Biology*; Elsevier, 2009; Vol. 33, pp 1–57. https://doi.org/10.1016/S0075-7535(08)00001-6.
(5) Yoo, J.; Kim, J.-Y.; Louis, J. M.; Gopich, I. V.; Chung, H. S. Fast Three-Color Single-Molecule FRET Using Statistical Inference. *Nat. Commun.* **2020**, *11* (1), 3336. https://doi.org/10.1038/s41467-020-17149-w.
(6) Kretschy, N.; Sack, M.; Somoza, M. M. Sequence-Dependent Fluorescence of Cy3- and Cy5-Labeled Double-Stranded DNA. *Bioconjug. Chem.* **2016**, *27* (3), 840–848. https://doi.org/10.1021/acs.bioconjchem.6b00053.
(7) Bender, J. A.; Raulerson, E. K.; Li, X.; Goldzak, T.; Xia, P.; Van Voorhis, T.; Tang, M. L.; Roberts, S. T. Surface States Mediate Triplet Energy Transfer in Nanocrystal–Acene Composite Systems. *J. Am. Chem. Soc.* **2018**, *140* (24), 7543–7553. https://doi.org/10.1021/jacs.8b01966.
(8) Beane, G. A.; Morfa, A. J.; Funston, A. M.; Mulvaney, P. Defect-Mediated Energy Transfer between ZnO Nanocrystals and a Conjugated Dye. *J. Phys. Chem. C* **2012**, 120125142738004. https://doi.org/10.1021/jp209638g.
(9) Nilsson, Z. N.; Beck, L. M.; Sambur, J. B. Ensemble-Level Energy Transfer Measurements Can Reveal the Spatial Distribution of Defect Sites in Semiconductor Nanocrystals. *J. Chem. Phys.* **2021**, *154* (5), 054704. https://doi.org/10.1063/5.0034775.
(10) Jin, T.; Lian, T. Trap State Mediated Triplet Energy Transfer from CdSe Quantum Dots to Molecular Acceptors. *J. Chem. Phys.* **2020**, *153* (7), 074703. https://doi.org/10.1063/5.0022061.
(11) Chirmanov, V.; Stanish, P. C.; Layek, A.; Radovanovic, P. V. Distance-Dependent Energy Transfer between Ga2O3 Nanocrystal Defect States and Conjugated Organic Fluorophores in Hybrid White-Light-Emitting Nanophosphors. *J. Phys. Chem. C* **2015**, *119* (10), 5687–5696. https://doi.org/10.1021/jp512417h.
(12) Wang, D.; Xing, G.; Gao, M.; Yang, L.; Yang, J.; Wu, T. Defects-Mediated Energy Transfer in Red-Light-Emitting Eu-Doped ZnO Nanowire Arrays. *J. Phys. Chem. C* **2011**, *115* (46), 22729–22735. https://doi.org/10.1021/jp204572v.
(13) Ahmed, S. M.; Szymanski, P.; El-Nadi, L. M.; El-Sayed, M. A. Energy-Transfer Efficiency in Eu-Doped ZnO Thin Films: The Effects of Oxidative Annealing on the Dynamics and the Intermediate Defect States. *ACS Appl. Mater. Interfaces* **2014**, *6* (3), 1765–1772. https://doi.org/10.1021/am404662k.
(14) Lustig, D. R.; Nilsson, Z. N.; Mulvey, J. T.; Zang, W.; Pan, X.; Patterson, J. P.; Sambur, J. B. Toward Imaging Defect-Mediated Energy Transfer between Single Nanocrystal Donors and

Single Molecule Acceptors. *Chem. Biomed. Imaging* **2023**, *1* (2), 168–178. https://doi.org/10.1021/cbmi.3c00015.
(15) Bora, T.; Lakshman, K. K.; Sarkar, S.; Makhal, A.; Sardar, S.; Pal, S. K.; Dutta, J. Modulation of Defect-Mediated Energy Transfer from ZnO Nanoparticles for the Photocatalytic Degradation of Bilirubin. *Beilstein J. Nanotechnol.* **2013**, *4*, 714–725. https://doi.org/10.3762/bjnano.4.81.
(16) Van Der Meer, B. W.; Van Der Meer, D. M.; Vogel, S. S. Optimizing the Orientation Factor Kappa-Squared for More Accurate FRET Measurements. In *FRET – Förster Resonance Energy Transfer*; Medintz, I., Hildebrandt, N., Eds.; Wiley, 2013; pp 63–104. https://doi.org/10.1002/9783527656028.ch04.
(17) Muñoz-Losa, A.; Curutchet, C.; Krueger, B. P.; Hartsell, L. R.; Mennucci, B. Fretting about FRET: Failure of the Ideal Dipole Approximation. *Biophys. J.* **2009**, *96* (12), 4779–4788. https://doi.org/10.1016/j.bpj.2009.03.052.
(18) Khrenova, M.; Topol, I.; Collins, J.; Nemukhin, A. Estimating Orientation Factors in the FRET Theory of Fluorescent Proteins: The TagRFP-KFP Pair and Beyond. *Biophys. J.* **2015**, *108* (1), 126–132. https://doi.org/10.1016/j.bpj.2014.11.1859.
(19) Van Der Meer, B. W. Kappa-Squared: From Nuisance to New Sense. *Rev. Mol. Biotechnol.* **2002**, *82* (3), 181–196. https://doi.org/10.1016/S1389-0352(01)00037-X.
(20) Sasmal, D. K.; Pulido, L.; Kasal, S.; Huang, J. Single-Molecule Fluorescence Resonance Energy Transfer in Molecular Biology. *Nanoscale* **2016**, *8* (48), 19928–19944. https://doi.org/10.1039/c6nr06794h.
(21) Fujimoto, K. J.; Miyashita, T.; Dewa, T.; Yanai, T. Determination of FRET Orientation Factor between Artificial Fluorophore and Photosynthetic Light-Harvesting 2 Complex (LH2). *Sci. Rep.* **2022**, *12* (1), 15091. https://doi.org/10.1038/s41598-022-19375-2.
(22) Corry, B.; Jayatilaka, D.; Martinac, B.; Rigby, P. Determination of the Orientational Distribution and Orientation Factor for Transfer between Membrane-Bound Fluorophores Using a Confocal Microscope. *Biophys. J.* **2006**, *91* (3), 1032–1045. https://doi.org/10.1529/biophysj.106.080713.
(23) Erdem, O.; Gungor, K.; Guzelturk, B.; Tanriover, I.; Sak, M.; Olutas, M.; Dede, D.; Kelestemur, Y.; Demir, H. V. Orientation-Controlled Nonradiative Energy Transfer to Colloidal Nanoplatelets: Engineering Dipole Orientation Factor. *Nano Lett.* **2019**, *19* (7), 4297–4305. https://doi.org/10.1021/acs.nanolett.9b00681.
(24) Wallace, B.; Atzberger, P. J. Förster Resonance Energy Transfer: Role of Diffusion of Fluorophore Orientation and Separation in Observed Shifts of FRET Efficiency. *PLoS ONE* **2017**, *12* (5), e0177122. https://doi.org/10.1371/journal.pone.0177122.
(25) Dale, R. E.; Eisinger, J.; Blumberg, W. E. The Orientational Freedom of Molecular Probes. The Orientation Factor in Intramolecular Energy Transfer. *Biophys. J.* **1979**, *26* (2), 161–193. https://doi.org/10.1016/S0006-3495(79)85243-1.
(26) Saini, S.; Srinivas, G.; Bagchi, B. Distance and Orientation Dependence of Excitation Energy Transfer: From Molecular Systems to Metal Nanoparticles. *J. Phys. Chem. B* **2009**, *113* (7), 1817–1832. https://doi.org/10.1021/jp806536w.
(27) Scott, R.; Heckmann, J.; Prudnikau, A. V.; Antanovich, A.; Mikhailov, A.; Owschimikow, N.; Artemyev, M.; Climente, J. I.; Woggon, U.; Grosse, N. B.; Achtstein, A. W. Directed Emission of CdSe Nanoplatelets Originating from Strongly Anisotropic 2D Electronic Structure. *Nat. Nanotechnol.* **2017**, *12* (12), 1155–1160. https://doi.org/10.1038/nnano.2017.177.

(28) Zhou, X.; Mandal, S.; Jiang, S.; Lin, S.; Yang, J.; Liu, Y.; Whitten, D. G.; Woodbury, N. W.; Yan, H. Efficient Long-Range, Directional Energy Transfer through DNA-Templated Dye Aggregates. *J. Am. Chem. Soc.* **2019**, *141* (21), 8473–8481. https://doi.org/10.1021/jacs.9b01548.
(29) Ghimire, A.; Shafran, E.; Gerton, J. M. Using a Sharp Metal Tip to Control the Polarization and Direction of Emission from a Quantum Dot. *Sci. Rep.* **2014**, *4* (1), 6456. https://doi.org/10.1038/srep06456.
(30) Park, D. J.; Ku, J. C.; Sun, L.; Lethiec, C. M.; Stern, N. P.; Schatz, G. C.; Mirkin, C. A. Directional Emission from Dye-Functionalized Plasmonic DNA Superlattice Microcavities. *Proc. Natl. Acad. Sci.* **2017**, *114* (3), 457–461. https://doi.org/10.1073/pnas.1619802114.
(31) Takashima, H.; Maruya, H.; Ishihara, K.; Tashima, T.; Shimazaki, K.; Schell, A. W.; Tran, T. T.; Aharonovich, I.; Takeuchi, S. Determination of the Dipole Orientation of Single Defects in Hexagonal Boron Nitride. *ACS Photonics* **2020**, *7* (8), 2056–2063. https://doi.org/10.1021/acsphotonics.0c00405.
(32) A DFT Study of Electron-Phonon Interactions for the C 2 C N and V N N B Defects in Hexagonal Boron Nitride: Investigating the Role of the Transition Dipole Direction. https://doi.org/10.1088/1361-648X/acde2b.
(33) Jungwirth, N. R.; Chang, H.-S.; Jiang, M.; Fuchs, G. D. Polarization Spectroscopy of Defect-Based Single Photon Sources in ZnO. *ACS Nano* **2016**, *10* (1), 1210–1215. https://doi.org/10.1021/acsnano.5b06515.
(34) Doherty, M. W.; Michl, J.; Dolde, F.; Jakobi, I.; Neumann, P.; Manson, N. B.; Wrachtrup, J. Measuring the Defect Structure Orientation of a Single \bf N\bf V^- Centre in Diamond. *New J. Phys.* **2014**, *16* (6), 063067. https://doi.org/10.1088/1367-2630/16/6/063067.
(35) Wang, R.; Liu, Q.; Dai, S.; Liu, C.; Liu, Y.; Sun, Z.; Li, H.; Zhang, C.; Wang, H.; Xu, C.; Shao, W.; Meixner, A. J.; Zhang, D.; Li, Y.; Zhen, L. Defect Emission and Its Dipole Orientation in Layered Ternary Znln $_2$ S $_4$ Semiconductor. *Small* **2023**, 2305658. https://doi.org/10.1002/smll.202305658.
(36) Geng, Y.; Jena, D.; Fuchs, G. D.; Zipfel, W. R.; Rana, F. Optical Dipole Structure and Orientation of GaN Defect Single-Photon Emitters. *ACS Photonics* **2023**, *10* (10), 3723–3729. https://doi.org/10.1021/acsphotonics.3c00917.
(37) Zheng, K.; Žídek, K.; Abdellah, M.; Zhu, N.; Chábera, P.; Lenngren, N.; Chi, Q.; Pullerits, T. Directed Energy Transfer in Films of CdSe Quantum Dots: Beyond the Point Dipole Approximation. *J. Am. Chem. Soc.* **2014**, *136* (17), 6259–6268. https://doi.org/10.1021/ja411127w.
(38) Garnett, E. C.; Ehrler, B.; Polman, A.; Alarcon-Llado, E. Photonics for Photovoltaics: Advances and Opportunities. *ACS Photonics* **2021**, *8* (1), 61–70. https://doi.org/10.1021/acsphotonics.0c01045.
(39) Giménez, S.; Rogach, A. L.; Lutich, A. A.; Gross, D.; Poeschl, A.; Susha, A. S.; Mora-Seró, I.; Lana-Villarreal, T.; Bisquert, J. Energy Transfer versus Charge Separation in Hybrid Systems of Semiconductor Quantum Dots and Ru-Dyes as Potential Co-Sensitizers of TiO $_2$ -Based Solar Cells. *J. Appl. Phys.* **2011**, *110* (1), 014314. https://doi.org/10.1063/1.3605486.
(40) Lustig, D. R.; Buz, E.; Mulvey, J. T.; Patterson, J. P.; Kittilstved, K. R.; Sambur, J. B. Characterizing the Ligand Shell Morphology of PEG-Coated ZnO Nanocrystals Using FRET Spectroscopy. *J. Phys. Chem. B* **2023**, *127* (41), 8961–8973. https://doi.org/10.1021/acs.jpcb.3c04900.

(41) Chen, L.; Chen, X.; Yang, X.; He, C.; Wang, M.; Xi, P.; Gao, J. Advances of Super-Resolution Fluorescence Polarization Microscopy and Its Applications in Life Sciences. *Comput. Struct. Biotechnol. J.* **2020**, *18*, 2209–2216. https://doi.org/10.1016/j.csbj.2020.06.038.
(42) Zhanghao, K.; Chen, L.; Yang, X.-S.; Wang, M.-Y.; Jing, Z.-L.; Han, H.-B.; Zhang, M. Q.; Jin, D.; Gao, J.-T.; Xi, P. Super-Resolution Dipole Orientation Mapping via Polarization Demodulation. *Light Sci. Appl.* **2016**, *5* (10), e16166–e16166. https://doi.org/10.1038/lsa.2016.166.
(43) Bell, T. D. M.; Clayton, A. H. A. The Transition from Single Molecule to Ensemble Revealed by Fluorescence Polarization. *Sci. Rep.* **2015**, *5* (1), 8158. https://doi.org/10.1038/srep08158.
(44) Varela, J. A.; Rodrigues, M.; De, S.; Flagmeier, P.; Gandhi, S.; Dobson, C. M.; Klenerman, D.; Lee, S. F. Optical Structural Analysis of Individual α-Synuclein Oligomers. *Angew. Chem. Int. Ed.* **2018**, *57* (18), 4886–4890. https://doi.org/10.1002/anie.201710779.
(45) Forkey, J. N.; Quinlan, M. E.; Goldman, Y. E. Measurement of Single Macromolecule Orientation by Total Internal Reflection Fluorescence Polarization Microscopy. *Biophys. J.* **2005**, *89* (2), 1261–1271. https://doi.org/10.1529/biophysj.104.053470.
(46) Backlund, M. P.; Lew, M. D.; Backer, A. S.; Sahl, S. J.; Moerner, W. E. The Role of Molecular Dipole Orientation in Single-Molecule Fluorescence Microscopy and Implications for Super-Resolution Imaging. *ChemPhysChem* **2014**, *15* (4), 587–599. https://doi.org/10.1002/cphc.201300880.
(47) Kim, J.; Chacón, R.; Wang, Z.; Larquet, E.; Lahlil, K.; Leray, A.; Colas-des-Francs, G.; Kim, J.; Gacoin, T. Measuring 3D Orientation of Nanocrystals via Polarized Luminescence of Rare-Earth Dopants. *Nat. Commun.* **2021**, *12* (1), 1943. https://doi.org/10.1038/s41467-021-22158-4.
(48) Camacho, R.; Täuber, D.; Scheblykin, I. G. Fluorescence Anisotropy Reloaded—Emerging Polarization Microscopy Methods for Assessing Chromophores' Organization and Excitation Energy Transfer in Single Molecules, Particles, Films, and Beyond. *Adv. Mater.* **2019**, *31* (22), 1805671. https://doi.org/10.1002/adma.201805671.
(49) Piston, D. W.; Rizzo, M. A. FRET by Fluorescence Polarization Microscopy. In *Methods in Cell Biology*; Elsevier, 2008; Vol. 85, pp 415–430. https://doi.org/10.1016/S0091-679X(08)85018-2.
(50) Ha, T.; Laurence, T. A.; Chemla, D. S.; Weiss, S. Polarization Spectroscopy of Single Fluorescent Molecules. *J. Phys. Chem. B* **1999**, *103* (33), 6839–6850. https://doi.org/10.1021/jp990948j.
(51) Hooley, E. N.; Carro-Temboury, M. R.; Vosch, T. Probing the Absorption and Emission Transition Dipole Moment of DNA Stabilized Silver Nanoclusters. *J. Phys. Chem. A* **2017**, *121* (5), 963–968. https://doi.org/10.1021/acs.jpca.6b11639.
(52) Chung, I.; Shimizu, K. T.; Bawendi, M. G. Room Temperature Measurements of the 3D Orientation of Single CdSe Quantum Dots Using Polarization Microscopy. *Proc. Natl. Acad. Sci.* **2003**, *100* (2), 405–408. https://doi.org/10.1073/pnas.0133507100.
(53) Jurow, M. J.; Morgenstern, T.; Eisler, C.; Kang, J.; Penzo, E.; Do, M.; Engelmayer, M.; Osowiecki, W. T.; Bekenstein, Y.; Tassone, C.; Wang, L.-W.; Alivisatos, A. P.; Brütting, W.; Liu, Y. Manipulating the Transition Dipole Moment of $CsPbBr_3$ Perovskite Nanocrystals for Superior Optical Properties. *Nano Lett.* **2019**, *19* (4), 2489–2496. https://doi.org/10.1021/acs.nanolett.9b00122.

(54) Lethiec, C.; Laverdant, J.; Vallon, H.; Javaux, C.; Dubertret, B.; Frigerio, J.-M.; Schwob, C.; Coolen, L.; Maître, A. Measurement of Three-Dimensional Dipole Orientation of a Single Fluorescent Nanoemitter by Emission Polarization Analysis. *Phys. Rev. X* **2014**, *4* (2), 021037. https://doi.org/10.1103/PhysRevX.4.021037.
(55) Chang, W.-S.; Ha, J. W.; Slaughter, L. S.; Link, S. Plasmonic Nanorod Absorbers as Orientation Sensors. *Proc. Natl. Acad. Sci.* **2010**, *107* (7), 2781–2786. https://doi.org/10.1073/pnas.0910127107.
(56) Hu, D.; Yu, J.; Wong, K.; Bagchi, B.; Rossky, P. J.; Barbara, P. F. Collapse of Stiff Conjugated Polymers with Chemical Defects into Ordered, Cylindrical Conformations. *Nature* **2000**, *405* (6790), 1030–1033. https://doi.org/10.1038/35016520.
(57) Ansbacher, T.; Srivastava, H. K.; Stein, T.; Baer, R.; Merkx, M.; Shurki, A. Calculation of Transition Dipole Moment in Fluorescent Proteins—towards Efficient Energy Transfer. *Phys. Chem. Chem. Phys.* **2012**, *14* (12), 4109. https://doi.org/10.1039/c2cp23351g.
(58) Loura, L. Simple Estimation of Förster Resonance Energy Transfer (FRET) Orientation Factor Distribution in Membranes. *Int. J. Mol. Sci.* **2012**, *13* (12), 15252–15270. https://doi.org/10.3390/ijms131115252.
(59) Debnath, D.; Sen, D.; Neog, T. T.; Saha, B.; Ghosh, S. K. Growth of ZnO Polytypes: Multiple Facets of Diverse Applications. *Cryst. Growth Des.* **2024**, acs.cgd.3c01076. https://doi.org/10.1021/acs.cgd.3c01076.
(60) Debroye, E.; Van Loon, J.; Yuan, H.; Janssen, K. P. F.; Lou, Z.; Kim, S.; Majima, T.; Roeffaers, M. B. J. Facet-Dependent Photoreduction on Single ZnO Crystals. *J. Phys. Chem. Lett.* **2017**, *8* (2), 340–346. https://doi.org/10.1021/acs.jpclett.6b02577.
(61) Marcato, T.; Krumeich, F.; Shih, C.-J. Confinement-Tunable Transition Dipole Moment Orientation in Perovskite Nanoplatelet Solids and Binary Blends. *ACS Nano* **2022**, *16* (11), 18459–18471. https://doi.org/10.1021/acsnano.2c06600.
(62) Gao, Y.; Weidman, M. C.; Tisdale, W. A. CdSe Nanoplatelet Films with Controlled Orientation of Their Transition Dipole Moment. *Nano Lett.* **2017**, *17* (6), 3837–3843. https://doi.org/10.1021/acs.nanolett.7b01237.
(63) Kumar, S.; Marcato, T.; Krumeich, F.; Li, Y.-T.; Chiu, Y.-C.; Shih, C.-J. Anisotropic Nanocrystal Superlattices Overcoming Intrinsic Light Outcoupling Efficiency Limit in Perovskite Quantum Dot Light-Emitting Diodes. *Nat. Commun.* **2022**, *13* (1), 2106. https://doi.org/10.1038/s41467-022-29812-5.
(64) Bai, P.; Hu, A.; Liu, Y.; Jin, Y.; Gao, Y. Printing and *In Situ* Assembly of CdSe/CdS Nanoplatelets as Uniform Films with Unity In-Plane Transition Dipole Moment. *J. Phys. Chem. Lett.* **2020**, *11* (11), 4524–4529. https://doi.org/10.1021/acs.jpclett.0c00748.

CHAPTER 6: MODELS AND MEASUREMENTS QUANTIFY PHOTON RECYCLING, CHARGE CARRIER DIFFUSION, AND PHOTON SCATTERING CONTRIBUTIONS TO PHOTOLUMINESCENCE IN InP NANOWIRE ARRAYS[5]

6.1 Overview

Nanowire arrays present many unique advantages for solar-to-chemical energy conversion. One possible advantage is photon recycling between neighboring nanowires has the potential to increase solar energy conversion efficiencies. Here we explore three underlying mechanisms of optical and electronic coupling between neighboring nanowires— incident photon scattering, photon recycling, and charge-carrier transport from the photo-excited nanowire to the neighboring nanowire via the underlying substrate— using single nanowire-level microscopy and spectroscopy measurements. We present a comprehensive analysis of light absorption and emission of a single nanowire at open circuit, and subsequent re-absorption and re-emission by a neighboring nanowire. We developed a novel correlated single nanowire microspectroscopy and widefield imaging methodology to spatially resolve photon communication pathways between neighboring nanowires and selectively image re-emitted and reflected photons. Unique multiphysics models have been developed to couple wave optics and semiconductor photophysics to especially isolate contributions from photon recycling and electronic transport to photon emission from neighboring nanowires. By systematically varying the morphologies of the nanowires modeled, we identified

[5]Reproduced with permissions from Lustig, D., Chen, F., Zhang, W., Bird, O., J., Fajardo Jr. Ardo, S., Talin, A., Dukovic, G., Hu, S., Bala Chandran, R., and Sambur, J., Models and Single Nanowire Measurements Quantify Photon Scattering, Recycling, and Diffusion in InP Nanowire Arrays. Journal of Physical Chemistry, C: 2025, *129* (17), 8270–8283. Copyright 2025, American Chemical Society.

pathways to maximize photon recycling between neighboring nanowires. We conclude that the measured photoluminescence is more strongly influenced by the diffusion of charge carriers as compared to photon recycling in materials with moderate-to-large charge-carrier mobilities (> 10 $cm^2\ V^{-1}\ s^{-1}$), and that photon recycling dictates photoluminescence intensity only when the charge-carrier mobility is low (< 1 $cm^2\ V^{-1}\ s^{-1}$). The experimental and simulation platforms developed herein for photon management strategies can be leveraged by the semiconductor photocatalysis community to enhance solar-to-chemical conversion efficiencies in semiconductor nanowire arrays.

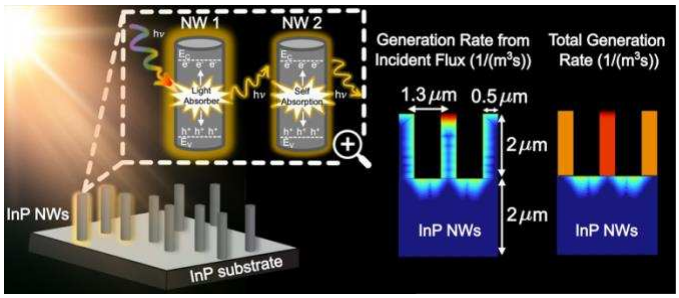

Figure 6.1. Chapter 5 overview: cartoon illustration of photon recycling in an InP NW array under illumination and COMSOL simulations predicting generation rate and total carrier generation rate.

6.2 Introduction

Photon recycling in light-absorbing materials is an iterative process of multiple re-absorption and re-emission events of photons emitted within the excited material due to radiative recombination.[1–5] In the solar energy conversion community, this photon recycling effect is a promising strategy to enhance energy conversion efficiency by increasing the fraction of incident photons that are used to perform useful work. Photon recycling has been previously reported to enhance the photoluminescence (PL) of perovskite films[4,6–19] and to improve the voltage characteristics of photovoltaics (PVs).[2,4,6,7,9,11,20,21] Additionally, recent simulations based on idealized photodiode models have shown that photon recycling can significantly enhance the

efficiency of solar fuels generation, especially when considering a stacked array of optically thin planar slabs.[22,23]

However, there is limited mechanistic understanding of the combined influences of photon recycling, incident light scattering, and re-emission following spatial diffusion of charge-carriers in nanostructured semiconductor materials for photoelectrochemical solar energy conversion applications. In particular, semiconductor nanowire (NW) arrays are promising photoelectrode architectures for solar fuels production because their long lengths maximize light absorption and their thin widths minimize carrier transport distances to the solid-liquid interface.[24–30] However, their feature sizes are comparable to wavelengths, which requires a rigorous method for treating light as an electromagnetic wave in order to understand photon recycling effects in these systems.[6] Here we chose to study III-V indium phosphide (InP) NW arrays because III-V semiconductor-based devices achieve >19% solar-to-hydrogen (STH) efficiency[31], their optical and electronic properties are tunable via composition and morphology modifications,[32] and the fixed 2D system allows us to image in real space light re-absorption and re-emission between NWs, which would otherwise be difficult in freely diffusing colloidal nanoparticle samples. Specifically, our objective is to: (a) quantify how much photon recycling contributes to radiative emission enhancement in NW arrays, and (b) project its effects on photocatalytic/photoelectrochemical performance.

In previous modeling efforts, the complexity of analytically solving carrier dynamics in nanostructures has led to significant work on PL emission modeling in NWs using Poisson's equation, drift-diffusion equations, and charge conservation principles.[33–35] Those models enable flexible tuning of various geometric and material properties, including carrier mobility, radiative recombination factor, and surface recombination velocity. Modeling of photon recycling, coupled with carrier dynamics, has been widely applied in photovoltaic devices, primarily relying on ray-

optical approximations.[36,37] Photon recycling treatments beyond the ray-optical approach are generally limited to optical estimates of open-circuit voltage enhancement using detailed-balance approaches[11,38] or rigorous solutions of Maxwell's equations within the dipole picture.[6,13,39] Additionally, most rigorous photon recycling models focus on morphologies like thin films[3,40] or individual NWs,[41–43] with few studies exploring multiple NWs and NW arrays. From the experimental measurement standpoint, ensemble-level PL measurements are typically used to characterize photon recycling in nanostructured systems.[44,45] However, ensemble-level measurements of semiconductor nanomaterial samples report on the average behavior of a heterogenous material system differing in nanomaterial size, shape, composition, and surface chemistry. Experiments that spatially resolve the photon recycling process between adjacent nanostructures are critical to understand how heterogeneous materials chemistry impacts the photon recycling process between two entities in the sample batch. Hence, there is a critical need to develop single particle-level experimental approaches that avoid ensemble-level average effects and compliment those results with a comprehensive model that combines wave-optics calculations with carrier dynamics to evaluate the impact of photon recycling on the energy conversion efficiency of NW-based photocatalytic systems.

Scheme 6.1 illustrates the fundamental optical processes in a semiconductor NW array system following initial photoexcitation at open circuit: charge carrier generation, charge carrier recombination, photon scattering from NW surfaces, and photon emission, with a focus on the interplay between light absorption and scattering. In Case 1, radiative recombination occurs without photon-mediated inter-NW communication. An initial above-bandgap photon excites a NW (gray circle in Scheme 6.1). Subsequently, a photogenerated electron-hole pair can recombine either radiatively to emit a photon or non-radiatively. We assume the dominant decay pathway for

charge-carriers in these materials is radiative recombination (yellow arrow in Scheme 6.1), as will be discussed below. Case 2 is an extension of Case 1, where an emitted photon is sequentially re-absorbed and re-emitted by neighboring NWs via a process termed photon recycling. Case 3 incorporates photon scattering from the central NW instead of initial photon absorption by the central NW, resulting in additional pathways for photons to travel within the NW array as an alternative process for photon-mediated inter-NW communication. In this work, we deconvolute the photophysical processes as shown in Scheme 6.1 by measuring, in a spatially resolved way, photons emitted from the NW array via PL versus photon scattering from NW surfaces. Our modeling efforts aim to predict the impact of NW morphology on key parameters such as absorption, light trapping, and photon recycling probabilities as highlighted in Scheme 6.1. This comprehensive approach allows us to identify the most promising design strategies for NW-based PEC systems with enhanced hydrogen production capabilities.

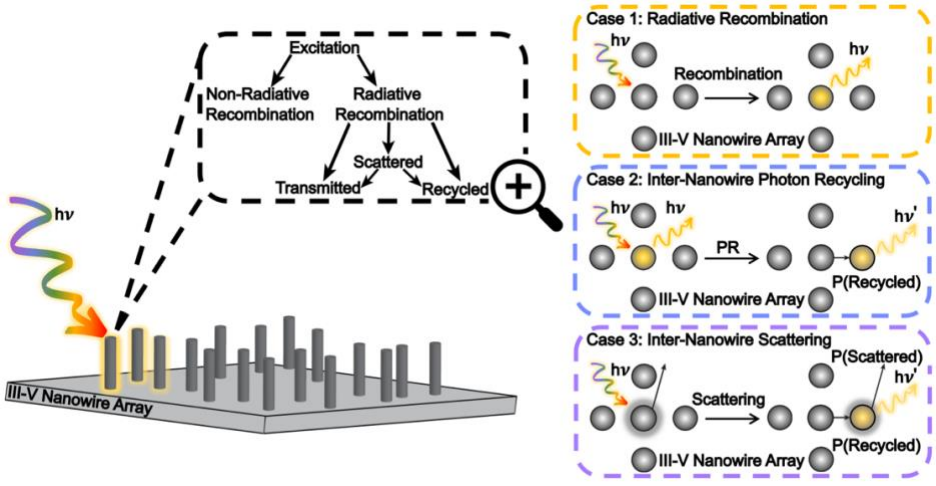

Scheme 6.1. Photophysical processes occurring in an ensemble of high-quality III-V NW arrays after initial excitation of the sample. Case 1, 2, and 3 represent experimentally observable scenarios via widefield imaging. In Case 1, a central NW absorbs a photon and undergoes radiative recombination. In widefield imaging experiments, the emitted photon results in PL signal. In Case 2, the central NW absorbs a photon and undergoes radiative emission. A neighboring NW absorbs the emitted photon from the central NW. Finally, the neighboring NW undergoes radiative emission. In Case 3, photon scattering occurs on the central NW surface. The neighboring NW absorbs the scattered photon and then undergoes radiative recombination. The key distinction between Case 2 and Case 3 is that PL from the central NW excites the neighboring NW in Case 2 whereas the incident illumination source excites the neighboring NW in Case 3.

In addition to photon recycling, carrier diffusion plays a pivotal role in governing energy transport within NW arrays.[16,46] Deconvoluting the contributions of charge-carrier diffusion and photon recycling remains challenging and has led to contradictory findings regarding the dominant energy transport mechanism in perovskite systems.[42,46–50] Resolving this ambiguity is essential to guide further optimization of materials and device designs. Therefore, a quantitative study on the carrier mobility comparing with the spatial PL signal will help us obtain a deep understanding of the deconvolution of different transport mechanisms.

Here, we use optical simulations and develop novel single NW-level widefield imaging experiments to quantify photon recycling and scattering between adjacent NWs in a NW array. Photon absorption, scattering, and recombination events are modeled to complement and improve interpretation of experimental data. The use of two modeling and simulation approaches is powerful. Monte Carlo (MC) rapidly captures discrete effects resulting from a photon's particle-like properties, while more computationally expensive finite element analysis captures additional effects resulting from a photon's wave-like properties. These models are necessary to deconvolute the contributions in the measured, spatially-resolved PL spectra due to: (i) photon recycling events – i.e., repetitive re-absorption and emission of photons; (ii) charge-carrier transport via diffusion and migration, and (iii) recombination of charge-carriers that were originally generated due to absorption of the scattered incident light. To this end, we develop and compare the performance and efficacy of two distinct modeling methods – a multiphysics model that couples wave optics and semiconductor photophysics and the other being a statistical, MC ray tracing simulations (we provide the community with the code used to carry out the calculations). The former approach provides rigorous capabilities to especially simulate nanoscale features especially when the characteristic length scale becomes comparable to wavelength, and can incorporate more attributes

of the samples tested, including the influences of the substrate and charge-carrier transport. The latter is computationally tractable and excels in providing fast predictions based on simplifying assumptions. The simulations provide key insights into why the PL and reflection ratios from the neighboring NW relative to the central photo-excited NW scale with inter-NW distance, diameter, and height. This study demonstrates that photon recycling can be utilized in NW array photoelectrodes to enhance net carrier generation rates, which holds promise for boosting solar energy conversion efficiency.

6.3 Experimental & Theoretical Methods

6.3.1 Sample preparation

Gallium nitride (GaN)-coated InP NW arrays were synthesized via a reactive ion etching process on patterned single crystal n-InP substrates (AXT, Inc., S doped, carrier concentration 2-6 $\times 10^{16}/cm^3$, crystal orientation (100 ± 0.5°). Figure D1 summarizes the NW array synthesis workflow, and Appendix D Section D1 contains detailed surface cleaning, sample preparation and handling, as well as characterization procedures. Briefly, a negative electron beam resist (DisChem HSi-Q) was spin-coated onto a pre-treated n-InP wafer. Next, NW array patterns were transferred onto the wafer using a Raith EBPG 5200+ electron beam lithography system. The pattern is then etched into the InP substrate via a chlorine-based Reactive Ion Etching (RIE) process[51] by Oxford PlasmaPro 100 Cobra ICP-RIE system. InP surfaces form a surface oxide layer under ambient conditions. In-O and P-O bonds introduce defect states in the electronic structure of InP and serve as surface recombination sites for photo-generated electron-hole pairs. A 5-nm thick atomic layer deposition (ALD)-grown GaN layer effectively coats the entire InP surface and minimizes surface oxide layer formation.[52] An 8-nm thick GaN passivation layer was deposited onto the NW array

pattern by using a Ultratech Fiji G2 ALD system using trimethylgallium (TMGa, Strem Chemicals, 99.9999%-Ga) and nitrogen plasma as the Ga and N sources, respectively.

6.3.2 Electron Microscopy and Raman/PL Spectroscopy Characterization

Correlated ex situ scanning electron microscopy (SEM) experiments were performed after optical microspectroscopy experiments. SEM images were collected on a JEOL JSM-6500 Field emission scanning electron microscope (FE-SEM) at an accelerating voltage of 15 keV and a working distance of 10 mm. Figure D2 shows representative SEM images of all the samples used in this study, taken on a Hitachi FE-SEM (SU8230) at an accelerating voltage of 10 keV. Raman and PL spectroscopic measurements were performed using an optical fiber-coupled Raman/PL microscope system coupled with a spectrometer (Horiba, iHR550) on an Olympus IX73 inverted optical microscope. Raman and PL signals were collected in a backscatter geometry by passing the photons through a spectrometer (1200 gr/mm) to a Synapse back-illuminated deep depletion charge-coupled device (CCD) detector. For Raman microspectroscopy measurements as shown in Figure D3a, a 20× air objective (Olympus UPlanFL N20×) focused a 40 mW 532 nm laser source (Horiba, Ondax THz) onto a 3.8 μm-diameter spot of the sample. The system was calibrated using the Stokes and anti-Stokes shift of a Si wafer, occurring at 521 and –521 cm^{-1}, respectively. For PL microspectroscopy measurements as shown in Figure D3b, a 100× air objective (Olympus PlanFL N100×) focused the same 40 mW 532 nm laser source onto a 1.2 μm-diameter spot of the sample.

6.3.3 Reflectance and Absorptance Characterization

Reflectance measurements were taken using a PerkinElmer Lambda 1050+ Spectrometer with a 150mm Integrating Sphere. A post-mountable standard iris (Thorlabs IDA20) and an EFL of 150.0 mm S-LAH64 Aspheric lenses were used to focus the incident light onto a 2 mm spot of

the sample shown in Figure D2b. The diffuse and total reflectivity measurements are shown in Figure D4. Absorptance data was calculated from the total reflectance using the assumption that there is no transmittance through the InP sample.

6.3.4 Spatially and Temporally Correlated PL Microspectroscopy and Widefield PL Imaging

The NW array samples were mounted on the motorized XY stage (Märzhäuser-Wetzlar TANGO) of an Olympus IX73 inverted optical microscope. A 0.3 mW, 415 nm laser (Oxxius, LBX-415–120-CSB-PPA) was directed through the back port of the microscope, reflected by a 414 nm dichroic mirror (Edmund Optics, 86330) in the filter cube, and aligned on the back aperture of a 100× objective, yielding a 0.49 μm-diameter laser spot, corresponding to a laser power density of 159 kW/cm^2. In a typical experiment, we raster the 415 nm laser across the NW array sample in 0.5 μm steps and collect data for 1 s at each pixel. The emission signal from the sample, which includes reflected light at the same wavelength as the incident laser and PL emission centered at 900 nm, was collected in a backscatter geometry via the microscope objective. A 50/50 beam splitter positioned below the objective directed half the emission signal to a spectrometer and the other half to a Hamamatsu Gemini W-view image splitter attached to a scientific complementary metal-oxide semiconductor (sCMOS, Teledyne Prime 95B) camera with 1200 × 1200 pixels. The image splitter produces two 1200 × 600 pixel images; the "PL image" is produced by passing photons through a 900/50 bandpass filter (corresponding to the peak emission from InP NWs) and the "reflection image" is produced using only a neutral density filter (Thor Labs, NE20B). Note, the number of reflected photons from the sample exceeds the PL photons by several orders of magnitude. Widefield PL and reflection images were continuously acquired at a 50 ms exposure time while the spectral data was acquired for a total time of 1 s. A data acquisition card (DATAQ DI-4108) synchronized each widefield image acquisition with the corresponding PL spectrum and

stage position. Appendix D Sections D3 (Figure D5-D11) and D4 (Figure D12 -D13) describe the detailed data processing and image analysis procedures, including the optical-to-SEM overlay procedure that quantitatively overlays optical imaging coordinates onto SEM Images. Widefield imaging control experiments are described in Appendix D Section D5 (Figure D14).

6.3.5 Geometric Predictions of Re-absorption Probability

To calculate the geometric probability of photon recycling, we first consider that a photon must be emitted from the first wire at a solid angle which will intersect the second wire. Appendix D Section D6 (Figure D15-D16) provides complete details and equations for the re-absorption probability calculations. Briefly, this approximation treats photons as infinitely small particles which travel in straight lines. Additionally, the intent is to provide a geometric upper limit on photon recycling and thus it is assumed that the PLQY = 100% and that all photons which "impact" a wire will be absorbed.

6.3.6 MC simulations

A MC simulation was developed to investigate photon recycling and reflection in the NW array.[52] Appendix D Section D7 (Figure D17-D18) provides complete simulation details. Briefly, the simulation model consisted of two identical NWs. One NW is subjected to continuous excitation and the other NW only receives light via PL or reflection from the first wire. The probability of photon re-absorption by PL or reflected photons was calculated using the geometric predictions described above, but also accounting for the reflectivity of the sample, Beer's law absorption, and PL quantum yield (PLQY). This model was focused on photon communication between wires and thus did not model the bulk substrate.

6.3.7 Continuum-Level Modeling Domain and Assumptions

Finite-element continuum-level modeling was performed in COMSOL Multiphysics. A stationary, two-dimensional (2D), continuum model was developed to simulate absorption of incident photons, re-absorption of emitted photons, and charge-carrier generation, recombination and transport in InP NWs. Figure 6.2 shows the modeling domain with three NWs, where the photon flux from the laser source is incident on the central NW. This is a reasonable choice as compared to modeling a periodic structure, because: (a) the experimentally fabricated samples have a random distribution of the NWs, and the (b) predictions for photon recycling probabilities with one neighboring NW on either side of the illuminated wire are not that different from the cases that considered two neighbors on either side. We find that the impact from the second neighboring wire is not big, and the ratio of the re-absorption probability between the second neighboring wire and the first neighboring wire is below 0.1 in most cases, as long as the nearest neighbor distance is larger than 0.7 μm, and the diameter is larger than 0.5 μm (Figure D15). While the fabricated samples have a 500 μm thick substrate, the model considers the substrate thickness to be 50 μm thick. This is done to speed-up the simulation time without impacting the results (Figure D16 shows less than 0.2% deviation in predictions for the re-absorption probability and the recombination rate in the neighboring wire). The baseline geometric parameters for the NW array are selected in Table 5.1 based on the experimentally fabricated samples with a diameter, D = 0.5 μm, height, h = 2 μm, and an average nearest neighbor distance, i.e., center-center distance, $d = 1.3$ μm between the wires varying in the range of 0.55 μm to 3.2 μm based on the distance distribution of the pseudo-random NW sample. The diameter and the height of the NWs were varied over a wide range to study the influences of the NW morphology on the overall absorptance, and additionally the influences of the different underlying mechanisms on photon recycling. The

lower and upper limits for the diameter (0.05 – 1.4 μm) and the height (0.4 – 2 μm) were selected so that these ranges are enough to predict the morphological effect on the optical process and indicate optimal NW structure for efficient hydrogen production.

This multiphysics model simultaneously solves for the electromagnetic field due to both the incident photon flux and the emitted photons due to recombination, the charge-carrier (electron and hole) concentrations, and the electrostatic potential in the semiconductor. Specific assumptions, governing equations and boundary conditions corresponding to each of these variables are discussed in Appendix D Section D8. All these transport equations are numerically discretized using finite element techniques and solved in COMSOL Multiphysics 6.1 by modifying inputs and adapting functionalities of two existing modules – (1) Electromagnetic Waves, Frequency Domain and (2) Semiconductor.

We opted for 2D modeling instead of 3D simulations primarily due to computational tractability, given the extensive parametric nature of this study. Our analysis involved over 34 simulation cases to examine the effects of carrier mobilities, geometric parameters, surface recombination velocity, and other factors. Performing all these simulations in 3D would be computationally prohibitive. Importantly, the key focus of our work is to analyze trends and 2D modeling offers sufficient accuracy for this purpose. To address concerns about potential discrepancies between 2D and 3D approximations, we performed simulations for a specific case using a 3D model and compared those results to the 2D model. The 3D results in Figure D19 show that the predicted PL ratio deviated by only 10% from the corresponding 2D results, confirming the validity of our approach. For the sake of simplicity, spatial-dependent mobility and different doping profiles are not taken into account. Our interpretations are limited by considering mobilities to be homogeneous throughout the sample, which may not be the case in nanostructured samples.

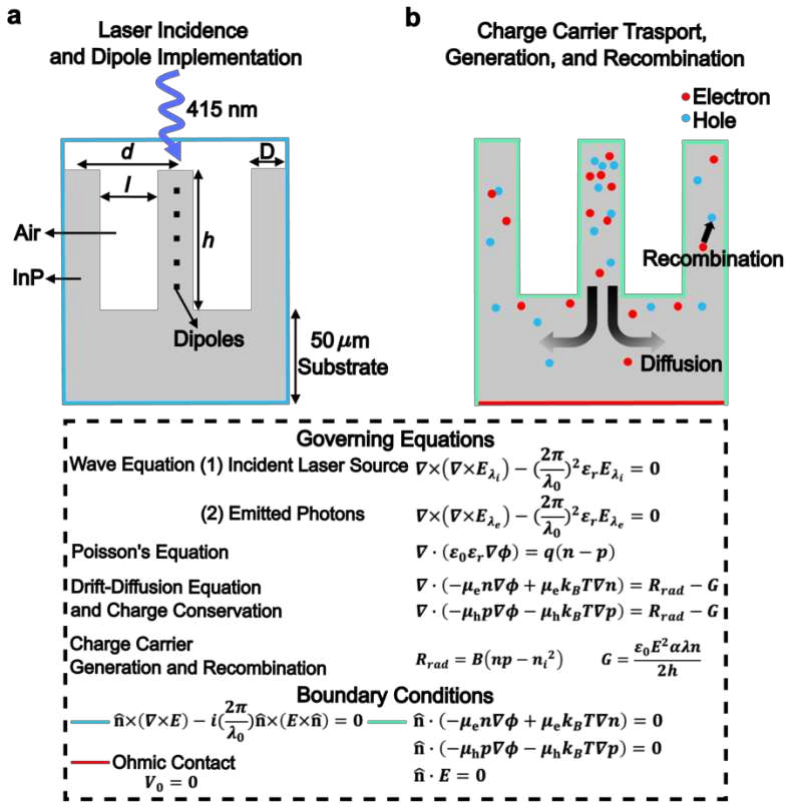

Figure 6.2. Schematic of the modeling domain with three InP NWs emerging from an InP substrate. The model considers: (a) a 415 nm laser illuminating a central NW, inducing an incident electromagnetic field. Dipoles are displayed vertically to characterize photon re-emission and re-absorption at 900 nm. The re-emitted photons can be absorbed in the NWs, the substrate, or escape from the nanostructure. (b) semiconductor physics includes charge conservation through the Poisson's equation, and the drift-diffusion equation for carrier transport, generation and recombination.

Table 6.1 Baseline values and ranges of parameters for the modeling parameters, including material properties and morphology.

Parameters, *Symbol* (Units)	**Baseline case**	**Range**
Absorption coefficient, α (m^{-1})	2.8×10^{6}	2.8×10^{6}, 8.4×10^{6}, 14×10^{6}
Electron mobility, μ_e ($cm^2/(Vs)$)	3	10^{-4}-5400
Hole mobility, μ_h ($cm^2/(Vs)$)	0.3	10^{-4}-200
Radiative recombination rate, B (cm^3/s)	1.2×10^{-10}	0.6×10^{-10}, 1×10^{-10}, 1.4×10^{-10}, 2×10^{-10}
Surface recombination velocity, v_s (cm/s)	0	0, 10^2, 10^3, 10^4, 10^5, 10^6
Nearest neighbor distance, d (μm)	1.3	0.55-3.2
Diameter, D (μm)	0.5	0.05-1.4
Height, h (μm)	2	0.4-2

6.4 Results and Discussion

Optical simulations predict spatial profiles of charge-carrier generation and recombination rates, and their concentrations, by simultaneously solving the governing transport equations Eq.

D6, D18, D22, D25-27. At any spatial location, the recombination rate, which is related to the measured PL, is dictated by the excess concentration of charge-carriers (electrons and holes) relative to their intrinsic concentration. These local charge-carrier concentrations are influenced by many factors including the generation of charge-carriers due to: (a) absorption of the incident photon flux, and (b) re-absorption of the radiatively emitted photons from neighboring NWs, i.e., photon recycling, and (c) transport of charge-carriers via diffusion and migration from one location to another. In the absence of an electric field, migration effects are not significant in this study.

Because multiple factors contribute to the spatially resolved PL measurements, our model predictions help to deconvolute these effects. Figure 6.3 shows the spatial profiles of the predicted charge-carrier generation and recombination rates, and their concentrations, for 0.5 μm-wide and 2 μm-tall NWs separated by 0.7 μm (Figure 6.3a – d) and 1.3 μm (Figure 6.3e – h), respectively. More than 90% of the incident light is absorbed within 60 nm from the top surface of the central NW, consistent with the modeled absorption coefficient of 3.8×10^{7} m^{-1} for InP at 415 nm. Therefore, the generation rate from the incident photon flux predominantly occurs within the central NW (Figure 6.3a,e), and there is very little generation of charge-carriers in the neighboring wires due to scattering of the incident light. Changing to a longer incident wavelength will produce a more homogenous carrier generation profile, further impacting the recombination profile. Thus, the modeling results are specific to the incident wavelength of the light source. In contrast, the total generation rate (Figure 6.3b,f) that includes both the re-absorption of incident and the radiatively emitted photons occurs both in the central and the neighboring NWs. Notably, the total generation rate, recombination rate (Figure 6.3c,g) and the charge-carrier concentrations (Figure 6.3d,h) are all more spatially evenly distributed than the exponential decay in the generation rate along the height of the NW from the incident flux alone. For the baseline morphology and modeled

parameters in Table 6.1, photon recycling and charge-carrier diffusion contributes to the majority (>99%) of the recombination rate in the neighboring wire, and 30% in the central wire. With all else being the same, increasing the spacing between the neighboring NWs from 0.7 μm to 1.3 μm led to around an 11% reduction respectively in the generation rates and the recombination rates. However, there is a slightly larger amount of generation within the substrate due to increased scattering of the incident light.

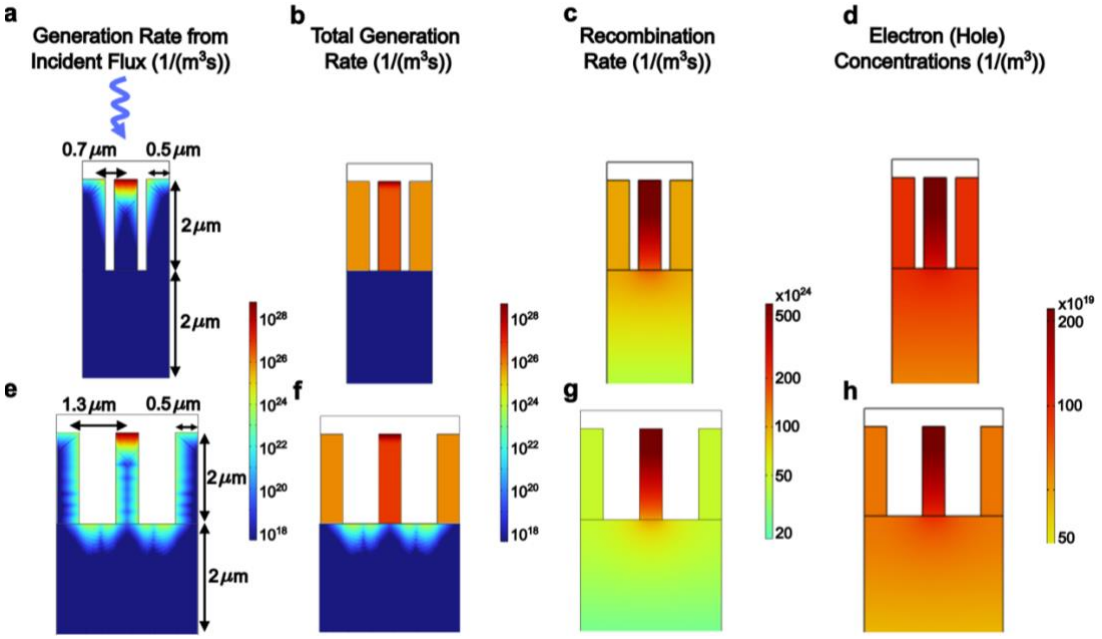

Figure 6.3. 2D profiles predicted for 0.5 μm-wide and 2 μm-tall NWs separated by (a-d) 0.7 μm and (e-h) 1.3 μm for the (a) volumetric charge-carrier generation rate (m^{-3} s^{-1}) from the incident photon flux, (b) volumetric total generation rate (m^{-3} s^{-1}) due to both the incident photon flux and the re-absorption of radiatively emitted photons, (c) total recombination rate (m^{-3} s^{-1}) and (d) electron concentrations (m^{-3}). Table 6.1 provides the baseline values for pertinent material parameters used in COMSOL simulations including charge-carrier mobilities of 3 cm^2/Vs for electrons and 0.3 cm^2/Vs for holes. Even though the modeled substrate modeled is 50 μm in height, we only depict a 2 μm portion to reveal spatial profiles within the NWs more clearly.

To explicitly determine contributions to the emission in the neighboring NW, we ran simulations in Figure 6.4 for a fixed NW morphology with baseline parameters (diameter = 0.5 μm, height = 2 μm, nearest neighbor distance = 1.3 μm), and as a function of charge-carrier mobilities ranging from 10^{-4} – 10^{2} cm^2 V^{-1} s^{-1}. Additionally, for each of these mobility values, we performed calculations with and without photon recycling in the model. These results provide

critical insights on how the relative contributions from photon recycling, charge-carrier diffusion and the incident flux drastically change with charge-carrier mobility.

For mobility values as small as 10^{-4} cm^2 V^{-1} s^{-1} it is reasonable to expect that charge-carrier diffusion contribution to radiative recombination (emission) in the neighboring wires will be very small. Therefore, the results for emission obtained with a small mobility value (10^{-4} cm^2 V^{-1} s^{-1}), and without photon recycling isolates contributions to emission from the incident and the scattered photon flux. And at a fixed mobility, contributions to emission from photon recycling can be obtained by comparing results with and without photon recycling. The remaining contribution is due to spatial diffusion of charge-carriers. For simplicity, in the calculations resulting in Figure 6.4 and Figure D20, we assumed equal mobilities for both electrons and holes as a simplification and to make comparisons more streamlined across different cases.

Figure 6.4 shows that while photon recycling is the dominant mechanism contributing to emission in the neighboring NW when the mobility values are smaller than 10^{-1} cm^2 V^{-1} s^{-1}, it quickly gets overshadowed by diffusion (>9 when charge-carrier mobility becomes larger than 10 cm^2 V^{-1} s^{-1}. For context, InP as a bulk material has reported hole mobilities of ~200 cm^2 V^{-1} s^{-1} [12], and our electron beam induced current measurements (Supporting Information Section D9) point towards NW sample hole mobilities in the range of 35 – 55 cm^2 V^{-1} s^{-1}.[53] Based on these bulk and the measured mobility values for InP, we expect the contribution from diffusion to far exceed photon recycling. Counterintuitively, the fractional contribution from the incident and scattered photon flux appears to increase with mobility. This is because more of charge-carriers generated within the central NW are re-absorbed and emitted from the substrate as compared to the neighboring NW (Figure D20), which then reduces the total rate of recombination in the neighboring NW, which lowers the denominator in the fractional emission contribution

calculations. Figure D20 also reveals how the fractional contribution from photon recycling to emission in the illuminated central NW decreases 10-fold when mobility increases from 10^{-4} to 100 $cm^2\ V^{-1}\ s^{-1}$. Overall, these results show that charge-carrier diffusion can be a central and a dominating cause of emission in the neighboring NW, in addition to photon recycling, subject to the charge-carrier mobility values of the actual sample. Therefore, we perform extensive testing on the influences of mobility over a wide range (Table 6.1) to especially draw comparisons against measurements.

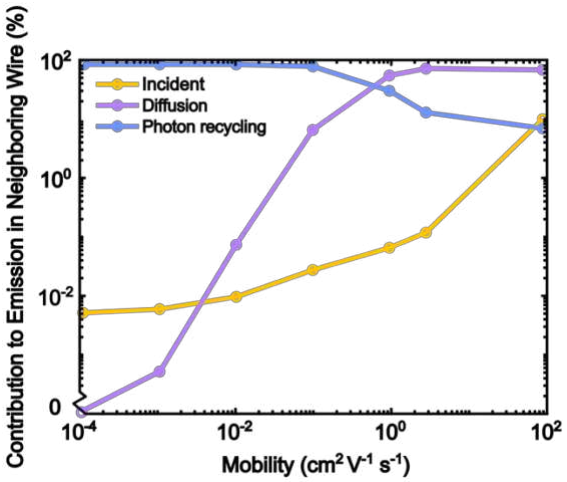

Figure 6.4. Fractional contribution to emission in the neighboring wire from the incident photon flux, carrier diffusion, and photon recycling. The simulation is based on a fixed NW morphology with baseline parameters (diameter = 0.5 μm, height = 2 μm, nearest neighbor distance = 1.3 μm). Equal mobilities are assumed for electrons and holes in a range from 10^{-4} – 10^2 $cm^2\ V^{-1}\ s^{-1}$.

Our imaging experiments aim to spatially resolve photons emitted from the neighboring NWs. Because it is challenging to compare absolute computational values against experimental measurements, we instead compare normalized quantities. In this work, the normalized quantity is defined as the "PL ratio", which quantifies the ratio of the rate of photons emitted from the neighboring NW to the rate of photons emitted from the central NW at 920 nm. Whereas the reflection intensity ratio refers to the photons reflected by the neighboring wire as compared to the central NW at 415 nm. We can estimate a total surface-integrated recombination rate for the central

(R_{cen}) and the neighboring NW (R_{nei}) by integrating the corresponding spatial profiles of the volumetric recombination rates, R_{rad} obtained in Figure 6.3.

$$R_{\mathrm{cen/nei}} = \iint R_{\mathrm{rad}}\, dS,$$

The PL ratio from model predictions can be computed as $\frac{R_{\mathrm{nei}}}{R_{\mathrm{cen}}}$, and this is compared against the measured PL intensity ratios at any location. We performed single NW-level microscopy and spectroscopy measurements to quantify the PL and reflection intensity ratios calculated above. The central hypothesis of our experimental approach is that widefield PL microscopy can spatially resolve the photon recycling process between two adjacent semiconductor nanostructures. To test this hypothesis, we designed an experiment that excites a single nanorod with a focused 415 nm laser beam and spatially and spectroscopically detects photons emitted from neighboring nanorods using widefield PL imaging and PL microspectroscopy. Figure 6.5a shows a schematic illustration of the correlated microspectroscopy and widefield imaging experimental setup. In a typical experiment, we mount the GaN-coated InP NW array sample on the stage of an inverted optical microscope and identify a 20×20 μm^2 area of interest using optical reflection microscopy (Figure D5). We selected GaN-coated InP NWs to study the photon recycling effect due to the predicted ≈50% PL quantum efficiency without surface passivation[54] and ≈75% PL quantum efficiency with surface passivation[55], which ensures that radiative recombination is the primary charge recombination mechanism in the semiconductor—a crucial factor for efficient photon recycling.[4] Supporting Information Section D2 describes the PLQY measurement used in this study. Next, a 415 nm laser beam excites an 0.19 μm^2 area of the sample using a 490 nm-diameter laser spot. The same microscope objective used to achieve the focused illumination also collects photons emitted or reflected from the sample in a backscatter geometry. We direct the collected photons to both a

spectrometer that measures PL spectra of InP NWs (Figure 6.5a-top) and an image splitter that filters the photon stream and produces two distinct PL and reflection widefield images on a sCMOS camera (Figure 6.5a-right; see Methods for details).

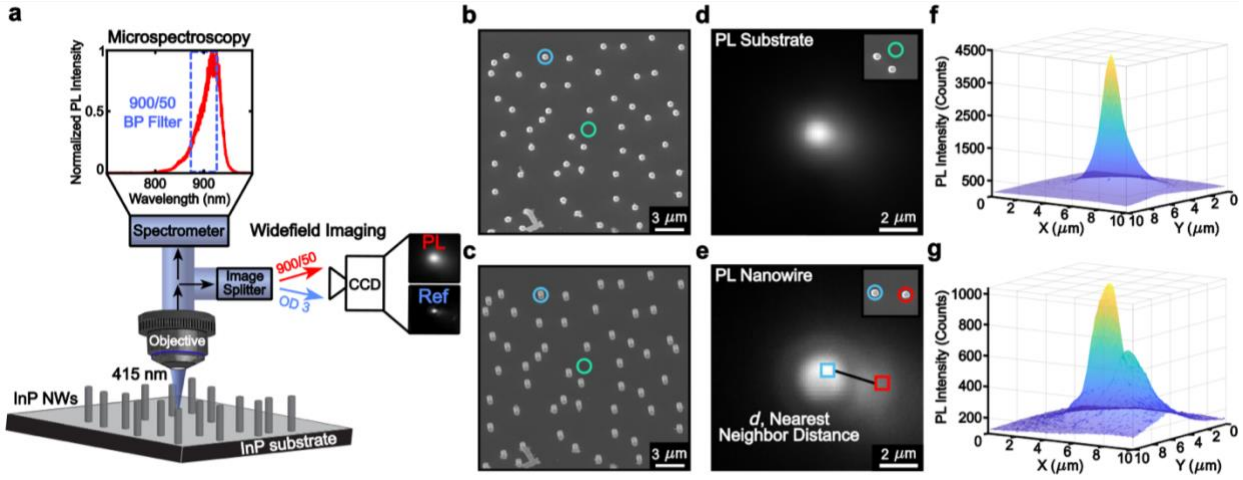

Figure 6.5. (a) Microspectroscopy and widefield imaging experimental setup. A 0.3 mW, 415 nm laser excites a 490 nm-diameter circular spot of the sample. A 100× air objective collects all photons emitted and reflected from the sample. A 50/50 beam splitter directs half the photons to an image splitter for widefield PL imaging and the other half to a spectrometer for microspectroscopy measurements. A motorized stage moves the sample in 0.5 μm steps during mapping experiments. The blue dashed box in the PL spectrum (top) indicates the bandpass filter placed in the image splitter. (b) SEM image of the GaN-coated InP NWs grown on an InP substrate. (c) same as (b), but with 15° tilt. (d) Widefield PL image upon exciting the substrate, as indicated by the green circle in (b,c). The inset shows a zoomed-in view of the region in (b). (e) Widefield PL image upon exciting a single NW, as indicated by the blue circle in (b,c). The inset shows a zoomed-in view of the SEM image region, where the blue circle indicates the laser excitation spot, and the red circle indicates the centroid location of the nearest NW. The blue and red boxes in (e) indicate the 5-by-5-pixel regions used for pixel intensity integration. The black line in (e) represents the computed nearest neighbor distance vector between the origin and neighboring NWs. (f)-(g) 3D intensity profiles of the widefield PL images in (d) and (e), respectively.

Figure 6.5 qualitatively shows how widefield PL images change upon exciting single NWs in the NW array sample. Figure 6.5b-c shows a representative SEM image of the NW array sample region. We chose to study a pseudo-random NW array pattern with a built-in heterogeneous distribution of NW-NW separation distances (*d*, ranging from 0.5-3 μm) because this morphology mimics that of a heterogeneous semiconductor photocatalysis reactor and allows us to amass single particle-level statistics from a single imaging experiment. Figure 6.5d,f shows 2D and 3D representations of a representative PL image upon exciting the InP substrate with a focused laser beam. Expectedly, a single Gaussian-like peak appears in the widefield PL image because photo-

excited carriers created within the sample volume beneath the Gaussian-like laser spot on the substrate contribute to the widefield PL image intensity. Figure D12 depicts the widefield images and 3D intensity profiles for the reflection channel. However, the PL image changes upon exciting a single NW that is located 2.4 μm from a neighboring NW (Figure 6.5e,g). The central PL peak intensity broadens, and a shoulder feature appears in the 3D representation (Figure 6.5g). Interestingly, the shoulder feature in the widefield PL image spatially correlates with the real-space position of the NW neighbor in the SEM image (Figure 6.5e). The PL intensity moves around the central NW, depending on the nearest NW neighbor location (see Figure D13a – D13b). Note, conventional PL microspectroscopy mapping experiments do not distinguish between photons emitted from the central NW and nearest neighbor NW because the microscope objective collects all photons from the sample and directs them to the spectrometer, as shown in Figure 6.5a–top. Control experiments show that PL images of isolated NWs exhibit a single Gaussian-like emission peak in PL images (similar to substrate PL images), which further suggests that PL emission from the NW neighbor is responsible for the shoulder feature in Figure 6.5e.

Having designed an experiment that distinguishes Case 1 from Cases 2 and 3 in Scheme 6.1, we then explored to what extent widefield imaging could distinguish between Case 2 from Case 3. To do so, we calculated PL emission intensity from the neighboring NW relative to the photo-excited NW (i.e., PL intensity ratio) from experimental widefield images and compared that value to the same calculation, but for scattered light only. Figure 6.5e illustrates how we calculate the PL and reflection intensity ratio using the integrated intensity of a 5-by-5-pixel box from the neighboring NW (red box in Figure 6.5e) divided by the integrated intensity of a 5-by-5-pixel box from the origin NW (blue box in Figure 6.5e). Supporting Information Section D3 describes the

detailed image analysis procedures to quantitively extract PL and scattered light intensities from PL images using spatial information contained in SEM images.

Figure 6.6 shows PL and reflection intensity ratio values as a function of nearest neighbor distance, *d,* which is the center-to-center distance between the central and the neighboring NW. The small unfilled squares in Figure 6.6a-b represent experimentally determined PL ratio and reflection intensity values from NW pairs and the large, filled squares show binned and averaged values to emphasize the general trend. Both the PL and reflection intensity ratio values monotonically decrease with increasing *d*. To further confirm that the PL and reflection ratio trends in Figure 6.6 indeed stem from photon communication between neighboring NWs, we examined how that ratio would change for a control experiment. To do so, we analyzed the signal responses upon exciting the InP substrate alone. The PL line profile was fitted with a Lorentzian function and is plotted as the red dashed line in Figure 6.6a (Figure D14a shows the widefield PL image). Note, the *x* axis in Figure 6.6a represents the distance from the excitation centroid and the grey box depicts the NW width. The dashed red line in Figure 6.6a decays much more rapidly than the experimental data points measured in the presence of NW neighbors. Hence, we conclude that our widefield imaging method can spatially resolve photons emitted from, or reflected by, neighboring NWs. This data shows that photon communication occurs within the NW arrays because we observe enhanced emission from the sample upon bringing NWs closer together. This enhanced emission in the neighboring wire highlights an ensemble photonic effect, either due to photon recycling or re-absorption and re-emission of scattered photons.

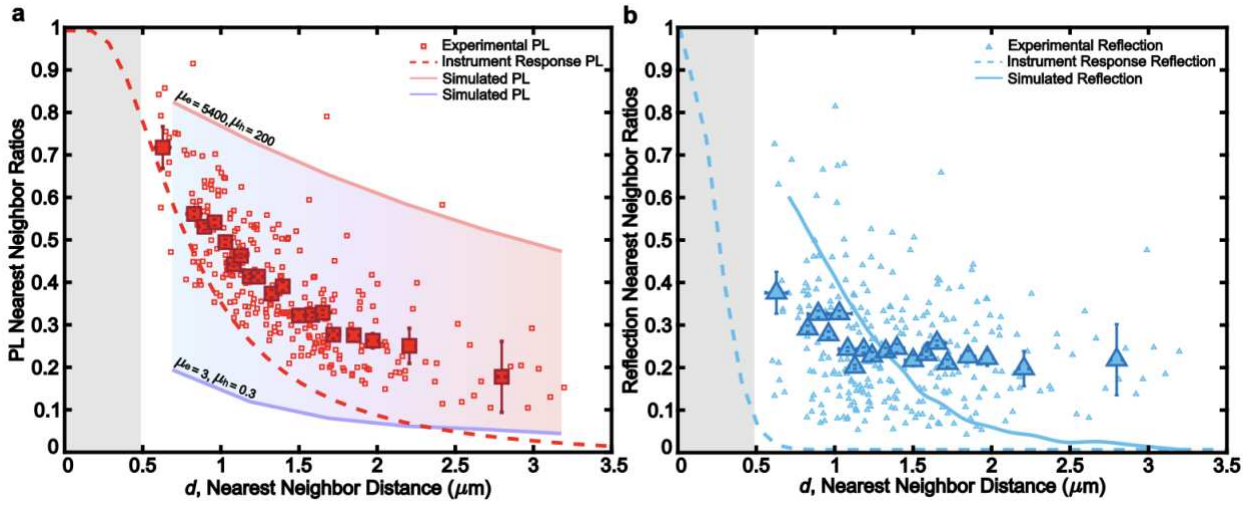

Figure 6.6. Experimentally determined PL and reflection ratios compared with modeling results. (a) PL nearest neighbor ratios as a function of nearest neighbor distance, *d*. The red squares represent the experimentally determined PL ratios, while the large red squares indicate the binned and averaged experimentally determined PL ratios (5 data points). The error bars indicate the standard error of the mean of the binned data points in both x and y. The purple and pink solid lines represent the simulated PL with low and high mobility scenarios, respectively, with labeled electron (μ_e) and hole mobility (μ_h) in units of cm^2/Vs. The red dashed line indicates the Lorentzian fit to the instrument response of the 415 nm excitation in the PL channel on the bare InP substrate. The gray shaded box depicts where the x-axis is defined as the distance from the center of the excitation on the bare InP substrate. (b) The same as (a), but for reflection nearest neighbor ratios. The blue dashed line represents the Gaussian fit to the instrument response in the reflection channel on the bare InP substrate. The blue solid line indicates the simulated reflection results.

We compared the simulated PL and reflection intensity ratios to experimental measurements. In our calculations, we integrate over all emission angles to determine the total emission rate. In widefield imaging experiments, the microscope objective collects photons emitted within a subset of angles defined by the numerical aperture. This difference may lead to discrepancies in the absolute emission rates, but does not significantly impact the comparison of PL ratios.[56] The shaded region in Figure 6.6a shows the simulated PL ratio for different charge-carrier mobilities. The purple line at low PL ratio represents the low mobility scenario, where electron mobility (μ_e) = 3 cm^2/Vs and the hole mobility (μ_h) = 0.3 cm^2/Vs. The pink line at high PL ratio values represents the high mobility scenario, where μ_e = 5400 cm^2/Vs and μ_h = 200 cm^2/Vs. The high mobilities (μ_e = 5400 cm^2/Vs, μ_h = 200 cm^2/Vs) are based on the bulk InP properties[26], and to consider a wide range, the low mobilities considered are much smaller (μ_e= 3 cm^2/Vs, μ_h = 0.3 cm^2/Vs) than what was predicted from electron beam induced current (EBIC)

measurements in Supporting Information Section D9. The hole mobility was reasonably assumed to be tenfold smaller based on effective masses of electrons and holes. Mobility is inversely related to the effective mass $m_{e/h}$, so $\mu_h \approx \mu_e \times \frac{m_e}{m_h} \approx \mu_e \times \frac{0.077}{0.64} \approx 0.12\mu_e$.[26] These predictions in Figure 6.6a reinforce that the charge-carrier mobility significantly influences the PL ratio, and is consistent with the results in Figure 6.4. This is expected as charge-carrier diffusion was previously shown to have a significant effect on the emission in the neighboring NWs. For the lowest charge-carrier mobilities (μ_e= 3 cm^2/Vs, μ_h= 0.3 cm^2/Vs) modeled in Figure 6.6a, the relative contribution of diffusion and photon recycling are 47.6% and 52.4% respectively towards emission in the neighboring NW. Even with these experimentally deduced mobility values, the predictions still deviate from the PL ratios that are experimentally measured. This is attributed to many factors including experimental measurement uncertainties, and additionally, the built-in assumptions in the model that only considered radiative recombination. When recombination is accounted for at the NW surfaces, for equivalent mobilities of the charge-carriers, the predicted PL ratio becomes smaller than when only considering radiative recombination (Figure D21). Surface recombination is expected to be present in nanostructures, consistent with its large surface area to volume ratio. However, to model this effect accurately, we need to calibrate the values of the surface recombination velocities experimentally. Overall, these results showcase the power and necessity for model-based interpretations in furthering the understanding of spatially resolved PL measurements. Charge-carrier diffusion is especially shown to be critical pathway in addition to photon recycling, to contribute to emission in neighboring NWs, and needs to be taken into account when correlating PL between NWs.

Although the experimental reflection values are lower than those for PL, they do not decay as rapidly as the reflection values observed on the bare substrate (Figure 6.6b, blue dashed line).

Notably, the reflection values do not drop to zero at long *d*, contrary to the predictions from the simulated result (Figure 6.6b, blue solid line) and the instrument response observed during the 415 nm excitation on the substrate (Figure 6.6b, blue dashed line). The reflected photons from the central NW can travel to neighboring NWs and scatter off their surfaces too, which explains the higher reflection ratio values and suggests additional reflection and scattering between these NW arrays (case 3 in Scheme 6.1). We believe this is likely due to an imperfect NW geometry and an artifact that the excitation spot size (≈500 nm) is the size of the NW diameter. Future experiments of examining pillar-like structures that are larger than the diameter of the laser spot size will mitigate this effect.

Having established that optical simulations can interpret and inform experiments, we explored to what extent NW morphology influences photon re-absorption probability among NW neighbors. To probe the effectiveness of the different modeling techniques, Figure 6.7 compares results from the COMSOL model to geometric calculations of the light re-absorption probability while varying interwire distance, diameter, and height using baseline conditions in Table 6.1. The re-absorption probability quantifies the chance that a photon will be re-absorbed by a neighboring wire after emission from the illuminated, central NW. This re-absorption probability is a critical input necessary to quantify the enhanced generation rate due to photon recycling in the COMSOL model (Eq. D20, D21), and directly applied in the geometric model. We note that the COMSOL model predicts the electric field distribution due to emission from point dipole sources along the central NW length, as compared to would be predicted purely from geometric arguments (see Methods and Supporting Information Section D7 for details).

As expected, there is an inverse correlation between the center-to-center nearest neighbor distance and the re-absorption probabilities due to the increasing loss of photons to the substrate

and through the to the top surface (Figure 6.7a, Figure D22a). For all cases modeled in Figure 6.7, there is a less than a 10% probability that the neighboring NW re-absorbs the emitted photon from the central NW. This low probability stems from the fact that most of the photon re-absorption occurs within the central NW (Figure D22). The trend with diameter is more complex (Figure 6.7b), initially increasing with diameter, but then decreasing for larger diameter wires (>0.5 μm). An optimum value arises due to the balance between increasing absorption in the central NWand a rapidly declining loss of emitted photons to the substrate and the top surface (Figure D22b). For the largest diameter NW (1.4 μm), 90% of the emitted photons are absorbed within the central NW. From a pure geometric viewpoint, initially increasing the NW diameter increases the absorption area in the central NW and, therefore, the total number of photons that could be re-absorbed. Additionally, increasing the NW diameter increases the capture cross section for re-absorption by the neighboring NW, leading to a higher probability of re-absorption. However, at sufficiently large diameters, the probability of a photon being emitted from the top or bottom NW surface increases, rather than from the lateral surface of the central NW, which causes the re-absorption probability to decrease. The direct electric field and geometry-based simulations agree up to 0.5 um-diameter NWs, but then deviate substantially for larger diameters, yielding a much sharper inversion of the trend from the former. This deviation is due to the geometric model not considering photon re-absorption by the substrate beneath as well as re-absorption within the central wire. Both these pathways are shown to rapidly decline with increasing NW diameter from the direct electric field simulations (Figure D22b). Both models show a positive correlation between NW height and re-absorption probability, attributed to the larger effective area to capture emitted photons in a longer wire than a shorter one (Figure 6.7c).

While the simple, and computationally inexpensive, geometry model is reasonably accurate for predicting re-absorption probabilities for changes to NW height and interwire distance, the diameter is not well predicted due to the substrate effects discussed above. This highlights the importance and power of direct electric field calculations, and additionally demonstrates that the geometric model predictions have the potential for improved accuracy through the inclusion of extra optical paths to account for photon re-absorption within the substrate and the central NW.

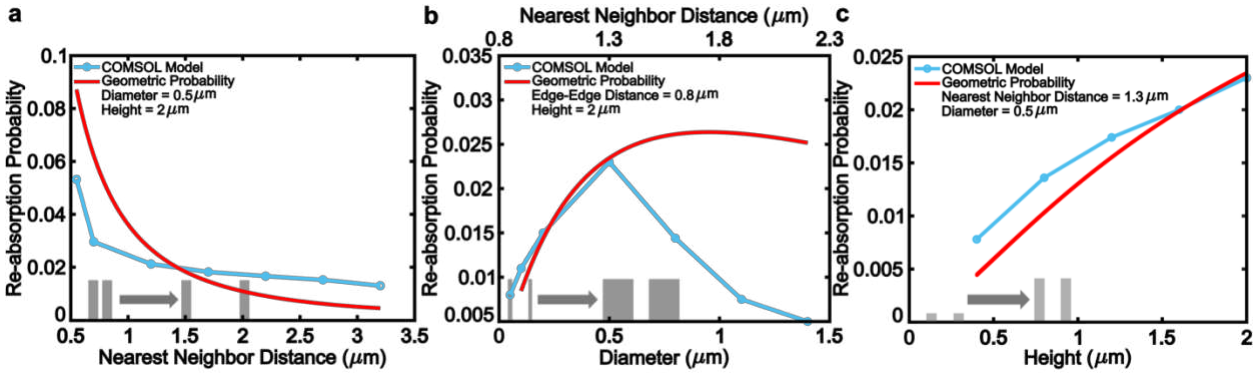

Figure 6.7. Predicted impact of NW (a) nearest neighbor distance, (b) diameter, and (c) height on photon re-absorption probability using baseline parameters in Table 6.1. Red lines are predicted using a maximum geometric calculation and blue lines are calculated from COMSOL modeling.

Next, we simulated how nearest neighbor distance, diameter, and height influence the experimentally accessible PL ratio value in Figure 6.8 using both COMSOL Multiphysics modeling and a computationally cheaper MC method. The COMSOL model fully couples the optical field with charge-carrier generation, recombination, and transport in the NWs and the substrate. The MC method only accounts for absorption and recombination events and does not consider charge-carrier transport or the presence of a substrate. One major difference between the models is that the charge-carrier mobilities strongly influence the COMSOL-predicted PL ratio values (Figure D23), whereas the MC model remains unaffected by this quantity. We include the

MC method in the Supporting Information (Section D7) so other researchers in the community can leverage the approach for predictive design of their NW array samples.

Both models predict an inverse correlation between PL ratio and *d* in Figure 6.8a. The magnitudes nearly match when the COMSOL model considers the low charge-carrier mobility situation as in Figure 6.6a (μ_e= 3 cm^2/Vs, μ_h = 0.3 cm^2/Vs) because the diffusion is no longer the dominant effect with these mobilities (Figure D20), which more closely mimics the assumption of no substrate in the MC model. Figure D17–D18 (MC) and Figure D21 (COMSOL) shows additional simulations that explore how PLQY, mobility, absorption coefficient, radiative recombination factor, and surface recombination velocity influence the PL ratio.

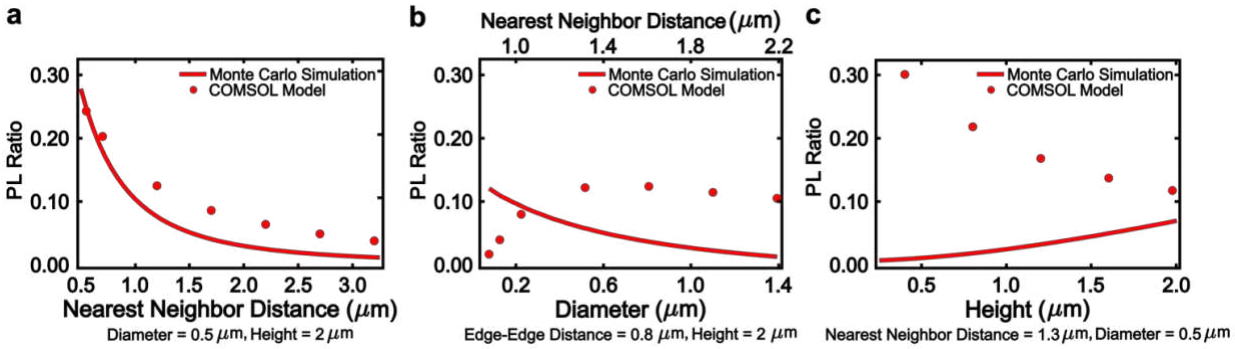

Figure 6.8. Simulated PL Ratio across variable geometry parameters. Solid lines are from the MC simulation and dots are from coupled simulations of the electric field and semiconductor physics. The parameters studied were a) nearest neighbor distance, b) NW diameter, and c) NW height. Baseline values from Table 6.1 are modeled for all other parameters in the COMSOL Model.

Interestingly, the two methods predict different trends for how NW diameter (Figure 6.8b) and height (Figure 6.8c) impact the PL ratio. The MC model predicts an inverse relationship between diameter and PL ratio, potentially due to increased upward light emission from wider wires. This both reduces the opportunities for inter-wire recycling (decreasing the numerator in the PL ratio) and also increases the amount of PL detected from the excited wire (increasing the denominator in the PL ratio). On the other hand, the COMSOL model first shows an increasing then decreasing trend with the diameter with an optimal value around 0.5 μm, which is similar to

the trend of re-absorption probability shown in Figure 6.7b. The MC model predicts a modest positive correlation between height and PL ratio (Figure 6.8c), primarily attributed to the increase in the re-absorption probability (Figure 6.7). However, the COMSOL model predicts a negative correlation, once again driven by the relatively influential effect of charge-carrier diffusion as compared to the recycling of emitted photons towards the recombination rates in the neighboring NWs (Figure D20). The predicted PL ratio from the MC model is influenced by high PLQY[57–59] and the degree of Stokes shift between the emitted and re-absorbed light[4,5,44,60], as any PL lower in energy than the semiconductor bandgap cannot be re-absorbed. For the materials tested in this study, 46% of the emitted light overlaps with the absorbance spectrum. This Stokes shift was not accounted for in the COMSOL model and may explain why the predicted PL ratios between the two models differ.

Finally, to provide context on how photon recycling could contribute to photocatalytic performance, we calculated the net rate of charge-carrier generation on a volume-averaged (m^{-3} s^{-1}) basis for the central wire in Figure 6.9 as a function of morphological parameters, with and without inclusion of photon recycling. This calculation is performed for the very low mobilities modeled (μ_e = 3 cm^2/Vs, μ_h = 0.3 cm^2/Vs), as the effect of photon recycling is expected to be the most pronounced for this case. This net generation rate is used as a representative metric that can relate to the volumetric rate of chemical/fuels production in photocatalytic NWs and is calculated as the difference between the generation and recombination rates predicted (as in Figure 6.3). This quantity is important to track because, photon recycling increases both the generation and the recombination rates, and they don't necessarily change by the same magnitude because of the presence of other parasitic pathways for charge-carrier recombination (e.g., through the substrate).

Therefore, higher generation rate due to photon recycling doesn't necessarily imply better photosynthetic performance since the recombination rate is going up at the same time.

For this low mobility case, there is a noticeable enhancement in the net charge-carrier generation rate within the central NW when photon recycling is factored on for all morphologies modeled. The trends with neighbor distance, NW diameter and height are all consistent with the trends shown in Figure D20 for the re-absorption probabilities within the central NW. Contrary to the emission intensity in the neighboring NWs, increasing distance between the central and the neighboring NWs benefits the net generation rate in the central NW. Beyond a diameter of 0.5 μm for the NWs, the enhancement to the net generation rate plateaus when photon recycling is factored in because of the increased losses to the substrate. Additionally, increasing the NW height enhances both recombination and generation rates to a similar extent, making photon recycling ineffective at altering the overall outcome in this case. Figure D24 displays the net generation rate profiles in the neighboring wire. As expected– since photon recycling is not included in the model– there is no significant charge-carrier generation in the neighboring NW across all cases. This is due to the minimal contribution from the incident field and, in the low mobility scenario presented, the limited effectiveness of charge-carrier diffusion.

Beyond the net generation rate, another important metric to quantify is the ratio of the generation to the recombination rate, as this is indicative of the charge-carrier generation under illumination of the nanostructured semiconductor materials, $V_{\mathrm{OC}} = \frac{kT}{q_e}\left(\log\left(\frac{Generation}{Recombination} + 1\right)\right)$. Figure D25 reveals that this generation/recombination ratio slightly decreases (by up to 10%), especially for the larger NW diameters, when photon recycling is taken into account in the model as compared to our predictions without photon recycling. The extent to which the charge-carrier generation under illumination depends on photon recycling or not is dependent on the mobility of

the charge-carrier species and is expected to decrease for the larger and more realistic material mobilities. We explored the effect of high mobility in Figure D25. In the high mobility case, the generation/recombination ratio versus nearest neighbor distance, diameter, and height follows a similar trend to that observed with low mobility (Figure D25). However, the curves with and without photon recycling nearly overlap for high-mobility cases, validating our conclusion that photon recycling plays a diminished role in high-mobility materials.

These results point towards the need to balance gains in the enhancements to re-absorption with the losses incurred from enhanced emission and therefore the charge-carrier generation under illumination due to photon recycling in the materials and designs for semiconductor NWs for photocatalysis. While outside the scope of this study, future model predictions will consider direct implications of electronic transport and photon recycling on solar-to-chemical conversion efficiencies.

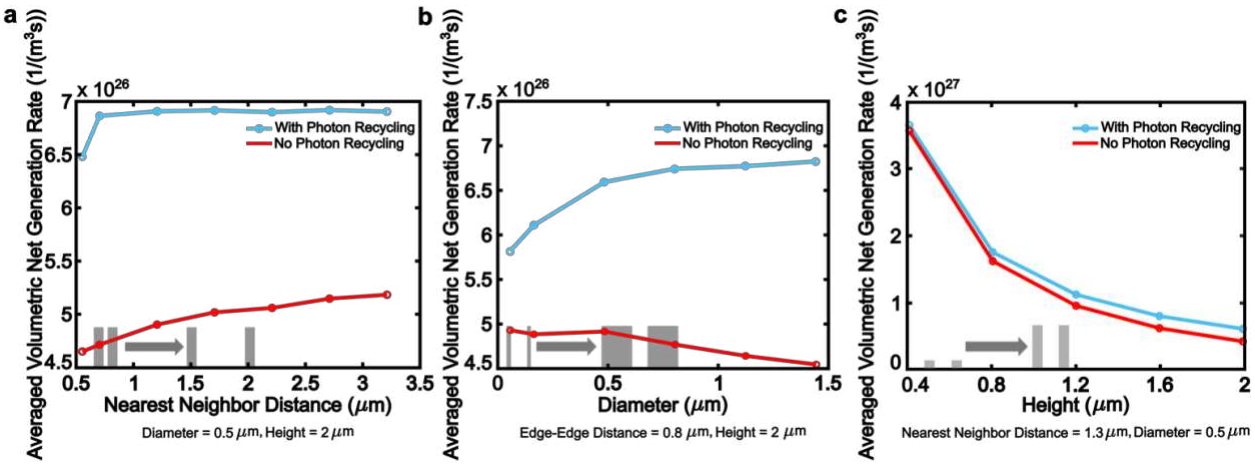

Figure 6.9. Averaged volumetric net generation rate in the central NW versus (a) nearest neighbor distance, (b) diameter, and (c) height using baseline values in Table 6.1. Net generation rate is defined as the difference between generation rate and recombination rate. Blue and red lines correspond to with photon recycling and no photon recycling, respectively.

6.5 Conclusion

We performed optical and photophysics simulations and single NW spectroscopy and microscopy experiments to investigate contributions of incident photon scattering, charge-carrier

diffusion, and photon recycling on the carrier generation/recombination rates in NW arrays. Results demonstrate the critical necessity for model-based interpretations to infer the causal factors for emission measured in neighboring NWs from spatially resolved PL measurements. Comparisons between the experimental measurements and model predictions showcase a good match in trends for the PL and reflection intensity ratios between the illuminated and the neighboring NWs. However, the magnitudes are highly sensitive to the charge-carrier mobilities and other select idealizing assumptions made in the model, especially the lack of surface recombination. Charge-carrier diffusion is quantitatively demonstrated to be a critical contributor to emission in the neighboring NWs in the case of moderate-to-high mobility materials (>10 cm^2 V^{-1} s^{-1}). However, photon recycling plays a more dominating role for the low mobility materials (<1 cm^2 V^{-1} s^{-1}). Our measurement and modeling approaches are independent of material composition, enabling researchers in the heterogeneous photocatalysis community to apply the methods developed herein to low-mobility semiconductors such as $BiVO_4$. Predictive models were applied to evaluate the effects of morphological parameters, where simple and fast geometry-based calculations match the more rigorous full-wave optical model predictions reasonably well for the reabsorption probabilities, except for trends with respect to the NW diameter. This reiterates the necessity to consider implications of all possible photon loss pathways, for instance through the substrate. Even with the idealization of only considering radiative recombination of charge-carriers, our projections for the net carrier generation rate and the charge-carrier generation under illumination in the centrally illuminated wire in a NW array, indicates rather modest benefits, if any, from photon recycling.

This study demonstrates that spatial PL measurements are influenced not only by optical coupling mechanisms, such as scattering and photon recycling, but also by electronic coupling

arising from charge-carrier diffusion in NW arrays. To address this, we developed a unique and tractable computational model that quantitatively predicts the extent to which charge-carrier diffusion (electronic coupling) dominates in NW arrays connected via a base substrate. Our results further show that optical coupling through photon recycling is particularly significant for NW arrays composed of low-mobility, but water-stable metal oxides (e.g., $BiVO_4$), commonly used in photocatalysis for solar-to-chemical transformations. Additionally, we demonstrate that photon recycling becomes a critical factor in systems where absorbers are freely suspended and not electronically connected by a substrate, such as particle-suspension systems and particulate sheets, highlighting the importance of controlling optical coupling in these configurations. Overall, this study establishes robust predictive and experimental frameworks to better understand and assess light management and electronic transport in nanoscale photosynthetic materials, paving the way to enhance the performance of next-generation sunlight-to-chemical energy conversion systems.

6.6 Author Contributions

According to CRediT criteria, my contributions to this work included conceptualization, data curation, formal analysis, investigation, methodology, visualization, writing – original draft, and writing – reviewing and editing. D.R.L. and W.Z. performed characterization measurements. W.Z. synthesized the materials used in this study. F.C. developed and performed multiphysics modeling in COMSOL. O.F.B. performed Monte Carlo simulations and geometry calculations. A.A.T. and J.F. performed EBIC measurements. F.C., R.B.C., and O.F.B. analyzed and interpreted modeling data. J.B.S., R.B.C., S.A., and S.H. assisted with conceptualization. S.A. and J.B.S. assisted with experimental design. D.R.L, F.C., O.B, W.Z., R.B.C and J.B.S wrote the initial full manuscript draft and all authors contributed to manuscript edits and revisions.

REFERENCES

(1) Van Der Laan, M.; De Weerd, C.; Poirier, L.; Van De Water, O.; Poonia, D.; Gomez, L.; Kinge, S.; Siebbeles, L. D. A.; Koenderink, A. F.; Gregorkiewicz, T. et al.; Photon Recycling in CsPbBr 3 All-Inorganic Perovskite Nanocrystals. *ACS Photonics* **2021**, *8* (11), 3201–3208. https://doi.org/10.1021/acsphotonics.1c00953.
(2) Miller, O. D.; Yablonovitch, E.; Kurtz, S. R. Strong Internal and External Luminescence as Solar Cells Approach the Shockley–Queisser Limit. *IEEE J. Photovolt.* **2012**, *2* (3), 303–311. https://doi.org/10.1109/JPHOTOV.2012.2198434.
(3) Cheng, Z.; Javed, N.; Zhao, F.; O'Carroll, D. M. Photon Recycling in Organic Semiconductor Films Using Plasmonic Metasurfaces. *Mater. Today Phys.* **2023**, *38*, 101241. https://doi.org/10.1016/j.mtphys.2023.101241.
(4) Raja, W.; De Bastiani, M.; Allen, T. G.; Aydin, E.; Razzaq, A.; Rehman, A. U.; Ugur, E.; Babayigit, A.; Subbiah, A. S.; Isikgor, F. H. et al.; Photon Recycling in Perovskite Solar Cells and Its Impact on Device Design. *Nanophotonics* **2021**, *10* (8), 2023–2042. https://doi.org/10.1515/nanoph-2021-0067.
(5) Gan, Z.; Chen, W.; Yuan, L.; Cao, G.; Zhou, C.; Huang, S.; Wen, X.; Jia, B. External Stokes Shift of Perovskite Nanocrystals Enlarged by Photon Recycling. *Appl. Phys. Lett.* **2019**, *114* (1), 011906. https://doi.org/10.1063/1.5081805.
(6) Abebe, M. G.; Abass, A.; Gomard, G.; Zschiedrich, L.; Lemmer, U.; Richards, B. S.; Rockstuhl, C.; Paetzold, U. W. Rigorous Wave-Optical Treatment of Photon Recycling in Thermodynamics of Photovoltaics: Perovskite Thin-Film Solar Cells. *Phys. Rev. B* **2018**, *98* (7), 075141. https://doi.org/10.1103/PhysRevB.98.075141.
(7) Brenes, R.; Laitz, M.; Jean, J.; deQuilettes, D. W.; Bulović, V. Benefit from Photon Recycling at the Maximum-Power Point of State-of-the-Art Perovskite Solar Cells. *Phys. Rev. Appl.* **2019**, *12* (1), 014017. https://doi.org/10.1103/PhysRevApplied.12.014017.
(8) Chen, J.; Ma, P.; Chen, W.; Xiao, Z. Overcoming Outcoupling Limit in Perovskite Light-Emitting Diodes with Enhanced Photon Recycling. *Nano Lett.* **2021**, *21* (19), 8426–8432. https://doi.org/10.1021/acs.nanolett.1c03035.
(9) Cho, C.; Jang, Y.-W.; Lee, S.; Vaynzof, Y.; Choi, M.; Noh, J. H.; Leo, K. Effects of Photon Recycling and Scattering in High-Performance Perovskite Solar Cells. *Sci. Adv.* **2021**, *7* (52), eabj1363. https://doi.org/10.1126/sciadv.abj1363.
(10) Cho, C.; Zhao, B.; Tainter, G. D.; Lee, J.-Y.; Friend, R. H.; Di, D.; Deschler, F.; Greenham, N. C. The Role of Photon Recycling in Perovskite Light-Emitting Diodes. *Nat. Commun.* **2020**, *11* (1), 611. https://doi.org/10.1038/s41467-020-14401-1.
(11) Kirchartz, T.; Staub, F.; Rau, U. Impact of Photon Recycling on the Open-Circuit Voltage of Metal Halide Perovskite Solar Cells. *ACS Energy Lett.* **2016**, *1* (4), 731–739. https://doi.org/10.1021/acsenergylett.6b00223.
(12) Staub, F.; Anusca, I.; Lupascu, D. C.; Rau, U.; Kirchartz, T. Effect of Reabsorption and Photon Recycling on Photoluminescence Spectra and Transients in Lead-Halide Perovskite Crystals. *J. Phys. Mater.* **2020**, *3* (2), 025003. https://doi.org/10.1088/2515-7639/ab6fd0.
(13) Nanz, S.; Schmager, R.; Abebe, M. G.; Willig, C.; Wickberg, A.; Abass, A.; Gomard, G.; Wegener, M.; Paetzold, U. W.; Rockstuhl, C. Photon Recycling in Nanopatterned Perovskite Thin-Films for Photovoltaic Applications. *APL Photonics* **2019**, *4* (7), 076104. https://doi.org/10.1063/1.5094579.

(14) deQuilettes, D. W.; Brenes, R.; Laitz, M.; Motes, B. T.; Glazov, M. M.; Bulović, V. Impact of Photon Recycling, Grain Boundaries, and Nonlinear Recombination on Energy Transport in Semiconductors. *ACS Photonics* **2022**, *9* (1), 110–122. https://doi.org/10.1021/acsphotonics.1c01186.
(15) Sridharan, A.; Noel, N. K.; Rand, B. P.; Kéna-Cohen, S. Role of Photon Recycling and Band Filling in Halide Perovskite Photoluminescence under Focussed Excitation Conditions. *J. Phys. Chem. C* **2021**, *125* (4), 2240–2249. https://doi.org/10.1021/acs.jpcc.0c09103.
(16) Motti, S. G.; Crothers, T.; Yang, R.; Cao, Y.; Li, R.; Johnston, M. B.; Wang, J.; Herz, L. M. Heterogeneous Photon Recycling and Charge Diffusion Enhance Charge Transport in Quasi-2D Lead-Halide Perovskite Films. *Nano Lett.* **2019**, *19* (6), 3953–3960. https://doi.org/10.1021/acs.nanolett.9b01242.
(17) Richter, J. M.; Abdi-Jalebi, M.; Sadhanala, A.; Tabachnyk, M.; Rivett, J. P. H.; Pazos-Outón, L. M.; Gödel, K. C.; Price, M.; Deschler, F.; Friend, R. H. Enhancing Photoluminescence Yields in Lead Halide Perovskites by Photon Recycling and Light Out-Coupling. *Nat. Commun.* **2016**, *7* (1), 13941. https://doi.org/10.1038/ncomms13941.
(18) Pazos-Outón, L. M.; Szumilo, M.; Lamboll, R.; Richter, J. M.; Crespo-Quesada, M.; Abdi-Jalebi, M.; Beeson, H. J.; Vrućinić, M.; Alsari, M.; Snaith, H. J. et al.; Photon Recycling in Lead Iodide Perovskite Solar Cells. *Science* **2016**, *351* (6280), 1430–1433. https://doi.org/10.1126/science.aaf1168.
(19) Yamada, T.; Yamada, Y.; Kanemitsu, Y. Photon Recycling in Perovskite CH3NH3PbX3 (X = I, Br, Cl) Bulk Single Crystals and Polycrystalline Films. *J. Lumin.* **2020**, *220*, 116987. https://doi.org/10.1016/j.jlumin.2019.116987.
(20) Ding, H.; Hong, H.; Cheng, D.; Shi, Z.; Liu, K.; Sheng, X. Power- and Spectral-Dependent Photon-Recycling Effects in a Double-Junction Gallium Arsenide Photodiode. *ACS Photonics* **2019**, *6* (1), 59–65. https://doi.org/10.1021/acsphotonics.8b01404.
(21) Ahrenkiel, R. K.; Dunlavy, D. J.; Keyes, B.; Vernon, S. M.; Dixon, T. M.; Tobin, S. P.; Miller, K. L.; Hayes, R. E. Ultralong Minority-Carrier Lifetime Epitaxial GaAs by Photon Recycling. *Appl. Phys. Lett.* **1989**, *55* (11), 1088–1090. https://doi.org/10.1063/1.101713.
(22) Ardo, S.; Keene, S.; Phun, G. Optically Thin Light-Absorbers for Increasing Photochemical Energy-Conversion Efficiencies. US20200140293A1, 2024.
(23) Keene, S. Detailed Balance Modeling of Novel Solar Fuels Designs. Ph.D. Dissertation, University of California, Irvine, Irvine, CA, 2018. https://escholarship.org/uc/item/4sj4n3vj. (accessed 2025-03-21).
(24) Andrei, V.; Roh, I.; Yang, P. Nanowire Photochemical Diodes for Artificial Photosynthesis. *Sci. Adv.* **2023**, *9* (6), eade9044. https://doi.org/10.1126/sciadv.ade9044.
(25) Dasgupta, N. P.; Yang, P. Semiconductor Nanowires for Photovoltaic and Photoelectrochemical Energy Conversion. *Front. Phys.* **2014**, *9* (3), 289–302. https://doi.org/10.1007/s11467-013-0305-0.
(26) Hochbaum, A. I.; Yang, P. Semiconductor Nanowires for Energy Conversion. *Chem. Rev.* **2010**, *110* (1), 527–546. https://doi.org/10.1021/cr900075v.
(27) Yang, P.; Yan, R.; Fardy, M. Semiconductor Nanowire: What's Next? *Nano Lett.* **2010**, *10* (5), 1529–1536. https://doi.org/10.1021/nl100665r.
(28) Esposito, D. V.; Lee, Y.; Yoon, H.; Haney, P. M.; Labrador, N. Y.; Moffat, T. P.; Talin, A. A.; Szalai, V. A. Deconvoluting the Influences of 3D Structure on the Performance of Photoelectrodes for Solar-Driven Water Splitting. *Sustain. Energy Fuels* **2017**, *1* (1), 154–173. https://doi.org/10.1039/C6SE00073H.

(29) Boettcher, S. W.; Warren, E. L.; Putnam, M. C.; Santori, E. A.; Turner-Evans, D.; Kelzenberg, M. D.; Walter, M. G.; McKone, J. R.; Brunschwig, B. S.; Atwater, H. A. et al.; Photoelectrochemical Hydrogen Evolution Using Si Microwire Arrays. *J. Am. Chem. Soc.* **2011**, *133* (5), 1216–1219. https://doi.org/10.1021/ja108801m.
(30) Hagedorn, K.; Forgacs, C.; Collins, S.; Maldonado, S. Design Considerations for Nanowire Heterojunctions in Solar Energy Conversion/Storage Applications. *J. Phys. Chem. C* **2010**, *114* (27), 12010–12017. https://doi.org/10.1021/jp103529v.
(31) Fehr, A. M. K.; Agrawal, A.; Mandani, F.; Conrad, C. L.; Jiang, Q.; Park, S. Y.; Alley, O.; Li, B.; Sidhik, S.; Metcalf, I. et al.; Integrated Halide Perovskite Photoelectrochemical Cells with Solar-Driven Water-Splitting Efficiency of 20.8%. *Nat. Commun.* **2023**, *14* (1), 3797. https://doi.org/10.1038/s41467-023-39290-y.
(32) Anttu, N.; Abrand, A.; Asoli, D.; Heurlin, M.; Åberg, I.; Samuelson, L.; Borgström, M. Absorption of Light in InP Nanowire Arrays. *Nano Res.* **2014**, *7* (6), 816–823. https://doi.org/10.1007/s12274-014-0442-y.
(33) Ren, D.; Scofield, A. C.; Farrell, A. C.; Rong, Z.; Haddad, M. A.; Laghumavarapu, R. B.; Liang, B.; Huffaker, D. L. Exploring Time-Resolved Photoluminescence for Nanowires Using a Three-Dimensional Computational Transient Model. *Nanoscale* **2018**, *10* (16), 7792–7802. https://doi.org/10.1039/C8NR01908H.
(34) Ren, D.; Rong, Z.; Somasundaram, S.; Azizur-Rahman, K. M.; Liang, B.; Huffaker, D. L. A Three-Dimensional Insight into Correlation between Carrier Lifetime and Surface Recombination Velocity for Nanowires. *Nanotechnology* **2018**, *29* (50), 504003. https://doi.org/10.1088/1361-6528/aae365.
(35) Tajik, N.; Haapamaki, C. M.; LaPierre, R. R. Photoluminescence Model of Sulfur Passivated P-InP Nanowires. *Nanotechnology* **2012**, *23* (31), 315703. https://doi.org/10.1088/0957-4484/23/31/315703.
(36) Parrott, J. E. Radiative Recombination and Photon Recycling in Photovoltaic Solar Cells. *Sol. Energy Mater. Sol. Cells* **1993**, *30* (3), 221–231. https://doi.org/10.1016/0927-0248(93)90142-P.
(37) Durbin, S. M.; Gray, J. L. Numerical Modeling of Photon Recycling in Solar Cells. *IEEE Trans. Electron Devices* **1994**, *41* (2), 239–245. https://doi.org/10.1109/16.277372.
(38) Martí, A.; Balenzategui, J. L.; Reyna, R. F. Photon Recycling and Shockley's Diode Equation. *J. Appl. Phys.* **1997**, *82* (8), 4067–4075. https://doi.org/10.1063/1.365717.
(39) Cui, Y.; Van Dam, D.; Mann, S. A.; Van Hoof, N. J. J.; Van Veldhoven, P. J.; Garnett, E. C.; Bakkers, E. P. A. M.; Haverkort, J. E. M. Boosting Solar Cell Photovoltage via Nanophotonic Engineering. *Nano Lett.* **2016**, *16* (10), 6467–6471. https://doi.org/10.1021/acs.nanolett.6b02971.
(40) Walker, A. W.; Hohn, O.; Micha, D. N.; Blasi, B.; Bett, A. W.; Dimroth, F. Impact of Photon Recycling on GaAs Solar Cell Designs. *IEEE J. Photovolt.* **2015**, *5* (6), 1636–1645. https://doi.org/10.1109/JPHOTOV.2015.2479463.
(41) Wang, X.; Khan, M. R.; Lundstrom, M.; Bermel, P. Performance-Limiting Factors for GaAs-Based Single Nanowire Photovoltaics. *Opt. Express* **2014**, *22* (S2), A344. https://doi.org/10.1364/OE.22.00A344.
(42) Oksenberg, E.; Fai, C.; Scheblykin, I. G.; Joselevich, E.; Unger, E. L.; Unold, T.; Hages, C.; Merdasa, A. Deconvoluting Energy Transport Mechanisms in Metal Halide Perovskites Using $CsPbBr_3$ Nanowires as a Model System. *Adv. Funct. Mater.* **2021**, *31* (22), 2010704. https://doi.org/10.1002/adfm.202010704.

(43) Kupec, J.; Stoop, R. L.; Witzigmann, B. Light Absorption and Emission in Nanowire Array Solar Cells. *Opt. Express* **2010**, *18* (26), 27589. https://doi.org/10.1364/OE.18.027589.
(44) Van Der Laan, M.; De Weerd, C.; Poirier, L.; Van De Water, O.; Poonia, D.; Gomez, L.; Kinge, S.; Siebbeles, L. D. A.; Koenderink, A. F.; Gregorkiewicz, T. et al.; Photon Recycling in CsPbBr 3 All-Inorganic Perovskite Nanocrystals. *ACS Photonics* **2021**, *8* (11), 3201–3208. https://doi.org/10.1021/acsphotonics.1c00953.
(45) Giovanni, D.; Righetto, M.; Zhang, Q.; Lim, J. W. M.; Ramesh, S.; Sum, T. C. Origins of the Long-Range Exciton Diffusion in Perovskite Nanocrystal Films: Photon Recycling vs Exciton Hopping. *Light Sci. Appl.* **2021**, *10* (1), 2. https://doi.org/10.1038/s41377-020-00443-z.
(46) Dursun, I.; Zheng, Y.; Guo, T.; De Bastiani, M.; Turedi, B.; Sinatra, L.; Haque, M. A.; Sun, B.; Zhumekenov, A. A.; Saidaminov, M. I. et al.; Efficient Photon Recycling and Radiation Trapping in Cesium Lead Halide Perovskite Waveguides. *ACS Energy Lett.* **2018**, *3* (7), 1492–1498. https://doi.org/10.1021/acsenergylett.8b00758.
(47) Gan, Z.; Wen, X.; Chen, W.; Zhou, C.; Yang, S.; Cao, G.; Ghiggino, K. P.; Zhang, H.; Jia, B. The Dominant Energy Transport Pathway in Halide Perovskites: Photon Recycling or Carrier Diffusion? *Adv. Energy Mater.* **2019**, *9* (20), 1900185. https://doi.org/10.1002/aenm.201900185.
(48) Ghimire, S.; Takahashi, K.; Takano, Y.; Nakamura, T.; Biju, V. Photon Recycling by Energy Transfer in Piezochemically Synthesized and Close-Packed Methylammonium Lead Halide Perovskites. *J. Phys. Chem. C* **2019**, *123* (45), 27752–27758. https://doi.org/10.1021/acs.jpcc.9b07003.
(49) Feng, M.; Ye, S.; Guo, Y.; Sum, T. C. Intrinsic Carrier Diffusion in Perovskite Thin Films Uncovered by Transient Reflectance Spectroscopy. *Nano Lett.* **2022**, *22* (17), 7195–7202. https://doi.org/10.1021/acs.nanolett.2c02511.
(50) Zheng, Y.; Naphade, R.; Mondal, N.; Bakr, O. M.; Mohammed, O. F.; Gartstein, Y. N.; Malko, A. V. Light Propagation and Radiative Exciton Transport in Two-Dimensional Layered Perovskite Microwires. *ACS Photonics* **2021**, *8* (1), 276–282. https://doi.org/10.1021/acsphotonics.0c01479.
(51) Karouta, F. A Practical Approach to Reactive Ion Etching. *J. Phys. Appl. Phys.* **2014**, *47* (23), 233501. https://doi.org/10.1088/0022-3727/47/23/233501.
(52) Shekarabi, S.; Zare Pour, M. A.; Su, H.; Zhang, W.; He, C.; Hanke, K. D.; Romanyuk, O.; Paszuk, A.; Jaegermann, W.; Hu, S. et al.; Photoemission Study of GaN Passivation Layers and Band Alignment at GaInP(100) Heterointerfaces. *ACS Appl. Mater. Interfaces* **2025**, *17* (4), 7087–7097. https://doi.org/10.1021/acsami.4c17453.
(53) James, F. Monte Carlo Theory and Practice. *Rep. Prog. Phys.* **1980**, *43* (9), 1145–1189. https://doi.org/10.1088/0034-4885/43/9/002.
(54) Sze, S. M.; Li, Y.; Ng, K. K. *Physics of Semiconductor Devices*, Fourth edition.; Wiley: Hoboken, NJ Chichester, West Sussex, 2021.
(55) Gao, Q.; Saxena, D.; Wang, F.; Fu, L.; Mokkapati, S.; Guo, Y.; Li, L.; Wong-Leung, J.; Caroff, P.; Tan, H. H. et al.; Selective-Area Epitaxy of Pure Wurtzite InP Nanowires: High Quantum Efficiency and Room-Temperature Lasing. *Nano Lett.* **2014**, *14* (9), 5206–5211. https://doi.org/10.1021/nl5021409.
(56) Black, L. E.; Cavalli, A.; Verheijen, M. A.; Haverkort, J. E. M.; Bakkers, E. P. A. M.; Kessels, W. M. M. Effective Surface Passivation of InP Nanowires by Atomic-Layer-Deposited Al 2 O 3 with PO x Interlayer. *Nano Lett.* **2017**, *17* (10), 6287–6294. https://doi.org/10.1021/acs.nanolett.7b02972.

(57) Van Der Burgt, J. S.; Garnett, E. C. Nanophotonic Emission Control for Improved Photovoltaic Efficiency. *ACS Photonics* **2020**, *7* (7), 1589–1602. https://doi.org/10.1021/acsphotonics.0c00152.
(58) Lyu, D.; Miao, Y.; Li, B.; Xiao, Z.; Wu, X.; Hu, X.; Jiang, X.-F.; Xu, Q.-H. Dual Blue Emission in Ruddlesden–Popper Lead-Bromide Perovskites Induced by Photon Recycling. *J. Phys. Chem. C* **2021**, *125* (33), 18308–18316. https://doi.org/10.1021/acs.jpcc.1c04891.
(59) Yamada, Y.; Hoyano, M.; Akashi, R.; Oto, K.; Kanemitsu, Y. Impact of Chemical Doping on Optical Responses in Bismuth-Doped CH_3 NH_3 $PbBr_3$ Single Crystals: Carrier Lifetime and Photon Recycling. *J. Phys. Chem. Lett.* **2017**, *8* (23), 5798–5803. https://doi.org/10.1021/acs.jpclett.7b02508.
(60) Zeder, S. J.; Aeberhard, U.; Ruhstaller, B.; Tress, W. Photon Recycling in Metal Halide Perovskites: Its Modeling and Relevance to Optoelectronic Devices. In *Metal Halide Perovskites for Generation, Manipulation and Detection of Light*; Elsevier, 2023; pp 507–545. https://doi.org/10.1016/B978-0-323-91661-5.00001-5.
(61) Fang, Y.; Wei, H.; Dong, Q.; Huang, J. Quantification of Re-Absorption and Re-Emission Processes to Determine Photon Recycling Efficiency in Perovskite Single Crystals. *Nat. Commun.* **2017**, *8* (1), 14417. https://doi.org/10.1038/ncomms14417.

CHAPTER 7: SINGLE-MOLECULE ANALYSIS OF METHYL VIOLOGEN BINDING TO CdSe/CdS CORE-SHELL QUNTUM DOTS VIA PHOTOLUMINESCENCE BLINKING[6]

7.1 Overview

This chapter investigates the binding behavior and photoinduced electron transfer dynamics of methyl viologen (MV^{2+}) on the surface of CdSe/CdS core-shell quantum dots through single-molecule fluorescence blinking analysis. Using total internal reflection fluorescence microscopy, we recorded fluorescence intensity trajectories of individual quantum dots in the absence and presence of methyl viologen. Bare quantum dots exhibited characteristic stochastic blinking with broad ON-state dwell time distributions, while MV-treated quantum dots showed increased OFF-state occupancy and suppressed emission, indicating efficient electron transfer to surface-bound MV^{2+}. Time-resolved photoluminescence measurements further supported a photoinduced electron transfer mechanism, with Stern–Volmer analysis confirming dynamic quenching behavior. This study demonstrates that single-molecule blinking trajectories provide a sensitive and high-resolution probe for quantifying electron transfer kinetics and surface binding behavior in quantum dot–molecule systems. The results offer new insights into catalyst loading effects, charge separation efficiency, and interfacial redox dynamics, providing a framework for optimizing quantum dot-based photocatalysts and molecular heterojunctions.

7.2 Introduction

Quantum dots (QDs) exhibit unique size-tunable optical and electronic properties that allow these

[6]This chapter is a manuscript in preparation, with the goal to be submitted for publication: Lustig, D., Prahdan, A., Click, S., Bird, O., Dukovic, G., and Sambur, J., Single-Molecule Analysis of Methyl Viologen Binding to CdSe/CdS Core-Shell Quantum Dots Via Photoluminescence Blinking.

materials to be valuable platforms for studying charge transfer processes at the single-particle level.[1–5] Among these processes, photoinduced electron transfer (PET) between QDs and molecular redox species is of particular interest for applications in photocatalysis, energy conversion, and biosensing.[6–10] Specifically, cadmium selenide (CdSe) and cadmium sulfide (CdS) QDs have been extensively used as model systems for studies of photoinduced charge transfer from semiconductor nanocrystals.[6] CdSe/CdS core-shell QDs, with their type-I band alignment and strong quantum confinement in the CdSe core, serve as ideal systems for probing charge transfer dynamics due to their enhanced photostability and bright, stable fluorescence.[11,12] When coupled to electron acceptors such as methyl viologen (MV), QDs can undergo PET that modulates their fluorescence intensity, providing a sensitive readout of charge transfer events.[2,13,14]

Importantly, a key motivation for understanding QD–molecule interactions stems from solar-to-chemical conversion applications such as photocatalytic water splitting.[15–18] Previous studies have demonstrated that loading nanoparticulate co-catalysts onto semiconductor photocatalysts significantly enhances hydrogen evolution reaction (HER) activity, up to an optimal threshold. For instance, loading $Rh_{2-y}Cr_yO_3$ onto a photocatalyst surface improves HER activity until a critical loading of 1.0 wt% Rh and 1.5 wt% Cr is reached.[19] Beyond this threshold, excessive cocatalyst coverage leads to reduced performance.[19] These results highlight that catalyst loading is not monotonic: too little coverage results in under-utilization of the surface, while too much surface coverage may block light absorption or induce charge trapping.

Given that HER involves a 2-electron transfer process[20], questions arise about whether multiple catalysts bound to a single QD could compete for electrons, or whether their spatial arrangement affects PET. Here, we ask two critical questions: *1. Can single-molecule fluorescence microscopy detect biding heterogeneity of surface catalysts? 2. Can fluorescence blinking resolve*

whether QDs exhibit different charge transfer kinetics depending on catalyst coverage? This chapter aims to address these questions using MV^{2+} as a molecular model for a redox-active cocatalyst.

Single-molecule fluorescence techniques allow for real-time monitoring of QD emission trajectories, which display characteristic blinking behavior as they switch between emissive "on" and non-emissive "off" states.[10,21–23] This blinking arises from charge carrier trapping, Auger recombination, and other photophysical processes, but can also reflect charge transfer events such as electron transfer to MV^{2+}.[23] One method to probe the effects of surface chemistry on the optical properties of individual QDs is through monitoring their photoluminescence intermittency, or blinking behavior.[22] By analyzing the statistical distributions of "on" and "off" dwell times, transition rates, and intensity fluctuations, insights can be gained into the underlying mechanisms of charge transfer and binding interactions at the single-particle level.

Additionally, a major challenge in photocatalysis research is accurately identifying how and where molecular acceptors bind to nanocrystal surfaces.[13,14] Furthermore, the influence of binding on charge transfer complicates interpretation– since increasing the number of bound acceptors can accelerate observed electron transfer rates. Single-molecule fluorescence techniques offer a powerful approach to circumvent these challenges. By monitoring individual QD trajectories, one can directly correlate blinking patterns with changes in local redox environment, molecular binding events, and charge transfer kinetics– without needing ensemble averaging.

This chapter aims to investigate the binding behavior of MV^{2+} to CdSe/CdS QDs by analyzing single-molecule fluorescence blinking trajectories. Through experimental measurements and statistical modeling, we characterize how MV^{2+} binding influences blinking kinetics, identify concentration-dependent effects, and develop a mechanistic model for PET-

mediated fluorescence quenching. Additionally, we explore whether blinking statistics can reveal not just the presence, but the quantity and spatial distribution of molecular catalysts like MV^{2+} on QD surfaces, potentially linking blinking dynamics to catalytic heterogeneity.

7.3 Methods

7.3.1 Materials

The following chemicals were purchased and used as received: cadmium oxide (CdO), octadecylphosphonic acid (ODPA), trioctylphosphine oxide (TOPO), trioctylphosphine (TOP), selenium (Se), Oleylamine, octadecene, octanethiol, and oleic acid. For washing, methanol, ethanol, acetone, octylamine, toluene, and hexanes were used.

7.3.2 Preparation of Cd-Oleate Precursor

In a 100 mL round bottom flask, 0.284 g (2.212 mmol) CdO and 22 mL oleic acid were evacuated on a Schlenk line at 120 °C for 30 min. Following degassing, the mixture was heated to 220 °C under an inert argon atmosphere, where the color of the solution changed from the reddish brown of CdO to colorless Cd-oleate. The reaction mixture was then cooled to 120 °C and degassed for 1 h to remove excess water formed from the reaction. The mixture was stored under argon via Schlenk line at room temperature and heated to 60 °C for use. The final concentration of the Cd-Oleate precursor was 0.1 M.

7.3.3 Synthesis of CdSe Quantum Dots

CdSe QDs were synthesized according to the previously published method by Carbone et al. with minimal modifications.[24] Briefly, 0.063 g (0.49 mmol) CdO, 0.2820 g (0.8455 mmol) ODPA, and 3.0010 g TOPO were evacuated in a 25 mL round bottom flask via a Schlenk line at 120 °C for 30 min. Following degassing, the reaction mixture was heated to 320 °C under an inert argon atmosphere, where the color of the solution changed from the reddish brown of CdO to colorless

Cd-ODPA. Once the solution was completely colorless and translucent, 1 g of TOP was injected and the solution was heated to 350 °C. Upon reaching 350 °C, a mixture of 60 mg (0.76 mmol) Se that was previously dissolved in 0.500 mL TOP was rapidly injected into the reaction mixture to induce nucleation of CdSe QDs. After 30 s of growth, the heating mantle was removed, and the solution was rapidly cooled to room temperature with an oil bath. To prevent solidification of TOPO, a mixture of 4 mL methanol and 4 mL toluene was injected once the solution cooled to 60 °C.

The produced CdSe QDs were washed under inert atmosphere by centrifugation at 3400 rpm for 20 min. The precipitated pellet of QDs was redispersed in 1 mL toluene, 1 mL octylamine, and precipitated with 15 mL methanol and centrifugation at 4400 rpm for 10 min. The precipitated pellet of QDs was next redispersed in 2 mL of toluene and precipitated then with 10 mL methanol and centrifugation at 4400 rpm for 10 min. The precipitated pellet of QDs was finally redispersed in 2 mL of hexanes and stored under an inert atmosphere. The purified QDs had a 1S exciton absorbance peak at 524 nm that corresponds to a 2.6 nm diameter. The diameter and concentration of the CdSe QDs in solution were estimated based on the absorption of the first excitonic peak using the corrected sizing curve reported by Jasieniak et al.[25] The stock solution concentration was calculated to be 441 μM CdSe QDs.

7.3.4 Synthesis of CdSe/CdS Core-Shell Quantum Dots

CdSe/CdS core-shell QDs were synthesized by growing a thick CdS shell over 2.6 nm diameter CdSe QDs via a modified continuous injection procedure. Briefly, 3 mL oleylamine and 3 mL octadecene (ODE) were degassed in a 50 mL round bottom flask at 120 °C for 30 min. Next, 227 μL (100 nmol) CdSe QD stock was injected and degassed for another 30 min. Following degassing, the reaction mixture was heated to 310 °C under an inert argon atmosphere. Once the

reaction reached 270 °C, a mixture of 6 mL 0.12 M octanethiol in ODE and 6 mL 0.1 M Cd-oleate in oleic acid were continuously injected at the rate of 5 mL/h. After 10 mL were injected over 2 h, the continuous injection was stopped, and 1.00 mL oleic acid was injected. The reaction mixture was annealed for 30 min at 310 °C and then removed from heat and allowed to cool to room temperature in an oil bath.

The produced CdSe/CdS core-shell QDs were washed under inert atmosphere by addition of 1 mL toluene, 1 mL methanol, and 3 mL ethanol, followed by centrifugation at 3400 rpm for 15 min. The precipitated pellet of QDs was redispersed in 1 mL toluene and precipitated with 1 mL ethanol and centrifugation at 3400 rpm for 10 min. The precipitated pellet of QDs was finally redispersed in 2 mL of hexanes and stored under an inert atmosphere.

7.3.5 Quantum Dot Characterization

The absorbance and emission properties of CdSe/CdS core-shell QDs were characterized by UV-Vis absorption spectroscopy and steady-state photoluminescence (PL) spectroscopy (Horiba Duetta Fluorescence and Absorbance Spectrometer). Absorbance spectra of the QD solutions were collected with a range of 300–600 nm and an integration time of 0.1 s. Steady-state PL spectra Spectra were collected by using an excitation wavelength of 355 nm. The emission bandwidth was kept at 5 nm and the dwell time at 0.05 s. All spectra were measured at room temperature using colloidal QD suspensions in hexanes and 1 cm pathlength quartz cuvettes. The purified core-shell QDs had a PL peak at 610 nm with 32 nm full width at half maximum (FWHM) and 90% photoluminescence quantum yield (PLQY). TEM micrographs show a final diameter 9.3 nm, which corresponds to ~6 monolayers (MLs) of CdS grown on the 2.6 nm CdSe core.

7.3.6 Ensemble-level Charge Transfer Measurements

Steady-state and TRPL spectroscopy were used to study PET between CdSe/CdS core-shell QDs and MV^{2+} electron acceptors. TRPL measurements were performed on an Edinburgh Instruments FS5 equipped with a 365 nm pulsed LED (EPLED, 100 kHz). The optical density of the exciton peak was adjusted to 0.1 for all colloidal QD samples to prevent QD aggregation and minimize reabsorption effects at the excitation wavelength. For the steady-state PL experiments, microliter volumes of a 1 mM ethanolic solution of MV were incrementally injected into 3 mL of a colloidal QD solution. PL spectra of QD/MV^{2+} mixtures were excited at 340 nm. All TRPL data was acquired at 612nm emission with a bandwidth of 5.20 nm and channel range of 2048. The time range was selected as 100 ns with stop conditions of 180 seconds. The instrument response function (IRF) was measured via laser scattering from a solution of colloidal silica (LUDOX). TRPL data was deconvoluted from the IRF using a general bi-exponential equation with a background offset (Edinburgh, Fluoracle). Figure E1 shows the measured IRF. The deconvoluted lifetimes decay profiles were normalized and plotted together, and the average lifetime was calculated for each decay plot using the Eq. 7.1, where A1 and A2 are amplitude coefficients, and τ_1 and τ_2 are fast and slow decay lifetimes, respectively.

$$\tau_{\text{avg}} = \frac{\mathrm{A}_1\tau_1^2 + \mathrm{A}_2\,\tau_2^2}{\mathrm{A}_1\tau_1 + \mathrm{A}_2\,\tau_2} \qquad \text{Eq. 7.1}$$

7.3.7 Sample Preparation for Imaging

For control experiments, 70 μL of the diluted QD solution in hexanes was drop cast on a clean quartz slide until complete evaporation. Then, 200 μL of the same QD solution was streamed over the quartz slide. A water droplet was placed between the QD-coated quartz slide and a #1 glass coverslip (19904). The water was chosen because (1) the QDs are not soluble in this media due to dispersion in hexanes and, therefore, the fluid prevents the QDs from detaching from the

quartz slide; (2) the QD emission decays in air; (3) the QDs detach from the slide if the experiments were performed in the same solvent used for ensemble-level testing; (4) the water is index-matched to our 60× water immersion objective (NA = 1.2, Olympus, UPLANSAPO60×/W). For QD/MV^{2+} PL quenching experiments, Methyl viologen dichloride hydrate (1.4 mg) was added to the CdSe/CdS stock solution and mixed over night at room temperature. The QD/MV^{2+} mixture was then prepared the same as for the control experiments, with the modification that an MV^{2+}/water mixture was used for imaging.

7.3.8 Single-Molecule Fluorescence Microscopy

Widefield microscopy measurements were performed on an Olympus IX73 inverted optical microscope equipped with a prism-type total internal reflection fluorescence (TIRF) microscopy setup. A 355 nm laser (Coherent Genesis CX) excites the CdSe/CdS QDs at a power density of 0.03 kW/cm^2. Photons emitted from the sample were collected through the objective, passed through a dichroic mirror (405 nm), long pass filter (cutoff wavelength: 440 nm) in the filter cube of the Olympus microscope, and a bandpass filter which was chosen to match the emission signal from the QDs (618/50 bandpass) until finally projected onto an EMCCD camera (Andor iXon 897). Fluorescence images were continuously acquired at a 20 ms frame rate for a total of 7000 images. The intensity trajectories of single ZnO NCs and dye molecules from the image stacks, or movies, were extracted using the detailed image analysis algorithm described in Appendix E.

7.4 Results

Figure 7.1a shows TEM micrographs with a diameter of 9.3 nm, which corresponds to ~6 MLs of CdS grown on the 2.6 nm CdSe core. Figure 7.1b shows the optical spectroscopic properties of the QDs. A typical absorbance spectrum is shown (solid green trace), showing strong

absorbance between 300 – 500 nm. The PL peak when excited with 355 nm light is approximately 610 nm with a 32 nm FWHM (blue dashed trace). The corresponding PL excitation (PLE) spectra shows a maximum at 385 nm when the PL is monitored at 610 nm (purple dashed trace).

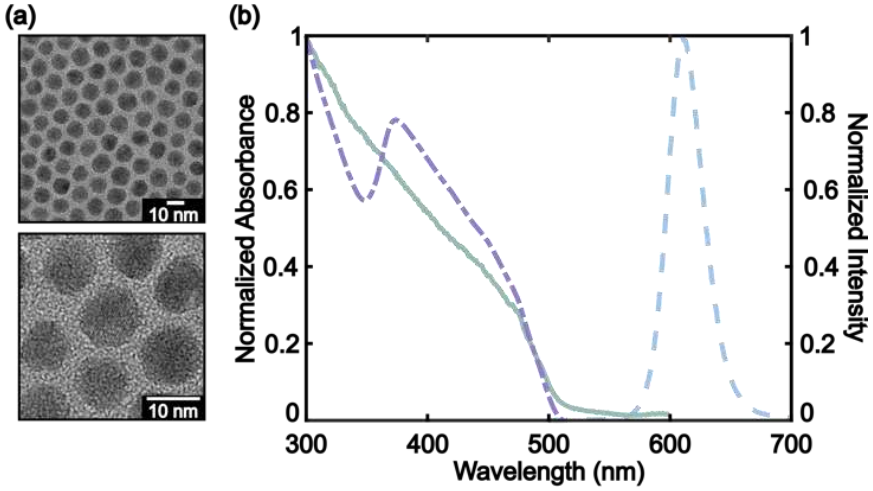

Figure 7.1 (a) TEM image of CdS/CdS core–shell quantum dots QDs. (b) Absorption (green), excitation (purple) and emission (blue) spectra of the QD ensemble in hexanes.

Electron transfer-mediated PL quenching of the QDs by MV^{2+} serves as a probe for the binding affinity of MV^{2+} for the surfaces of the QDs.[13] The efficiency with which MV^{2+} quenches the PL of these QDs through PET depends on the binding affinity of MV^{2+} to their surfaces.[13] Figure 7.2a shows the quenching of the steady-state PL intensities of CdSe/CdS QDs upon exposure to increasing concentrations of MV^{2+}. The cartoon schematic in Figure 7.2a shows the conceptual model wherein MV^{2+} binds to the QD surface and accepts an electron from the excited QD, leading to nonradiative recombination and suppression of PL. As the MV^{2+} concentration increases, the steady-state PL spectra shows a progressive decrease in PL intensity, confirming efficient quenching my MV^{2+} due to charge transfer.

Additionally, Figure 7.2b shows that the time-resolved PL decay curves of the QDs reveal faster decay kinetics with increasing MV^{2+} concentrations, indicating that the quenching process

occurs via dynamic (i.e., diffusional or surface-bound) electron transfer.[26] The PL decay profiles were fit using a biexponential function:

$$I(t) = A_1 e^{-\tau/\tau_1} + A_2 e^{-\tau/\tau_2} \quad \text{Eq. 7.2}$$

where A1 and A2 are amplitude coefficients, and τ_1 and τ_2 are fast and slow decay lifetimes, respectively. To understand the quenching dynamics between MV^{2+} and the QDs, Stern-Volmer analysis was applied on steady state emission and TRPL data using the following Stern-Volmer equations:

$$\frac{I_0}{I} = 1 + K_{SV}[Q] \quad \text{Eq. 7.3}$$

$$\frac{\tau_0}{\tau} = 1 + K_{SV}[Q] = 1 + K_q \tau_0 [Q] \quad \text{Eq. 7.3}$$

where, I_0 represents the emission intensity of the QDs and I represents the intensity of the QDs in the presence of the quencher (MV^{2+}). K_{sv} is the Stern-Volmer constant and [Q] is the quencher concentration in the sample. τ_0 represents the lifetime of the QDs and τ represents the lifetime of samples containing both the QDs and the quencher. K_q is the bimolecular quenching constant. The steady-state Stern-Volmer plot (Figure 7.2c) shows a linear increase in PL quenching with MV^{2+} concentration, suggesting that each MV^{2+} molecule independently contributes to quenching. Likewise, the lifetime-based Stern-Volmer plot (Figure 7.2d) confirms dynamic quenching, as evidenced by the concentration-dependent reduction in average lifetime. Together, these results provide strong evidence that MV^{2+} mediates efficient electron transfer from the QD to the acceptor, consistent with its role as a redox-active quencher. Table 7.1 displays the information extracted from the TRPL fitting procedure and the values shown for the Stern-Volmer plot in Figure 7.2d.

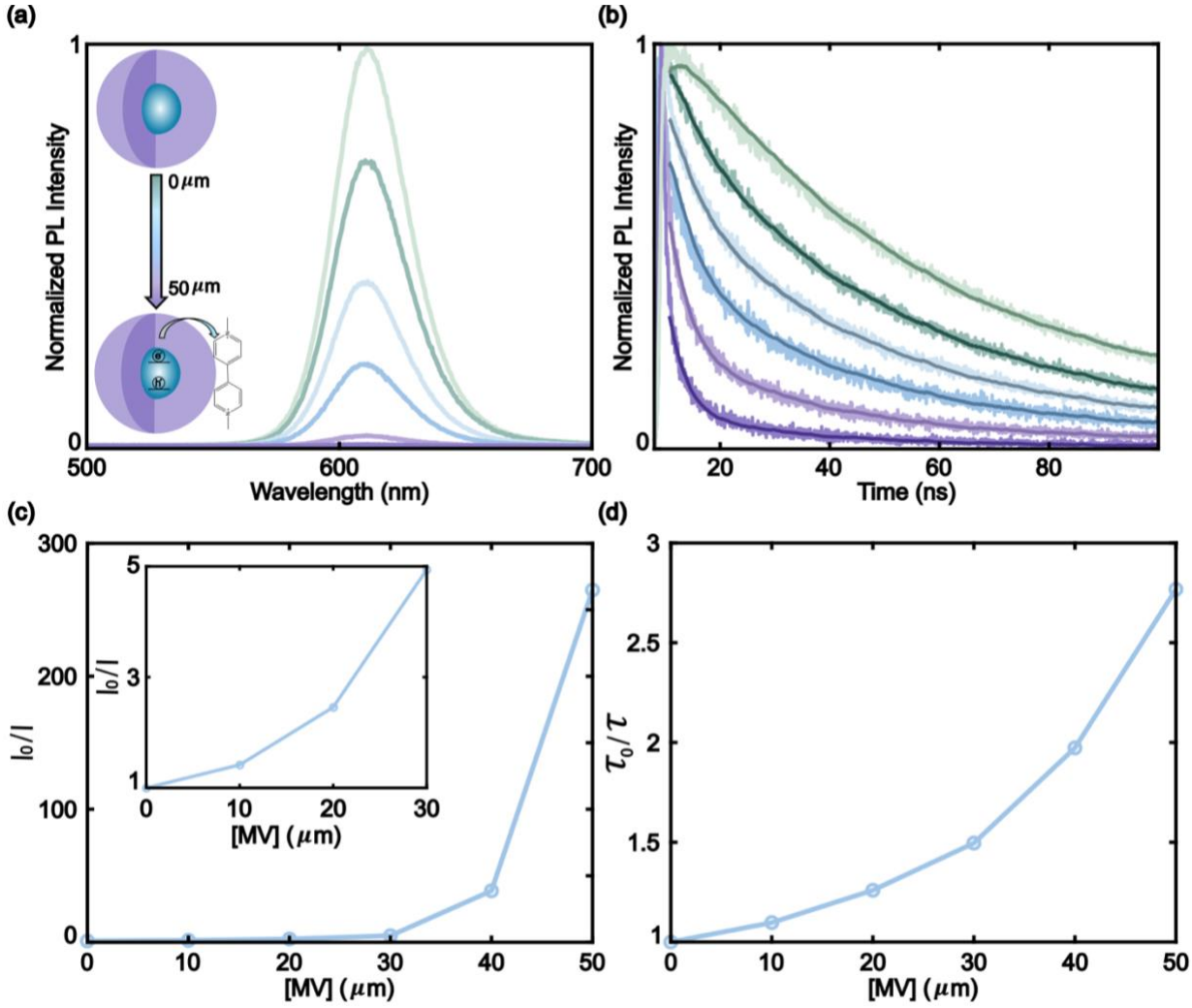

Figure 7.2 (a) Normalized steady-state PL spectra for CdSe/CdS QDs with increasing concentration of MV^{2+}. The light green trace represents the emission spectrum of bare QDs. All other traces represent QD/MV^{2+} mixtures. The excitation wavelength was 355 nm. The inset is a cartoon schematic of the physical adsorption of MV^{2+} electron acceptor molecules on the QD surface resulting in PL quenching. (b) Normalized time-resolved PL decay curves of QDs with increasing MV^{2+}concentration as described in Table 7.1. Solid darker colored lines represent bi-exponential fits using Eq. 7.1. (c) Steady-state Stern-Volmer plot of concentration-dependent quenching of PL intensity with increasing MV^{2+}concentration. (d) Time-resolved Stern-Volmer plot showing the relative change in average lifetimes with the successive addition of MV^{2+}.

Table 7.1 Information extracted from the TRPL fitting procedure used for Stern-Volmer plots.

[MV] (μm)	MV:QD ratio	τ_1 (ns)	τ_2 (ns)	A_1	A_2	τ_{avg} (ns)	τ_0/τ_{avg}
0	1:0	43.0	0.00	3.96	0.00	43.0 (τ_0)	1
10	1:30	5.28	41.0	1.18	2.76	39.1	1.10
20	1:60	4.84	37.0	1.12	1.50	34.1	1.26
30	1:120	3.92	32.5	0.62	0.490	28.7	1.50
40	1 :150	3.19	27.9	0.770	0.270	21.8	1.97
50	1:180	2.72	24.8	0.343	0.052	15.5	2.77

We analyzed the single-QD blinking trajectories for 744 bare QDs and 805 QD/ MV^{2+} pairs. Figure 7.3 shows representative single-molecule fluorescence intensity trajectories of bare CdSe/CdS QDs and their corresponding intensity histograms, used to analyze the native blinking behavior in the absence of MV^{2+}. Each single-molecule trajectory was corrected for drift during the movie acquisition (Figure E2) and background subtraction was performed (Figure E3), using a procedure based on previous work reported by our group.[27] Each trajectory (left panels of Figure 7.3a–c) shows the time-dependent blinking behavior of an individual quantum dot over a 500-second acquisition window, while the right panels present the associated intensity histograms overlaid with Gaussian fits used to determine on and off states. Insets in the trajectory plots show fluorescence localization images confirming single QD identification. Across all trajectories, the fluorescence fluctuates between high and low states, characteristic of blinking dynamics arising from spontaneous transitions between bright emissive (on) and dark non-emissive (off) states.

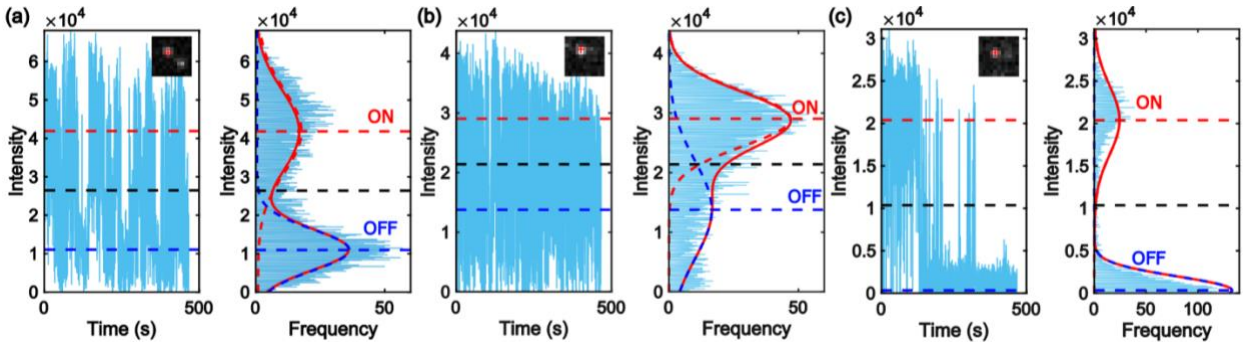

Figure 7.3 Representative single-QD blinking fluorescence intensity trajectories and corresponding intensity distributions for 3 different bare QDs. The inset shows the widefield image of the QD. The distributions are fit with two gaussian functions (blue and red dashed lines) and a mixed gaussian model (red solid line). The on (red dashed line), average (black dashed line), and off (blue dashed line) thresholds are determined from the average of the gaussian functions and when the two gaussian functions overlap.

Figure 7.3a shows the QD exhibits frequent switching between on and off states, with a clear bimodal histogram distribution. Gaussian fits to the histogram reveal two well-separated peaks corresponding to the on and off states, indicated by red and blue dashed lines, respectively. This

bimodality enables straightforward thresholding for dwell time analysis. The inset fluorescence spot confirms the localization of a single QD. Figure 7.3b depicts a second QD that remains mostly on throughout the duration of measurement, with only shallow excursions to lower intensity levels. The corresponding histogram shows a unimodal distribution skewed toward higher intensities, indicating that the off state is less accessible or shorter-lived for this QD, possibly due to fewer trap states. Figure 7.3c highlights a more complex blinking profile, where the quantum dot intermittently enters long-lived off states, or photobleached. The intensity histogram is broader and less symmetric, with an extended tail toward lower intensities. This QD exhibits dynamic heterogeneity, with transitions between clearly defined on and off levels, but also significant fluctuation in intermediate intensity regions. Overall, these trajectories establish a baseline for comparing the effects of MV or other electron acceptors. The on/off state thresholds (black, red, and blue dashed lines) are used to discretize trajectories and quantify dwell times for future kinetic modeling. These bare QD trajectories are consistent with power-law distributed blinking commonly observed in colloidal QDs[22,23,28] and serve as essential controls for interpreting quenching behavior in the presence of surface-bound electron acceptors.

Figure 7.4 displays representative single-molecule fluorescence trajectories of CdSe/CdS QDs in the presence of MV^{2+}. These traces illustrate the quenching effect of MV^{2+} through increased frequency and persistence of off states, a hallmark of PET. Figure 7.4a shows a QD that exhibits nearly complete quenching for most of the recording duration, punctuated by short-lived ON excursions. The histogram reveals a narrow intensity distribution dominated by a single peak at low intensity, consistent with an MV-induced persistent off state. Both the on and off thresholds are indicated, but the histogram lacks a distinguishable on peak, emphasizing the suppression of emissive events.

Figure 7.4b presents a QD with pronounced blinking behavior. The trajectory alternates between clear on and off levels, and the histogram shows a well-resolved bimodal distribution. Gaussian fits to the intensity data clearly differentiate two populations, enabling robust thresholding and dwell time analysis. The frequent switching and long off periods are indicative of MV-mediated PET events, where charge separation traps the QD in a non-emissive state. The histogram reveals a clear bimodal distribution, with a dominant off population. This behavior is consistent with efficient electron transfer to MV^{2+}, trapping the QD in a non-emissive, oxidized state until slow back-electron transfer or MV desorption restores the on state. Figure 7.4c shows a QD that spends most of the measurement in the on state, but with intermittent dark excursions. The intensity histogram is asymmetric, with a broad on distribution and a lower frequency off population. While this QD retains relatively high brightness, the emergence of quenching events reflects partial MV binding or dynamic association–dissociation behavior.

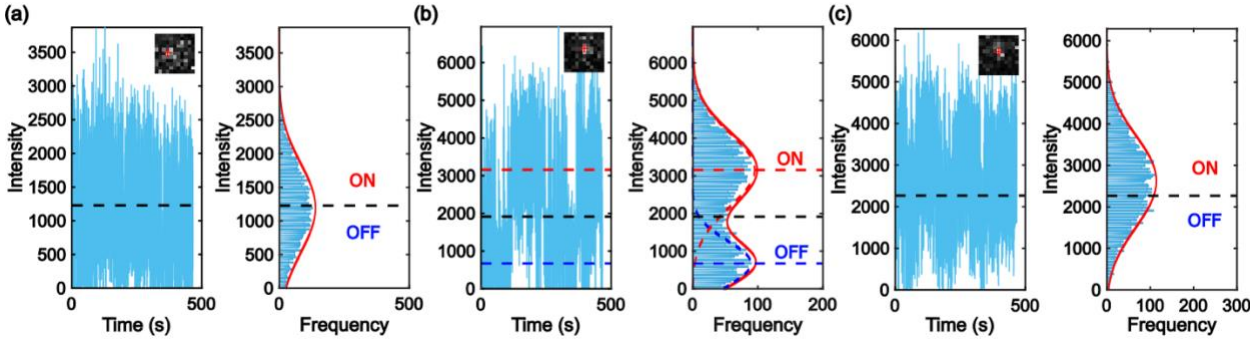

Figure 7.4 Representative single-QD blinking fluorescence intensity trajectories and corresponding intensity distributions for 3 different QD/ MV^{2+} pairs. The inset shows the widefield of the QD. The distributions are fit with two gaussian functions (blue and red dashed lines) and a mixed gaussian model (red solid line). The on (red dashed line), average (black dashed line), and off (blue dashed line) is determined from the average of the gaussian functions and when the two gaussian functions overlap.

Together, these trajectories demonstrate the PET-induced quenching effect of MV^{2+} on QD blinking. Compared to bare QDs (Figure 7.3), these MV-treated QDs display lower average intensities, increased off state frequency, and more suppressed on populations. This supports the hypothesis that surface-bound MV^{2+} modulates QD photophysics by accepting photoexcited

electrons, stabilizing the charge-separated state and extending the dark state dwell times. These single-particle measurements provide direct, high-resolution insight into the interaction dynamics between QDs and molecular electron acceptors, which is not easily accessible through ensemble measurements.

7.5 Discussion

Figure 7.3 and Figure 7.4 collectively demonstrate how methyl viologen (MV^{2+}), a redox-active electron acceptor, alters the fluorescence blinking behavior of individual CdSe/CdS quantum QDs. In Figure 7.3, which shows QDs in the absence of MV^{2+}, the blinking trajectories are characterized by stochastic switching between emissive on and non-emissive off states. The frequency and duration of these transitions vary from particle to particle, but the majority of QDs exhibit relatively balanced on/off times or spend most of the time in the bright state. Histograms of emission intensity frequently show a clear bimodal distribution, and on state populations dominate in many cases. This native blinking is attributed to intrinsic processes such as charge trapping, surface states, and Auger-mediated nonradiative recombination.

In contrast, Figure 7.4 presents QDs measured in the presence of MV^{2+} and reveals significant changes in blinking statistics. The trajectories display longer dark states and, in some cases, almost complete quenching of the PL (Figure 7.4a). The intensity histograms often skew toward lower intensities, indicating increased off state occupancy. Several trajectories exhibit frequent, long-lived off events, and the histograms show unimodal or even off-dominated distributions. This behavior is consistent with efficient PET from the QD to MV^{2+}, which leads to fluorescence quenching by forming a charge-separated state. The persistence of the off state suggests that back-electron transfer is slow, supporting a model in which MV^{2+} stabilizes the oxidized QD and delays recovery of the emissive state. Additionally, some QDs in Figure 7.4c

retain intermittent bright states, implying partial quenching or dynamic binding/unbinding of MV^{2+}. This heterogeneity highlights the molecule-to-molecule variation in binding strength and orientation, which is only accessible through single-molecule measurements.

Figure 7.5 compares the ensemble-compiled dwell time histograms for single-molecule blinking trajectories of CdSe/CdS QDs in the absence (blue) and presence (purple) of MV^{2+}. These histograms represent the distribution of on-state durations collected from many individual trajectories. The shape of each distribution provides insight into the underlying photophysical dynamics that govern QD fluorescence intermittency. For bare QDs (blue distribution), the on-time distribution displays a heavy-tailed, non-exponential decay with two prominent peaks. This behavior is well-described by a power-law distribution with exponential truncation, indicative of multiple blinking mechanisms and a broad range of rate constants governing return to the off state.[28] The first peak corresponds to short-lived emissive bursts, while the second reflects longer on states before the QD transitions into a dark, non-emissive state. The broad tail of the distribution confirms that the blinking is governed by complex kinetics involving charge trapping/detrapping and Auger processes.[23]

In contrast, the purple distribution shows the on-time distribution for QDs exposed to MV^{2+}. Here, the distribution narrows significantly and lacks the long tail seen in the bare QDs. The overall distribution is well fit by a single exponential decay (red dashed line), suggesting a more uniform and faster transition from the on to off state. This change in statistical behavior is consistent with a quenching mechanism dominated by PET to MV^{2+}. In this case, once the QD is excited, the electron is rapidly transferred to a bound MV^{2+} molecule, suppressing PL and shortening the duration of the on state. The reduced variability in on times across the population implies that the PET process introduces a more deterministic quenching pathway, overriding the

more complex intrinsic blinking dynamics observed in bare QDs. Together, these results reinforce the model in which MV^{2+} binding accelerates QD deactivation via PET and suggest that single-molecule dwell time statistics can serve as sensitive indicators of molecular binding and electron transfer kinetics. The loss of heavy-tailed blinking upon MV addition provides direct evidence that electron acceptors reshape the fluorescence intermittency landscape, suppressing long-lived bright states and promoting efficient quenching pathways.

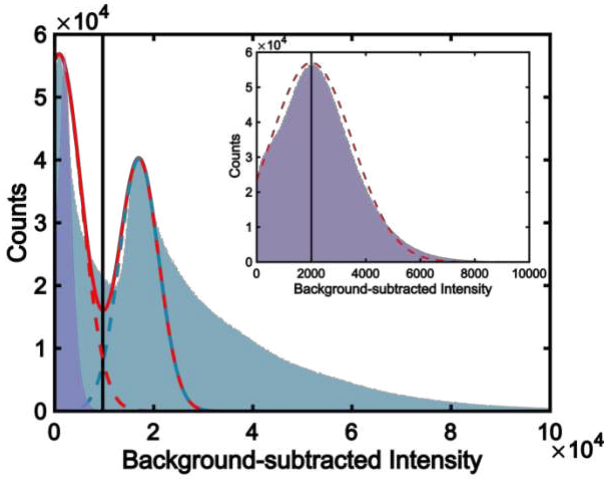

Figure 7.5 Combined distribution of single-QD blinking fluorescence intensity trajectories of 744 bare QDs (blue distribution) and for 805 QD/MV^{2+} pairs (purple distribution). The inset shows the zoomed-in view of the QD/MV^{2+} pair distribution. The distributions are fit with two gaussian functions (blue and red dashed lines) and a mixed gaussian model (red solid line). The black solid lines are when the two gaussian functions overlap and the average of the QD/MV^{2+} pair distribution from the gaussian fitting.

Scheme 7.1 schematically illustrates various photophysical and electron transfer pathways involved in QD blinking behavior, both in the absence and presence of a surface-bound electron acceptor such as MV^{2+}. As shown in Scheme 7.1a, a photoexcited electron–hole pair (exciton) relaxes radiatively via band-edge recombination, resulting in photon emission (i.e., an on state). Scheme 7.1b introduces nonradiative pathways: the electron or hole may become trapped at surface states or defects, interrupting radiative recombination and resulting in a temporary off state. Such intrinsic blinking is characteristic of bare QDs and leads to power-law distributed dwell times.[22,23,28] Scheme 7.1c shows possible multiexciton generation leading to Auger recombination,

where the energy of an exciton is non-radiatively transferred to a second charge carrier, further quenching emission and introducing blinking intermittency.[23] Scheme 7.1d introduces an alternative deactivation route via PET to a molecular acceptor, MV^{2+}. Upon excitation, the QD rapidly transfers its electron to MV^{2+}, leaving behind a hole and forming a charge-separated state. Because the QD cation cannot emit a photon until the electron is returned (via back-electron transfer), the system remains in an off state. This process is central to quenching observed in MV-treated QDs and results in mono-exponential on-time distributions, as shown in Figure 7.5. This schematic underscores the distinct mechanistic contributions to blinking: radiative vs. nonradiative decay, Auger recombination, and PET to external quenchers. The addition of MV^{2+} alters the blinking dynamics by introducing a fast and efficient pathway for deactivating the excited state, thereby reducing the frequency and duration of on events. It also illustrates why MV-induced blinking differs kinetically from native QD blinking, with fewer intermediate states and greater dwell-time regularity. This framework provides the physical basis for interpreting the changes in blinking statistics upon MV addition and supports the use of fluorescence intermittency as a probe for interfacial electron transfer kinetics.

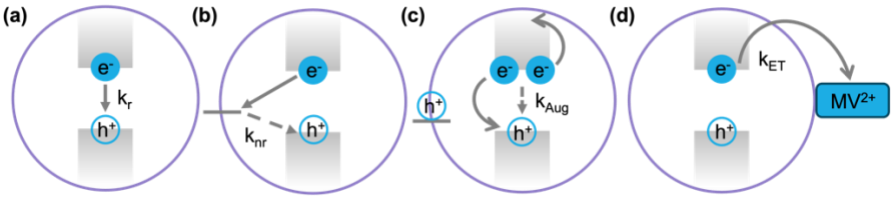

Scheme 7.1 Cartoon schematic illustrating various photophysical and electron transfer pathways involved QD blinking behavior, both in the absence and presence of a surface-bound electron acceptor such as MV^{2+}.

7.6 Conclusion

This chapter demonstrates how single-molecule fluorescence blinking trajectories can be leveraged to probe the binding and charge transfer behavior of MV^{2+} on CdSe/CdS core-shell QDs. By comparing the blinking statistics of bare QDs to those treated with MV^{2+}, we observed a distinct

increase in off state frequency and duration upon MV addition, consistent with efficient PET to the surface-bound redox-active acceptor. Single-particle trajectories revealed substantial heterogeneity across individual QDs, with some remaining mostly bright, others largely quenched, and many displaying intermediate blinking patterns. Intensity histograms and threshold-based dwell time analysis showed that MV not only shortened on-state durations, but also induced an apparent shift from power-law to mono-exponential kinetics, signaling a transition from intrinsic blinking to PET-mediated quenching. Ensemble dwell time histograms further confirmed that MV binding narrows the on-state distribution and suppresses long-lived emissive states. These findings were supported by Stern–Volmer analysis and biexponential lifetime fitting, which revealed that both PL intensity and lifetime decreased with increasing MV^{2+} concentration, indicative of dynamic quenching through surface-bound electron transfer. Mechanistic schematics and statistical modeling suggested that MV serves as a competitive deactivation pathway, stabilizing the charge-separated state and slowing recovery of fluorescence. Importantly, this study highlights that blinking trajectories encode rich mechanistic information not just about charge transfer rates, but also about molecular binding behavior, catalyst loading, and heterogeneity in interfacial interactions. By correlating changes in blinking statistics with MV^{2+} concentration and QD morphology, we establish a powerful, non-invasive method to quantify molecular-scale charge transfer processes. This approach lays the foundation for future efforts to spatially resolve catalyst distribution and optimize photocatalytic efficiency through single-nanocrystal analysis.

7.7 Author Contributions

My contributions to this work included conceptualization, data curation, formal analysis, investigation, methodology, visualization, and writing. Dr. Sophia Click synthesized core-shell CdSe/CdS quantum dots and performed TEM analysis. Aradhana Pradhan collected steady-state

and TRPL data and computed Stern-Volmer plots under the guidance of D.R.L. D.R.L. performed all single-molecule experiments and analyzed and interpreted data. Prof. Gordana Dukovic and J.B.S. assisted with conceptualization. Dr. Sophia Click and J.B.S. assisted with experimental design.

REFERENCES

(1) Vokhmintcev, K. V.; Samokhvalov, P. S.; Nabiev, I. Charge Transfer and Separation in Photoexcited Quantum Dot-Based Systems. *Nano Today* **2016**, *11* (2), 189–211. https://doi.org/10.1016/j.nantod.2016.04.005.
(2) Li, Q.; Wu, K.; Zhu, H.; Yang, Y.; He, S.; Lian, T. Charge Transfer from Quantum-Confined 0D, 1D, and 2D Nanocrystals. *Chem. Rev.* **2024**, *124* (9), 5695–5763. https://doi.org/10.1021/acs.chemrev.3c00742.
(3) Mimona, M. A.; Rimon, M. I. H.; Zohura, F. T.; Sony, J. M.; Rim, S. I.; Arup, M. M. R.; Mobarak, M. H. Quantum Dot Nanomaterials: Empowering Advances in Optoelectronic Devices. *Chem. Eng. J. Adv.* **2025**, *21*, 100704. https://doi.org/10.1016/j.ceja.2025.100704.
(4) Cotta, M. A. Quantum Dots and Their Applications: What Lies Ahead? *ACS Appl. Nano Mater.* **2020**, *3* (6), 4920–4924. https://doi.org/10.1021/acsanm.0c01386.
(5) Mahadevu, R.; Pandey, A. Thermodynamic Model for Quantum Dot Assemblies Formed Because of Charge Transfer. *ACS Omega* **2018**, *3* (1), 266–272. https://doi.org/10.1021/acsomega.7b01486.
(6) Leng, H.; Loy, J.; Amin, V.; Weiss, E. A.; Pelton, M. Electron Transfer from Single Semiconductor Nanocrystals to Individual Acceptor Molecules. *ACS Energy Lett.* **2016**, *1* (1), 9–15. https://doi.org/10.1021/acsenergylett.6b00047.
(7) Hildebrandt, N.; Spillmann, C. M.; Algar, W. R.; Pons, T.; Stewart, M. H.; Oh, E.; Susumu, K.; Díaz, S. A.; Delehanty, J. B.; Medintz, I. L. Energy Transfer with Semiconductor Quantum Dot Bioconjugates: A Versatile Platform for Biosensing, Energy Harvesting, and Other Developing Applications. *Chem. Rev.* **2017**, *117* (2), 536–711. https://doi.org/10.1021/acs.chemrev.6b00030.
(8) Jose, A. R.; Vikraman, A. E.; Girish Kumar, K. Photoinduced Electron Transfer between Quantum Dots and Pralidoxime: An Efficient Sensing Strategy. *New J. Chem.* **2017**, *41* (19), 10828–10834. https://doi.org/10.1039/C7NJ00795G.
(9) Tvrdy, K.; Frantsuzov, P. A.; Kamat, P. V. Photoinduced Electron Transfer from Semiconductor Quantum Dots to Metal Oxide Nanoparticles. *Proc. Natl. Acad. Sci.* **2011**, *108* (1), 29–34. https://doi.org/10.1073/pnas.1011972107.
(10) Chen, J.-S.; Li, M.; Cotlet, M. Nanoscale Photoinduced Charge Transfer with Individual Quantum Dots: Tunability through Synthesis, Interface Design, and Interaction with Charge Traps. *ACS Omega* **2019**, *4* (5), 9102–9112. https://doi.org/10.1021/acsomega.9b00803.
(11) Peng, X.; Schlamp, M. C.; Kadavanich, A. V.; Alivisatos, A. P. Epitaxial Growth of Highly Luminescent CdSe/CdS Core/Shell Nanocrystals with Photostability and Electronic Accessibility. *J. Am. Chem. Soc.* **1997**, *119* (30), 7019–7029. https://doi.org/10.1021/ja970754m.
(12) Nguyen, H. A.; Hammel, B. F.; Sharp, D.; Kline, J.; Schwartz, G.; Harvey, S.; Nishiwaki, E.; Sandeno, S. F.; Ginger, D. S.; Majumdar, A.; Yazdi, S.; Dukovic, G.; Cossairt, B. M. Colossal Core/Shell CdSe/CdS Quantum Dot Emitters. *ACS Nano* **2024**, *18* (31), 20726–20739. https://doi.org/10.1021/acsnano.4c06961.
(13) Peterson, M. D.; Jensen, S. C.; Weinberg, D. J.; Weiss, E. A. Mechanisms for Adsorption of Methyl Viologen on CdS Quantum Dots. *ACS Nano* **2014**, *8* (3), 2826–2837. https://doi.org/10.1021/nn406651a.
(14) Bird, O. F.; Drbohlav, K. M.; Gowdy, E. K.; Flinkingshelt, F. A.; Pellows, L. M.; Hammel, B. F.; Layne, B. W.; Ardo, S.; Yang, J. Y.; Miller, K. A.; Dukovic, G. Revealing the Influence of Binding Motifs on Electron Transfer and Recombination Kinetics for CdSe Quantum Dots

Functionalized with a Modified Viologen. *J. Phys. Chem. C* **2025**, *129* (11), 5556–5570. https://doi.org/10.1021/acs.jpcc.5c00740.
(15) Song, H.; Luo, S.; Huang, H.; Deng, B.; Ye, J. Solar-Driven Hydrogen Production: Recent Advances, Challenges, and Future Perspectives. *ACS Energy Lett.* **2022**, *7* (3), 1043–1065. https://doi.org/10.1021/acsenergylett.1c02591.
(16) Sun, P.; Xing, Z.; Li, Z.; Zhou, W. Recent Advances in Quantum Dots Photocatalysts. *Chem. Eng. J.* **2023**, *458*, 141399. https://doi.org/10.1016/j.cej.2023.141399.
(17) Gui, X.; Lu, Y.; Wang, Q.; Cai, M.; Sun, S. Application of Quantum Dots for Photocatalytic Hydrogen Evolution Reaction. *Appl. Sci.* **2024**, *14* (12), 5333. https://doi.org/10.3390/app14125333.
(18) Chen, S.; Takata, T.; Domen, K. Particulate Photocatalysts for Overall Water Splitting. *Nat. Rev. Mater.* **2017**, *2* (10), 17050. https://doi.org/10.1038/natrevmats.2017.50.
(19) Hisatomi, T.; Maeda, K.; Takanabe, K.; Kubota, J.; Domen, K. Aspects of the Water Splitting Mechanism on $(Ga_{1-x}Zn_x)(N_{1-x}O_x)$ Photocatalyst Modified with $Rh_{2-y}Cr_yO_3$ Cocatalyst. *J. Phys. Chem. C* **2009**, *113* (51), 21458–21466. https://doi.org/10.1021/jp9079662.
(20) Walter, M. G.; Warren, E. L.; McKone, J. R.; Boettcher, S. W.; Mi, Q.; Santori, E. A.; Lewis, N. S. Solar Water Splitting Cells. *Chem. Rev.* **2010**, *110* (11), 6446–6473. https://doi.org/10.1021/cr1002326.
(21) Routzahn, A. L.; Jain, P. K. Luminescence Blinking of a Reacting Quantum Dot. *Nano Lett.* **2015**, *15* (4), 2504–2509. https://doi.org/10.1021/acs.nanolett.5b00068.
(22) Gallagher, S.; Kline, J.; Jahanbakhshi, F.; Sadighian, J. C.; Lyons, I.; Shen, G.; Hammel, B. F.; Yazdi, S.; Dukovic, G.; Rappe, A. M.; Ginger, D. S. Ligand Equilibrium Influences Photoluminescence Blinking in $CsPbBr_3$: A Change Point Analysis of Widefield Imaging Data. *ACS Nano* **2024**, *18* (29), 19208–19219. https://doi.org/10.1021/acsnano.4c04968.
(23) Reid, K. R.; McBride, J. R.; La Croix, A. D.; Freymeyer, N. J.; Click, S. M.; Macdonald, J. E.; Rosenthal, S. J. Role of Surface Morphology on Exciton Recombination in Single Quantum Dot-in-Rods Revealed by Optical and Atomic Structure Correlation. *ACS Nano* **2018**, *12* (11), 11434–11445. https://doi.org/10.1021/acsnano.8b06472.
(24) Carbone, L.; Nobile, C.; De Giorgi, M.; Sala, F. D.; Morello, G.; Pompa, P.; Hytch, M.; Snoeck, E.; Fiore, A.; Franchini, I. R.; Nadasan, M.; Silvestre, A. F.; Chiodo, L.; Kudera, S.; Cingolani, R.; Krahne, R.; Manna, L. Synthesis and Micrometer-Scale Assembly of Colloidal CdSe/CdS Nanorods Prepared by a Seeded Growth Approach. *Nano Lett.* **2007**, *7* (10), 2942–2950. https://doi.org/10.1021/nl0717661.
(25) Jasieniak, J.; Smith, L.; Van Embden, J.; Mulvaney, P.; Califano, M. Re-Examination of the Size-Dependent Absorption Properties of CdSe Quantum Dots. *J. Phys. Chem. C* **2009**, *113* (45), 19468–19474. https://doi.org/10.1021/jp906827m.
(26) Singh, V. K.; Mishra, H.; Ali, R.; Umrao, S.; Srivastava, R.; Abraham, S.; Misra, A.; Singh, V. N.; Mishra, H.; Tiwari, R. S.; Srivastava, A. In Situ Functionalized Fluorescent WS_2 -QDs as Sensitive and Selective Probe for Fe^{3+} and a Detailed Study of Its Fluorescence Quenching. *ACS Appl. Nano Mater.* **2019**, *2* (1), 566–576. https://doi.org/10.1021/acsanm.8b02162.
(27) Lustig, D. R.; Nilsson, Z. N.; Mulvey, J. T.; Zang, W.; Pan, X.; Patterson, J. P.; Sambur, J. B. Toward Imaging Defect-Mediated Energy Transfer between Single Nanocrystal Donors and Single Molecule Acceptors. *Chem. Biomed. Imaging* **2023**, *1* (2), 168–178. https://doi.org/10.1021/cbmi.3c00015.

(28) Verberk, R.; Van Oijen, A. M.; Orrit, M. Simple Model for the Power-Law Blinking of Single Semiconductor Nanocrystals. *Phys. Rev. B* **2002**, *66* (23), 233202. https://doi.org/10.1103/PhysRevB.66.233202.

CHAPTER 8: SUMMARY AND OUTLOOK

This dissertation research advances the nanoscale understanding of photonic and electronic processes in photocatalytic nanomaterials through the development and application of advanced optical spectroscopy and single-molecule imaging techniques. In response to the growing global need for sustainable energy solutions, the work explores how defect states, energy transfer (EnT) dynamics, photon recycling, and interfacial charge transfer govern the performance of hybrid semiconductor nanomaterials designed for solar energy conversion and photocatalysis.

Chapters 1 through 5 establish a framework for understanding defect-mediated energy transfer in colloidal zinc oxide (ZnO) nanocrystals (NCs) coupled to molecular dye acceptors. Chapter 2 demonstrates a Förster resonance energy transfer (FRET) spectroscopy-based approach that can assess the permeability of molecules through PEG-coated ZnO NCs. In this approach, ZnO NCs serve as FRET donors and freely diffusing molecules in the bulk solution are FRET acceptors. We quantified the EnT efficiency as a function of ligand chain length using time-resolved photoluminescence lifetime (TRPL) spectroscopy and within the framework of FRET theory. Chapter 3 introduces single-molecule fluorescence microscopy to localize active donor–acceptor pairs and identify the nanoscale origin of energy transfer heterogeneity. Chapter 4 quantifies how sample-to-sample variability affects energy transfer efficiency by analyzing hundreds of single NC/dye conjugates, revealing that 80% of specifically bound NC/dye pairs exhibit high EnT activity. Chapter 5 provides future directions and potential experiments to measure the defect donor dipole and assesses photon directionality in NC/dye systems.

Chapter 6 shifts focus to photon recycling, a photonic strategy for enhancing light

utilization in nanowire arrays. Using hyperspectral imaging and photoluminescence mapping, the study reveals that driving forces for photon communication were charge-carrier diffusion through the substate and demonstrates that spatial PL measurements are influenced not only by optical coupling mechanisms, such as scattering and photon recycling, but also by electronic coupling arising from charge-carrier diffusion in NW arrays. Chapter 7 builds upon the photophysical foundation laid in earlier chapters by addressing the dynamics of interfacial electron transfer at the single-nanocrystal level. Specifically, it investigates CdSe/CdS core-shell quantum dots interacting with methyl viologen, a model electron acceptor. Through total internal reflection fluorescence (TIRF) microscopy and statistical dwell time analysis, the work shows that PET to MV^{2+} modifies QD blinking behavior, increases off-state frequency, and reshapes on-time distributions from power-law to mono-exponential forms. These findings provide direct kinetic evidence for surface-bound charge separation and quantify how acceptor binding modulates QD photophysics. The chapter further demonstrates that single-molecule blinking analysis can be used to extract molecular binding behavior and PET kinetics with nanometer-scale resolution, capabilities that traditional ensemble measurements cannot offer.

Together, the chapters in this dissertation present a unified strategy for dissecting photonic and electronic transfer pathways at the single-particle level, providing new methodologies for optimizing nanomaterial systems for solar-to-chemical conversion. By integrating ensemble and single-molecule techniques, this work not only uncovers fundamental mechanisms of light harvesting and charge separation, but also provides design rules for tailoring nanomaterial interfaces to enhance photocatalytic performance.

APPENDICES

APPENDIX A: SUPPORTING INFORMATION FOR CHAPTER 2

A1. Absorbance Spectra of PEG-Silane Ligands

Figure A1 shows absorbance spectra of all PEG ligand chain lengths. The ligands exhibit negligible light absorption at the 340 nm excitation wavelength chosen for the steady-state and time-resolved PL experiments. The concentration of all the PEG-silane ligands in ethanol was 0.0104 M.

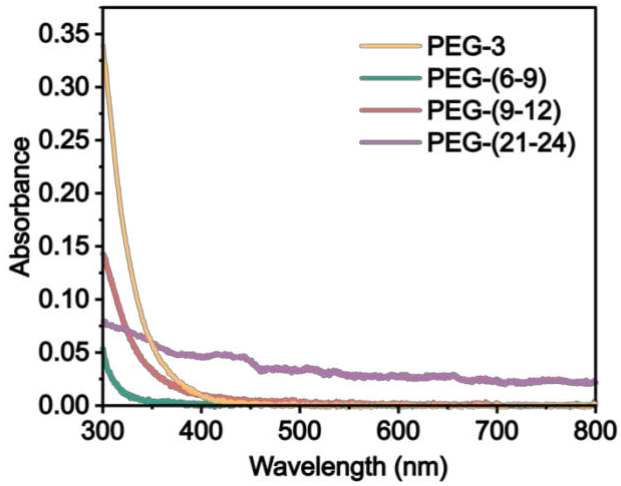

Figure A1. Absorbance spectra for all PEG-silane ligands measured in ethanol.

A2. ZnO Size Determination via XRD

The XRD peak profiles of ZnO NCs were analyzed by the Halder-Wagner (H-W) method to extract crystal size from XRD peak broadening.[1,2] The H-W method is based on the assumption that peak broadening is a convolution of both Lorentzian and Gaussian functions.[1,2] The full width at half maximum of the physical profile can be written per Halder-Wagner method as:

$$\left(\frac{\beta^*_{h\kappa\ell}}{d^*_{h\kappa\ell}}\right)^2 = \frac{1}{D}\frac{\beta^*_{h\kappa\ell}}{{d^*_{h\kappa\ell}}^2} + \left(\frac{\varepsilon}{2}\right)^2 \qquad \text{Eq. A1}$$

where $\beta^*_{h\kappa\ell} = \frac{\beta_{h\kappa\ell}cos\theta}{\lambda}$, the full width at half of the maximum intensity for different diffraction planes and $d^*_{h\kappa\ell} = \frac{2d_{h\kappa\ell}sin\theta}{\lambda}$, the lattice distance between the (hkl) planes and for a cubic crystal, *D* represents the crystallite size in nm and ε represents the lattice strain.[1,2]

Figure A2 shows the H-W size analysis for the ZnO-3 sample with $(\beta^*_{h\kappa\ell}/d^*_{h\kappa\ell}{}^2)$ term along the x-axis and $(\beta^*_{h\kappa\ell}/d^*_{h\kappa\ell})^2$ along the y-axis for each peak of the XRD pattern. The black line represents a linear fit to the data, where the slope and intercept report on the average crystallite size and intrinsic lattice strain, respectively. The estimated standard deviation (E.S.D.), a measure of certainty associated with each data point, is used to calculate the average particle size, as shown by the red data points.

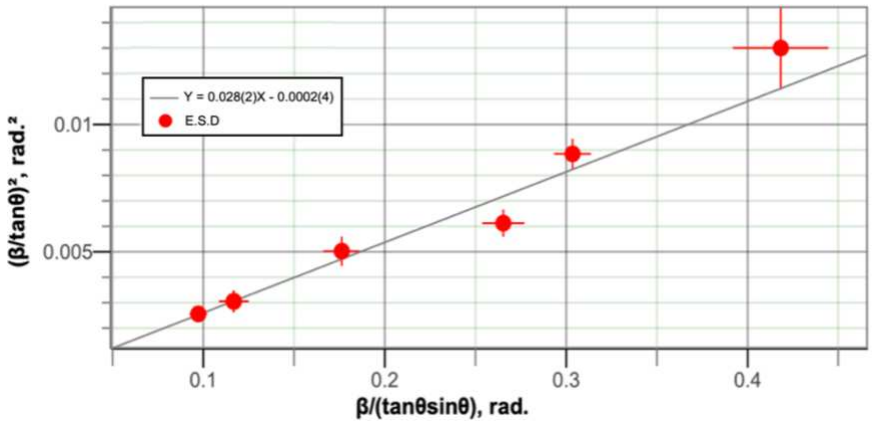

Figure A2. Representative H-W plot for the ZnO-3 sample, where $(\beta^*_{h\kappa\ell}/d^*_{h\kappa\ell}{}^2)$ is the x axis and $(\beta^*_{h\kappa\ell}/d^*_{h\kappa\ell})^2$ is the y axis. The red dots show the E.S.D to calculate the average particle size. The gray line shows the equation (Y=0.028(2)X – 0.0002(4)) used for fitting.

A3. IRF Deconvolution

TRPL data was deconvoluted from the IRF. Figure A3 shows the IRF deconvolution procedure using an IRF deconvolution fit (red line). This allows us to separate the sample response from the instrument response. The raw data is shown as the black data points and the IRF is shown as the blue line. The deconvoluted fits were used for further TRPL analysis.

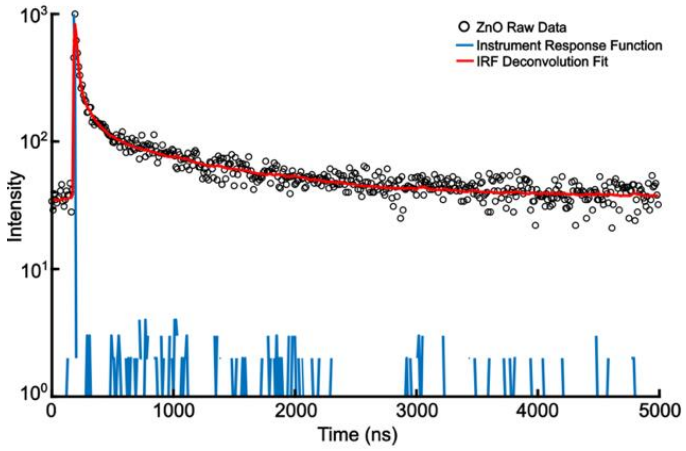

Figure A3. Example of TRPL deconvolution fitting. Raw TRPL decay of ZnO NCs (black points), the IRF (blue), and the deconvoluted fit (red).

A4. A555 Dye Control

Figure A4 shows the steady-state PL spectrum of A555 dye excited with 340 nm light. This excitation wavelength was the same excitation energy used for steady-state and time-resolved FRET experiments. Figure A4 shows minimal dye emission counts when the dye alone is excited with 340 nm light.

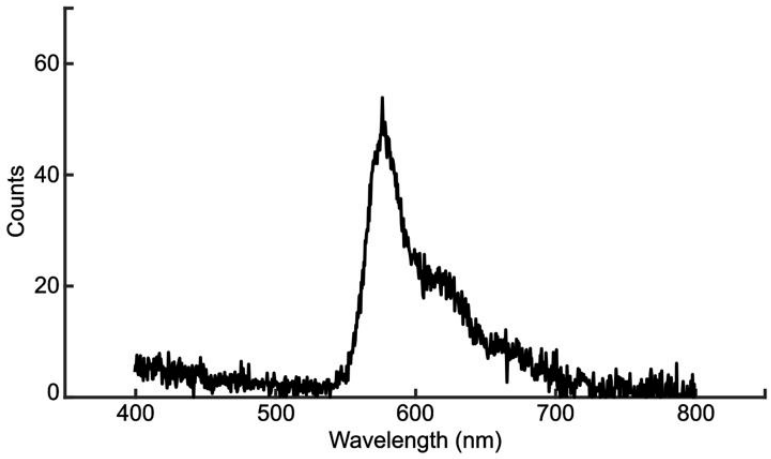

Figure A4. Steady-state PL spectrum of 128 nM A555 in ethanol with 340 nm excitation light.

A5. Stochastic Binding Model: TRPL Analysis

Figure A5 shows TRPL decay curves for all ZnO NC samples. TRPL decay curves for ZnO NCs alone were fit with Eq. 1 from the main text. Decay curves for mixtures of NCs and A555

were fit with Eq. 2 from the main text. Additionally, each NC sample was exposed to high bulk dye (300 nM) to observe the maximum possible EnT efficiency when, presumably, every possible surface binding site was occupied by acceptor molecules (pink data points).

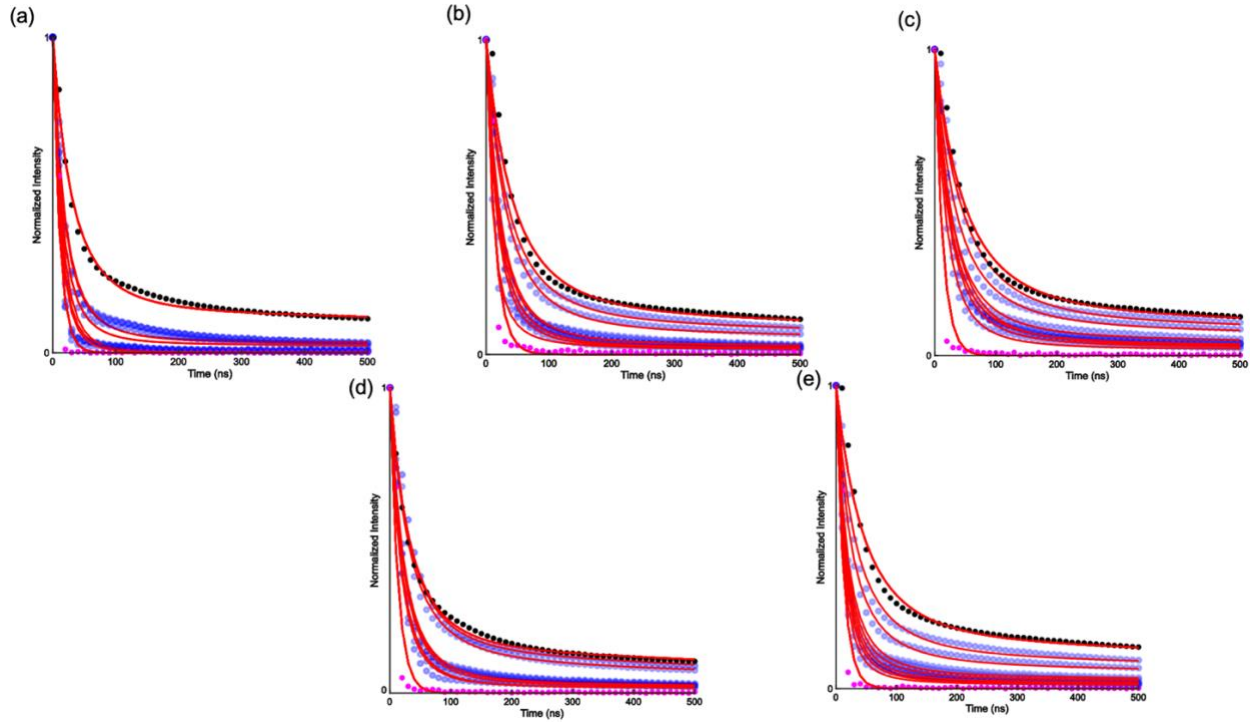

Figure A5. TRPL decay curves for all ZnO samples. Black data points are ZnO NCs alone, blue points are mixtures of ZnO NCs and A555 dye (2-128 nM dye), pink data points are ZnO NCs exposed to a saturated concentration of A555 dye (300 nM). Red lines are fits using Eqs. 5 and 6. a) ZnO-0 b) ZnO-3 c) ZnO-(6-9) d) ZnO-(9-12) e) ZnO-(21-24).

A6. Langmuir Adsorption Isotherm

The stochastic binding model assumes a Langmuir adsorption isotherm.[3,4] λ_S vs [A555] data were fit with the Eq. A2 where [A_{ad}] is the concentration of adsorbed dye molecules, K is the Langmuir equilibrium constant, [A] is the concentration of dye added to the solution in nM, and S_0 is the number of available binding sites. Here, $\lambda_S = [A_{ad}]$. Values of K obtained from the TRPL fitting procedure are shown in Figure A6.

$$[A_{ad}] = \frac{K[A]}{1 + K[A]} S_0 \qquad \text{Eq. A2}$$

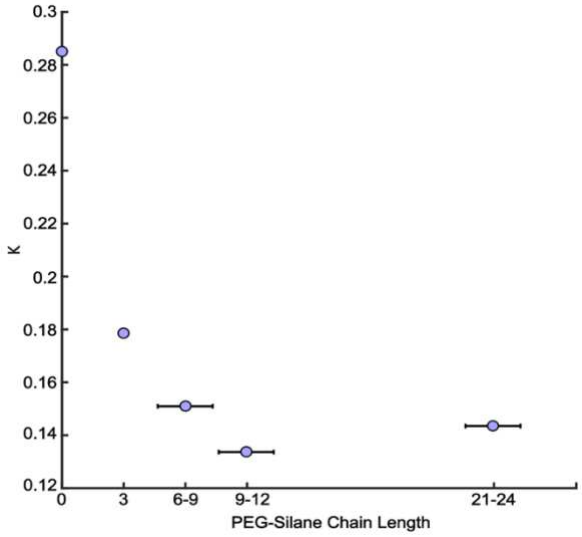

Figure A6. Equilibrium binding constant, *K*, calculated with Eq. A2 for all ZnO samples.

A7. Forster Radius Calculation

We calculate R_0 according to Eq. A3:

$$R_0 = \sqrt[6]{\frac{9000 \ln(10) \kappa^2 Q_D J}{128 \pi^5 N_A n^4}} \qquad \text{Eq. A3}$$

where κ^2 is the orientation factor that accounts for the relative orientation of the donor and acceptor dipoles (assuming $\kappa^2 = 2/3$).[3] Q_D is the emission quantum yield of the donor in the absence of the acceptor. J is the overlap integral of the donor emission and acceptor absorbance, N_A is Avogadro's constant, and n is the refractive index of the medium.

A8. Lower Magnification TEM Images

Figure A7 shows lower magnification TEM images of Figure 2.6a,b in the main text.

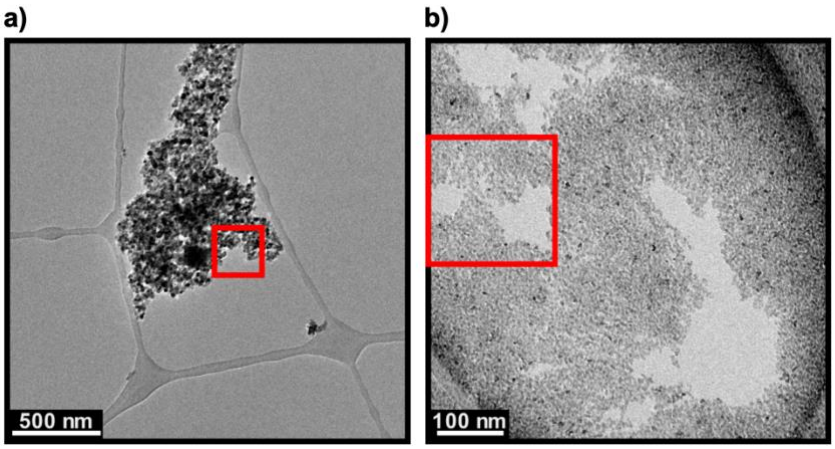

Figure A7. Lower magnification TEM images of ZnO nanoparticles on lacey carbon TEM grid. a) Uncoated ZnO particle aggregate suspended over a hole in the lacey carbon grid. Red box indicates region shown in Figure 2.6a. b) PEG-silane-coated ZnO particles forming layered film of ZnO nanoparticles suspended over a hole in the lacey carbon grid. Red box indicates region shown in Figure 2.6b.

Table A1. Photophysical properties of all ZnO NCs. Uncertainties are 95% confidence intervals from the fits. ZnO-0 NC concentration was estimated from previous work performed by Nilsson et al.[5]

Type of NC	Size (nm)	Defect PL QY (%)	J ($M^{-1}cm^{-1}nm^4$)	R_0 (nm)	Estimated Ligand Length, R (nm)	Bulk Concentration (nM)	Radiative Decay Rate (k_0 ns^{-1})	Trapping Rate (kqt ns^{-1})	Number of Traps ($\bar{\lambda}t$)
ZnO-0	4.3 ± 0.5	1.7	3.0×10^{15}	3.1	0	≈ 70	$5.2 \times 10^{-4} \pm 3.1 \times 10^{-5}$	$0.015 \pm 5.2 \times 10^{-4}$	1.9 ± 0.03
ZnO-3	5.8 ± 0.5	4.4	3.3×10^{15}	3.7	2.4	33	$6.2 \times 10^{-4} \pm 5.4 \times 10^{-5}$	$0.011 \pm 5.4 \times 10^{-4}$	1.9 ± 0.052
ZnO-(6-9)	5.7 ± 0.4	2.6	3.2×10^{15}	3.3	3.7	66	$5.5 \times 10^{-4} \pm 5.1 \times 10^{-5}$	$0.010 \pm 5.1 \times 10^{-4}$	1.8 ± 0.052
ZnO-(9-12)	5.0 ± 0.6	6.1	3.4×10^{15}	3.9	5.0	94	$7.6 \times 10^{-4} \pm 2.4 \times 10^{-5}$	$0.014 \pm 3.3 \times 10^{-4}$	1.9 ± 0.02
ZnO-(21-24)	3.7 ± 0.7	13.7	3.5×10^{15}	4.5	10.3	98	$5.8 \times 10^{-4} \pm 4.8 \times 10^{-5}$	$0.011 \pm 5.8 \times 10^{-4}$	1.7 ± 0.047

REFERENCES

(1) Nath, D.; Singh, F.; Das, R. X-Ray Diffraction Analysis by Williamson-Hall, Halder-Wagner and Size-Strain Plot Methods of CdSe Nanoparticles- a Comparative Study. *Mater. Chem. Phys.* **2020**, 239, 122021. https://doi.org/10.1016/j.matchemphys.2019.122021.

(2) Sen, S. K.; Barman, U. C.; Manir, M. S.; Mondal, P.; Dutta, S.; Paul, M.; Chowdhury, M. A. M.; Hakim, M. A. X-Ray Peak Profile Analysis of Pure and Dy-Doped α- MoO_3 Nanobelts Using Debye-Scherrer, Williamson-Hall and Halder-Wagner Methods. *Adv. Nat. Sci. Nanosci. Nanotechnol.* **2020**, 11 (2), 025004. https://doi.org/10.1088/2043-6254/ab8732.

(3) Sadhu, S.; Tachiya, M.; Patra, A. A Stochastic Model for Energy Transfer from Cds Quantum Dots/Rods (Donors) to Nile Red Dye (Acceptors). *The Journal of Physical Chemistry C* **2010**, *114* (6), 2842–2842.

(4) Beane, G. A.; Morfa, A. J.; Funston, A. M.; Mulvaney, P. Defect-Mediated Energy Transfer between ZnO Nanocrystals and a Conjugated Dye. *The Journal of Physical Chemistry C* **2012**, *116* (5), 3305–3310.

(5) Nilsson, Z. N.; Beck, L. M.; Sambur, J. B. Ensemble-Level Energy Transfer Measurements Can Reveal the Spatial Distribution of Defect Sites in Semiconductor Nanocrystals. *The Journal of Chemical Physics* **2021**, *154* (5), 054704.

APPENDIX B: SUPPORTING INFORMATION FOR CHAPTER 3

B1. Sample Preparation

ZnO NCs were synthesized following the procedure in our previous publication with the only modification being that a single aliquot was taken after 6 hours reaction time. This method yielded 4.5 nm-diameter particles based on the size series depicted in reference S1.[1] ZnO NC-coated quartz slides were typically prepared by spin coating 70-150 nM solutions of ZnO NCs onto a cleaned quartz slide at 1000 RPM. A 0.1 nM ethanolic solution of A555 dye was drop-cast directly on top of the NCs. The droplet of dye was allowed to stand on the slide for one minute before being completely removed by brisk nitrogen stream. The quartz slides were pre-cleaned by immersion in a 3:1 solution of sulfuric acid and hydrogen peroxide for at least 12 hours. Slides were then rinsed with 10 MΩ water and stored in spectrophotometric grade ethanol until use.

Immediately prior to placing the sample on the microscope, a #1 glass coverslip was placed onto the sample side of the slide, sandwiching a drop of Immersol W 2010 immersion oil (Zeiss) between the slide and coverslip. The immersion oil solvent kept the NCs and dyes adsorbed on the quartz slide because neither object was soluble in that solvent. We also observed that the NC emission was more stable in Immersol media than in air, presumably because O_2 quenches the ZnO defect emission.[2]

B2. Imaging Setup and Data Acquisition

Fluorescence images were acquired using the total internal reflection fluorescence (TIRF) setup pictured in Figure 3.3a of the main text. The sample was placed onto an Olympus IX73 inverted microscope with the coverslip side facing down and brought into optical focus using transmitted white light. Next, a small drop of index matching oil was placed onto the top surface of the slide and a quartz prism was placed on top of the oil and held in place so that the sample

slide could move freely under the prism while maintaining good contact. 355 and 532 nm laser light was directed into the prism at the critical angle for TIR. The evanescent excitation field excited NCs and molecules on the slide surface while limiting the penetration of the field into the bulk solution, reducing background signal.

Illumination was provided by two laser sources: a 355 nm laser (Coherent Genesis CX) selectively excites the ZnO NCs while the 532 nm laser (Coherent Obis) selectively excites the A555 molecules. Photons emitted from the sample were collected through a 60× microscope objective (NA = 1.2, Olympus, UPLANSAPO60x/W) before passing through a long pass filter (cutoff wavelength: 440 nm). Then the photons enter the image splitter (Hamamatsu Gemini W-view) which uses a dichroic mirror (cutoff wavelength: 550 nm) to split the image based on wavelength. One image is the "dye channel" because the photon stream passes through a 585/40 bandpass filter. The second bandpass filter (490/60) was chosen to pass the ZnO defect emission and exclude any photons from A555, forming the "defect channel".

The two channels were projected onto an EMCCD camera (Andor iXon 897) to produce a single image, split vertically (Figure B1). The split images allow for the behavior of the NCs to be observed without interference from A555 by using the defect channel while also allowing for observations of the A555 in the dye channel. Data was acquired as a stream of fluorescence images from the camera, forming a "movie". Movies were analyzed to determine the behavior of the ZnO and A555 separately after they had been mixed following the sample preparation procedure outlined above. Because the ZnO defect emission is so broad, the NC emission should appear in both channels, making the NCs easy to distinguish from non-NC objects.

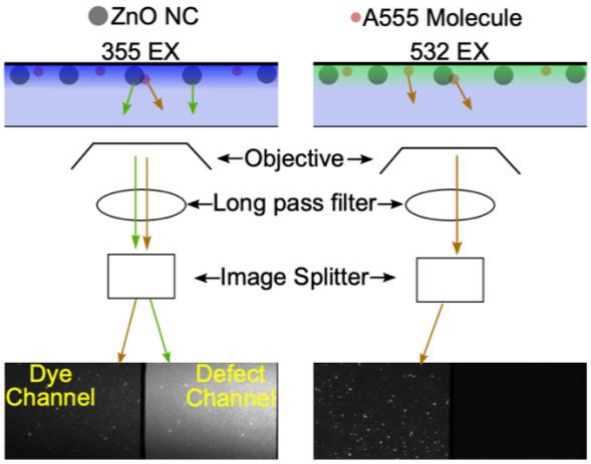

Figure B1. Cartoon depiction of the prism-type total internal reflection fluorescence microscopy setup.

B3. Image Processing

B.3.1 Segmenting movies by 355 nm and 532 nm laser illumination

In a typical experiment both laser sources are used to observe the locations of A555 molecules using 532 nm excitation and the behavior of ZnO NCs with 355 nm excitation. The sample is exposed to each laser in one second pulses with half a second of dark time between each pulse. Alternating the excitation wavelength allows for A555 molecules to be observed independently of the NCs throughout the entire movie. The movies can then segmented according to the illumination condition (355 or 532 nm excitation) and detection channel (dye or defect).

We used MATLAB to segment the images of an entire movie according to the illumination condition. To do so, we calculated the average frame intensity trajectory from all pixels of every image shown in Figure B1-bottom left, creating the average pixel intensity verses time plot shown in Figure B2a. Figure B2b shows a zoom-in view of the first 60 s of the experiment. Here, the average pixel intensity (black line) shows distinct square-wave-like features due to the alternating excitation source. The two lasers create two distinct intensity levels visible in Figure B2b. The 355 nm laser produces higher intensity peaks than the 532 nm excitation laser. We determine the laser

on/off points by taking the derivative of the trajectory in Figure B2a and determining the distinct positive and negative derivative transitions using blue and green triangles (the results are shown in Figure B2b).

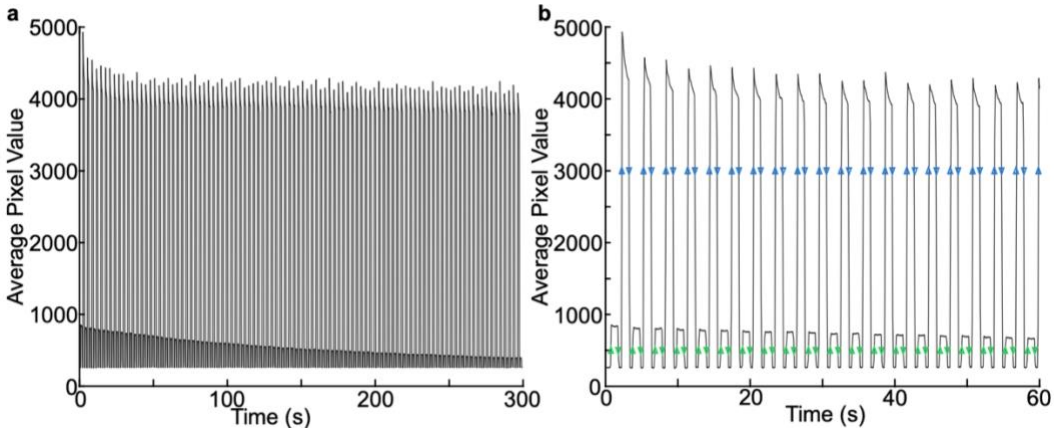

Figure B2. a) Representative average pixel value versus time trajectories from all images in the movie with 0.1 nM A555 deposited onto ZnO NCs. b) The same trajectory as shown in a) but with a shortened time axis to better show the data. Blue triangles in b) mark the frames where the 355 nm laser turns on and off. The green triangles mark the frames where the 532 nm laser turns on and off.

B.3.2 Selecting regions of interest (ROIs) and transforming ROIs from the defect channel to the dye channel

Having segmented the movies by illumination condition, we selected ROIs in the defect channel and transformed them to the dye channel to ensure our intensity trajectory calculations of NCs and dyes under 355 nm and 532 nm illumination originated from the same locations in the image. This step was necessary because NCs do not appear in the dye channel under 532 nm illumination and dye molecules do not appear in either channel under 355 nm illumination. To do so, we computed a single average image from all frames under 355 nm illumination (Figure B3a). We clicked the centroid position of each bright object in the defect channel during 355 nm excitation and created a 4×4 pixel box centered around each bright spot (a subset of ROIs are shown in Figure B3b-left). Those ROIs will be referred to as the NC ROIs to distinguish them from dye ROIs. This procedure yielded 1,078 NC ROIs (see Scheme B1 below). We also created

background NC ROIs of equal size and adjacent to the NC ROIs to create background subtracted PL intensity trajectories (see Figure B4).

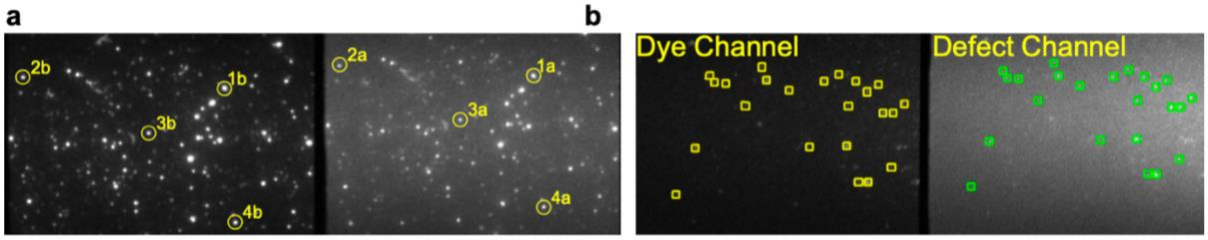

Figure B3. Fluorescence images of ZnO NCs under 6mW 355 nm excitation projected through the imagesplitter. The yellow circles in a) denote the spots that were used to calculate the transformation matrix. b) Results of the transformation process, where the ROIs in the defect channel (green boxes) were transformed to the dye channel (yellow boxes). Background ROIs are omitted from this image for clarity.

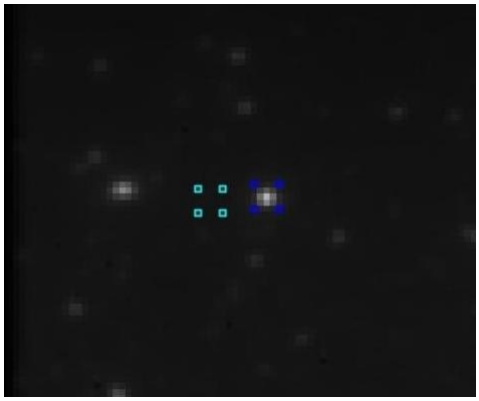

Figure B4. Cropped fluorescence image showing NC ROIs (blue squares define the corners) and background NC ROIs (cyan squares).

After creating the ROIs in the ZnO defect channel, they were transformed to the dye channel using a geometric transformation matrix. The matrix was created by selecting sets of matching coordinates in both images; ZnO NCs appear in both channels under 355 nm laser illumination (Figure B3a). These sets of points were passed to the MATLAB function "fitgeotrans", which outputs a geometric transformation matrix. The transformation matrix is then applied to the vertices of the ROIs created in the defect channel, creating a new set of vertices which have been translated onto the dye channel, as shown in Figure B3b. This transformation is applied to both the NC ROIs and the background ROIs. We estimate the error in the overlay procedure is 25 nm.[3] After selecting the ROIs, the average pixel intensity in each ROI of each

frame was calculated for both channels. This forms an intensity versus time trajectory for any ROI, as shown in the main text.

Dye ROIs were created by averaging frames in the dye channel during 532 nm excitation (Figure B5). We clicked the centroid position of each bright object in the dye channel during 532 nm excitation and created a 4×4 pixel box centered around each bright spot.

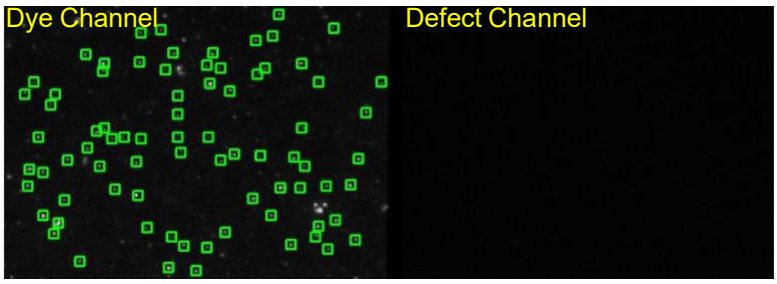

Figure B5. Fluorescence image of A555 molecules under 6mW 532 nm excitation. Green boxes represent the vertices of the dye ROIs.

B.3.3. Distinguishing Single Nanocrystals from Nanocrystal clusters.

The ZnO NC coverage on the quartz substrate is heterogeneous, containing both single ZnO NCs and NC clusters. For example, Figure B6 shows a florescence image of ZnO NCs under 355 nm excitation. The yellow arrows indicate two objects in each channel that are much larger and brighter than most of the other objects in the image. These large, bright spots can likely be attributed to NC clusters. We developed the following image analysis algorithm, schematically shown in Scheme B1, to quantitatively distinguish single NCs from NC clusters.

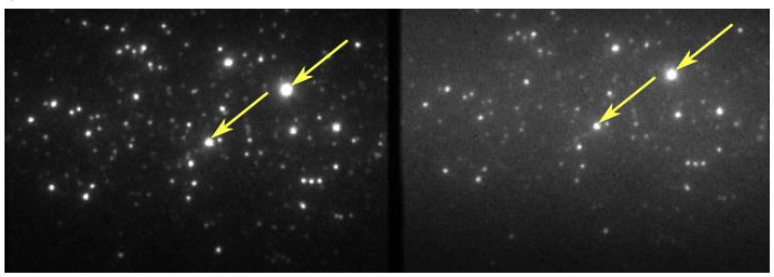

Figure B6. Wide field florescence image of ZnO nanocrystals. Yellow arrows point to objects that are considerably larger and brighter than the majority of other objects (clusters).

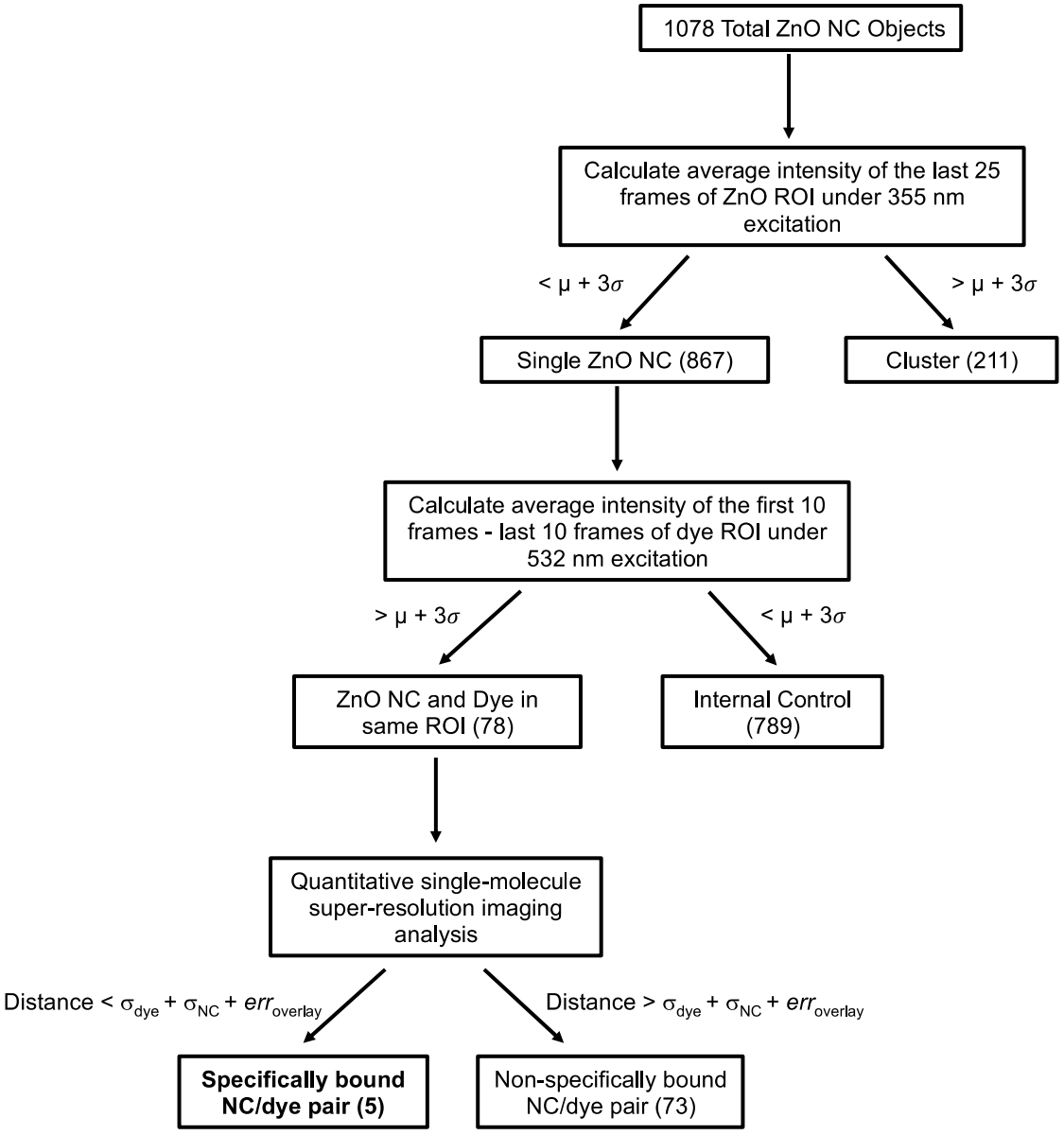

Scheme B1. Flow chart outlining the image analysis algorithm and filtering steps to quantify single dye molecules, single NCs, and specifically and non-specifically bound NC/dye pairs. "Th" represents threshold value. The numbers in parenthesis represent the number of filtered entities after each step.

To separate single NCs from NC clusters, we calculated the intensity for all 1,078 NC ROIs. Figure B7 shows a representative histogram for one of our movies of the average intensity values from the last 25 frames from all ROIs in the defect channel during 355 nm excitation. We assign the large population at low intensity to single NCs and the high intensity objects to clusters. We defined an intensity threshold for single NCs by fitting the large population with a single

component Gaussian function to establish the mean (μ) and standard deviation (σ) of the single particle population. The intensity threshold (Th in Scheme B1) was defined as three times the standard deviation above the mean (μ+3σ). The vertical grey line in Figure B7 serves as the intensity threshold for single ZnO NCs, meaning any NC whose intensity is less than this amount is defined as a single ZnO NC. We repeat this procedure for each movie.

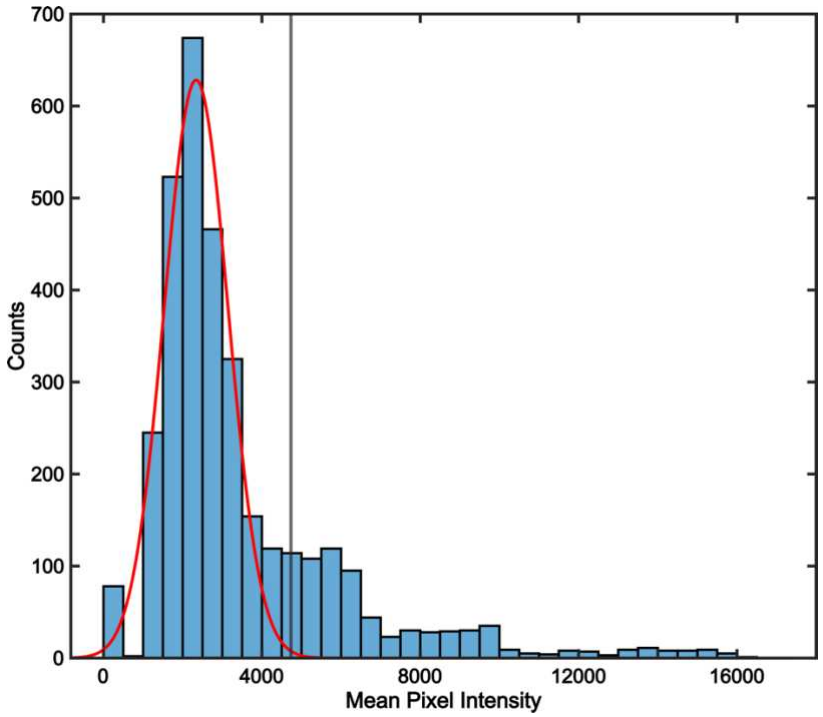

Figure B7. Histogram of average PL emission intensity of all bright objects in the defect channel under 355 nm excitation. The red line is a Gaussian fit to the large population at low intensity that can be assigned to single ZnO NCs. The vertical line represents the mean plus 3 standard deviations of the Gaussian fit result. That vertical line serves as the intensity threshold for single ZnO NCs, meaning any NC whose intensity is less than this amount is defined as a single ZnO NC.

B.3.4. Do single NCs also have a dye molecule located in the same diffraction-limited volume?

To determine which NCs do and do not have a dye molecule present in the same ROI, we examined the intensity trajectory from an NC ROI *in the dye channel during 532 nm excitation*. Figure B10a shows a representative trajectory of a dye molecules observed in the dye channel under 532 nm excitation. To determine whether a dye molecule was also present in the same NC ROI, we calculated the average intensity of the first 10 frames and subtracted that value from the

average intensity of the last 10 frames. Figure B8 shows a representative histogram of those results for one movie and was repeated for all 867 single NCs. We observed a large, low intensity population that can be attributed to "empty" ROIs. The high intensity population can be attributed to dye molecules that are initially present in the ROI. Fluorescence intensity trajectories of the diffraction-limited spots show single-step photobleaching (Figure B10), further confirming our assignment of these spots as single molecules. We fit the histogram with a Gaussian function to establish a mean and standard deviation for the low intensity "empty" population. We defined an intensity threshold as three times the standard deviation above the mean ($\mu + 3\sigma$). Any objects greater than this threshold (gray line in Figure B8) are defined as dye molecules in a NC ROI. In doing so, we identify all single NCs with a dye molecule located in the same diffraction-limited space.

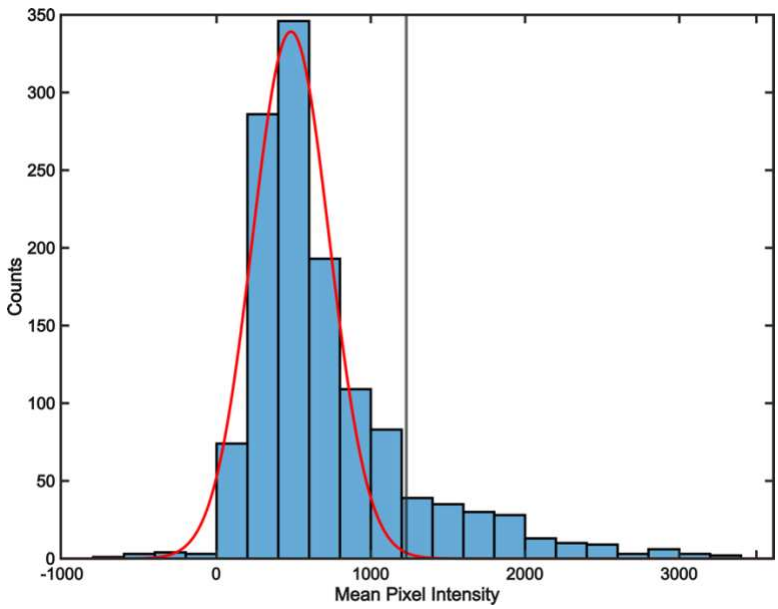

Figure B8. Histogram of NC ROI intensities located in the dye channel under 532 nm excitation. The intensities represent the average intensity of the last 10 frames subtracted from the average intensity of the first 10 frames. The red line is a Gaussian fit to the large population at low intensity that can be assigned to non-dye objects present in the ROI. The vertical line represents the mean plus 3 standard deviations of the Gaussian fit result. The vertical line serves as the intensity threshold for A555 dyes, meaning any ROI whose intensity is greater than this amount is defined as a dye.

B.3.5. Distinguishing specifically bound from non-specifically-bound NC/dye pairs

The details of the super-resolution imaging analysis and MATLAB code are provided in the Supplementary Information of Sambur et al[3]. Super-resolution analysis fits were performed for the 78 candidate ROIs that contain a single NC and a dye molecule. Each candidate spot in each frame was fit with a 2D Gaussian function during the first 1 s under both 355 and 532 nm excitation to determine the centroid position of the NC and dye, respectively. We obtain the centroid positions of the dye and NC during the first 1 s of the experiment (see blue and green data points in Figure 3.4 of the main text). We calculated the localization error according to Eq. 6 in Mortensen et al.[4] and plotted those values as error bars on the blue and green data points in Figure 3.4 of the main text. Figure B9 shows the distribution of localization error values in both *x* and *y* dimensions for NC ROIs under 355 nm illumination. The average localization error is 39.7 nm.

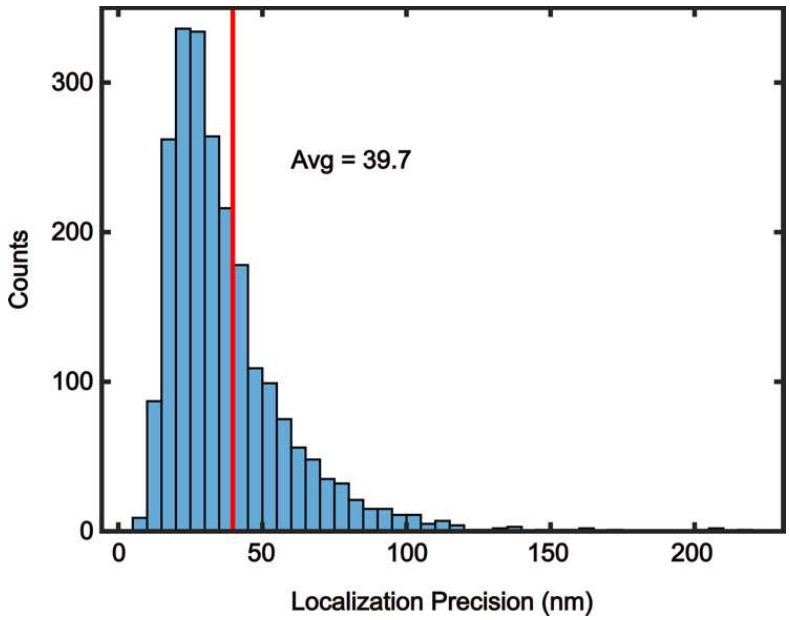

Figure B9. Histogram of the localization error in both the x and y dimensions for ZnO NC ROIs illuminated with 355 nm light. The values were calculated according to ref. 4. The gray bar represents the average localization error (39.7 nm).

To distinguish specifically bound versus non-specifically bound NC-dye pairs, we first assumed the NC and dye do not move during the acquisition time and, therefore, calculated the average *x* and *y* coordinates of the NC and dye to determine their positions with super-optical

resolution (large black data points in Figure 3.4 of the main text). We also calculated the standard deviation (σ) of the centroid positions of the dye and NC from all the individual frames. σ_{dye} and σ_{NC} represents the error in the mean position of the dye and NC, respectively (indicated by a circle with radius μ in Figure 3.4 of the main text). Note, the error in the overlay procedure ($err_{overlay}$) is approximately 25 nm.[3] If the separation distance between the NC and dye were less than ($\sigma_{dye} + \sigma_{NC} + err_{overlay}$), then we defined the NC-dye pair as specifically bound.

B4. Photobleaching Behavior

Fluorescence intensity trajectories of single dye molecules exhibited abrupt photobleaching. Figure B10 shows a trajectory from an ROI in the dye channel under 532 nm excitation. Only the intensity values recorded during 532 nm excitation are shown. Two sharp intensity drops are observed, one at early times and another at 125 seconds. These intensity drops are likely caused by sequential photobleaching events of two different molecules. Figure B10b shows a histogram of these photobleaching events for 296 dye molecules. The average photobleach time was 53 seconds (red line), which is long enough to observe intensity fluctuations in the defect channel under 355 nm excitation.

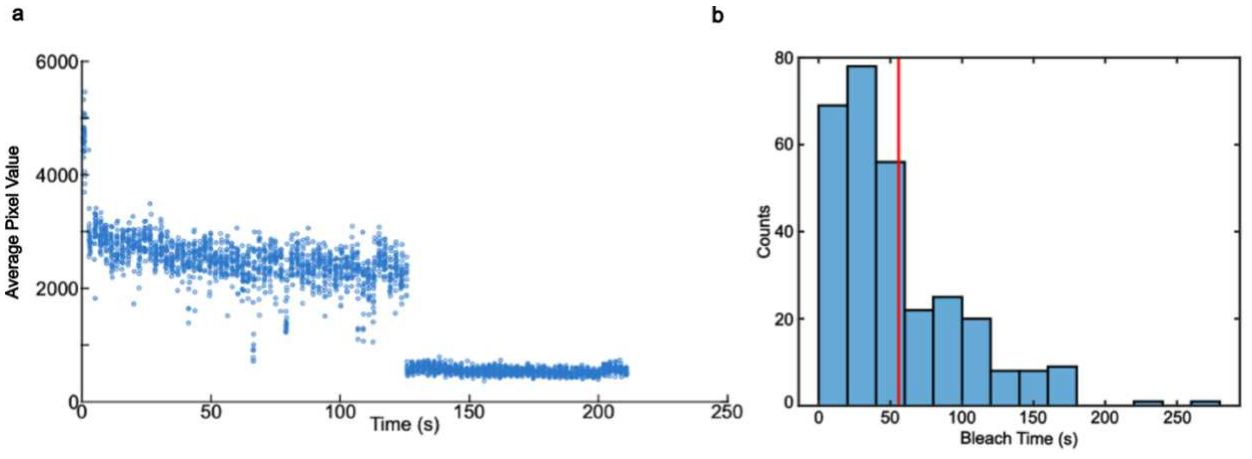

Figure B10. Intensity trajectory from a single dye ROI under 532 nm excitation. a) intensity trajectory from a ROI created in the dye channel. Each blue point represents the average intensity inside the ROI during one frame of the movie. b) Histogram of photobleach times for 296 A555 dye molecules. The red line displays the average photobleach time of 53 seconds.

B5. Estimating the Number of Defect Sites per NC

Table B1 displays calculations of defects/NC based on previously reported defect concentrations. To calculate defects/NC, it was assumed that the NCs were a sphere, and the NC volume was calculated from the TEM data in Figure 3.2a of the main text.

Table B1. Calculated defects/NC based on previously reported defect concentrations.

Defect Type	Sample	Experimental Conditions	Method	Defect Concentration (cm^{-1})	Defects/NC	Source
Oxygen Vacancies	72-atom supercells of wurtzite ZnO	High temperature equilibrium grown ZnO	First-principles calculations	1×10^{17}	0.0048	Lany and Zunger[4]
Oxygen Vacancies	Bulk ZnO	700 °C	Hybrid density functionals	1×10^{19}	0.48	Clark *et al.*[5]
Zn vacancies	Undoped bulk ZnO crystals grown by the seeded vapor phase	10–300 K	Positron annihilation measurements	2×10^{15}	9.5×10^{-4}	Saarinen *et al.*[6]
Zinc interstitial	Simulated wurtzite ZnO	900 K	Local Density Approximations	1×10^{19}	0.48	Oba *et al.*[7]
Oxygen vacancies and Zinc interstitials	Bulk ZnO crystals grown by the seeded chemical vapor transport	Annealed in zinc vapor at 1100 °C for 30 min	Smakula's equation	2×10^{18}	0.081	Halliburton *et al.*[8]

B6. Monte Carlo Simulations of NC-Dye Coverages

We performed Monte Carlo simulations to calculate how many non-specifically bound NC-dye pairs one would expect to observe based on random co-localization. We randomly placed 145 NCs and 244 dye molecules in a 44.4 μm × 64.9 μm area (corresponding to a 167 pixel × 244 pixel region of our image) and determined the number of occurrences where 1 NC and 1 dye were

located within a 266 nm × 266 nm area (one square pixel). The NC and dye quantities correspond to the average number of NCs and dyes observed after 6 deposition experiments. We observed at least one non-specifically bound NC-dye pair in 5,808/10,000 simulations, and 8,664 total pairs (Figure B11). Therefore, one would expect to observe one non-specifically bound NC-dye pair in 58% of the deposition experiments. Experimentally, we observed 73 non-specifically bound NC-dye pairs in 6 deposition experiments. The higher number of experimental observations is likely because the carboxylic acid group interacts with the oxide surface. The Monte Carlo simulations did not consider interactions between the NCs and dyes.

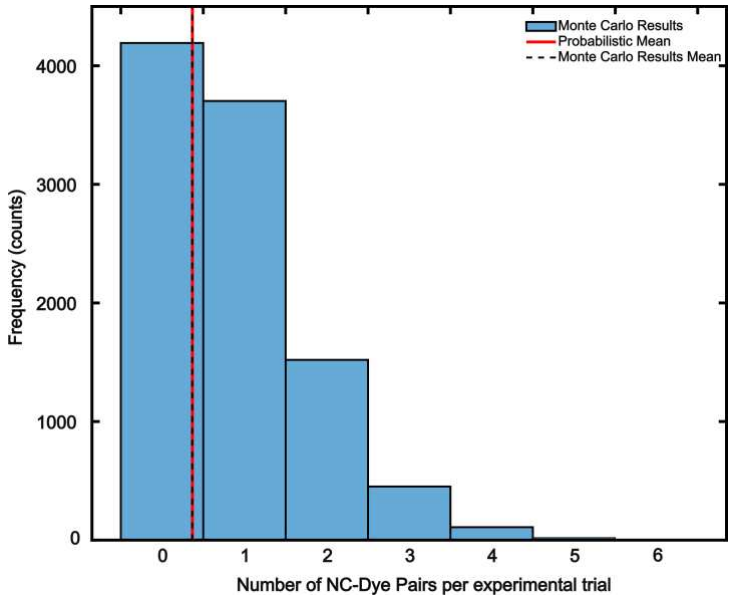

Figure B11. Distribution of the number of non-specifically bound NC-dye pairs observed after randomly placing 145 NCs and 244 dye molecules in a 44.4 μm × 64.9 μm area. The results represent the cumulative number of pairs observed after 10,000 Monte Carlo simulations.

REFERENCES

(1) Nilsson, Z. N.; Beck, L. M.; Sambur, J. B. Ensemble-Level Energy Transfer Measurements Can Reveal the Spatial Distribution of Defect Sites in Semiconductor Nanocrystals. *J. Chem. Phys.* **2021**, *154* (5), 054704. https://doi.org/10.1063/5.0034775.

(2) van Dijken, A.; Meulenkamp, E. A.; Vanmaekelbergh, D.; Meijerink, A. Influence of Adsorbed Oxygen on the Emission Properties of Nanocrystalline ZnO Particles. *J. Phys. Chem. B* **2000**, *104* (18), 4355–4360. https://doi.org/10.1021/jp993998x.

(3) Sambur, J. B.; Chen, T.-Y.; Choudhary, E.; Chen, G.; Nissen, E. J.; Thomas, E. M.; Zou, N.; Chen, P. Sub-Particle Reaction and Photocurrent Mapping to Optimize Catalyst-Modified Photoanodes. *Nature* **2016**, *530* (7588), 77–80. https://doi.org/10.1038/nature16534.

(4) Mortensen, K. I.; Churchman, L. S.; Spudich, J. A.; Flyvbjerg, H. Optimized Location Analysis for Single- Molecule Tracking and Super-Resolution Microscopy. *Nat. Methods* **2010**, *7* (5), 377-381. https://doi.org/10.1038/nmeth.1447.

(5) Lany, S.; Zunger, A. Dopability, Intrinsic Conductivity, and Nonstoichiometry of Transparent Conducting Oxides. *Phys. Rev. Lett.* **2007**, *98* (4), 045501. https://doi.org/10.1103/PhysRevLett.98.045501.

(6) Clark, S. J.; Robertson, J.; Lany, S.; Zunger, A. Intrinsic Defects in ZnO Calculated by Screened Exchange and Hybrid Density Functionals. *Phys. Rev. B* **2010**, *81* (11), 115311. https://doi.org/10.1103/PhysRevB.81.115311.

(7) Saarinen, K.; Hautakangas, S.; Tuomisto, F. Dominant Intrinsic Acceptors in GaN and ZnO. *Phys. Scr.* **2006**, *T126*, 105–109. https://doi.org/10.1088/0031-8949/2006/T126/024.

(8) Oba, F.; Choi, M.; Togo, A.; Tanaka, I. Point Defects in ZnO: An Approach from First Principles. *Sci. Technol. Adv. Mater.* **2011**, *12* (3), 034302. https://doi.org/10.1088/1468 6996/12/3/034302.

(9) Halliburton, L. E.; Giles, N. C.; Garces, N. Y.; Luo, M.; Xu, C.; Bai, L.; Boatner, L. A. Production of Native Donors in ZnO by Annealing at High Temperature in Zn Vapor. *Appl. Phys. Lett.* **2005**, *87* (17), 172108. https://doi.org/10.1063/1.2117630.

APPENDIX C: SUPPORTING INFORMATION FOR CHAPTER 4

C1. TEM and Size Analysis of APTMS-capped ZnO NCs

ZnO NC diameters were determined by bright-field TEM imaging modes. The diameters of 50 NCs from each sample were measured using Fiji software.[1,2] Figure C1 shows histograms and single-component Gaussian fits that yielded the mean (5.2 nm) and standard deviation (1.2 nm) for the NC diameter. Figure C2 shows additional high-resolution TEM images of APTMS-capped ZnO NCs.

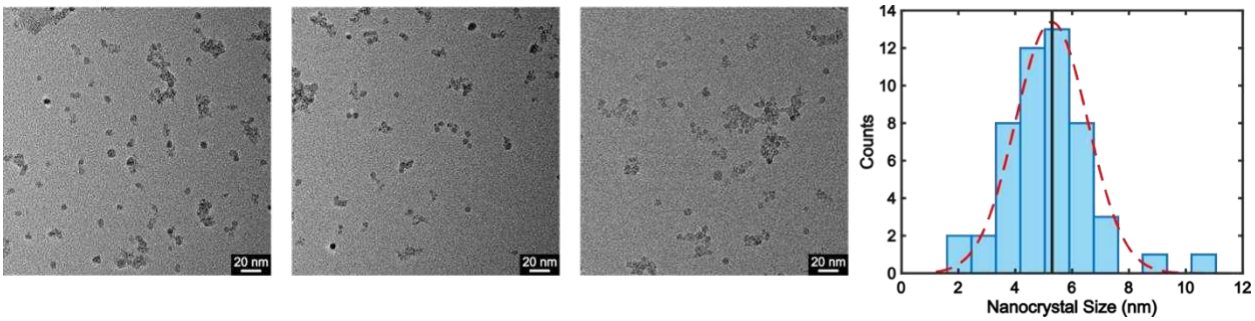

Figure C1. Determination of ZnO NC diameters. Bright-field TEM images of NC samples and nanocrystal size distribution for 50 nanocrystals.

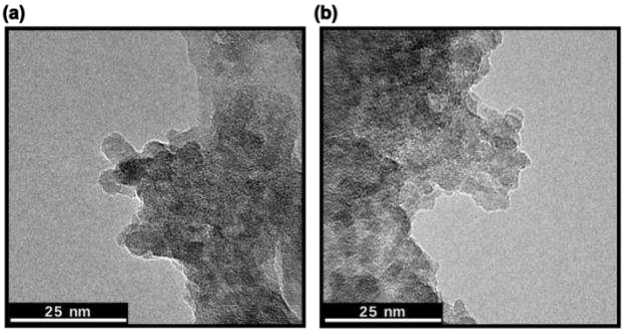

Figure C2. Additional high-resolution bright-field TEM images of APTMS-capped ZnO NCs on a lacey carbon grid.

C2. STEM-EDS Imaging of A555/APTMS/ZnO Conjugates

A high-angle annular dark-field (HAADF) scanning transmission electron microscopy (STEM) image of the A555/APTMS/ZnO conjugate sample is shown in Figure C3a. The corresponding X-ray energy-dispersive spectroscopy (EDS) maps and spectrum (Figure C3b)

confirm zinc (Zn) and oxygen (O) from the ZnO NCs. Additionally, the presence of silicon (Si) is detected, consistent with the APTMS coating. Although sulfur (S) was expected due to its elemental presence in the A555 dye, it was not detected in the EDS analysis, likely due to the small atomic percentage of S if, on average, the sample consists of 40% isolated ZnO NCs and 60% of 1 dye/NC nanoconjugates.

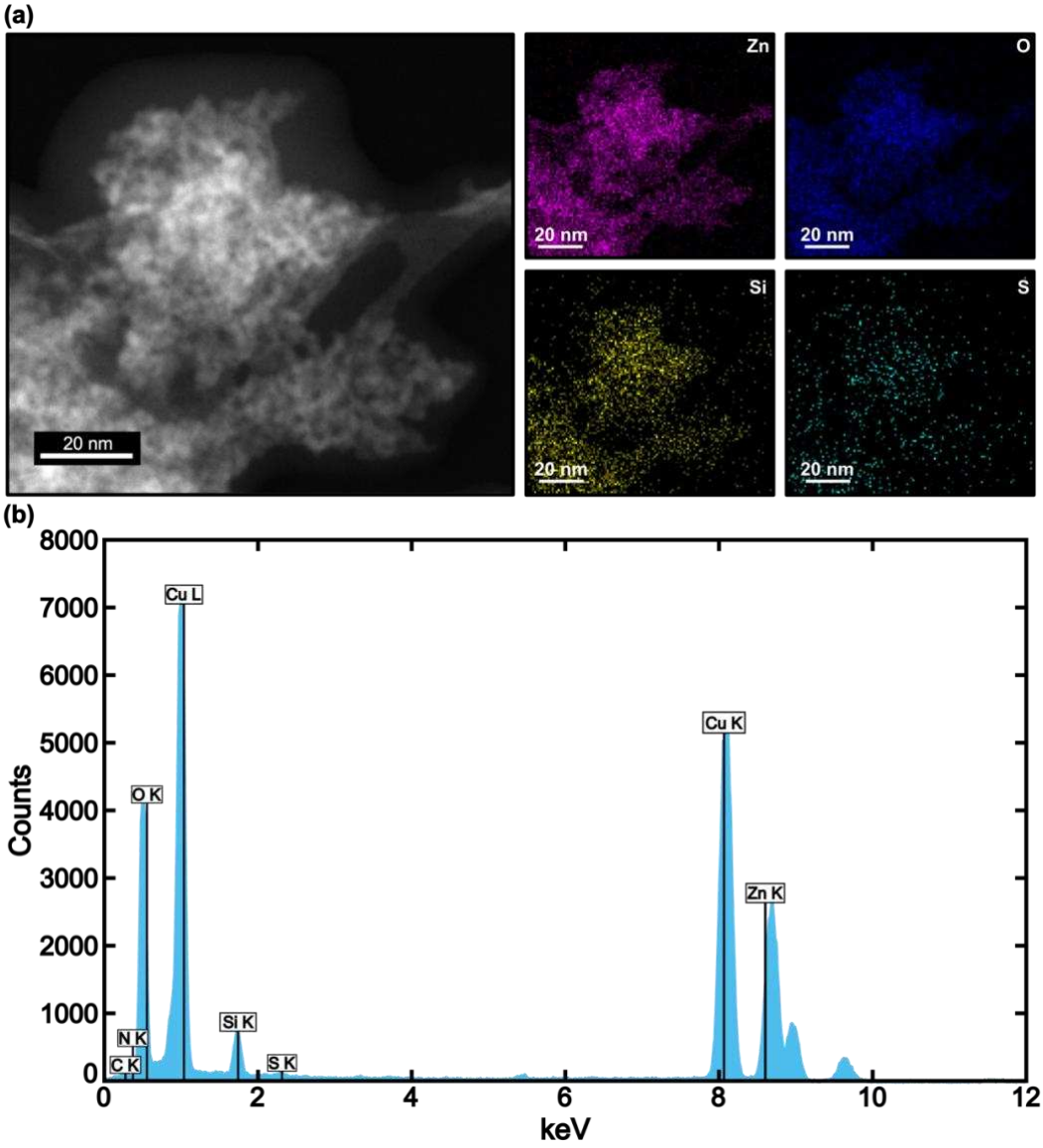

Figure C3. HAADF-STEM image of A555/APTMS/ZnO conjugates with corresponding STEM-EDS elemental mapping of Zn, O, Si, and S. (b) Corresponding STEM-EDS spectrum.

Table C1. Statistical comparison of the populations before and after the intensity thresholding procedure to quantify single NCs for the conjugated sample (current study) and randomly mixed sample (previous study).[3] Single NCs were further analyzed for identification of specifically bound NC/dye pairs as described in the main text.

NC Case	Fractional Population in Conjugated Sample	Fractional Population in Randomly Mixed Sample
Total NCs	182	1078
Single NCs	155/182 (85%)	867 (80%)
Clusters	27/182 (15%)	211 (20%)

C3. Widefield PL Images

Figure C4 shows the widefield images for the trajectories shown in Figure 4.4 of the main text. Figure C4a shows an isolated ZnO NC under 532 nm excitation and Figure C4b shows an isolated ZnO NC under 355 nm excitation. (c-d),(e-f) same as (a-b) for a non-specifically bound NC/dye pair and a specifically bound NC/dye pair respectively. To obtain single-molecule PL intensity trajectories, we clicked the centroid of each bright object in the dye channel under 532 nm excitation and in the defect channel during 355 nm excitation and created a 4-by-4 pixel boxes, in which the intensity is averaged over the duration of the movie. The pink boxes are located dye molecules and the blue boxes are located ZnO NCs.

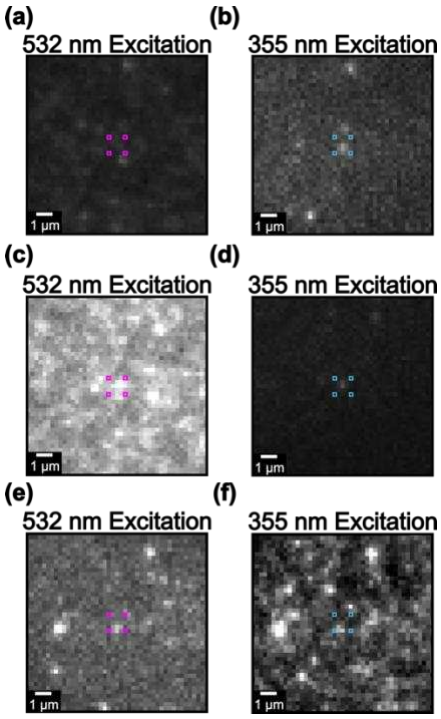

Figure C4. Widefield PL images corresponding to the trajectories shown in Figure 4.4 of the main text of (a) an isolated ZnO NC under 532 nm excitation and (b) an isolated ZnO NC under 355 nm excitation. (c-d),(e-f) same as (a-b) for a non-specifically bound NC/dye pair and a specifically bound NC/dye pair respectively.

C4. Localization Precision Determination

We calculated the localization error according to Eq. 6 in Mortensen et al.[3] and plotted those values as error bars for the blue and pink data points in Figure 4.4 of the main text. Figure C5 shows the distribution of localization error values in both *x* and *y* dimensions for NC ROIs under 355 nm illumination. The average localization error is 30.6 nm, determined from the Gaussian fit (red dashed line).

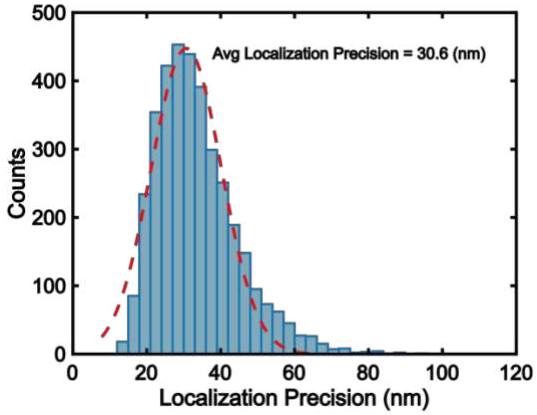

Figure C5. Histogram of the localization error in both the *x* and *y* dimensions for ZnO NC ROIs illuminated with 355 nm light. The values were calculated according to Ref. 3. The average localization error (30.6 nm) was determined via Gaussian fitting (red dashed line).

C5. Event Analysis

Figure C6 shows the event analysis determination procedure for the specifically bound NC/dye pair as shown in Figure 4.4q of the main text. Figure C6a shows the same trajectory as shown in Figure 4.4q of the main text, where instead of the channel ratio being shown, the fluctuation magnitude is shown (turquoise points), which is calculated by taking the difference between the average channel ratio value (red dashed line in Figure 4.4q of the main text) and each channel ratio value (white points in Figure 4.4q of the main text) at every frame. Figure C6b shows the corresponding fluctuation magnitude distribution. Figure C6c-d is the same as Figure C6a-b, with the labeled positive and negative events depicted as red and blue stars respectively as determined from the global threshold analysis shown in Figure 4.5a of the main text.

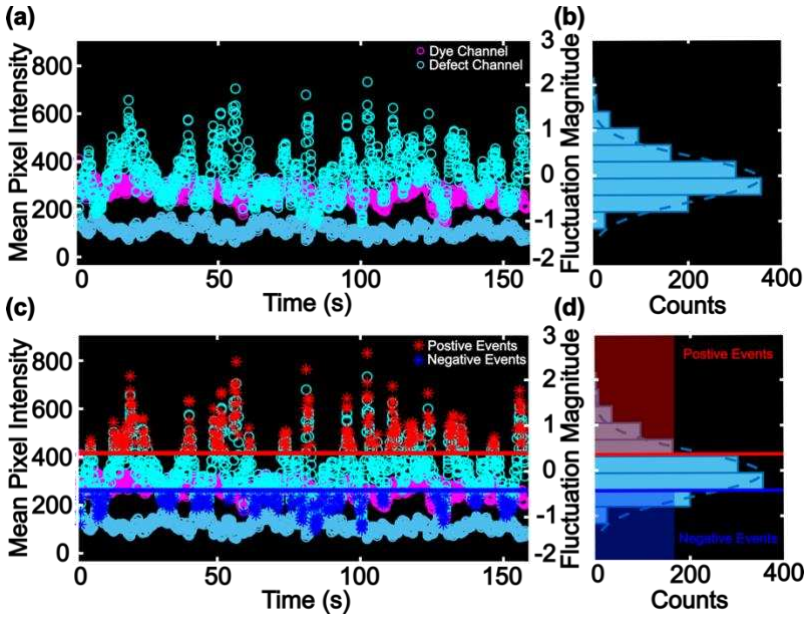

Figure C6. Event analysis determination for the specifically bound NC/dye pair as shown in Figure 4.4q of the main text. (a) Figure 4.4q of the main text with fluctuation magnitude (turquoise points), calculated by taking the difference between the average channel ratio value (red dashed line in Figure 4.4q of the main text) and each channel ratio value (white points in Figure 4.4q of the main text) at every frame. (b) Corresponding fluctuation magnitude distribution with a gaussian fit (blue dashed line). (c) labeled positive (red stars) and negative events (blue stars) with corresponding positive and negative thresholds (red and blue solid lines) as determined from global threshold analysis shown in Figure 4.5 of the main text. (d) Corresponding fluctuation magnitude distribution showing the positive and negative events.

To further investigate events in the candidate pair trajectories, a custom Matlab script compares positive and negative events in candidate pair trajectories as a function of donor-to-acceptor distances using super-resolution fluorescence data. First, the script cross-references the frame numbers of the identified positive and negative events from our super-resolution data. This step involves extracting the frame numbers where these events occur and matching them to the corresponding rows in the super-resolution dataset. Separate analyses are performed for data collected under both 355 nm and 532 nm excitations. A key parameter, "nogreenframestoavg", determines the number of acceptor frames averaged for precise position estimation. The script iterates through positive fluorescence events for each trajectory and extracts donor coordinates under 355 nm excitation and corresponding acceptor coordinates under 532 nm excitation for the nearest time frame. The donor-acceptor distance is computed for each event using Euclidean distance, with error propagation performed to estimate the uncertainty in distance measurements.

For each trajectory, the channel ratio is computed, and its error is determined using standard error propagation based on the relative uncertainties of dye and defect intensities. The deviation of the ratio from its trajectory average is then calculated, with its error derived by combining the uncertainties of the ratio and the average value.

REFERENCES

(1) Schindelin, J.; Arganda-Carreras, I.; Frise, E.; Kaynig, V.; Longair, M.; Pietzsch, T.; Preibisch, S.; Rueden, C.; Saalfeld, S.; Schmid, B.; Tinevez, J.-Y.; White, D. J.; Hartenstein, V.; Eliceiri, K.; Tomancak, P.; Cardona, A. Fiji: An Open-Source Platform for Biological-Image Analysis. *Nat. Methods* **2012**, *9* (7), 676–682. https://doi.org/10.1038/nmeth.2019.

(2) Schneider, C. A.; Rasband, W. S.; Eliceiri, K. W. NIH Image to ImageJ: 25 Years of Image Analysis. *Nat. Methods* **2012**, *9* (7), 671–675. https://doi.org/10.1038/nmeth.2089.

(3) Mortensen, K. I.; Churchman, L. S.; Spudich, J. A.; Flyvbjerg, H. Optimized Localization Analysis for Single-Molecule Tracking and Super-Resolution Microscopy. *Nat. Methods* **2010**, *7* (5), 377–381. https://doi.org/10.1038/nmeth.1447.

APPENDIX D: SUPPORTING INFORMATION FOR CHAPTER 6

D1. Material Fabrication

The fabrication sequence of Indium Phosphide (InP) nanowire (NW) arrays is outlined in Figure D1. The process begins with a cleaning step for the n-InP wafer (AXT, Inc.) with Oxygen plasma at 100W setting for 1 min, followed by spin-coating DisChem SurPass3000 as the adhesion promoter at 3000 rpm for 30s. The InP wafer was rinsed with deionized water for 60 seconds, followed by a baking step on the hot plate at 180 °C for 5 min. DisChem HSi-Q 6% is spin-coated onto the substrate at 1000 rpm, followed by annealing at 120 °C for 2 min.

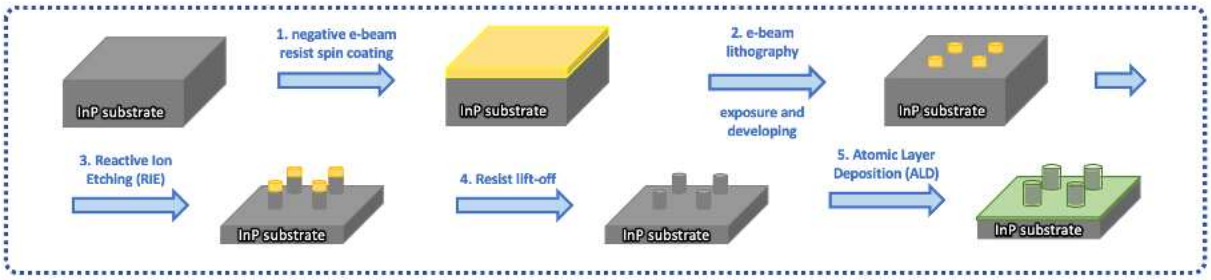

Figure D1. Schematic flowchart depicting the steps for the fabrication process of GaN coated InP NWs on an InP substrate. The key steps shown include e-beam lithography, RIE, and ALD.

The NW array patterns are defined with a Raith EBPG 5200+ electron beam lithography system. The beam file with a 150 nA current and 400 um aperture is selected, resulting in a spot size of 58 nm. The electron beam dose for the NW array patterns is set to 3,600 uC/cm^2. The exposed InP wafer is developed in 25% Tetramethylammonium hydroxide (TMAH) solution at room temperature for 30 seconds, then rinsed with deionized water for 1 min. The pattern is then etched into the InP substrate via a chlorine-based Reactive Ion Etching (RIE) process by Oxford PlasmaPro 100 Cobra ICP-RIE system.[1] Hydrogen, Argon, and Chlorine gas flowrates are set to 12, 4, and 7 sccm, respectively. The Radio Frequency (RF) power is set to 120W, and the Inductively Coupled Plasma (ICP) power is set to 1000W during etching. The etching time is 4 min and 30 seconds, resulting in an etching depth of ~2um. The patterned e-beam resist is lifted-

off by soaking in 10:1 Buffered Oxide Etchant for 1 min, followed by rinsing in deionized water for 1 min.

The gallium nitride (GaN) passivation layer deposition was performed by Ultratech Fiji G2 Atomic Layer Deposition (ALD) system. Trimethylgallium (TMGa, Strem Chemicals, 99.9999%-Ga) was used as the gallium precursor, and Nitrogen plasma served as the nitrogen precursor. Ultra-high purity grade Argon and Nitrogen gas tanks (Airgas, Inc.) were used as the gas supply for the ALD system. The temperatures of the TMGa precursor cylinder, the delivery line, and the susceptor were maintained at 25 °C, 150 °C, and 350 °C respectively. Each ALD cycle consisted of a 0.015 s pulse of TMGa at a flow rate of 30 sccm Argon carrier gas, 80 sccm Argon plasma, and 5sccm Nitrogen gas with turbo pump disconnected, resulting in a process pressure of 0.16 mbar. Subsequently, within a 60-second timeframe, the ALD cycle continued with three 20-second intervals of 300 W plasma. These intervals involved simultaneous flow rates of 30 sccm Argon carrier gas, 200 sccm Argon plasma, and 40 sccm Nitrogen gas, with the turbo pump connected and maintaining a process pressure of 0.04 mbar. Notably, within these 60 seconds, the plasma power, specifically set at 300 W, underwent intermittent activation and deactivation cycles. A total of 200 super cycles are performed while the InP NW sample is in the ALD chamber, resulting in a GaN layer with thickness of 8 nm measured by Ellipsometry (J.A. Woollam M-2000).

D2. Material Characterization

D.2.1 Electron Microscopy Characterization

Ex situ scanning electron microscopy (SEM) experiments were performed after optical mapping experiments. Figure D2 shows the SEM images of all the samples used in this study.

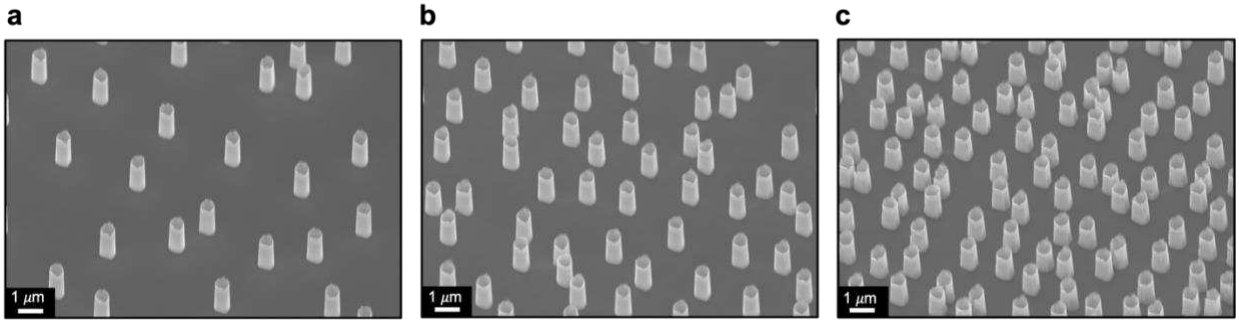

Figure D2. SEM images (15° tilt) for GaN coated InP NWs on an InP substrate depicted a pseudo-random square pattern. The diameter is 500 nm, the height is 2 μm and the pitch varies between 500 nm – 3 μm. (a) largest nearest neighbor distance sample (average distance: 2 μm), (b) middle nearest neighbor distance (average distance: 1.3 μm), (c) smallest nearest neighbor distance (average distance: 0.9 μm). Images were taken at an accelerating voltage of 15 keV and a working distance of 10 mm.

D.2.2 Microspectroscopy Characterization

Microspectroscopy of the GaN-coated InP NWs on an InP substrate is shown in Figure D3. A 532 nm laser was used for both Raman and PL measurements. Figure D3a shows the Raman spectrum of an individual InP NW. Here, two peaks marked with blue dashed lines correspond to transverse optical (TO) and longitudinal optical (LO) phonon modes.[2,3] The TO mode of InP is at 296 cm^{-1} and the LO mode is at 340 cm^{-1}. Figure D3b shows the PL spectrum of an InP NW. The NWs display an intense PL emission with a PL max at 920 nm.[4]

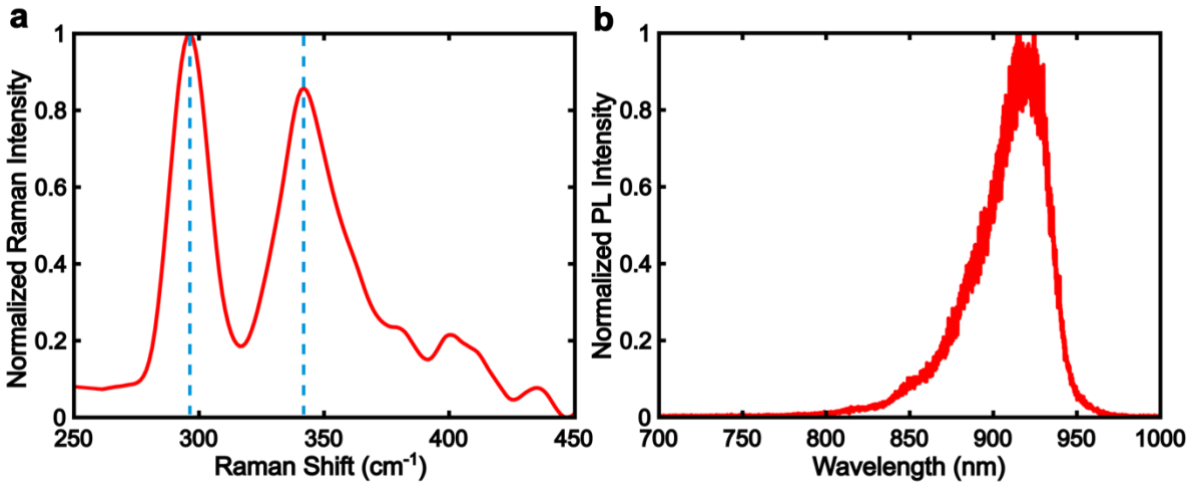

Figure D3. Microspectroscopy of the InP NW sample. (a) Raman spectra of InP NWs on an InP substrate. The blue dashed lines show peaks at 296 and 340 cm^{-1}. (b) PL spectra of InP NWs on an InP substrate. A 532 nm laser was used to excite the sample. The PL max is at 920 nm.

D.2.3 Reflectance and Absorptance Characterization.

The measured reflectance and calculated absorptance spectra are shown in Figure D4. The blue spectral trace is the measured total reflectance, and the black spectra trace is the measured diffuse reflectance. The absorptance spectrum was calculated using the following equation:

$$A = 1 - R_T - T$$

where A is the absorptance (%), R_T is the total measured reflectance (%), and T is the transmittance (%).[5] The transmittance in the sample is assumed to be zero for wavelengths shorter than 850 nm.

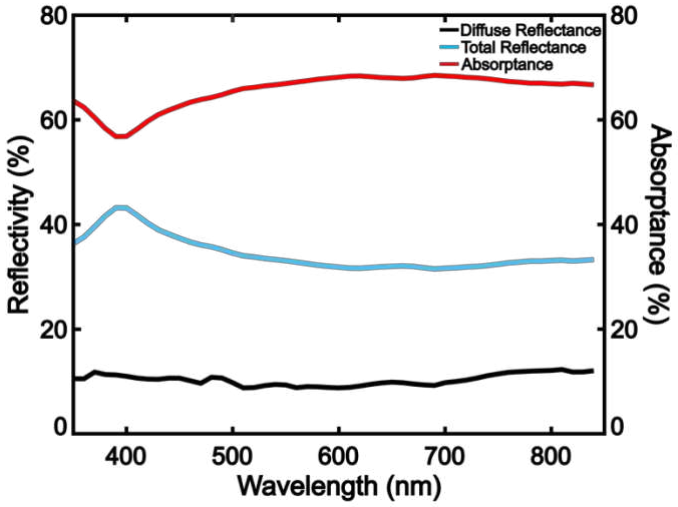

Figure D4. Reflectance and absorbance spectra of the InP NW sample. The blue spectral trace is the measured total reflectance, and the black spectra trace is the measured diffuse reflectance. The absorbance spectrum was calculated using the total measured reflectance with the assumption that there is no transmittance in the sample.

D.2.4 Photoluminescent Quantum Yield Determination (PLQY)

Based on literature values utilizing a similar material synthesis, the PL quantum efficiency is estimated to be as high as ≈75% with surface passivation.[6] We calculated the PLQY of the sample in three steps: (1) convert the arbitrary counts in the PL spectrum of Figure D3b to units of photons per second, (2) integrate over the PL spectrum to obtain the total number of photons emitted by the sample, and (3) divide the total number of photons by the number of incident photons used to excite the sample. To complete step 1, we illuminated the detector with a calibrated

monochromator source and determined the proportionality constant at every wavelength that relates the number of photons striking the detector to the number of counts produced by the software. We then applied that proportionality constant to the sample spectrum at every wavelength to obtain a PL spectrum in units of photons per second versus wavelength. We integrated that result (1.7×10^{16} photons) and divided by the total number of incident photons striking the sample (1.1×10^{17} photons), yielding a PLQY of 16%.

D3. PL and Reflection Measurements and Image Analysis Routines

D.3.1 Reflection and Photoluminescence Map Generation.

Widefield reflection and photoluminescence (PL) movies were analyzed using a hand-written Matlab code to process dual-view imaging data to generate reflection and PL intensity maps. The function begins by identifying the on and off points of the microscope stage and detector trigger signals based on a threshold, creating a digital signal to distinguish when the stage is stationary. We previously described the digital signal processing routine.[7] The derivative of these digital signals is used to pinpoint the exact on and off points for both the stage and detector signals. The key point is we link widefield images acquired on the sCMOS detector at each stage position, which defines the laser excitation position on the sample, to Raman/PL microspectroscopy data taken on the spectrometer detector.

Figure D5 shows a representative optical reflection image of an entire sample region that was selected for correlated reflection and PL mapping experiments. When the laser strikes the sample, we acquire a series of PL and reflection images using the dual view detection setup described in the main text.

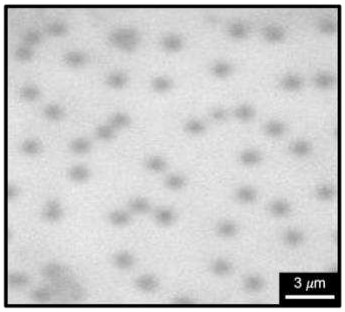

Figure D5. Optical reflection image of the InP NW array sample.

Our code averages all frames at a fixed excitation location, producing a single average reflection (Figure D6a) and PL (Figure D6b). This process is repeated for all specified coordinates, and the integrated intensities from each image are recorded as a function of stage position. Finally, we construct reflection (Figure D6c) and PL (Figure D6d) maps of the sample area in Figure D5 by plotting the summed intensity versus X and Y stage position. The InP NWs appear in the reflection and PL intensity maps, and their patterns match the dark objects (i.e., InP NWs) in Figure D5.

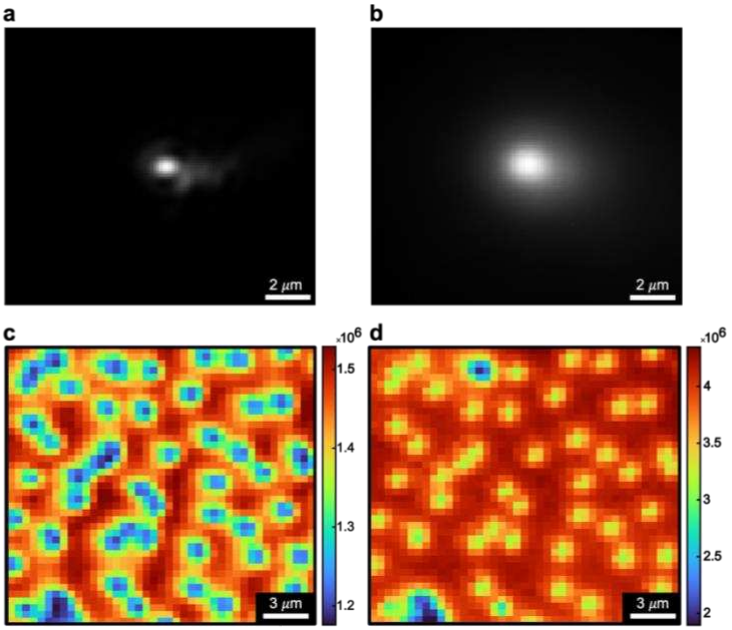

Figure D6. (a) Representative widefield reflection image upon exciting the InP substrate. (b) Representative widefield PL image upon exciting the InP substrate. (c) Reflection map of integrated intensities from cropped widefield reflection images. (d) PL map of integrated intensities from cropped widefield PL images.

D.3.2 Centroid Overlay of Electron and Optical Microscopy Images

We developed an image analysis procedure to overlay centroid coordinates in two different images using the imtransform function in MATLAB (see Supplementary Information in Reference 8)[8]. The first step of the procedure is to rotate a Scanning Electron Microscope (SEM) image (Figure D7a) to match the orientation of a widefield optical reflection image and the reflection map as shown in Figure D7b,c. Next, we select the centroid coordinates of the same objects in the optical and SEM images. The coordinates of the labeled NWs plotted as red x's in Figure D7a.

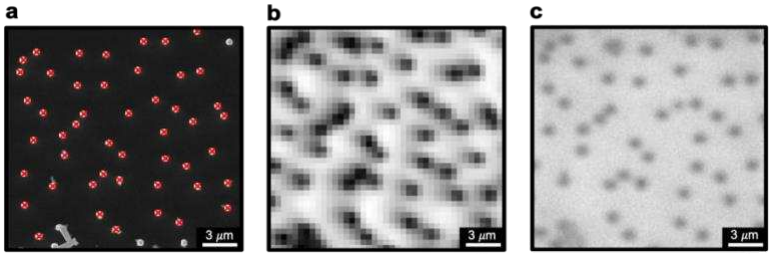

Figure D7. (a) SEM image of the NW array sample. The red x's mark the selection of a single NW used for further analysis. (b) Reflection map of integrated intensities from cropped widefield reflection images. (c) Reflection image of the sample on the optical microscope, showing the area for mapping.

D.3.3 Global Transformation

To accurately determine the centroid positions of NWs in the reflection map, we developed a global transformation algorithm that transforms the centroid locations identified in the SEM image onto the reflection map. With these accurate centroid coordinates, the reflection map can then be used to select the widefield images for further analysis. This code aligns the NW positions identified in the SEM image with the reflection map by selecting correlated points in both images, computing a geometric transformation, and applying this transformation to map the SEM coordinates onto the reflection map. The first step of the procedure is to identify control point pairs in both images. For example, the four red x's represent the centroid positions of four individual NWs by manually clicking the center of each NW as shown in Figure D8a. Figure D8b shows the reflection map of the same sample region in Figure D8a with the same red x's representing the

centroid positions of the same NWs. We use the "imtransform" function in Matlab to overlay the SEM coordinates onto the reflection map using the spatial transformation defined by the four control point pairs (red x's, Figure D8a). The transformed coordinates are then visualized on the reflection map (Figure D8c) for further analysis.

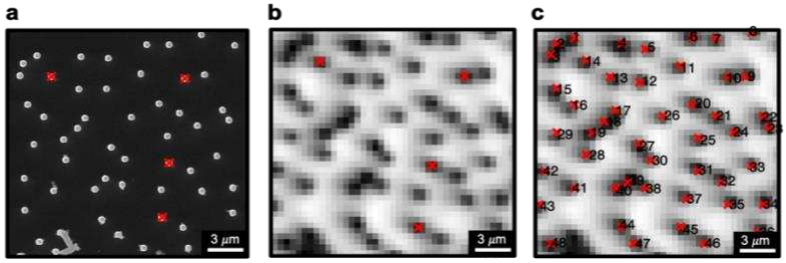

Figure D8. (a) SEM image of the NW array sample. The red x's mark the selection "moving coordinates", which are the points being transformed onto the reflection map. (b) Reflection map of integrated intensities from cropped widefield reflection images. The red x's mark the selection of "fixed coordinates", which are the matching points selected on the SEM image. (c) Reflection map after all 48 single NW coordinated have been transformed.

D.3.4 Local Transformation for Localizing Nearest Neighbor NWs

The next step is designed to determine the distance from one NW to its nearest neighbor in units of micrometers. This process involves using the SEM image and the coordinates of the globally transformed NW centroids. The user clicks on four points in the SEM image: the NW of interest (origin), the nearest neighbor, and two additional NW locations anchoring around the nearest neighbor as shown in Figure D9a. In the reflection map, the user clicks on the corresponding origin NW and the corresponding two anchoring NW coordinates as shown in Figure D9b. These pairs of points are then used to compute a local transformation around the origin NW of interest.

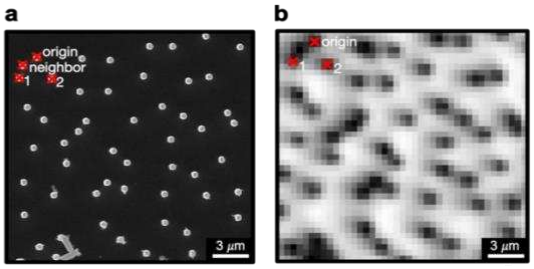

Figure D9. (a) SEM image of the NW array sample with the following marked points: NW of interest (origin), nearest neighbor NW, and two anchoring points around the neighboring NW. (b) Reflection map with the same marked points as in (a).

D.3.5 Calculating PL and Reflection Ratios as a Function of Distance

The PL and reflection ratios between the origin and nearest neighbor NW calculates the PL intensity ratio and the distance between origin points and their nearest neighbors in a set of widefield images. For each origin point, the function retrieves the corresponding widefield image, identifies the peak center via two options: option one is to fit the widefield image with a Voigt function to output the center position based on the maximum value of the fit, or option two is to use the maximum pixel value as the center position. An example of the Voigt fitting procedure is shown in Figure D10.

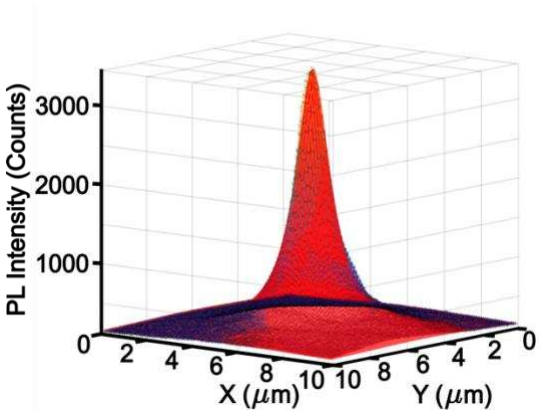

Figure D10. Three-dimensional PL intensity profile of a PL widefield image. The black x data points show the raw intensity image data, and the red mesh profile represents the fitted Voigt distribution to extract the center position of the NW.

Then, the code defines a 5-by-5-pixel box around the center value to compute the integrated intensity and standard deviation of the PL intensities, which is depicted as the blue box in Figure

D11a. We can refer to these boxes as the region of interest (ROI). The code repeats this process for the nearest neighbor using the coordinates determined previously, which is depicted as the red box in Figure D11a. The function then visualizes the integration boxes on the widefield image and computes the Euclidean distance between the origin and the nearest neighbor, along with the ratio of their integrated PL intensities. The function repeats this process for the reflection widefield images, as shown in Figure D11b. Due to the intense scattering and unpredictability of the widefield reflection images, the origin NW was found using the maximum pixel intensity of the image and the vector connecting the nearest neighbor NW is from a set center position found from the Voigt fitting (Figure D10). The outputs are arrays of various nearest neighbor distances defined from the center of an origin NW and intensity ratios for both reflection and PL.

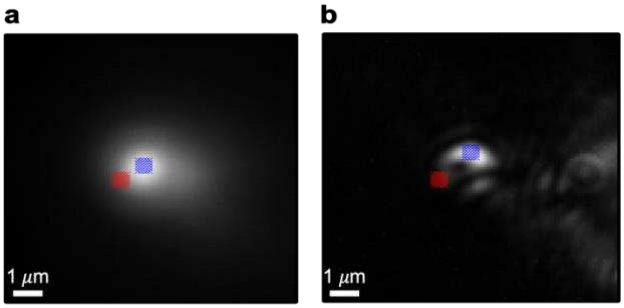

Figure D11. (a) Widefield PL image of a nearest neighbor pair. The origin NW ROI is shown as the blue pixel box and the nearest NW ROI is shown as the red pixel box. The pair displayed is selected using the points from Figure D9. (b) Widefield reflection image of a nearest neighbor pair. The vector to the nearest neighbor is drawn from a set center position for all the reflection widefield images.

D4. Widefield Imaging Experiments and PL/Reflection Intensity Ratio Analysis

The widefield reflection image of the 415 nm excitation on the substrate is shown in Figure D12a, using the same substrate region as shown in Figure 6.5d in the Main Text. Figure D12b shows the corresponding reflection image of the nearest neighbor pair depicted in Figure 6.5e of the Main Text. Figure D12c-d show the corresponding 3D intensity profile of the widefield images.

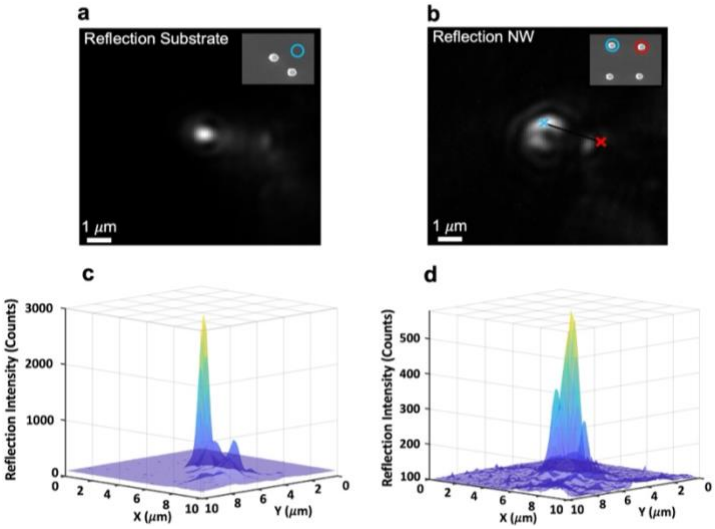

Figure D12. (a) Representative widefield reflection image of the excitation parked on the InP substrate. The inset shows an SEM image of the physical location of the laser on the sample (blue circle). (b) Widefield reflection image upon exciting a single NW. The inset shows a zoomed-in view of the SEM image region, where the blue circle indicates the laser excitation spot, and the red circle indicates the centroid location of the nearest NW. (c)-(d) 3D intensity profiles of the widefield reflection images in (a) and (b), respectively.

The PL and reflection intensities moves around the central NW (blue x in widefield images and blue circle in the inset SEM images in Figure D13), depending on the nearest NW neighbor (red x in widefield images and red circle in the inset SEM images in Figure D13) location.

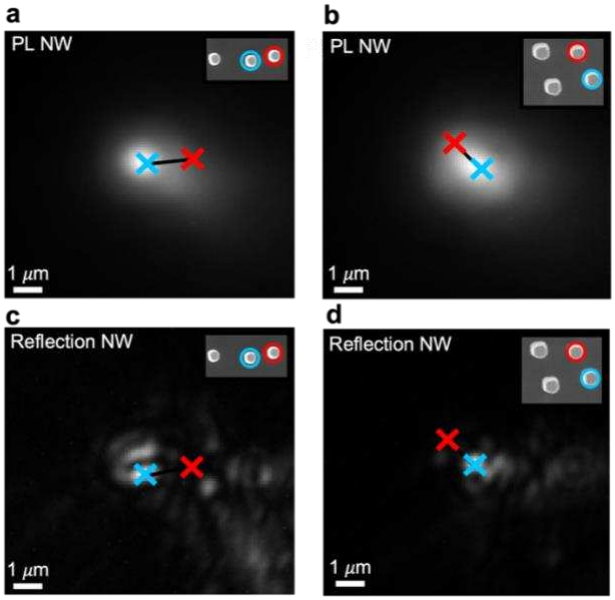

Figure D13. (a)-(b) Widefield PL images of a nearest neighbor pair. The origin NW ROI is shown as the blue x and the nearest NW ROI is shown as the red x. The black vector is the distance vector between the centroid locations of the NW. (c)-(d) Widefield reflection images of a nearest neighbor pair corresponding to (a) and (b) respectively.

D5. Line Profile Analysis of the Instrument Response Function using the InP Substrate

The PL and reflection experimental results from NW pairs were compared to line profile results resulting from illumination of the bare substrate, which is a useful control in our system. Figure D14 shows the line profiles for the excitation on the bare substrate in both the PL and reflection channels. Figure D14a shows the excitation source on the bare substrate. The red dashed line in the inset shows where the line profile was taken on the widefield image. The line profile is plotted as the blue solid line and was fit with a Lorentzian distribution plotted as the red dashed line. Half of the fit is plotted as a red dashed line in Figure 6.6a of the main text. Figure D14b is the line profile of the excitation source on the substrate in the reflection channel. Compared to the PL, the reflection line profile is much narrower and rapidly decays. Half of the fit is plotted as the blue dashed line in Figure 6.6b of the main text.

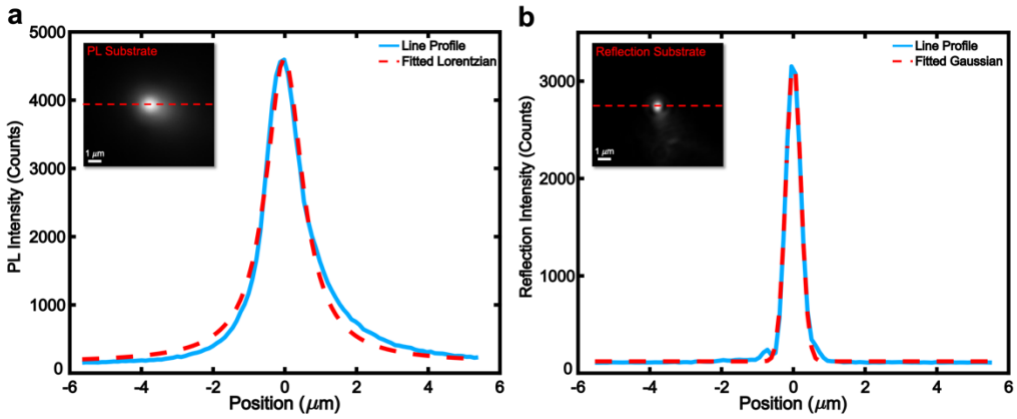

Figure D14. (a) Line profile of the widefield PL image of a 415 nm laser excitation parked on the InP substrate. The blue solid line is the line profile, and the red dashed line is the Lorentzian distribution fit. (b) Same as (a), but for the reflection line profile. The red dashed line is the Gaussian distribution fit.

D6. Details of Geometric Re-absorption Probability Calculations

The calculator used to generate the geometry calculations described below was written in Matlab R2022a and can be accessed at:

https://github.com/OliviaFBird/Monte-Carlo-Simulations-for-Photon-Recycling-in-Nanowire-Arrays/blob/main/m241029_PR_NWArray_GeometricCalculator.m.

The geometric probability of re-absorption is broken down into the multiplication of 3 parts: the probability that light will be emitted from the side of a NW (P_{Eside}), the probability of being within an angle that will intersect another wire in the plane of the wire array (P_{XY}), and the probability that the photon will be emitted at an angle to intersect another wire at an appropriate height, rather than passing above or below it (P_Z). All trigonometric calculations assume that the NW are perfect cylinders.

$$P_{tot} = P_{ESide} \times P_{XY} \times P_Z \qquad \text{Eq. D1}$$

To calculate the probability of side emission it is assumed that a photon can be emitted from the wire's surface at any point with equal likelihood. Thus, the chance that it will be emitted from the side is simply the surface area of the side of the wire divided by the surface area of the entire wire.

$$P_{Eside} = \frac{2 \times \pi \times r \times h}{(2 \times \pi \times r \times h) + (2 \times \pi \times r^2)} \qquad \text{Eq. D2}$$

where *r* is the radius of the wire and *h* is the height of the wire. The probability of emitting photons from the wire at an appropriate angle in the XY plane is the angle which will be occluded by a wire of radius (*r*) at a distance away of (*d*) then divided by the total possible angle.

$$P_{XY} = \frac{2 \times \tan^{-1}\left(\frac{r}{d}\right)}{2 \times \pi} \qquad \text{Eq. D3}$$

The probability that emission will be neither over no under the neighboring wire is once again calculated by determining the angle occluded by neighboring wire divided by the total possible angle of the z-axis (along the height of the wire). This value is dependent on the height the photon leaves the initial wire (*z*), and it is assumed that all *z*-heights are equally probable. For the calculations in Figure 6.7 the probability was calculated for all *z*-heights along the wire (in 1 nm increments) and the average probability was used.

$$P_Z = \sum_{z=1}^{h} (\pi - \tan^{-1}(\frac{d-r}{h-z}) - \tan^{-1}(\frac{d-r}{z})) / (h \times \pi) \qquad \text{Eq. D4}$$

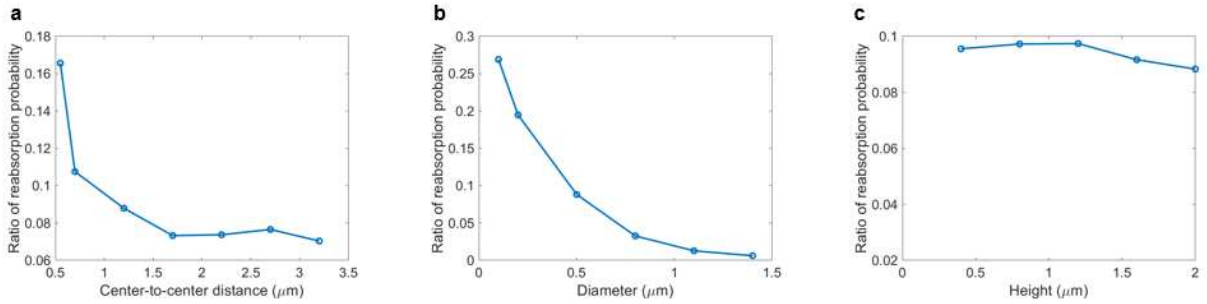

Figure D15. Ratio of the re-absorption probability between the second neighboring wire and the first neighboring wire if considered two neighbors on either side. The parameters studied were (a) center-to-center distance, (b) NW diameter, and (c) NW height.

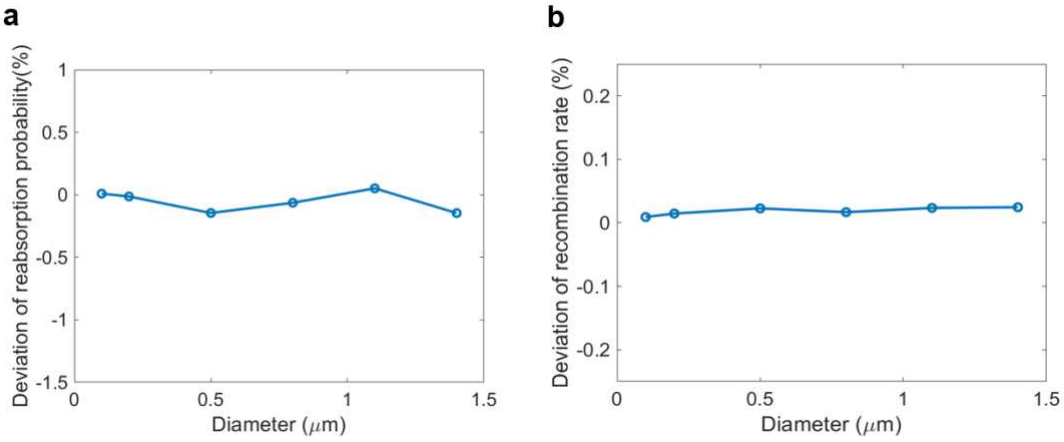

Figure D16. Deviations of (a) re-absorption probability and (b) recombination rate in the neighboring wire when the substrate is modeled at thickness of 50 μm rather than 500 μm.

D7. Details of Monte Carlo Simulations

A Monte Carlo (MC) simulation was developed to investigate photon recycling and reflection in the NW array. The simulation model consisted of two identical NWs, with one subjected to continuous excitation and the other capable of receiving light only through PL or reflection from the first wire. The simulation was written and run in Matlab R2022a. Five variable parameters were tested: interwire distance, NW diameter, NW height, PLQY, and the fraction of reflected light scattering sideways vs upward. The simulation can be accessed at:

https://github.com/OliviaFBird/Monte-Carlo-Simulations-for-Photon-Recycling-in-Nanowire-Arrays/blob/main/m241029_PR_NWArray_MonteCarlo.m

The base case simulation parameters matched experimental data wherever present including NW dimensions (diameter = 0.5 μm, height = 2 μm, nearest neighbor distance = 1.3 μm), and laser parameters (0.3 mW, 415 nm). For the variable diameter dependence (Figure 6.8b in the Main Text) the edge-to-edge distance was held constant at 0.8 μm rather than the center-to-center distance to ensure that the impact of increasing diameter was not convoluted with the impact of moving wires closer. A PLQY of 0.5 and outward scattering fraction of 0.1 were chosen as the base case for these parameters. Reflection probabilities were calculated using Fresnel's equations and previously determined refractive indices; these values match the experimentally determined reflection below 840 nm, but extends further into the red so the reflection of PL light can also be modeled.[9] Absorption probabilities were derived from the Beer-Lambert Law using previously determined absorption coefficients.[9]

To model optical interactions, reflected light was categorized as either upward (detectable) or outward, with the latter having a probability of interacting with the second wire based on geometric parameters P_{XY} (Eq. D3) and P_Z (Eq. D4). Each absorbed photon generates one excited electron-hole pair which has three possible outcomes at each step: radiative recombination, non-radiative recombination, or persistence until the next excitation. The competition between these processes was simulated using a direct kinetic MC method[10,11], using the equation:

$$1 = A \times (k_{pho} + k_{Rad} \times N_e + k_{Non-Rad} \times N_e) \qquad \text{Eq. D5}$$

where: A is a normalization constant, k_{pho} is the experimental laser excitation frequency, k_{Rad} is the radiative recombination rate constant for InP.[12] $k_{Non\text{-}Rad}$ is the non-radiative recombination rate constant and is calculated from the k_{Rad} and PLQY, and N_e is the number of excited electrons in

the wire. A random number (0 – 1) is generated and its position in the stack described in Eq. D5 is used to determine which step occurs next. The direction of light emission was determined based on surface areas (Eq. D2) and upward emitted light was detected while outward emitted light had a possibility to be re-absorbed by the neighboring wire, determined by the geometric re-absorption probability while also accounting for the possibilities of reflection and transmission even within the required solid angle. In addition to the solid angle the emitted light must be an appropriate wavelength to be absorbed, determined by the overlap integral between the experimental PL spectrum and calculated absorptance.

There are a few key assumptions used this model. Photons were treated as infinitely small particles moving in straight lines (and thus probability of interaction can be determined by geometric relations). Infinite charge mobility within NWs was assumed, leading to photon emission with equal probability from any point on the NW surface. Wires are treated as perfect cylinders neglecting microscale roughness or specific faceting. Additionally, the simulation focused on energy transmission through NWs, excluding bulk substrate effects. Finally, for computational efficiency, rather than simulating each photon individually photons were simulated in bunches of 10^6 which move together, resulting in 6.27×10^8 total excitation bunches for each experiment.

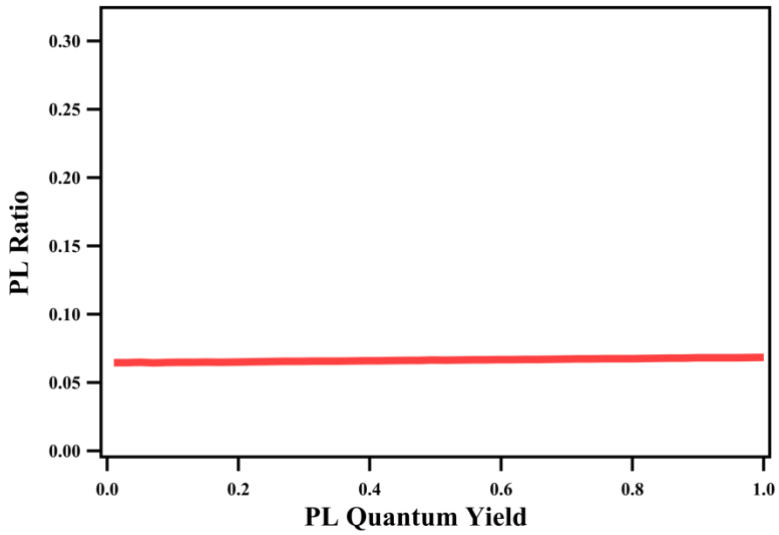

Figure D17. Monte Carlo simulation of the PL ratio over PLQY ranges from 0.01 to 1.00. From this simulation we find that increasing PLQY does slightly increase the PL ratio due to more opportunities for photon recycling. However, this effect is weak, as a higher PLQY will increase the PL observed from both the initially excited wire and the neighbor wire, thus the ratio remains relatively constant.

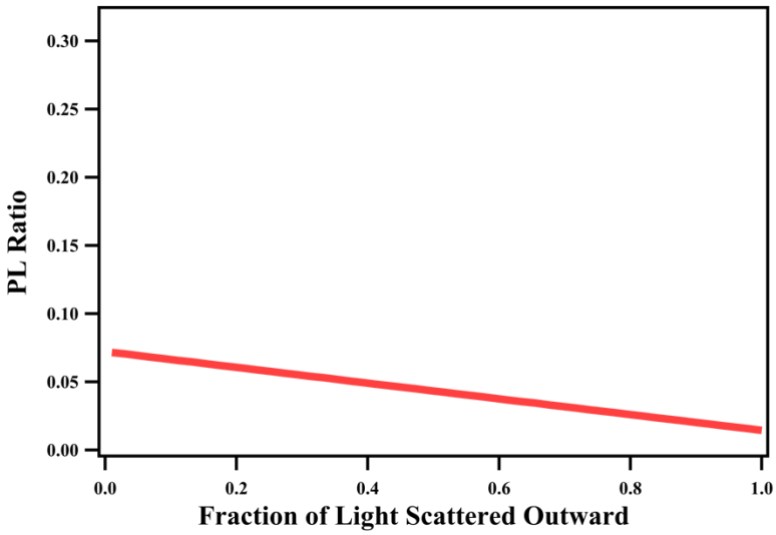

Figure D18. Monte Carlo simulation of the PL ratio vs the fraction of light scattered outward. All other light is scattered upward. From this simulation we find that as more light is scattered upward the observed PL ratio increases. This may initially be counterintuitive as having light scatter outward off the initially excited wire provides more opportunities to be absorbed by the neighboring wire. However, the dominating effect is the fraction of light scattered off the neighboring wire that can be detected, which requires the light be reflected upward.

D8. Coupled Wave Optics and Semiconductor Photophysics COMSOL Model

D.8.1 Electric Field

The optical model treats light as an electromagnetic wave and solves the classic Maxwell's equations for the electric and the magnetic fields.[19] Treating light as a wave makes our approach

more applicable to nanoscale morphologies, and especially when the characteristic length scales become comparable to the wavelengths of either the incident or the emitted photons. Prior work demonstrates that if the NWs are smaller than or comparable to the wavelength of light, diffraction and scattering become significant, leading to deviations from Beer's law.[5] Also, Maxwell-Garnett effective medium theory is not suitably applied for our case, since Maxwell-Garnett theory assumes low volume fractions of inclusions and weak electromagnetic interaction in between, which is not met in the NW array.[20]

For the optical modeling, the 2D domain comprises of three NWs, the substrate, and the surrounding air. The air at the top is truncated to a height of 2.5 μm such that it covers the maximum modeled height of the NWs of 2 μm, and additionally, further expanding the space occupied by air has negligible impact on the model predictions. Note that incident light absorption and emission is modeled at two distinct wavelengths - the incident laser source wavelength in the experiments is $\lambda_i = 415$ nm and the emission wavelength, $\lambda_e = 900$ nm.

For the sake of simplicity, the emission of photons is only tracked at the peak emission wavelength of 900 nm, which is based on the measured PL spectra of InP NWs on an InP substrate (Figure D3b), and the absorption is only captured at 415 nm. Therefore, the electric fields corresponding to the incident light source and the emission are separately solved at distinct wavelengths with wavelength-specific refractive index *n* and absorption coefficient α. The electric field, E, whether it is E_{i,λ_i} or E_{e,λ_e}, satisfies the steady-state wave equation in Eq. D6,

$$\nabla \times (\nabla \times E) - \left(\frac{2\pi}{\lambda_0}\right)^2 \varepsilon_r E = 0, \qquad \text{Eq. D6}$$

where λ_0 is the wavelength of light in vacuum and λ_0 can be either λ_i or λ_e based on we are modeling for the electric field of the incident laser source or the photon emission. ε_r is the relative

electric permittivity of the medium; in air $\varepsilon_r = 1$. For InP, the relative electric permittivity is related to the complex refractive index as, $\sqrt{\varepsilon_r} = n + ik$. Eq. D7 can be derived from the classic Maxwell's equations for the electric and the magnetic field as shown in Eq. D7-D12.

$$\nabla \times E = -\frac{\partial B}{\partial t} \quad \text{Eq. D7}$$

$$\nabla \times B = \mu_0 \epsilon_0 \frac{\partial \mathrm{E}}{\partial t} \quad \text{Eq. D8}$$

Here, B is the magnetic field, μ_0 and ϵ_0 is the vacuum permeability and permittivity. Take the curl of the first equation and substitute the second equation,

$$\nabla \times (\nabla \times E) = -\mu_0 \epsilon_0 \frac{\partial^2 E}{\partial t^2} \quad \text{Eq. D9}$$

The speed of light in vacuum is related to the permeability and permittivity by:

$$c_0 = \frac{1}{\sqrt{\mu_0 \epsilon_0}} \quad \text{Eq. D10}$$

For harmonic time dependence, where the electric field varies sinusoidally as $e^{-i\omega t}$, we can replace the second time derivative with $-\omega^2$. Therefore, the equation can be derived to

$$\nabla \times (\nabla \times E) - \left(\frac{2\pi}{\lambda_0}\right)^2 E = 0 \quad \text{Eq. D11}$$

In a medium with relative permittivity ε_r, the wave equation modifies to:

$$\nabla \times (\nabla \times E) - \left(\frac{2\pi}{\lambda_0}\right)^2 \varepsilon_r E = 0 \quad \text{Eq. D12}$$

Figure 6.2a in the Main Text solves the electromagnetic field in the modeling domain surrounded by the blue boundary and apply the scattering boundary condition, while they are two separate simulations at different frequencies: one solves the electric field due to the incident light

of $\lambda_i = 415$ nm shining on the central wire, and another solves for the emitted photons at $\lambda_e = 900$ nm. Scattering boundary condition is applied at all the boundaries for the modeling domain (blue lines in Figure 6.2a of the Main Text),

$$\hat{\mathrm{n}} \times (\nabla \times E) - i(\frac{2\pi}{\lambda_0})\hat{\mathrm{n}} \times (E \times \hat{\mathrm{n}}) = 0 \qquad \text{Eq. D13}$$

$\nabla \times E$ is related to the magnetic field via Maxwell's equation, so the first term represents the tangential component of the magnetic field. The second term represents the tangential component of the electric field adjusted by the wavenumber $\frac{2\pi}{\lambda_0}$, and the imaginary unit i indicates a phase relationship between the electric and magnetic fields. This equation ensures the tangential components of the electric and magnetic fields are balanced at the boundary. Physically, it enforces to model a domain with open boundaries, where an electromagnetic wave will pass without any reflection. That means, we want to use boundary conditions along the outside that are transparent to any reflected waves from the NW structure, and these waves will just escape. Doing so will let our truncated domain at the top be a reasonable approximation of infinite air space.

Port boundary conditions are applied at the top of the central wire and the bottom of the substrate. Wave excitation is turned on for the top port and turned off for the bottom port. We have considered normal incidence with the electric field polarized along the z-axis, which is the direction perpendicular to the 2D domain.

D.8.2 Electric field from emitted photons.

To solve for E_{e,λ_e}, the same governing equations as in Eq. D7-D12 are applied, but with modifications in the problem set-up. Point dipole sources are used to simulate emission of photons from the recombination of charge-carriers in the semiconductor material. An array of 5 electric point dipoles is inserted along the height of the NW in the center that is illuminated with an external

laser source (Figure 6.2a in the Main Text). Every dipole is assigned an arbitrary, but uniform value for the magnitude of the dipole moment, P. The choice of the dipole moment magnitude is inconsequential in our calculations because this workflow is ultimately used to obtain fractional probabilities of an emitted photon at one location being re-absorbed at the same or a different location. At each dipole position, two discrete orientations in x- and y-directions are simulated since no preferred direction is assumed, and the corresponding electric field is averaged over both directions.

From the electric field of emitted photons, the re-absorption probability is calculated and interpreted as fractional probabilities of an emitted photon being re-absorbed at different locations, and it is calculated at the emission wavelength $\lambda_e = 900$ nm. The re-absorption probability of each dipole j is obtained by,

$$p_{\mathrm{j}} = \frac{\iint P_{\mathrm{abs},\lambda,\mathrm{j}}}{P_{\mathrm{dip,j}}} = \frac{\iint \frac{\pi c_0}{\lambda_e} |E_{\lambda_e}|^2 \mathrm{Im}\{\varepsilon_{\lambda_e}\}}{\int \hat{\mathrm{n}} \cdot S_{\lambda_e}} = \frac{\iint \frac{\pi c_0}{\lambda_e} |E_{\lambda_e}|^2 \mathrm{Im}\{\varepsilon_{\lambda_e}\}}{\int \hat{\mathrm{n}} \cdot \frac{1}{2}(E_{\lambda_e} \times H_{\lambda_e})} \qquad \text{Eq. D14}$$

The numerator is the spatial integration of the optical power absorbed per unit volume, and the integration can be conducted at different locations, including the central wire ($p_{\mathrm{cen,j}}$), the neighboring wire ($p_{\mathrm{nei,j}}$), and the substrate ($p_{\mathrm{sub,j}}$). The denominator represents the dipole power, which is calculated by the integration of the power outflow over a small non-absorbing cavity surrounding the dipole. Inside the cavity, the refractive index is the same as InP, while the extinction coefficient is set as zero. The power outflow can be calculated by the cross product of the electric field E_{λ_e} and magnetic field H_{λ_e}, which is related to the electric field by the Maxwell's equation,

$$H_{\lambda_e} = -\frac{1}{i\omega_{\lambda_e}\mu_0} \nabla \times E_{\lambda_e} \qquad \text{Eq. D15}$$

where μ_0 is the vacuum permeability, and ω is the angular frequency. Then, the re-absorption probability is averaged over the 5 dipoles at each location, for example, at the neighboring wire,

$$p_{\mathrm{nei}} = \frac{\sum_1^5 p_{\mathrm{nei,j}}}{5} \qquad \text{Eq. D16}$$

To justify the effect of dipole numbers on this averaged re-absorption probability, more dipoles are put inside the central NW. We take the case of D = 1.4 μm as an example. Along with the five dipoles that already exist, 12 more arrays of five dipoles are inserted along the diameter of the NW with a step of 0.1 μm. There are 65 dipoles in total, and then the procedure above is followed to obtain the averaged re-absorption probability. Compared with 5 dipoles, the deviations of p_{cen}, p_{nei}, and p_{sub} are 1.5%, 7.3%, and 5.5%, respectively. As the dipole is moved closer or farther away from the neighboring wire, $p_{\mathrm{nei,j}}$ will become larger or smaller. However, after averaging, p_{nei} is not significantly affected by the number of dipoles.

D.8.3 Volumetric Rate of Charge-Carrier Generation.

The rate of the optical power absorbed per unit volume, $P_{abs,\lambda}$, is related to the local electric field and the optical material properties as in Eq. D17,

$$P_{\mathrm{abs},\lambda} = \frac{\pi c}{\lambda} |E_\lambda|^2 \mathrm{Im}\{\varepsilon_\lambda\} \qquad \text{Eq. D17}$$

where, $\varepsilon_\lambda = \varepsilon_r \varepsilon_0$ is the electric permittivity, with ε_0 being the vacuum permittivity. The imaginary portion of the electric permittivity is used in these calculations. The volumetric rate of charge-carrier generation is then obtained from the power absorbed as,

$$G_\lambda = \frac{P_{\mathrm{abs},\lambda}}{\frac{hc}{\lambda}} = \frac{\pi |E_\lambda|^2 \mathrm{Im}\{\varepsilon_\lambda\}}{h} \qquad \text{Eq. D18}$$

In our calculations, the absorption coefficient, α_λ is related to the $\mathrm{Im}\{\varepsilon_\lambda\} = \frac{\varepsilon_0 \alpha_\lambda \lambda n}{2\pi}$. The total rate of generation of photons at any spatial location in the modeling domain is the sum of the generation of photons, both from the incident light source, G_{i,λ_i}, and due to re-absorption of emitted photons, i.e. due to photon recycling, from any location within the domain, $G_{\mathrm{pr},\lambda_e}$

$$G_{\mathrm{total}} = G_{\mathrm{i},\lambda_i} + G_{\mathrm{pr},\lambda_e} \qquad \text{Eq. D19}$$

To obtain G_{i,λ_i}, we apply the same equation as in Eq. D19, but for $G_{\mathrm{pr},\lambda_e}$, the method is a little different. For the central wire,

$$G_{\mathrm{pr,cen}} = \overline{R_{\mathrm{cen}}} \times p_{\mathrm{cen}} + 2\overline{R_{\mathrm{nei}}} \times p_{\mathrm{nei}} \qquad \text{Eq. D20}$$

for the neighboring wire,

$$G_{\mathrm{pr,nei}} = \overline{R_{\mathrm{cen}}} \times p_{\mathrm{nei}} + \overline{R_{\mathrm{nei}}} \times p_{\mathrm{cen}} \qquad \text{Eq. D21}$$

where $\overline{R_{\mathrm{cen(nei)}}}$ is the averaged value of the recombination rate over the central (neighboring) wire, $p_{\mathrm{cen(nei)}}$ is the averaged re-absorption probability over dipoles at different locations.

The new generation rate, defined as the sum of the initial optical generation rate and the photon recycling generation rate, is imported into the next iteration of the numerical solver to compute the resulting recombination rate until converged. If photon recycling is not considered, then $G_{\mathrm{pr},\lambda_e}$ is equal to zero, and the total generation rate is the initial optical generation rate due to the external light source.

D.8.4 Semiconductor Photophysics

Standard steady-state equations for charge and species – electrons and holes – conservation is modeled; drift-diffusion equations are modeled for electrons and holes.[21] Specific governing

equations are detailed below. The static behavior of the charge carriers in the semiconductor is calculated by solving Poisson's equation,

$$\nabla \cdot (\varepsilon_0 \varepsilon_\mathrm{r} \nabla \phi) = -\rho = q(n - p) \qquad \text{Eq. D22}$$

in which ρ is the net charge concentration, n and p are the electron and hole concentration, q is the elementary charge and ϕ is the electric potential. The dynamic behavior of the carriers is calculated by solving the drift-diffusion equations for electrons and holes inside the semiconductor,

$$i_\mathrm{e} = \mu_\mathrm{e} n \nabla E_\mathrm{C} + \mu_\mathrm{e} k_\mathrm{B} T \nabla n \qquad \text{Eq. D23}$$

$$i_\mathrm{h} = \mu_\mathrm{h} p \nabla E_\mathrm{V} - \mu_\mathrm{h} k_\mathrm{B} T \nabla p \qquad \text{Eq. D24}$$

Here, the current density of carriers is composed of two parts. The first term on the right side is the drift current, and the second term is the diffusion current. $\mu_{\mathrm{e/h}}$ are the mobilities of electrons and holes. E_C and E_V are the conduction band and valence band energy levels, given by $E_\mathrm{C} = -q(\phi + \chi)$ and $E_\mathrm{V} = -q(\phi + \chi + E_\mathrm{g})$, where χ is the electron affinity and E_g is the bandgap. The total current is contributed by either the carrier drift due to the applied bias or the carrier diffusion due to the concentration gradient. In this model, there is no bias applied, so the diffusion will play the dominant role in the carrier transport. The final steady-state electron and hole transport equations are:

$$\nabla \cdot (-\mu_\mathrm{e} n \nabla \phi + \mu_\mathrm{e} k_\mathrm{B} T \nabla n) = R_\mathrm{e,rad} - G_\mathrm{e} \qquad \text{Eq. D25}$$

$$\nabla \cdot (-\mu_\mathrm{h} p \nabla \phi - \mu_\mathrm{h} k_\mathrm{B} T \nabla p) = R_\mathrm{h,rad} - G_\mathrm{h} \qquad \text{Eq. D26}$$

The right side is the net electron or hole recombination rate, and radiative recombination $R_{\mathrm{e/h,rad}}$ is considered herein. The generation rate $G_{\mathrm{e/h}}$ is calculated by Eq. D19. The radiative recombination is given by,

$$R_{\mathrm{e/h,rad}} = B(np - {n_i}^2) \qquad \text{Eq. D27}$$

in which $n_{\mathrm{i}} = \sqrt{N_{\mathrm{C}}N_{\mathrm{V}}}\exp\left(-E_{\mathrm{g}}/2/k_{\mathrm{B}}/T\right)$ is the intrinsic density, E_{g} is the bandgap energy of the material and N_{C} and N_{V} are the conduction and valence band densities of states, respectively. These are material and temperature-dependent properties, and the intrinsic density is calculated as 6.91×10^{12} 1/m^3 at a temperature of 293 K. The temperature and wavelength dependent radiative recombination factor B is calculated by,

$$B = \frac{2\pi c}{{n_i}^2\lambda^2}\int_{E_g}^{\infty}\frac{1}{\lambda^2}\alpha\exp\left(-\frac{hc}{\lambda k_{\mathrm{B}}T}\right)d\lambda \qquad \text{Eq. D28}$$

which is a material and temperature dependent property as well. α is the absorption coefficient, is related to the imaginary part of refractive index k by $\alpha = 4\pi k/\lambda$. Regarding the boundary condition, when there is no surface recombination considered, the insulation condition is applied at all the semiconductor interfaces (green lines in Figure 6.2b of the Main Text) except the bottom of the substrate,

$$\begin{aligned} \hat{\mathrm{n}} \cdot D &= 0, \\ \hat{\mathrm{n}} \cdot i_{\mathrm{e}} &= 0, \\ \hat{\mathrm{n}} \cdot i_{\mathrm{h}} &= 0, \end{aligned} \qquad \text{Eq. D29}$$

since there is no external load and photocurrent in the model. $\hat{\mathrm{n}} \cdot i_{\mathrm{e/h}} = 0$ is the boundary condition for the electron and hole carriers, meaning there are no carriers exiting the NWs. $\hat{\mathrm{n}} \cdot D = 0$ is the boundary condition for ϕ. D is the electric displacement field and is equal to $-\varepsilon\nabla\phi$. If there is no

surface charge on the interface, the normal component of D is continuous. We added an ideal ohmic contact (red line in Figure 6.2b of the Main Text) at the bottom, at a large distance from the NWs and applied zero voltage to ensure that the NW domain is solved numerically at zero bias so that no electric field would affect the motion of the carriers. There is another boundary condition for the carriers based on local thermodynamic equilibrium at the contact,

$$n = \frac{1}{2}(N_{\mathrm{D}}^{+} - N_{\mathrm{A}}^{-}) + \frac{1}{2}\sqrt{(N_{\mathrm{D}}^{+} - N_{\mathrm{A}}^{-})^2 + 4n_{\mathrm{i}}^2} \qquad \text{Eq. D30}$$

$$p = -\frac{1}{2}(N_{\mathrm{D}}^{+} - N_{\mathrm{A}}^{-}) + \frac{1}{2}\sqrt{(N_{\mathrm{D}}^{+} - N_{\mathrm{A}}^{-})^2 + 4n_{\mathrm{i}}^2} \qquad \text{Eq. D31}$$

in which N_{A}^{-} and N_{D}^{+} are ionized acceptor and donor concentrations, which are not included in this model, so the boundary condition is simplified to $n = p = n_i$. When surface recombination is considered, it will add an extra term to the insulation boundary condition at all the NW interfaces.

$$\frac{1}{q}\hat{\mathrm{n}} \cdot i_{\mathrm{e/h}} = R_{\mathrm{s,e/h}} \qquad \text{Eq. D32}$$

The surface recombination is given by,

$$R_{\mathrm{s,e/h}} = \frac{np - {n_i}^2}{(n + n_1)/v_{\mathrm{s,h}} + (p + p_1)/v_{\mathrm{s,e}}} \qquad \text{Eq. D33}$$

with the electron and hole surface recombination velocity $v_{\mathrm{s,e/h}}$. The electron and hole defect densities are calculated according to

$$n_1 = n_i \exp\left(\frac{\Delta E_t}{kT}\right) \qquad \text{Eq. D34}$$

$$p_1 = n_i \exp\left(\frac{-\Delta E_t}{kT}\right) \qquad \text{Eq. D35}$$

where $\Delta E_t = E_t - E_i$ is the difference between the defect level and the intrinsic level. By correctly setting the boundary conditions, the carriers would recombine at the sidewalls or scatter among the NWs, rather than contribute to a photocurrent.

D.8.5 Supplementary Figures

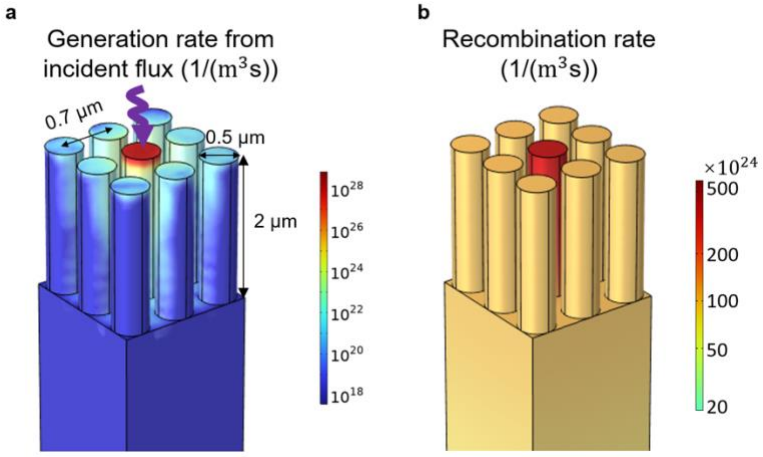

Figure D19. 3D profiles predicted for 0.5 μm-diameter and height 2 μm-tall NWs separated by 0.7 μm for the (a) volumetric charge-carrier generation rate (m^{-3} s^{-1}) from the incident photon flux, and (b) total recombination rate (m^{-3} s^{-1}).

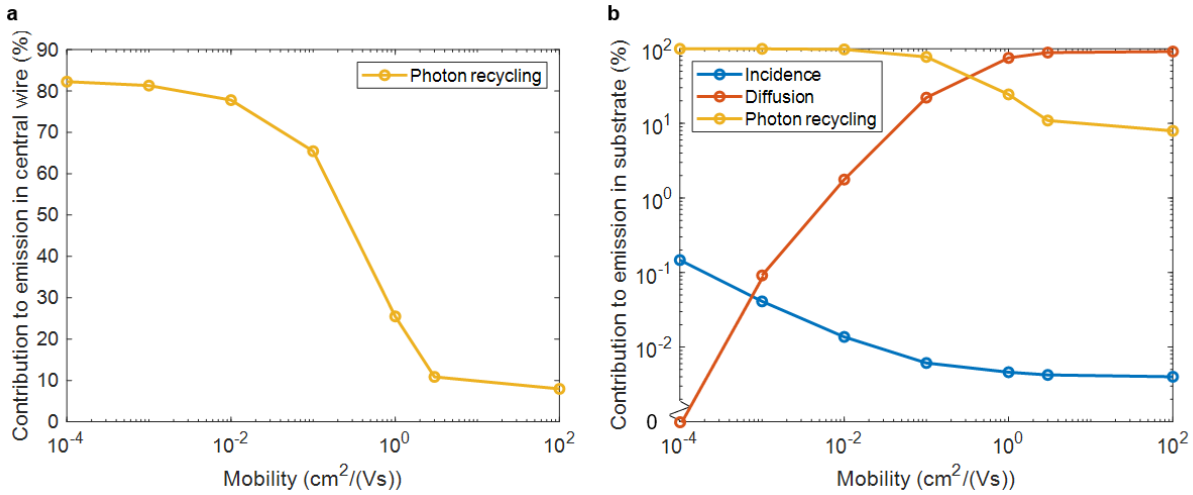

Figure D20. Respective contribution percentage to total emission in (a) central wire and (b) substrate, from incident source, carrier diffusion, and photon recycling with the variation of carrier mobility. Electron and hole mobilities are assumed to be the same with a range from 10^{-4} to 100 cm^2/Vs. Baseline geometric parameters are used: diameter = 0.5 μm, height = 2 μm, nearest neighbor distance = 1.3 μm.

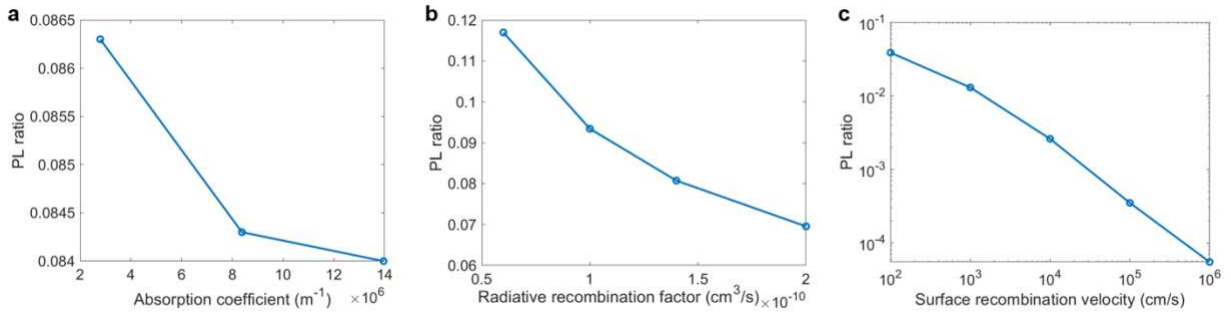

Figure D21. PL ratio with the variation of (a) absorption coefficient, (b) radiative recombination factor, and (c) surface recombination velocity.

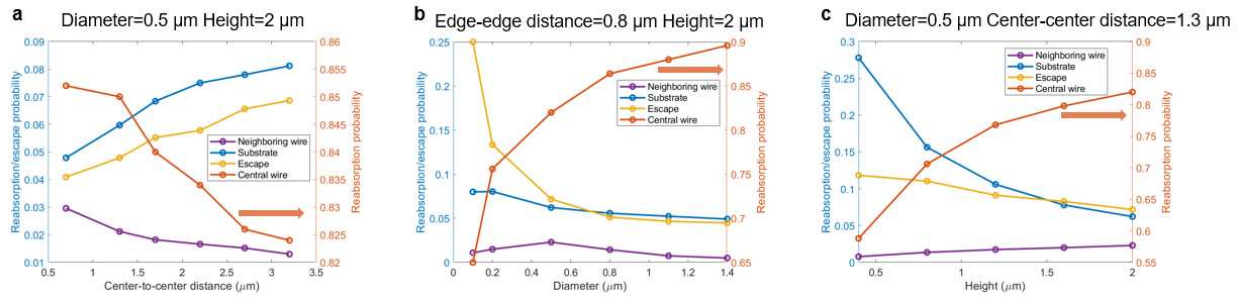

Figure D22. Re-absorption probabilities in the central/neighboring wire/substrate and escape probability with various geometric parameters: (a) center-to-center distance, (b) diameter, and (c) height. The re-absorption probability in central wire uses the right y axis, and the other three probabilities use the left y axis.

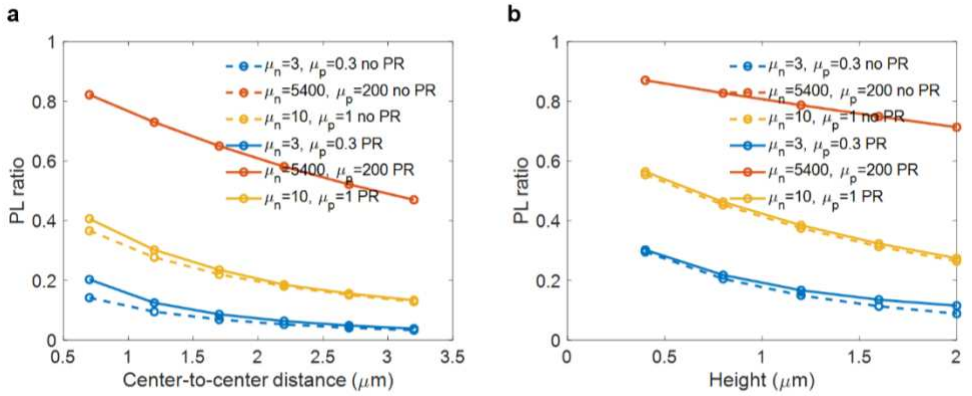

Figure D23. Simulated PL ratio across variable geometry parameters and carrier mobilities. The parameters studied were (a) center-to-center distance, and (b) NW height. Curves with the same color are with the same mobilities. Solid lines are simulated with photon recycling considered, and dashed lines are simulated without photon recycling.

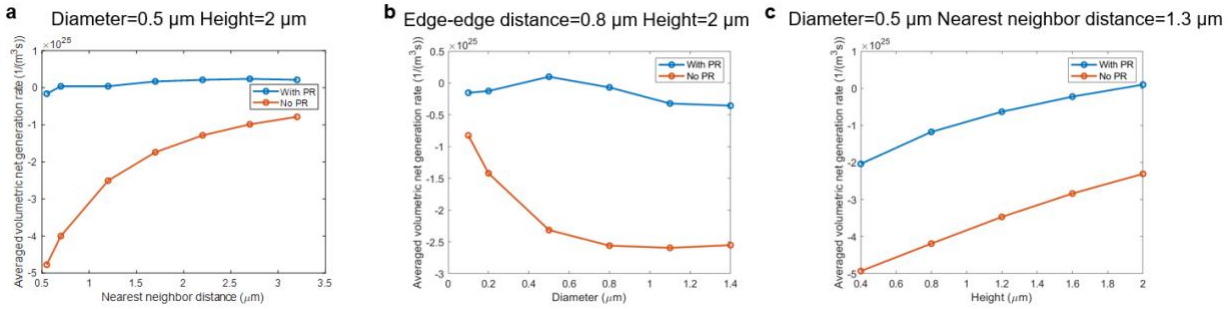

Figure D24. Averaged volumetric net generation rate in the neighboring NW versus (a) nearest neighbor distance, (b) diameter, and (c) height using baseline values in Table 6.1. Net generation rate is defined as the difference between generation rate and recombination rate. Blue and orange lines correspond to with photon recycling and no photon recycling, respectively.

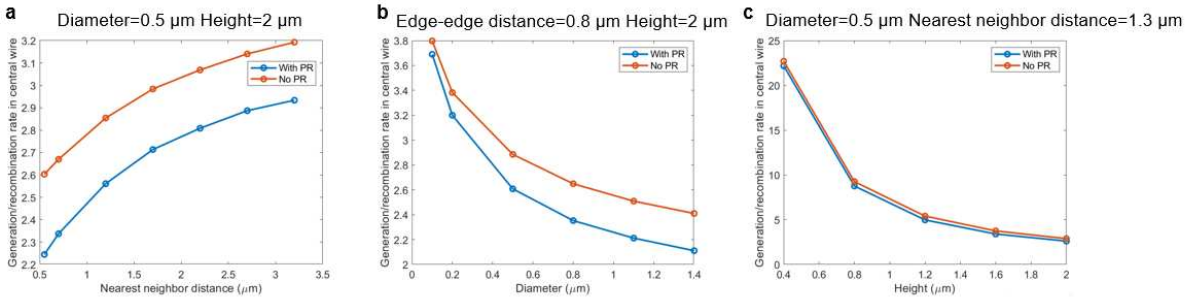

Figure D25. Ratio of generation rate and recombination rate in the central NW versus (a) nearest neighbor distance, (b) diameter, and (c) height using baseline values in Table 6.1. Generation and recombination rates are obtained by integrating the corresponding spatial profiles of the volumetric generation and recombination rates.

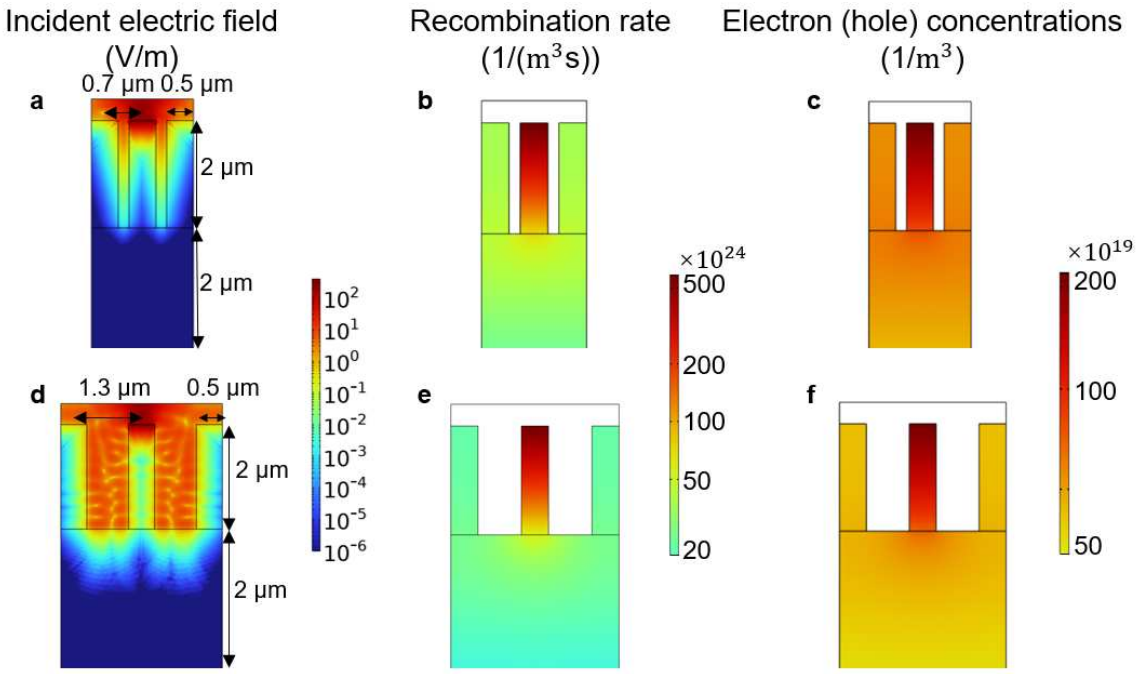

Figure D26. 2D profiles in the COMSOL model for (a),(d) incident electric field, (b),(e) recombination rate, and (c),(f) electron (hole) concentrations. Photon re-emission and re-absorption are not considered. The top and bottom panels are with two different nearest neighbor distances, 0.7 μm and 1.3 μm, respectively, and other NW geometric

parameters are fixed as shown in the figure: diameter = 0.5 μm, height = 2 μm. A truncated substrate of 2 μm is shown here. Other parameters involved in the model refer to the baseline values in Table 6.1 of the Main Text, including refractive index, absorption coefficient, mobility, radiative recombination factor, and surface recombination velocity.

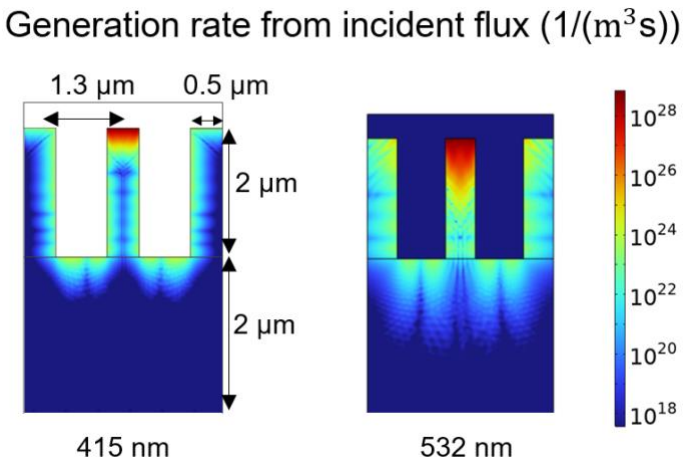

Figure D27. Generation rates from two light sources with different wavelengths of 415 nm and 532 nm.

D9. Electron Beam Induced Current (EBIC) Measurements

Electron beam induced current (EBIC) measurements were performed in an SEM retrofitted with a nanomanipulator probe, using a previously described procedure.[13,14] Briefly, the as-grown InP NWs were mounted on an Al specimen holder using vacuum compatible Ag colloid paint that also formed the backside Ohmic contact. Individual NWs were then contacted with a W tip coated with Au, as shown in Figure D28a. Current-voltage (I-V) measurements, collected with the bias applied to the tip and shown as inset, are consistent with n-doping of the InP NWs. The EBIC maps (Figure D28b) are generated by scanning the electron beam accelerated to 10 kV, while collecting the generated current using a Keithley 428 transimpedance amplifier connected to a data acquisition system. Plots of the EBIC signal, I_{EBIC}, versus the distance x from the probe along the NW length are shown in Figure D28c for three NWs, along with fits to Eq. D36,

$$I_{EBIC} = I_o exp\left(-\frac{x}{L_D}\right) \qquad \text{Eq. D36}$$

where I_o is a constant, and L_D is the hole diffusion length. The calculated diffusion lengths along with the uncertainty derived from the fits, are also shown in Figure D28c. Note that at this

accelerating voltage, the approximate electron-hole generation diameter is approximately 50 nm, based on a Monte Carlo simulation of electron trajectories in InP.[15] To calculate the hole mobility, we first estimated the diffusivity, $D = {L_D^2}/{\tau}$, where τ is the hole lifetime. Using the published value for hole lifetime in InP NWs of ~1.5 ns[16], and using the Einstein relation for mobility, we obtain a mobility range of ~35 – 55 cm^2/Vs. Compared to ~200 cm^2/Vs typically observed for bulk InP[17], the lower mobility for the NWs is consistent with increased surface recombination in nanostructures due to higher surface to volume ratio and the challenge of passivating semiconductor surfaces.[18]

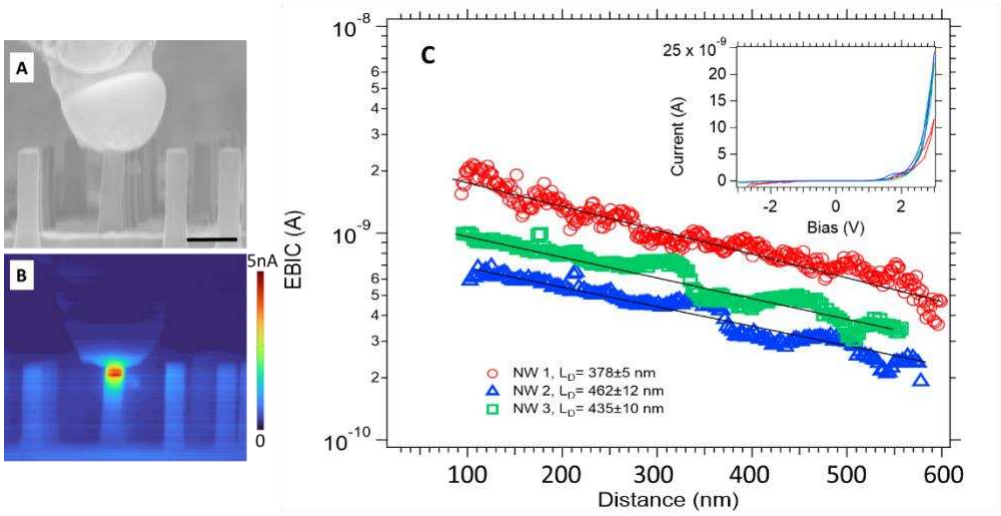

Figure D28. (a) An SEM image of a W/Au probe touching an InP NW. (b) An EBIC map showing hole collection efficiency collected at 10 kV accelerating voltage. (c) EBIC signal plotted versus distance from the probe contact along the NW length with fits to Eq. D36, and an inset of the I-V characteristics indicating Schottky barrier formation at the NW/probe interface.

REFERENCES

(1) Karouta, F. A Practical Approach to Reactive Ion Etching. *J. Phys. Appl. Phys.* **2014**, *47* (23), 233501. https://doi.org/10.1088/0022-3727/47/23/233501.
(2) Zannier, V.; Trautvetter, J.; Sivan, A. K.; Rossi, F.; De Matteis, D.; Abad, B.; Rurali, R.; Sorba, L.; Zardo, I. InAs–InP Superlattice Nanowires with Tunable Phonon Frequencies. *Adv. Phys. Res.* **2024**, *3* (6), 2300157. https://doi.org/10.1002/apxr.202300157.
(3) Park, J. H.; Pozuelo, M.; Setiawan, B. P. D.; Chung, C.-H. Self-Catalyzed Growth and Characterization of In(As)P Nanowires on InP(111)B Using Metal-Organic Chemical Vapor Deposition. *Nanoscale Res. Lett.* **2016**, *11* (1), 208. https://doi.org/10.1186/s11671-016-1427-4.
(4) Dhaka, V.; Pale, V.; Khayrudinov, V.; Kakko, J.-P.; Haggren, T.; Jiang, H.; Kauppinen, E.; Lipsanen, H. Synthesis and Properties of Ultra-Long InP Nanowires on Glass. *Nanotechnology* **2016**, *27* (50), 505606. https://doi.org/10.1088/0957-4484/27/50/505606.
(5) Anttu, N.; Abrand, A.; Asoli, D.; Heurlin, M.; Åberg, I.; Samuelson, L.; Borgström, M. Absorption of Light in InP Nanowire Arrays. *Nano Res.* **2014**, *7* (6), 816–823. https://doi.org/10.1007/s12274-014-0442-y.
(6) Black, L. E.; Cavalli, A.; Verheijen, M. A.; Haverkort, J. E. M.; Bakkers, E. P. A. M.; Kessels, W. M. M. Effective Surface Passivation of InP Nanowires by Atomic-Layer-Deposited Al_2O_3 with PO_x Interlayer. *Nano Lett.* **2017**, *17* (10), 6287–6294. https://doi.org/10.1021/acs.nanolett.7b02972.
(7) Evans, R. C.; Nilsson, Z. N.; Sambur, J. B. High-Throughput Single-Nanoparticle-Level Imaging of Electrochemical Ion Insertion Reactions. *Anal. Chem.* **2019**, *91* (23), 14983–14991. https://doi.org/10.1021/acs.analchem.9b03487.
(8) Wang, L.; Sambur, J. B. Efficient Ultrathin Liquid Junction Photovoltaics Based on Transition Metal Dichalcogenides. *Nano Lett.* **2019**, *19* (5), 2960–2967. https://doi.org/10.1021/acs.nanolett.9b00070.
(9) Adachi, S. Optical Dispersion Relations for GaP, GaAs, GaSb, InP, InAs, InSb, AlxGa1−xAs, and In1−xGaxAsyP1−y. *J. Appl. Phys.* **1989**, *66* (12), 6030–6040. https://doi.org/10.1063/1.343580.
(10) Gillespie, D. T. A General Method for Numerically Simulating the Stochastic Time Evolution of Coupled Chemical Reactions. *J. Comput. Phys.* **1976**, *22* (4), 403–434. https://doi.org/10.1016/0021-9991(76)90041-3.
(11) Bortz, A. B.; Kalos, M. H.; Lebowitz, J. L. A New Algorithm for Monte Carlo Simulation of Ising Spin Systems. *J. Comput. Phys.* **1975**, *17* (1), 10–18. https://doi.org/10.1016/0021-9991(75)90060-1.
(12) Bothra, S.; Tyagi, S.; Ghandhi, S. K.; Borrego, J. M. Surface Recombination Velocity and Lifetime in InP. *Solid-State Electron.* **1991**, *34* (1), 47–50. https://doi.org/10.1016/0038-1101(91)90199-9.
(13) Triplett, M.; Yang, Y.; Léonard, F.; Talin, A. A.; Islam, M. S.; Yu, D. Long Minority Carrier Diffusion Lengths in Bridged Silicon Nanowires. *Nano Lett.* **2015**, *15* (1), 523–529. https://doi.org/10.1021/nl503870u.
(14) Zutter, B.; Chen, Z.; Barrera, L.; Gaieck, W.; Lapp, A. S.; Watanabe, K.; Kudo, A.; Esposito, D. V.; Bala Chandran, R.; Ardo, S.; Talin, A. A. Single-Particle Measurements Reveal the Origin of Low Solar-to-Hydrogen Efficiency of Rh-Doped $SrTiO_3$ Photocatalysts. *ACS Nano* **2023**, *17* (10), 9405–9414. https://doi.org/10.1021/acsnano.3c01448.

(15) Demers, H.; Poirier-Demers, N.; De Jonge, N.; Drouin, D. CASINO Monte Carlo Simulations of Scanning Transmission Electron Microscopy. *Microsc. Microanal.* **2010**, *16* (S2), 258–259. https://doi.org/10.1017/S1431927610059490.
(16) Malheiros-Silveira, G. N.; Lu, F.; Bhattacharya, I.; Tran, T.-T. D.; Sun, H.; Chang-Hasnain, C. J. III–V Compound Semiconductor Nanopillars Monolithically Integrated to Silicon Photonics. *ACS Photonics* **2017**, *4* (5), 1021–1025. https://doi.org/10.1021/acsphotonics.6b01035.
(17) Sze, S. M.; Li, Y.; Ng, K. K. *Physics of Semiconductor Devices*, Fourth edition.; Wiley: Hoboken, NJ Chichester, West Sussex, 2021.
(18) Léonard, F.; Talin, A. A. Electrical Contacts to One- and Two-Dimensional Nanomaterials. *Nat. Nanotechnol.* **2011**, *6* (12), 773–783. https://doi.org/10.1038/nnano.2011.196.
(19) Griffiths, D. J. *Introduction to Electrodynamics*, 4th ed.; Cambridge University Press, 2017. https://doi.org/10.1017/9781108333511.
(20) Hu, L.; Chen, G. Analysis of Optical Absorption in Silicon Nanowire Arrays for Photovoltaic Applications. *Nano Lett.* **2007**, *7* (11), 3249–3252. https://doi.org/10.1021/nl071018b.
(21) Nelson, J. *The Physics of Solar Cells*; Imperial College Press, 2003.

APPENDIX E: SUPPORTING INFORMATION FOR CHAPTER 7

E1. Instrument Response Function (IRF)

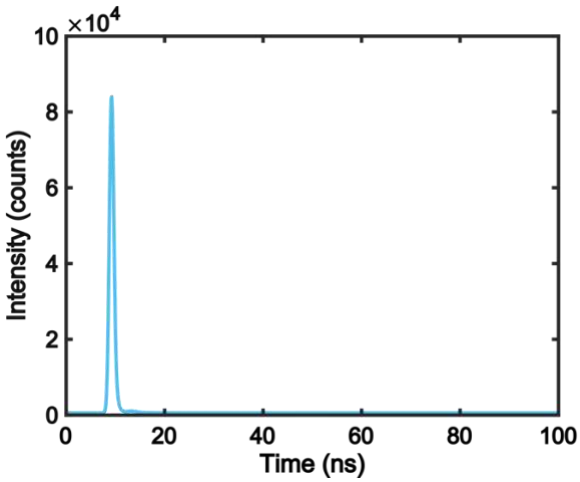

Figure E1. The IRF was measured via laser scattering from a solution of colloidal silica (LUDOX). TRPL data shown in the main text was deconvoluted from the IRF using a general bi-exponential equation with a background offset.

E2. Single-Molecule Blinking Analysis

To analyze single-molecule fluorescence trajectories of nanocrystals (NCs), a custom MATLAB script was used to process a movie file consisting of .tif images. The movie was loaded as a 3D matrix containing the full image sequence. A reference image for ROI selection was generated by averaging all frames to minimize noise, unless there was drift where the first frame was used instead. A zoomed-in region centered within the field of view was defined to facilitate easier selection of NCs and even TIRF illumination. Within this region, manual clicking of nanocrystal positions generated a set of regions of interest (ROIs). Background ROIs were manually created by clicking a nearby region free of signal, enabling local background correction for each nanocrystal.

To extract time-dependent fluorescence intensity trajectories from a stack of microscopy images, a function was created which uses the following inputs: the full movie frames, the raw and background ROIs, spatial offset coordinates from the zoom-in region, the acquisition frame rate,

and the total estimated drift in pixels over the course of the movie, which was determined via analyzing movies in ImageJ. For each ROI, the function first maps the local coordinates of the raw and background masks to global coordinates by adding the appropriate offsets. It then loops through each frame in the movie and applies a frame-specific vertical shift ("yDrift") to simulate or correct for sample drift over time. This drift is distributed linearly across frames based on the "totalDrift" parameter and the number of frames. Figure E2 shows the effect of the drift correction by varying the drift pixel value on the single-molecule blinking trajectories. To verify the accuracy of the drift correction, the script plotted the centroid positions of each ROI overlaid on both the first and last frames of the movie. This allowed visual confirmation that drift compensation aligned nanocrystals consistently across time.

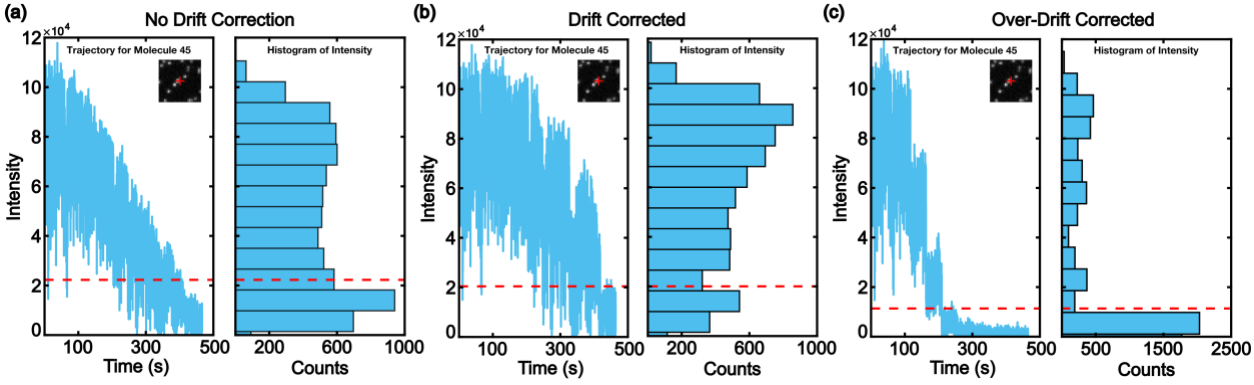

Figure E2. The effect of varying pixel drift on single-molecule blinking trajectories. (a) An example of when no drift-correction was applied. (b) An example of when a 5 pixel drift was applied. (c) An example of when a 10 pixel drift was applied.

Next, the function calculates the total raw signal as the sum of pixel intensities within the NC ROI. The background signal is computed as the average pixel intensity in the background ROI, which is then subtracted from the NC sum to yield a background-corrected fluorescence value. This background-corrected intensity is stored in a matrix called "finalTrajectories", where each row corresponds to a movie frame and each column to a different ROI (i.e., a single nanocrystal). The background subtracted process is shown in Figure E3.

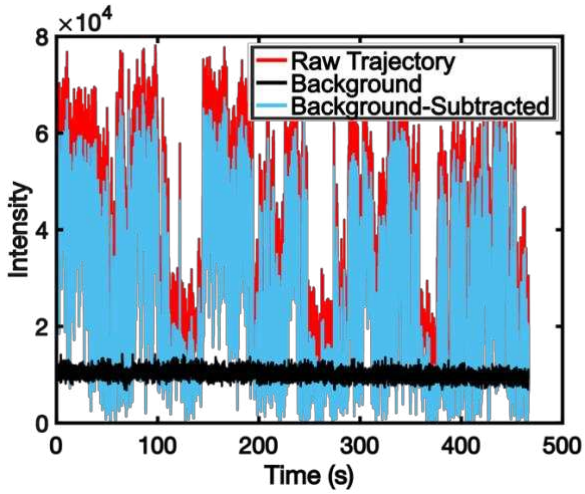

Figure E3. Background subtraction procedure. The red trace shows a raw trajectory, the black trace shows the background trajectory, and the blue trace shows the background subtracted trajectory.